UNIVERSITY OF CALIFORNIA

Santa Barbara

Phase Equilibria and Toughness of Zirconia-Based Thermal Barrier Coatings

A Dissertation submitted in partial satisfaction of the requirements for the degree of

Doctor of Philosophy

in

Materials

by

Chandra Ann Macauley

Committee in Charge:

Professor Carlos G. Levi, Chair

Professor Anton Van der Ven

Professor Ram Seshadri

Professor Michael J. Gordon

December 2016

The dissertation of Chandra Ann Macauley is approved

Michael J. Gordon

Ram Seshadri

Anton Van der Ven

Carlos G. Levi, Committee Chair

November 2016

Phase Equilibria and Toughness of Zirconia-Based Thermal Barrier Coatings

By

Chandra Ann Macauley

ACKNOWLEDGEMENTS

As with any worthwhile pursuit, my graduate school experience has been transformative. I have many people to thank for their roles in enabling my scientific, professional and personal development during my doctorate. First and foremost, I am grateful for the time and energy my advisor, Professor Carlos Levi, devoted to me during my time at UCSB. Carlos, thank you for giving me opportunities to interact closely with industry, foster international research collaborations and present my work at national and international conferences. I must also acknowledge the other members of my dissertation committee including Professors Anton Van der Ven, Ram Seshadri, and Michael Gordon for their commitment of time and energy to support my professional development.

I have enjoyed being a part of the friendly and collaborative environment of the structural materials group. Matt and Kyle Begley deserve special thanks for playing a part in fostering a sense of community by opening their home for the well-loved BTS events. I would like to thank all present and past members of the Levi group for sharing their experimental expertise, scientific understanding and advice on how to navigate the challenges of graduate school. In particular, thank you to Jessica Krogstad (now at UIUC) and David Poerschke for sharing their knowledge and passions as mentors and friends. Thanks to Stefan Heinze for the many engaging scientific discussions that always started with “Can I ask you a quick question?”. I am grateful for Daesung Park’s patience and willingness to share his expertise in electron microscopy. I am thankful for the generous Mathematica assistance, ultimate Frisbee tips, and friendship of Michael Rossol. I would also like to asknowledge Jason Van Sluytman, Kaylan Wessels, Erin Donohue and Elisa Zaleski for their advice and friendship. Throughout my time at UCSB I had the privilege of

working with and mentoring three interns. In particular I would like to acknowledge Abel Fernandez for his constant curiosity and eagerness to learn new skills over the last ~3 years. His dedication to research resulted in a substantial contribution to this work. I am also thankful for the experimental assistance of interns Maritza Sanchez and Connie Phung.

Most of the research in this document was performed in the collaborative environment at UCSB, making use of the Materials Processing Laboratory and the Materials Research Laboratory Central Facilities (NSF DMR-1121053). Research progress would have been significantly hindered if not for the expertise of the technical and research staff that keep these facilities running. I would like to thank Deryck Stave, Stephan Krämer and Mark Cornish, in particular. I owe much of my electron microscopy knowledge to the extraordinary patience and teaching skills of Stephan. I thank Deryck and Mark for many useful discussions over the years and Gareth Seward in the Earth science microscopy facility for sharing his knowledge of electron probe micro-analysis.

I would like to acknowledge support from a Graduate Opportunity Fellowship from the University of California (2011) and a National Science Foundation Graduate Research Fellowship (2011-2016). This work was funded through an NSF-GOALI program, DMR-1105672, in collaboration with GE Global Research Center. The program fostered unique interactions with industry and resulted in rewarding relationships and collaborations. I am grateful for the mentorship of Don Lipkin, whose commitment to maintaining the connection to UCSB is critical to the success of the GOALI program. I also thank Curt Johnson for many stimulating discussions and advice. There are many people at GE and more broadly in the SYDES “family” who deserve acknowledgement – the advice and insights they provided at annual review meetings shaped this work.

I am grateful for the assistance of many collaborators in academia as well. Sanjay Sampath and Vaishak Viswanathan (Stony Brook University) deposited materials that enabled the investigation of segregation in alternative thermal barrier coating materials. I thoroughly enjoyed working with Julie Cairney and Peter Felfer (now professor at FAU Erlangen) at the Australian Center for Microscopy and Microanalysis at the University of Sydney. I would also like to acknowledge the many students, staff and other professors who made my stay at the ACMM productive and enjoyable. Through my collaboration with Kevin Hemker, Binwei Zhang and Jessica Krogstad at Johns Hopkins University I gained an appreciation for the challenges of mechanical testing and benefitted from their professional development advice. Although our work is not in this document, I am grateful to Kyle Webber and Philipp Geiger (previously at TU Darmstadt, now at FAU Erlangen) for their willingness to attempt experiments that had not been conducted before. Many of these collaborations would not have been possible without funding from the International Center for Materials Research (DMR 08-43934), which supported my research at the University of Sydney ACMM and TU Darmstadt as well as travel to Irsee, Germany and India for conferences.

Several incredible teachers who fueled my curiosity and encouraged me to pursue science and engineering have illuminated my path toward this achievement. In particular I would like to thank Mr. Lane Durray, Mr. Fred Michels, Mr. Rich McFate, Professor Paul Gannon (MSU), Professor Sarah Codd (MSU) and Professor Joe Seymour (MSU).

My acknowledgements would not be complete without recognizing the many close friends who supported me throughout my PhD. The Girls Study Group (GSG), made up of Chelsea Catania, Leah Kuritzky, and Abby Goldman, helped me succeed in the first couple

years of graduate school and beyond. I owe a tremendous thanks to my roommates over the years, especially Jackie Avallone, Megan Butala, and Katie O'Hara, for serving as scientific sounding boards, presentation muses and perhaps most importantly, my emotional support system.

To my parents, thank you for encouraging my curiosity, whether by buying me screwdrivers to take apart my toys, or helping me cut apart your Christmas lights to light my LEGO house. Your support of my endeavors, in the laboratory or in other countries, means the world to me. Kayleen – I am inspired by your kind heart and am so grateful to have you as a sister and friend. Finally, thank you, Andrew, for your unwavering support either in person or via Skype. There is no one else with whom I would rather explore continents, watch documentaries, or embark on the adventure of a lifetime.

VITA OF CHANDRA ANN MACAULEY

November 2016

Education

University of California Santa Barbara

- PhD Candidate, Materials Department, 2013

Montana State University, Bozeman

- BS, Department of Chemical and Biological Engineering, 2011

Fellowships

- International Center for Materials Research International Research Fellowship, Australian Center for Microscopy and Microanalysis, Australia (2015)
- National Science Foundation Graduate Research Fellowship (2011-2016)
- Graduate Opportunity Fellowship (201-2012)
- Tau Beta Pi Graduate Fellowship (2011-2012)

Publications

Felfer, P., I. McCarroll, **C. Macauley**, J. Cairney. "A simple approach to atom probe sample preparation by using shadow masks." (2016). *Ultramicroscopy*. 160, pp 163-167.

Anderson, I.E., R.A. Shircliff, **C. Macauley**, D.K. Smith, B.G. Lee, S. Agarwal, P. Stradins, and R.T. Collins. "Silanization of Low-Temperature-Plasma Synthesized Silicon Quantum Dots for Production of a Tunable, Stable, Colloidal Solution." (2012). *Journal of Physical Chemistry*. 116 (6) pp 3979-3987.

Macauley, C., P. Gannon, M. Deibert and P. White. "The influence of pre-treatment on the oxidation behavior of Co coatings on SOFC interconnects." (2010). *International Journal of Hydrogen Energy.* Vol. 36, Issue 7, pp. 4540-4548.

Van Sluytman, J. S., **C. A. Macauley**, C. G. Levi. "Tetragonal zirconia phase stability in the $YO_{1.5}$-$TaO_{2.5}$-ZrO_2 system." (2017). *Scripta Materialia*. In Preparation.

Macauley, C. A, A. Fernandez, J. S. Van Sluytman, C. G. Levi. "Phase equilibria in the ZrO_2-$YO_{1.5}$-$TaO_{2.5}$ system at 1500°C." (2017). *Journal of the European Ceramic Society.* In Preparation.

Macauley, C. A, A. Fernandez, J. S. Van Sluytman, C. G. Levi. "Phase equilibria in the ZrO_2-$YO_{1.5}$-$TaO_{2.5}$ system at 1250°C." (2017). *Journal of the European Ceramic Society*. In Preparation.

A. Fernandez, **C. A. Macauley**, D. Park, and C. G. Levi, "Phase Equilibria in the $YO_{1.5}$-$TaO_{2.5}$ System," *Journal of Alloys and Compounds*. In Preparation.

Presentations – Invited

Macauley, C. A. "Phase equilibria in the ZYTO system." (2013) *Johns Hopkins University, Mechanical Engineering Department,* Baltimore, MD, USA.

Macauley, C. A. "Investing in yourself: Is graduate school right for you?" (2014) *California State University, Northridge, Department of Chemistry and Biochemistry*. Northridge, California, USA.

Presentations – Contributed

Macauley, C. A., C. G. Levi. "Influence of Microstructure on the Toughness of Multi-Phase Compositions in the ZYTO System." (2016) *Indo-US Bilateral Workshop on Ceramic Coatings and Multilayers*, Coorg, Karnataka, India,

Macauley, C. A., C. G. Levi. "Opportunities and Challenges of Multiphase Ceramic Topcoats." (2016) *40th International Conference and Expo on Advanced Ceramics and Composites*, Daytona, FL, USA.

Macauley, C. A., B. Zhang, J. A. Krogstad, K. Hemker, C. G. Levi. "Toughening mechanisms in the $TaO_{2.5}$-$YO_{1.5}$-ZrO_2 system." (2015) *11th International Conference on Ceramic Materials and Components for Energy and Environmental Applications*, Vancouver, BC, Canada.

Macauley, C. A., J. Van Sluytman, A. Fernandez, C. G. Levi. "Phase relations in the $TaO_{2.5}$-$YO_{1.5}$-ZrO_2 system and implications for thermal barrier coatings." (2015) *International Conference on Metallurgical Coatings & Thin Films*, San Diego, CA, USA.

Macauley, C. A., C. G. Levi, D. M. Lipkin, S. Sampath. "The Influence of Process Parameters on the Microstructure Evolution of ZrO_2-CeO_2-TiO_2 Thermal Barrier Coatings", (2014) *38th International Conference and Expo on Advanced Ceramics and Composites*, Daytona, FL, USA.

Macauley, C. A., E. M. Donohue, D. M. Lipkin, C. G. Levi. "Investigating CeO_2+TiO_2 stabilized ZrO_2 for application in thermal barrier coatings." (2013) *International Conference on Metallurgical Coatings & Thin Films*, San Diego, CA, USA.

Macauley, C. A., P. White, P. Gannon, M. Deibert. "The influence of pre-treatment on the oxidation behavior of Co coatings on SOFC interconnects." (2009) *AIChE Pacific Northwest Regional Conference*, Vancouver, British Columbia, Canada.

Presentations – Poster

Macauley, C. A., A. N. Fernandez, S. G. Heinze, C. G. Levi, "Influence of microstructure on the toughness of compositions in the ZYTO system," (2016) *Winter Study Group on High Temperature Materials*, University of California, Santa Barbara, CA, USA.

Macauley, C. A., J.S. Van Sluytman, A. Fernandez, C.G. Levi, "Elucidation of the Yttria-Tantala-Zirconia Phase Diagram," (2014) *ECI Thermal Barrier Coatings IV*, Irsee, Germany

Macauley, C. A., V. Viswanathan, D. Lipkin, S. Sampath, C. Levi. "Influence of processing parameters on CeTiSZ thermal barrier coatings." (2014) *Materials Research Outreach Program Symposium*, Santa Barbara, CA, USA.

Macauley, C. A., V. Viswanathan, D. Lipkin, S. Sampath, C. Levi. "Influence of processing parameters on CeTiSZ thermal barrier coatings." (2014) *Winter Study Group on High Temperature Coatings*, Santa Barbara, CA, USA.

Macauley, C. A., D. Lipkin, C. Johnson, C. G. Levi. "Advanced Gas Turbine Coatings: Thermal Barrier Coatings (TBCs)-beyond Yttria Stabilized Zirconia (YSZ)," (2012) *GE Global Research Center*, Niskayuna, NY, USA.

Macauley, C. A., K. Hoyt, P. White, P. Gannon. "The influence of Cr_xO_y microstructure on the oxidation behavior of CoMn coatings on SOFC/SOEC interconnects." (2011) *Montana Space Grant Consortium Symposium*, Bozeman, MT, USA.

Professional Affiliations and Service

- American Ceramic Society (ACers)
- The Materials Information Society (ASM)
- The Minerals, Metals and Materials Society (TMS)
- Tau Beta Pi Engineering Honor Society
- Graduate Students for Diversity in Science (GSDS) - UCSB

ABSTRACT

Phase Equilibria and Toughness of Zirconia-Based Thermal Barrier Coatings

Chandra Ann Macauley

Thermal barrier coating (TBC) systems are critical to the performance of gas turbine engines in the aviation and power generation industries. As engine operating temperatures are increased to improve efficiency, ceramic topcoats that depend on a metastable tetragonal phase, namely *t'*-8YSZ (ZrO_2 + 8 ± 0.5 mol% $YO_{1.5}$), rapidly degrade. Alternative TBC compositions that exhibit combinations of properties superior to 8YSZ are needed to meet the efficiency targets of next generation gas turbines. In this work, two approaches are pursued based on either a single-phase, non-transformable tetragonal structure or multiphase compositions that offer the possibility of adequate toughness and resistance to molten silicates.

Previous laboratory investigations of the CeO_2-TiO_2-ZrO_2 (CeTiSZ) system revealed a relatively large, non-transformable tetragonal field with exceptional tetragonality is stable at 1350°C. In the present work, challenges with transitioning the earlier laboratory results to industrial scale coatings are elucidated. Two important effects not previously encountered in the deposition of current TBCs are identified. Understanding the driving force for segregation during deposition as well as the potential reducibility of the cations upon heating is critical to maintaining stable phase equilibria in thermally sprayed coatings. The reduction of cerium (IV) upon heating places an inherent limit on the temperature capabilities of CeTiSZ coatings.

Contrary to the CeTiSZ system, the ZrO_2-$YO_{1.5}$-$TaO_{2.5}$ (ZYTO) system does not experience reduction of the cations at high temperatures. A stable, non-transformable

tetragonal phase exists at temperatures up to 1500°C, albeit in a much narrower composition range. Although the ZrO_2-rich region of the ternary had been studied previously, there was a paucity of information on the phase equilibria in the rest of the diagram. Systematic investigation of the entire $YO_{1.5}$-$TaO_{2.5}$ binary phase diagram elucidates the equilibrium phases and serves as a solid foundation for the investigation of the ZYTO ternary. For the first time, isothermal sections of the complete ZYTO ternary are experimentally determined at 1250°C and 1500°C. Two-phase fields in the ZYTO ternary suggest that multiphase compositions with improved combinations of properties may be possible. Specifically, a large two-phase field in which fluorite and $YTaO_4$ (YT) are stable offers the potential to increase the toughness of fluorite, which, with sufficient rare earth content, can mitigate damage caused by molten silicates. Additionally incorporating YT as a second phase has the potential to improve the CMAS resistance of phase stable tetragonal compositions.

Similar to the phase equilibria, there was a dearth of information on the toughness values and associated toughening mechanisms of compositions in the ZrO_2-lean portion of the ZYTO phase diagram. Micro-indentation and micro-3-point bend experiments indicate that YT contributes to the toughness of multiphase samples. It is shown for the first time that samples containing YT exhibit microstructural features clearly consistent with domain wall motion, the fundamental mechanism underpinning ferroelastic toughening.

TABLE OF CONTENTS

CHAPTER 1: INTRODUCTION

There are tremendous economic and environmental incentives for the power generation and aero-propulsion industries to increase the efficiency of gas turbines. Both industries are experiencing remarkable growth. Thanks in part to the large supply of inexpensive natural gas from fracking, it is expected that natural gas power generation will surpass coal generation for the first time in 2016 [16EIA2]. While natural gas accounts for 33% of the electricity consumption in the US today [16EIA], that fraction is expected to increase because over 58% of projected capacity additions are natural gas-powered [16EIA2]. Furthermore, $742 billion (~1% of world GDP) was spent to transport over 3.5 billion airline passengers in 2015, a number which is expected to double by 2034 [15Pea, 15IATA]. Given the massive scope of these industries, small efficiency gains save billions of dollars and reduce combustion emissions by millions of tons each year [16Hin, 15Cor].

Gas turbine technology is central to both power generation and aviation industries. In a gas turbine (GT), Figure 1.1, intake air is first compressed before being mixed with fuel and the fuel is combusted. The hot combustion gases are then directed through a series of alternating stationary and rotating airfoils in the turbine, producing mechanical energy. The efficiency of gas turbines is limited by the capabilities of the structural materials in the hot gas path. As dictated by thermodynamics, the efficiency of a heat engine increases with operating temperature. Additionally the efficiency of GTs can be increased by reducing dependence on cooling air, which is diverted from the compressor and pumped through the turbine blades/buckets as shown in Figure 1.2. While film cooling and convective heat transfer inside the airfoils enable the components to withstand the extreme temperatures, it results in an efficiency debit, Figure 1.3 [16Pad, 09Per].

The development of structural materials with improved properties for hot gas path components has spanned over 60 years and has resulted in significant improvements in system performance, Figure 1.4. Improvements in alloy composition and processing of the nickel-based superalloys, from which most hot section components are fabricated, have contributed to the baseline increase in operating temperature. The introduction of the thermal barrier coating (TBC) system in addition to internal cooling enabled further surface temperature increases without exceeding the metal capabilities. The TBC system, Figure 1.5, is composed of a low thermal conductivity, columnar ceramic coating on top of a thermally grown oxide (TGO) of alumina, which forms during operation and prevents oxygen ingress into the metallic components. While the TBC system encompasses much more than the ceramic topcoat, it is the topcoat that is commonly referred to as a TBC, and will be for the remainder of this dissertation. Below the TGO is an aluminum-rich bond coat, which serves as an aluminum reservoir and prevents diffusion from the nickel-based superalloy. Improvements in the strength and oxidation resistance of the bond coat, e.g. [16Jor], are needed to fully exploit the thermal protection of the topcoat. However if the surface temperatures of the ceramic topcoat are to be increased, further increases in the temperature capabilities of the bond coat are also required.

To perform their function, the ceramic topcoat must satisfy several demands simultaneously, such as low thermal conductivity, phase stability, processability, resistance to molten silicates, and adequate toughness [12Cla]. The current, industry-standard topcoat, based on 8 ± 0.5mole% $YO_{1.5}$-stabilized zirconia (8YSZ), relies on a metastable non-transformable tetragonal phase, *t'*, and therefore is limited by loss of phase stability [13Lip] and inability to mitigate coating degradation caused by molten silicates [12Lev, 06Kra]. A suitable single-phase replacement for 8YSZ has thus remained elusive. Novel TBCs with improved properties relative to 8YSZ are needed to withstand the higher temperatures and harsher environments of more efficient gas turbine engines in the aviation and power generation

industries. This work has approached this challenge in two ways: first by stabilizing zirconia with isovalent, but different sized cations in the CeO_2-TiO_2-ZrO_2 system and second by stabilizing zirconia using aliovalent cations in the ZrO_2-$YO_{1.5}$-$TaO_{2.5}$ system. In each system, the objective was to elucidate the phase evolution and equilibria as well as determine the toughness and possible toughening mechanisms.

To address these topics, the dissertation is organized as follows. A review of concepts and relevant literature, including a review of toughening mechanisms, is presented in Chapter 2. Experimental methods, characterization techniques and mechanical testing procedures are described in Chapter 3. Thermal stability and toughness studies in the CeO_2-TiO_2-ZrO_2 system as well as lessons learned when transitioning from lab scale pellets to industry-scale coatings are described in Chapter 4.

Applying these lessons, the focus then shifts to work in the ZrO_2-$YO_{1.5}$-$TaO_{2.5}$ (ZYTO) system beginning with elucidation of the $YO_{1.5}$-$TaO_{2.5}$ binary in Chapter 5. Knowledge gained in the investigation of the binary system informed the determination of the ZYTO isothermal sections at 1250 and 1500°C, presented in Chapter 6.

With an understanding of the equilibrium phases at high temperatures it was possible to identify promising compositions in the ZYTO system. Investigating the toughness and toughening mechanisms of those compositions using a micro-three-point bend technique, among other methods, is the subject of Chapter 7.

Finally, the broad conclusions and implications of this work as well as future directions for the development these concepts are discussed in Chapter 8.

Figures

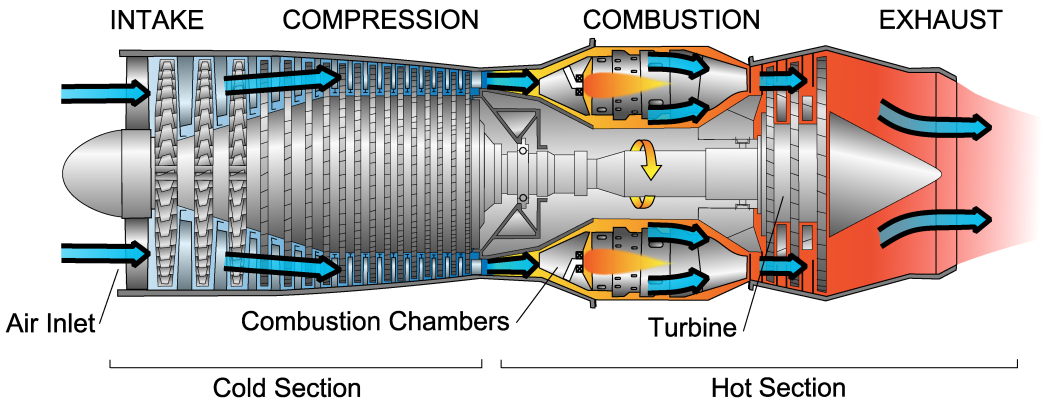

Figure 1.1 Schematic of the thermal barrier coating system from https://commons.wikimedia.org/wiki/File:Jet_engine.svg

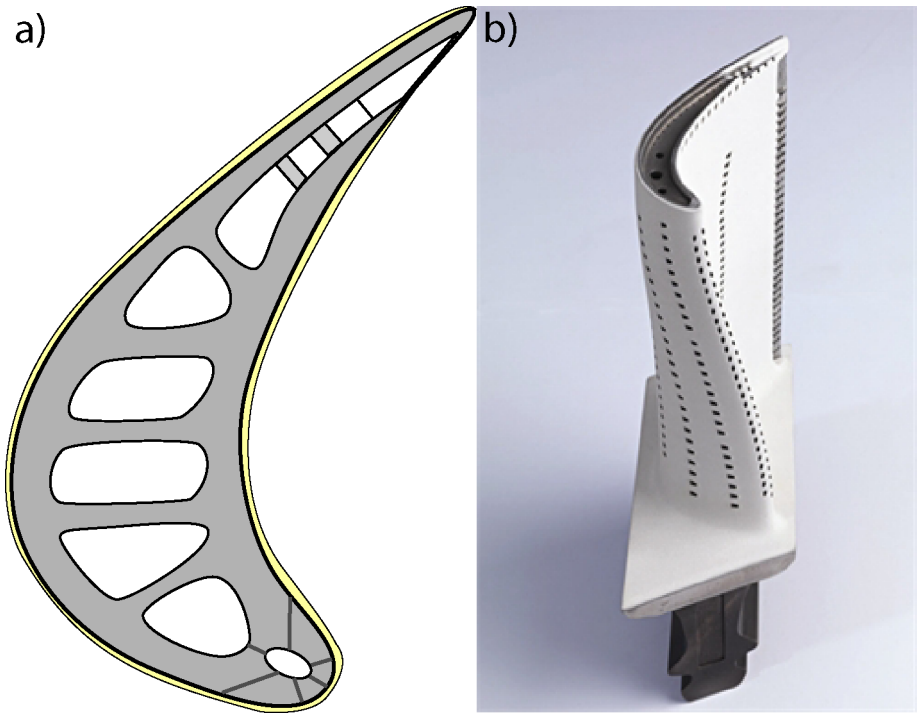

Figure 1.2 Air passes through (a) internal channels and exits through (b) holes on the surface of the blade to cool the part. Figure (a) from C. G. Levi and (b) from Winbro Group Technologies.

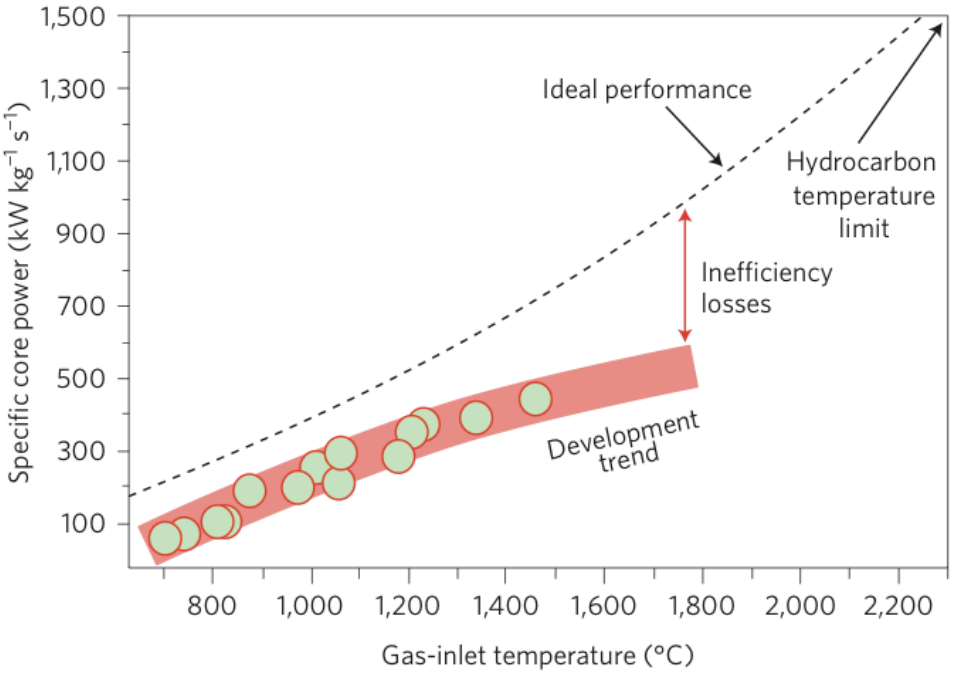

Figure 1.3 Redirection of intake air through the blade to provide film cooling results in reduced efficiency [16Pad].

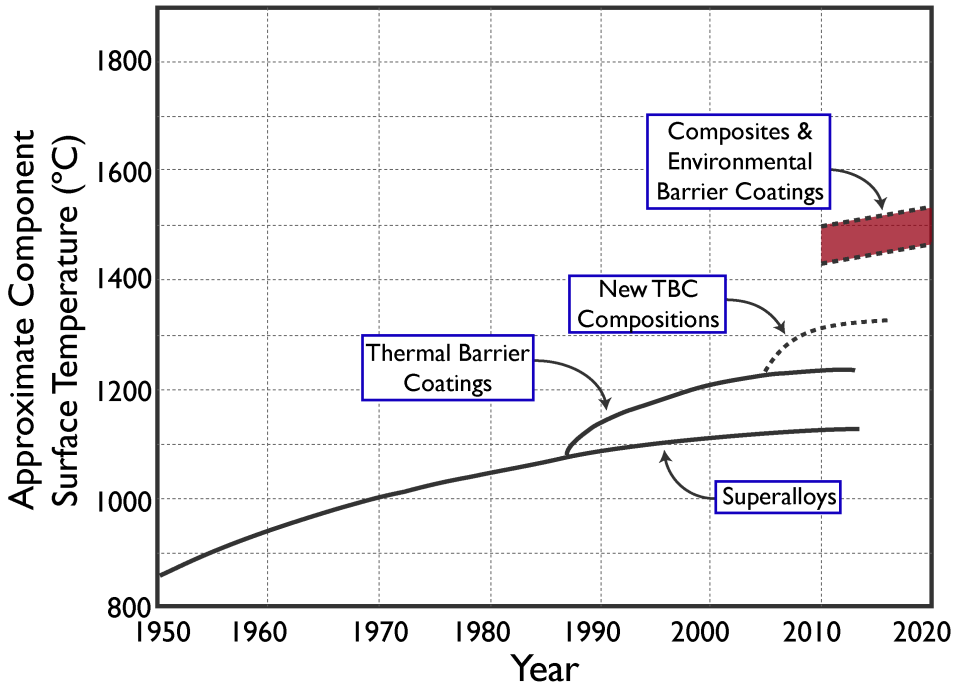

Graph adapted from F.W. Zok, A.G. Evans, and R. Schafrik

Figure 1.4 Development of advanced structural materials has led to increased component temperatures and the concomitant improvements in engine efficiency.

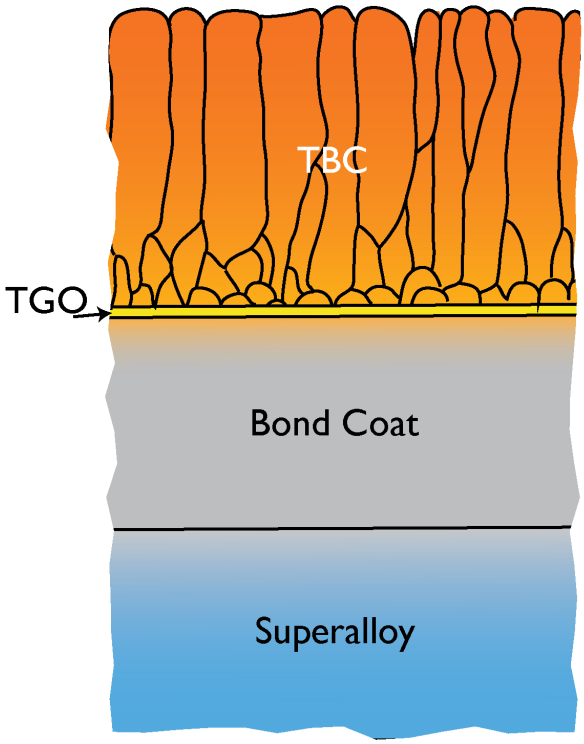

Figure 1.5 Schematic of the thermal barrier system, adapted from Jessica Krogstad.

CHAPTER 2: BACKGROUND

For the last 30 years, 8 ± 0.5mole% $YO_{1.5}$ stabilized zirconia (8YSZ) has been the industry standard thermal barrier coating (TBC) due to its seemingly optimal combination of properties. Burner rig and furnace cycle tests in the 1970's showed that TBC compositions of ~6-8 mole $YO_{1.5}$ had significantly longer lifetimes than ~20 mole% $YO_{1.5}$ (20YSZ) coatings [79Ste], which have lower thermal conductivity [00Bis], Figure 2.1. However the debit in thermal resistivity is well worth the improvement in coating durability.

The TBC system in general and the ceramic topcoat in particular epitomize the challenges of multi-functional materials. This chapter will first provide an overview of the often-competing properties a TBC must exhibit and the compromises therein. It is clear that 8YSZ is lacking in several of the required properties for next generation engines, including phase stability, thermal conductivity, sintering resistance and ability to mitigate damage by molten silicates. Drawing insights from stabilization and toughening mechanisms in zirconia, this dissertation will focus on investigating the phase stability and toughness of alternative TBCs.

2.1 Considerations and requirements for TBCs

The primary function of TBCs is to provide thermal protection via their low thermal conductivity, but the extremely aggressive thermo-chemical and thermo-mechanical environment in which they operate demands they meet several other performance criteria. The crystal structure (phase) and microstructure of TBCs must be stable with long thermal exposures at high temperature, as long as 30,000 hours for power generation. Additionally it is important that the TBC is able to accommodate thermal strain and exhibit adequate extrinsic toughness, both of which can be improved by engineering the microstructure via current coating deposition technologies. To improve coating adhesion, TBCs must be

chemically stable with the thermally grown oxide (TGO). In addition to all of these properties, novel TBCs must also mitigate attack by molten silicates, especially in propulsion applications [96Bor, 12Lev]. An understanding of these properties provides a foundation on which novel TBCs can be developed, motivating the overview presented in the following paragraphs.

2.1.1 Low thermal conductivity

In order to perform its function as a thermal barrier, a TBC must first and foremost have low thermal conductivity. Dense 8YSZ has a thermal conductivity (k) of 5 W/mK [00Bis], but that value can be significantly modified by engineering the microstructure of the coating [12Sam]. As-deposited coatings incorporate 10-30% porosity, which reduces the thermal conductivity of 8YSZ to 20-60% of its dense value, depending on the coating technique [03Kul, 12Sam, 06Flo]. Throughout service, however, the thermal conductivity of YSZ coatings increases due to sintering of pores in the microstructure [09Tan, 06Flo]. It is therefore advantageous for novel TBCs to exhibit slow densification.

While the effective thermal conductiviy can be reduced by altering the coating microstructure, it is important to consider the factors that contribute to a material's intrinsic thermal conductivity. The main mechanism for heat transport through zirconia below 1200°C occurs via lattice phonons. The simplist equation for thermal conductivity (k) by Debye can be found in most solid state physics textbooks as:

$$k = \frac{C_V V_m \Lambda}{3} \qquad 2.1$$

Where C_v is the specific heat capacity, V_m is the acoustic velocity, and Λ is the phonon mean free path. A common strategy to reduce k is to decrease Λ. In fact, the minimum k is defined by when Λ is equal to the interatomic spacing. There are various mechanisms by which Λ,

and consequently *k*, can be reduced. These include lattice defects such as oxygen vacancies and atom mass contrast and lattice strain caused by different size ions, as discussed below.

Oxygen vacancies are excellent phonon scatterers and are responsible for the relatively low *k* of dense 8YSZ as well as many other trivalently stabilized zirconia ceramics [14Fer]. As discussed in Section 2.2, oxygen vacancies are necessary to maintain charge balance when a trivalent cation substitutes in tetravalent ZrO_2 By increasing the concentration of oxygen vacancies, *k* decreases, as seen in Figure 2.2. Rare earth-rich compositions such as $Y_2Zr_2O_7$ have lower *k* than 8YSZ [04Lev, 00Vas, 05Cla]. Unfortunately, durability, as measured by cyclic lifetime or toughness, also decreases with increasing trivalent dopant concentration, i.e. Figure 2.1, [04Lev] due to the lack of intrinsic toughening mechanisms [07Sch].

Thermal conductivity can be reduced in the absence of oxygen vacancies by introducing substitutional defects [01Rag]. It is also important that the substitutional cations have high atomic masses [05Cla] since *k* scales inversely with the square root of the mean atomic mass of the compound. For example compositions that are stabilized by Yb^{3+} (173amu) have lower thermal conductivities than materials stabilized with Y^{3+} (88.9amu) [11Liu]. Substitutional defects are most effective at reducing *k* when there is also mass disorder among the cations present, which further reduces the phonon mean free path, Λ [14Lim, 10She2, 05Cla]. Mass disorder, or mass contrast, refers to the differences in atomic mass of cations that sit on the same crystallographic sites. Examining 8YSZ in light of the importance of mass disorder reveals the efficacy of oxygen vacancies at reducing *k* since Y^{3+} (88.9amu) and Zr^{4+} (91.2amu) have nearly the same mass. The solid solution tetragonal (*t*) phase in the ZrO_2-$YO_{1.5}$-$TaO_{2.5}$ (ZYTO) system, which lacks oxygen vacancies because it is stabilized by equimolar concentrations of $YO_{1.5}$ and $TaO_{2.5}$, is an excellent example of a material with high mass disorder. The atomic mass of Ta (180.9amu) is approximately double that of Y and Zr. Thermal conductivities of *t* in the ZYTO system are equal to or

lower than that of 8YSZ [10She2, 01Rag]. The mass disorder is so high in many of the crystalline phases in the ZYTO system that k is relatively insensitive to changes in composition or phase content [14Lim]. The thermal conductivity of t in the ZYTO system can be further reduced by substituting small amounts of $GdO_{1.5}$ for $YO_{1.5}$, likely due to a combination of the higher atomic mass of Gd (157.25amu) relative to Y and increased mass disorder [10Son]. It has also been postulated that utilizing cations with differing ionic radii introduces strain in the crystal lattice which decreases k [03Sch]. This is one possible explanation for why k decreases with increasing dopant cationic radii. Another method of decreasing Λ, which is important in the field of thermoelectrics, is the introduction of grain boundaries. While grain and interphase boundaries do reduce k in nano-grained materials, the effect is small once grains are larger than 200nm [14Lim]. Grains in TBCs are often much larger than 200nm and grow with thermal exposure, thus the influence of grain boundaries at decreasing k is not relevant for TBCs.

These mechanisms of reducing thermal conductivity are by no means mutually exclusive. The zirconates are excellent examples of materials that utilize oxygen vacancies, different sized cations, large average atomic mass and mass disorder to reduce thermal conductivity. Rare earth zirconates have the formula $RE_2Zr_2O_7$ and have the pyrochlore crystal structure. The high temperature (700-1200°C) thermal conductivity of Gd, Eu, Sm, Nd, and La zirconates ranges from 1.1 to 1.7W/mK, which is less than half the thermal conductivity of 8YSZ [00Mal, 00Vas, 98Sur, 03Leh].

It is desirable that novel TBC materials have an even lower thermal conductivity than 8YSZ, to yield larger reductions in temperature with equivalent thickness. By utilizing one or more of the intrinsic mechanisms described above in combination with clever coating deposition processes, novel TBCs with even lower thermal conductivity can be envisioned. However,

as will be described below, compromises must be made between reductions in thermal conductivity and a multitude of other TBC requirements.

2.1.2 Phase stability

Another important property of TBCs is the absence of deleterious phase transformations at temperature or during thermal cycling, especially those involving disruptive volume changes that can induce microcracking and degradation of mechanical properties. This is generically known as "phase stability". Pure ZrO_2 is cubic (fluorite, *F*, $Fm\bar{3}m$) above 2377°C until it melts at ~2710°C. It transforms to tetragonal (*t*, $P4_2/nmc$) below 2377°C and then to the monoclinic form (baddeleyite, *m*, $P2_1/c$) below ~1205°C [04Wan]. The latter transformation involves a large dilatation (~4%) and is therefore disruptive. Addition of $YO_{1.5}$ stabilizes ZrO_2 against the $t \rightarrow m$ transformation, and eventually against the $F \rightarrow t$ transformation, as illustrated in the $YO_{1.5}$-ZrO_2 binary in Figure 2.3. As deposited, 8YSZ comprises a single-phase, "non-transformable" tetragonal structure known as *t*-prime (*t'*), which is metastable due to its location in the two-phase, $t + F$ or $m + F$, regions. At high temperatures, such as those in current gas turbine engines (~1200°C), the thermodynamic and kinetic driving forces are sufficient for *t'* to separate into the equilibrium yttria-lean tetragonal phase (*t*) and the yttria-rich cubic (*F*) phase. Contrary to previously accepted understanding, this phase separation begins within minutes at 1482°C [11Kro, 15Kro] but the *t* phase remains non-transformable due to a combination of mechanical constraint to the expansion associated with the transformation, owing to the surrounding *F* phase, and its presence in small, domains coherent with *F*. Once lamellae of the equilibrium tetragonal and *F* phases coarsen beyond a critical size and become incoherent, the $YO_{1.5}$-lean tetragonal can transform to monoclinic (*m*) on cooling [11Kro]. The metastability of *t'*-8YSZ places an inherent limit on the temperatures at which it can used for the desired service lifetimes (~30,000 hours). Since most TBCs in service utilize *t*-ZrO_2-based coatings, there is a tremendous incentive to

develop competitive compositions that are phase stable at higher temperatures while retaining the desirable attributes of 8YSZ. Because the mechanical performance of the TBC is associated with its tetragonal structure and degrades as the structure becomes cubic, as suggested by in Figure 1, it is desirable to retain tetragonality in the crystal structure of the novel compositions. Given its importance to novel TBCs, phase stability and evolution are major foci in this thesis. The stabilization mechanisms employed in ZrO_2-based ceramics are discussed in detail in Section 2.2.

2.1.3 Adequate toughness

The use of ceramics as thermal barriers has implicit disadvantages in terms of toughness. Ceramics tend to possess relatively low values for toughness, but since many of the life limiting events depend on crack propagation through the ceramic layer [08Eva], toughness is critical to the durability of the system. Particularly critical is the minimization of foreign object damage (FOD) and erosion, which are either due to impact of airborne particles ingested with the intake air or generated by wear of upstream components [99Nic, 06Eva, 10Fle, 07Wel]. Dense 8YSZ exhibits an intrinsic toughness of 40 J/m^2 [07Sch] however the effective toughness can be increased to 350J/m^2 by proper design of the coating microstructure [13Don]. Given its critical role in the durability of TBCs and its dependence on composition, toughness is another central focus of this dissertation. Toughening mechanisms as well as methods to experimentally determine toughness are described in detail later in this chapter.

2.1.4 Processing routes

Refractory ceramics not only have low toughness, but also exhibit a large mismatch in thermal expansion with the underlying metallic components. The coefficient of thermal

expansion (CTE) of 8YSZ, $11x10^{-6}$/K [96Jon], although high among refractory oxides, is significantly lower than that of the underlying Ni-based superalloy ($15\text{-}17x10^{-6}$/K) [06Pol]. This is problematic when the ceramic-coated metal is thermally cycled, as is the case in gas turbines. Severe mechanical problems, including coating failure, could occur as a result of thermal cycling. To mitigate this problem, a strain-tolerant microstructure of the ceramic coating can be engineered during deposition.

Current TBCs are usually deposited by two different methods. The most common coating deposition technique is atmospheric (air) plasma spray (APS) in which feedstock powder passes through plasma at high velocities, partially or entirely melting the particles. The particles/droplets deposit on the substrate as 'splats', building up to form a coating [04Fau]. By increasing deposition temperatures, vertical cracks form in the porous APS coatings, producing a dense vertically cracked (DVC) microstructure, Figure 2.4(a) that has improved compliance and thus strain tolerance during cyclic thermal exposures [12Sam].

A second, more elaborate technique is electron beam physical vapor deposition (EBPVD), in which a target material is heated with an electron gun in vacuum, melting the target and forming a vapor cloud [85Str]. By suspending a heated and rotating substrate above the source, a coating is deposited from the vapor as a columnar, textured array of single-crystals with thin gaps (segmentations) between them. In addition to the higher cost of EBPVD, it is more difficult to deposit coating compositions where the component oxides have significantly different vapor pressures in the melt. The strain tolerance of EBPVD coatings is arguably greater than that of APS coatings under similar conditions, although the more porous APS coatings have superior thermal insulation efficiency [12Sam]. While APS is still more widely used, especially in power generation and aeroengine combustors [12Sam] the performance of EBPVD coatings favors them for use in critical components such as turbine blades in jet engines [99Nic].

In recent years, a new technique has been developed to combine the advantages of APS and EBPVD coatings. A relatively new technique, suspension plasma spray (SPS), is able to deposit porous or columnar coatings that have lower thermal conductivity than APS coatings [15Gan]. By suspending particles in solution, it is possible to spray submicron- and nanometer-sized particles with SPS, a distinct advantage over APS. SPS coatings have improved thermomechanical compliance relative to APS but without the excess cost of EBPVD. However the toughness of SPS coatings may be lower than EBPVD owing to their more porous microstructure and the higher porosity may make SPS coatings more vulnerable to the penetration of molten deposits.

It is important that any TBC be easily processable using practical methods, as is the case for 8YSZ. One of the reasons for 8YSZ's processability is that there is little driving force for phase segregation during thermal spraying. The partition coefficient, k_*, is an indicator of the potential for segregation during solidification. For a given interfacial temperature T^*, k_* is defined as the ratio of the composition of the solid to that of the liquid, $k_*=C_{S^*}/C_{L^*}$, given by the equilibrium phase diagram at T^*. When $k_*<1$, the solute (dopant) is rejected from the solid as it forms, accumulating in the liquid. As seen in the $YO_{1.5}$-ZrO_2 binary in Figure 2.3(a), the liquidus and solidus are nearly flat at 7-8 mole% $YO_{1.5}$ (i.e. $C_S \approx C_L$), giving a partition coefficient very close to unity. Thus there is not a significant driving force for segregation within the solidification microstructure of 8YSZ splats. Similarly, vapor processing of 8YSZ yields a deposit of the same composition as the source from which it is evaporated. Because chemical segregation during processing can exacerbate problems with phase stability, mechanical properties and environmental resistance, it is critical that such inhomogeneities be minimized in TBCs.

2.1.5 Thermochemical compatibility with the TGO

Another requirement of ceramic topcoats is that they are compatible with the thermally grown oxide (TGO), which is α-Al_2O_3 in current TBC systems. If new TBC compositions form adverse reaction products with Al_2O_3, as is the case with rare earth-rich compositions such as gadolinium zirconate (GZO) [05Lec], an interlayer of 8YSZ is usually applied between the bond coat and topcoat. In addition to providing a diffusion barrier between the rare earth rich top layer and the TGO, 8YSZ also improves the toughness and thermal cycling durability of zirconate based TBCs [00Mal, 01Sub]. However the added processing complexities of depositing bi-layer TBCs is less desirable from a manufacturing perspective. Thus, it would be ideal if alternate TBCs do not react with the TGO.

2.1.6 Resistance to molten silicates

As engine operating temperatures increase to near or above the melting point (~1240°C) of siliceous contaminants that are ingested into jet engines, additional failure mechanisms arise. These contaminants are generally known as calcium-magnesium alumino-silicates (CMAS), with composition that varies according to the geographical operating history of the engine [12Lev]. At low temperatures the particulate matter impacts TBCs resulting in erosion [07Wel]. At high temperatures the CMAS melts and quickly infiltrates porous 8YSZ coatings. The schematic in Figure 2.5 illustrates the ensuing coating degradation. Thermochemical interactions result in the dissolution of 8YSZ in contact with the molten CMAS and precipitation of other related oxide phases [06Kra, 16Poe, 12Lev]. Under the imposed thermal gradient the CMAS solidifies within the infiltrated 8YSZ, significantly degrading the TBC's ability to accommodate the CTE mismatch strains during thermal cycling [15Jac]. Such stiffening may result in spallation of the TBC and thus loss of thermal protection [08Kra, 12Lev, 15Jac, 09Li, 96Bor]. Other CMAS-induced failure mechanisms

include bond coat cavitation and chemical attack of the thermally grown oxide (TGO), as depicted in Figure 2.6 [12Lev].

In order to mitigate CMAS-induced degradation, novel TBC compositions must react with the melt quickly to produce a volume of precipitated products that sufficiently fill the spaces between TBC columns, preventing further infiltration. The reaction products responsible for inhibiting infiltration in zirconate TBCs are apatite ($Ca_2RE_8(SiO_4)_6O_2$ where RE = La, Nd, Sm, Gd, Y, Yb) and fluorite [08Kra2, 15Poe]. This behavior is exemplified by gadolinium zirconate, $Gd_2Zr_2O_7$ (GZO), Figure 2.7. CMAS resistant TBCs must have adequate amounts of rare earth cations so that when the TBC is dissolved, silicate phases can precipitate at a rate competitive with infiltration. The larger RE cations are more effective at rapidly crystallizing the silicate melt and their relative effectiveness increases with the concentration of rare earth in the coating material [15Poe]. The high concentrations of RE (at least 50 mole%) needed to effectively mitigate molten silicate attack stabilize the pyrochlore and δ-phase crystal structures. For example, as the concentration of $YO_{1.5}$ is increased in YSZ, the fluorite and δ phase are stabilized, as seen in the $YO_{1.5}$-ZrO_2 binary diagram in Figure 2.3. Fluorite derivative phases such as the zirconates offer the benefits of phase stability, improved sintering resistance and lower thermal conductivity [00Vas, 05Cla, 04Lev]. Unfortunately these structures have intrinsically low toughness (~7 J/m^2 for dense specimens) since the fluorite structure lacks the ferroelastic toughening mechanism available in tetragonal systems [06Lec, 08Eva, 13Don].

Although investigating the CMAS resistance of novel TBCs coatings is not the core focus of this dissertation, understanding the factors that improve a TBCs ability to mitigate molten silicate attack is pertinent for identifying next generation TBCs.

2.1.7 Motivation for alternate TBCs

In summary of the preceding sections, there are several reasons why 8YSZ has been an excellent material choice for TBCs. However, it is clear that as turbine temperatures increase the shortcomings of 8YSZ become limiting. 8YSZ was selected as the oxide top-coat for TBCs because of its low, temperature invariant thermal conductivity and its stability in the combustion environment, but it has remained the top-coat of choice because of its mechanical durability [08Eva]. Additionally, 8YSZ is thermodynamically compatible with the underlying thermally grown oxide (TGO), α-Al_2O_3. An added advantage of 8YSZ is that there is little driving force for phase segregation during coating deposition. However 8YSZ is clearly not without its drawbacks, especially as gas turbine engine temperatures continue to increase. In addition to its limited phase stability, 8YSZ lacks sufficient resistance to molten silicates and would benefit from reduced thermal conductivity and increased toughness [12Cla, 08Eva, 04Lev, 16Pad]. The shortcomings of 8YSZ significantly hinder if not prevent its use in hotter, more efficient gas turbines. These limitations highlight the need to explore and identify alternative topcoat compositions with improved combinations of properties. Given the numerous often-competing properties that TBCs must exhibit it is imperative to prioritize combinations of properties when investigating novel TBCs. This dissertation will focus on the combination of phase stability and adequate toughness in novel TBCs that also exhibit low thermal conductivity.

2.2 Stabilization mechanisms in zirconia

Understanding how zirconia is stabilized provides valuable insight to potential stabilization mechanisms in next-generation TBCs. As described in Section 2.1.2, pure zirconia can take on one of three polymorphs depending on temperature. The crystal structures of ZrO_2 are shown in Figure 2.8. The cubic phase is only stable at high temperatures because the Zr^{4+} cation (0.84Å) is too small to fit in the site coordinated by eight equidistant oxygen ions. At

the high temperatures at which fluorite is stable, thermally-induced oxygen vacancies [82Ho] and increased lattice vibrations result in an average cubic structure [98Kis]. Oxygen vacancies begin to form at 1900°C and are so critical to the stability of the cubic structure that *F* is not stable until the stoichiometry has reached $ZrO_{1.56}$ [82Ho]. Below 2370°C, the oxygen ions systematically displace along the {001} directions, resulting in the elongation of the c-axis to form the tetragonal (*t*) structure. At temperatures below 1205°C, the undersized nature of the Zr^{4+} cation results in overcrowding on the anion lattice that is relieved by reducing the symmetry to seven-fold coordination in the monoclinic structure or through intrinsic/extrinsic stabilization of the high symmetry structures.

The two phases stable at lower temperatures (*t*, *m*) are closely related to the high temperature fluorite structure, as seen in Figure 2.8. While there is a small (<1%), often-neglected, volume change associated with the $F \rightarrow t$ transformation, the volume expansion (~4%) [81Kri] associated with the $t \rightarrow m$ transformation is much more significant [87Heu, 77Por, 00Han]. The $t \rightarrow m$ transformation has significant technological applications as it is the basis of a widely utilized toughening mechanism known as transformation toughening [72Gar, 82McM, 87Heu, 77Por, 00Han], which will be discussed in Section 2.3.1. The monoclinic structure is stable at room temperature because in it, Zr achieves the preferred seven-fold coordination.

The underlying stabilization mechanisms in zirconia must be understood to appreciate the design challenges associated with maintaining tetragonal symmetry in the high-temperature cyclic environment of typical TBCs. Dopant cations can be introduced to mimic the intrinsic stabilization mechanisms of pure zirconia. These cations can be divided into two groups: (i) those that stabilize the cubic symmetry or (ii) those that stabilize the tetragonal symmetry. As will become evident below, the dopant ionic size relative to the host cations and preferred oxidation state largely determine what symmetry a particular dopant stabilizes.

2.2.1 Trivalent dopants

Trivalent dopants such as Y^{3+} are the most common stabilizers used in most TBCs in use today. While divalent dopants such as Ca^{2+} and Mg^{2+} are important in low temperature corrosion and wear resistant components they will not be discussed in detail because they are not relevant to TBCs. Similar to divalent cations, trivalent cations employ two stabilization mechanisms that involve: (i) introduction of oxygen vacancies and (ii) dilation of the cation sublattice sites. The oversized (ionic radius=1.019Å), Y^{3+} cation is a prototypical example of a trivalent dopant that stabilizes the cubic phase via introduction of oxygen vacancies and to a lesser degree, dilation of the cation lattice, It is widely known that oxygen vacancies caused by increased temperature or by the substantial use of aliovalent dopants, stabilize the cubic structure [91Hil]. The oxygen vacancies relieve the anion overcrowding around the zirconium cation. Kroger Vink notation can be used to illustrate the introduction of anion vacancies:

$$M_2O_3 \xrightarrow{ZrO_2} 2M'_{Zr} + 3O_O^X + V_0^{**} \qquad 2.2$$

Doping with Y^{3+} or many other trivalent rare earth cations also causes a dilation in the cation sublattice. However by introducing structural disorder in their vicinity, oxygen vacancies contribute significantly more to the stabilization of zirconia than the size of the cation [02Fab]. This trend is inferred from Figure 2.9, which shows how the tetragonality (c/a) of zirconia stabilized by considerably different size rare earth cations (Nd, Sm, Y, Er, Yb) decreases with increasing dopant concentration [88Yos]. The transition from the tetragonal to cubic structures occurs at approximately the same dopant concentration, regardless of the ionic radius, provided the ionic radius is larger than Zr^{4+}. As will be discussed in Section 2.3.2, the tetragonality is closely tied to the toughness of stabilized zirconia ceramics via a mechanism based on ferroelastic domain switching. Therefore the decrease in tetragonality is not desirable for novel TBCs.

2.2.2 Tetravalent dopants

In the absence of large populations of oxygen vacancies, as is the case for isovalent dopants, distortions caused by differences in ionic radii play a more significant role in stabilization. This behavior is exemplified by dopants such as Ce^{4+} and Ti^{4+}.

$$MO_2 \xrightarrow{ZrO_2} M_{Zr}^{X} + 2O_O^X \qquad 2.3$$

In tetravalently stabilized zirconia, the ionic radii dictate whether the tetragonal or cubic structure is stabilized. The tetragonality (c/a) as a function of dopant content for several tetravalent dopants is plotted in Figure 2.10. For oversized dopants such as Ce^{4+}(0.97Å), which dilate the local structure to reduce anion overcrowding, the decrease in tetragonality with increasing dopant content is much more gradual compared to what is observed with trivalent dopants (Figure 2.9). In contrast, incorporation of undersized tetravalent dopants such as Ti^{4+} (0.74 Å), which introduce systematic anion diplacements, tetragonality actually increases. By combining the oversized Ce^{4+} with undersized Ti^{4+} cations, a stable tetragonal phase is formed with unprecedented levels of tetragonality, Figure 2.11 [13Kro2].

There are several advantages to avoiding large oxygen vacancy populations. In addition to providing higher tetragonality, a larger compositional design space is also available in tetragonal structures that lack oxygen vacancies [13Kro2]. By comparing the isovalent CeO_2-TiO_2-ZrO_2 (CeTiSZ) system to the trivalent ZrO_2-$YO_{1.5}$-$YbO_{1.5}$ (ZYYO) system, Figure 2.12(a) and (b), respectively, it is clear that tetravalent dopants provide a significantly larger tetragonal design space than trivalent dopants. In CeTiSZ, the tetragonal field extends to a combined Ce+Ti concentration of ~28mole% where as the maximum Y+Yb solubility is only ~5mole% in the ZYYO system. The stark difference in phase fields is due to the drastically different stabilization mechanisms employed in each system. While only a small amount of oxygen vacancies (introduced by trivalent dopants) is stable in the tetragonal

structure, the synergistic combination of stabilization mechanisms that do not rely on oxygen vacancies in CeTiSZ results in a larger tetragonal field.

2.2.3 Charge compensating dopants

Zirconia stabilized by charge compensating dopants is similar to isovalently-stabilized zirconia, in that both do not depend on oxygen vacancies. By combining trivalent and pentavalent dopants that usually have dissimilar ionic radii, highly tetragonal structures can be stabilized. In Kroger-Vink notation the stabilization mechanism for equimolar pentavalent (*L*) and trivalent (*M*) dopants is depicted as

$$L_2O_5 + M_2O_3 \xrightarrow{ZrO_2} 2M'_{Zr} + 2L^*_{\mathrm{Zr}} + 8O_O^X \qquad 2.4$$

The addition of smaller pentavalent cations like Ta^{5+} to ZrO_2 or YSZ actually increase the distortion in the crystal structure, destabilizing both the cubic and tetragonal phases [91Kim, 90Kim]. Since oxygen vacancies are highly effective at stabilizing the cubic and tetragonal structures [94Li1] the destabilizing effect of pentavalent cations can be attributed to the decreased concentration of oxygen vacancies and the larger distortion around the smaller dopant [94Li3]. Therefore the solubility of $TaO_{2.5}$ in ZrO_2, even at 1500°C is relatively low, 3.9 mole%, [91Zhe]. However this reasoning is not applicable to equimolar $YO_{1.5}$- and $TaO_{2.5}$-doped ZrO_2, such as that in the $YTaO_4/ZrO_2$ quasibinary within the ZrO_2-$YO_{1.5}$-$TaO_{2.5}$ (ZYTO) system, which lacks oxygen vacancies but still exhibits a stable tetragonal phase [91Kim, 90Kim, 06Pit, 07Pit, 04Rag]. When combined with equimolar amounts of a trivalent dopant like Y^{3+}, significantly higher concentrations of pentavalent cations (~18 mole%) are stable in the tetragonal structure, as exemplified by the ZYTO system, Figure 2.13. In the ZYTO system, one oxygen vacancy is removed for every 2 Ta^{5+} added. Contrary to what happens with trivalent dopants [88Yos, 94Li1], the tetragonality of $YTaO_4$-stabilized ZrO_2 increases with dopant concentrations [91Kim, 07Pit, 94Li3]. The

stabilization mechanism is ascribed to short range ordering of the oversized Y^{3+} and undersized Ta^{5+} cations which relieves the de-stabilizing oxygen overcrowding around Zr^{4+} [94Li3]. The dopants form a substitutional solid solution in the tetragonal structure. The pentavalent cations are tetrahedrally coordinated with shorter, stronger oxygen bonds than that of Zr-O. The trivalent cations have 8-fold oxygen coordination [94Li3].

2.2.4 Characterization

Phase stability, and more broadly phase equilibria, of novel TBC systems have previously been investigated using a variety of techniques. These include x-ray diffraction (XRD) [11Bha2, 90Dur, 09Fu, 91Kim, 90Kim, 15Kro, 13Lip, 07Pit, 83Tan, 91Zhe, 91Yok], Raman spectroscopy [11Bol, 11Lim], electron probe microanalysis (EPMA) [16Poe], and transmission electron microscopy (TEM). The results from each technique are complementary, as each has its own advantages and disadvantages. XRD requires minimal sample prep and is relatively easy to perform, allowing lattice parameters and phase fractions to be determined quickly, making XRD the most common technique used to determine bulk structure of materials. However the atomic mass dependence of the structure factor results in the strong intensity of the cation sublattice overpowering changes on the anion sublattice. Additionally, information about local distortions or ordering is averaged out. In contrast, Raman spectroscopy is sensitive to displacements on the anion sublattice, especially those associated with *m*-ZrO_2 [71Phi]. Similar to XRD, performing Raman experiments is relatively straightforward. Many phase equilibria studies rely on diffraction experiments without complimentary characterization to substantiate the results. Direct observation of the microstructure provides a new perspective, especially if phase transformations occur on cooling. If grain size (>1μm), sample density, and surface preparation are sufficient, EPMA performed with standards can be used to determine elemental composition with high accuracy (<<1 mole %). However for smaller grained

materials, energy dispersive spectroscopy on a TEM must be used. Compared to XRD and Raman, sample preparation and experimentation takes significantly longer for TEM. However TEM enables site-specific, chemical and structural analysis. Many microstructure studies have failed to include complimentary techniques to analyze the bulk material. Particularly in the study of metastable phases like *t'*, it is crucial that combinations of techniques, such as XRD and TEM, are employed to accurately determine phase stability and evolution [12Kro, 11Kro].

2.2.5 Relevance to novel TBCs

Stabilization of the tetragonal phase in zirconia ceramics is critical to TBCs, largely due to its superior toughness relative to previously studied non-tetragonal phases. It is important that novel TBCs maintain a tetragonal structure to retain the desirable ferroelastic toughening mechanism. Since high tetragonality is a key parameter in the effectiveness of ferroelastic domain switching and trivalent dopants result in reduced tetragonality relative to 8YSZ, trivalent dopants do not offer a viable path to novel TBCs with the desired mechanical behavior. Therefore tetravalent and charge-compensating dopants are of interest for their ability to produce phase stable tetragonal phases with high tetragonality. The CeTiSZ system has shown promise in lab-scale experiments; however, it is unclear how this material will behave when deposited via atmospheric plasma spray.

While ZrO_2-rich TBCs with the tetragonal structure are of interest because viable toughening mechanisms are in operation, it is possible that novel TBCs with different crystal structures may also exhibit effective toughening mechanisms. Due to the interest in ZrO_2-rich tetragonal phases, there is a paucity of information regarding the phase equilibria in the ZrO_2-lean portion of phase diagrams.

2.3 Toughening Mechanisms in zirconia

TBCs must withstand significant thermo-mechanical strains due to the difference in coefficient of thermal expansion between the TBC and the metallic substrate. Additionally, TBCs must endure impacts from the ingestion of particulate matter into the engine, especially in aviation. Since TBCs only protect the turbine blades so long as they are intact, it is self-evident why TBCs must exhibit adequate toughness to withstand the relevant failure modes. Several toughening mechanisms based on crack tip shielding may be active in ceramics like zirconia. These mechanisms include, transformation toughening, and ferroelastic switching, which are discussed in detail in the following sections [93Law].

2.3.1 Transformation toughening

The discovery of transformation toughening in partially stabilized zirconia (PSZ) revolutionized low temperature applications [75Gar]. In PSZ, CaO or MgO is added to ZrO_2 such that the final composition is in a cubic phase field at high temperatures but in a tetragonal + cubic phase field at lower temperatures, Figure 2.14(a). Heat treatment at lower temperatures results in the precipitation of coherent, tetragonal precipitates. The tetragonal-monoclinic ($t \rightarrow m$) transformation occurs sluggishly in PSZ while cooling to room temperature, and the tetragonal phase is constrained from transforming by the cubic matrix. The transformation is triggered by the stress field associated with a crack, causing some of the particles within the process zone (+/- r_c from the crack plane) to transform as shown in Figure 2.14(b) and Figure 2.15. The increase in toughness that results from this mechanism can be described by

$$\Delta G_c \cong 2 r_c \sigma_M \varepsilon_M V_f \qquad 2.5$$

where r_c is the distance the process zone extends above and below the crack plane, σ_M is the stress required to initiate the transformation, ε_M is the transformation strain and V_f is the fraction of particles within the process zone that have transformed [92Bec, 93Law, 00Cou]. A process zone is formed as the crack propagates, and the resulting increase in toughness can be attributed to two mechanisms, both of which increase the amount of work required for fracture after the transformation. Crack shielding or a reduction of the stress field at the crack tip develops due to the transformation. Additionally, energy dissipated in the transformation is no longer available to grow the crack.

Various properties influence the efficacy of the transformation toughening mechanism. The coherency of the tetragonal matrix is critical in inhibiting the $t \rightarrow m$ transformation [78Han, 00Han]. Governed by lattice mismatch strain, coherency is lost and the particles spontaneously transform to *m* once they coarsen beyond a critical size. Conversely if the tetragonal grain size is too small, σ_M is very high resulting in a small r_c and thus reduced toughening [82Heu, 81Eva]. Thus there is an optimal grain size that provides the largest toughening with this mechanism.

2.3.2 Ferroelastic domain switching

Ferroelastic domain switching is the currently accepted mechanism that is responsible for the desirable toughness of tetragonal 8YSZ [98Vir, 86Vir]. In this mechanism, illustrated in Figure 2.16(a), the tetragonal domains in YSZ change to a more favorable orientation when a coercive stress, τ_C, is applied to materials that already contain domains [07Mer, 98Vir, 86Vir]. As the volume fraction of favorably oriented grains increases, the extent of the other two less-favorable domains shrink [91Cha]. Domain wall motion dictates the propagation of ferroelastic switching and is the primary factor controlling toughening in crystals that already contain domains [01Bai]. Some energy from the applied stress is used to move the

domain walls, reducing the energy available to propagate the crack. In vapor deposited coatings that may not contain multiple tetragonal variants (depending on if the $T_0(F \rightarrow t)$ line has been crossed), it is posited that nucleation of tetragonal domains controls the ferroelastic mechanism and thus a higher stress, τ_{nucl} is required to first nucleate the domains before propagation, Figure 2.16(b), [07Mer]. These energy-dissipating processes leads to crack-tip shielding, which reduces the stress at the crack tip relative to the remotely applied stress. The increase in toughness that results from this mechanism is proposed to follow a simple model derived from transformation toughening concepts

$$\Delta\Gamma_{ss} \approx 2hf\tau_C\gamma_T \qquad 2.6$$

where h is the process zone size, f is the fraction of the domains in the process zone that have switched, τ_c is the coercive stress required to move the domain boundaries, and γ_T is the transformation strain [07Mer]. The coercive strain is related to tetragonality (c/a) based on the equation

$$\gamma_T \approx \frac{2}{3}(c/a - 1) \qquad 2.7$$

as given in [07Mer]. Based on this relationship, the toughness contribution from ferroelastic switching scales with tetragonality, to first order. However it is clear that the process zone size, coercive stress, and transformation strain are not independent, since toughness has not been observed to increase linearly with tetragonality [13Kro2, 07Pit, 07Sch]. It has been suggested that coercive stress may increase with tetragonality, resulting in a smaller process zone and reduced contribution to toughness [98Vir, 07Pit]. Similar to conventional plastic deformation in ductile materials, ferroelastic switching is strain rate dependent [98Vir]. This is because the domain wall motion, which governs domain switching, is a strain rate dependent phenomenon.

It is worth noting that both transformation toughening and ferroelastic switching can occur in the same material. It is believed that metastable tetragonal microstructures will first undergo ferroelastic switching before transforming to monoclinic. For either mechanism to contribute to toughness, the initiation stress must be lower than the fracture stress.

2.3.3 Characterization

Elucidation of the active toughening mechanism is achieved using several characterization techniques, often analyzing the samples before and after fracture experiments or comparing results from bulk material to data obtained near a crack. XRD has been used as evidence of transformation toughening [72Gar2, 75Gar, 72Gar] and even more extensively as proof of ferroelastic switching [90Jue, 98Vir, 86Vir, 90Meh, 13Don]. If sufficient amounts of the monoclinic phase are present, XRD peaks associated with the monoclinic are visible. To detect ferroelastic switching in tetragonal samples, the relative intensities of the 002/200 or 004/400 XRD peaks change as a result of an applied stress (i.e. grinding, fracture, compression), as shown in Figure 2.17. If ferroelastic switching is do be detected on fracture surfaces, such as those in double cantilever beam experiments, it is necessary to use a surface sensitive XRD analysis technique to avoid significant contributions from the un-switched bulk material.

Raman spectroscopy has also been used to detect both transformation toughening and ferroelastic switching. Given the sensitivity of Raman spectroscopy to anion displacements, monoclinic ZrO_2 is easily observed using this technique [71Phi]. When used to analyze micro-indents (discussed in Section 2.3.5) it is necessary to probe around the cracks as well as in the indents themselves to verify that monoclinic is not present. By integrating the intensity of the Raman peaks associated with the direction of the tetragonal c-axis, evidence of ferroelastic switching has also been observed [11Bol]. Similar to XRD, it is necessary to

minimize the interaction volume from which the Raman signal originates to see changes in peak intensity.

Microstructural and crystallographic analysis is conducted using TEM to verify toughening mechanisms and measure the size of the process zone [91Cha, 07Mer, 13Kro2]. Detection of transformation toughening is rather obvious in bright field (BF) TEM images due to the presence of large twins indicating *m*-ZrO_2 [87Heu]. Imaging of the ferroelastic process zone is more complex, given the small size of the tetragonal variant domains [91Cha]. Selected area electron diffraction (SAED) is used in combination with dark field (DF) imaging to confirm which tetragonal variants are present [01Bai]. The size of the process zone is measured based on the presence of all three tetragonal variants in initially single-domain vapor-deposited samples [07Mer] or by the prevalence of two variants in polydomain single crystals [01Bai, 91Cha].

Despite their increasing complexity, in-situ experiments have also been conducted to measure the coercive stress of ferroelastic switching. In situ compression experiments conducted on single crystals of 5.8 mol% $YO_{1.5}$ indicate the coercive stress of the tetragonal phase is temperature insensitive and varies from 700-500 MPa between 500°C and 1400°C [01Bai].

2.3.4 Relevance to TBCs

Transformation toughening is not applicable to 8YSZ TBCs at engine operating temperatures since there is no thermodynamic driving force for the transformation to monoclinic to occur above 1205°C [04Wan]. Moreover, the reversible transformation to monoclinic on cooling is detrimental to the cyclic durability of the coatings, as discussed briefly in Section 2.1.2. Therefore ferroelastic switching is the accepted mechanism that is responsible for the improved durability of tetragonal-based coatings. Creative doping

schemes have been employed to increase tetragonality as a way to increase toughening from ferroelastic switching [13Kro2, 07Sch]. For ferroelastic switching to be effective, a material must either have domains already or be able to form domains with and applied stress, and the domain walls must be mobile at stresses below the fracture stress.

2.3.5 Techniques to experimentally determine toughness

Various experimental techniques are used to measure the toughness of ceramics. Arguably one of the most common techniques is microindentation. Introduced by Anstis *et al.*, the technique involves measuring radial cracks that result from Vickers indents at various loads [81Ans]. Although the technique is utilized liberally in the study of ceramics because it is quick, convenient and allows site-specific analysis using small amounts of material, many of its requirements and shortcomings are overlooked. Micro-indentation is not a standardized toughness test but it was never intended to be used as such [15Mar]. The experimentally determined 'calibration constants' determined by Anstis and Lawn are only applicable for "well behaved", small grained (<1μm), dense, isotropic ceramics free of residual stress and with a Young's modulus to hardness ratio (E/H) of 10-20 [81Ans]. Even when these requirements are met, the toughness values produced by micro-indentation are only ~30% accurate [81Ans, 15Mar]. However micro-indentation is a valuable exploratory tool to study the mechanical behavior of ceramics and provides qualitative comparisons of samples from the approximately the same thermal history, density, grain size, and E/H ratio.

Another toughness technique that has been used to calculate the toughness of ceramics since the 1970's is the 3-point bend test [74Sim]. Unlike micro-indentation, it is an ASTM standard (E 1820) toughness test, and thus the K_{1C} value can be determined provided enough samples are tested. However the standard 3-point bend test requires complex sample preparation and prohibitively large amounts of material (for precursor derived powders) with

beam dimensions on the order of 5cm x 3cm x 0.6cm [74Sim]. Like micro-indentation or any other toughness measurement technique, 3-point bend is sensitive to material fabrication (heat treatment, grain size, porosity) and the presence of residual stresses [15Mar]. One distinct advantage of the 3-point bend technique is the fracture surface can be characterized, providing an additional source of information to determine toughening mechanisms.

A final experimental technique used to measure toughness of ceramic samples is the double cantilever beam (DCB) test [13Don]. For TBCs, the DCB test has several advantages such as the ability to observe R-curve behavior while measuring engine-relevant, in-plane toughness of porous coatings. While DCB experiments revealed a bridging mechanism that significantly contributes to the toughness of coatings [13Don], the technique requires time-intensive sample preparation and is highly sensitive to the coating microstructure.

2.4 Scope and Objectives of Research

As this background illustrates, TBCs must exhibit numerous, often-competing properties. A TBC system that satisfies the requirements of phase stability, low thermal conductivity, adequate toughness and CMAS-resistance at temperatures >1350°C has yet to be identified. The overarching objectives of this dissertation are to understand the phase equilibria and toughness of thermal barrier coatings (TBCs) that have the potential to exhibit superior combinations of properties to the industry standard 8 ± 0.5mole% $YO_{1.5}$-stabilized zirconia (8YSZ). The compositions investigated can be categorized into two groups: (i) single-phase, non-transformable tetragonal compositions that have adequate toughness and (ii) two-phase compositions that enable the combination of adequate toughness and CMAS resistance. It is expected that the fundamental scientific contributions developed in the areas of phase equilibria and toughness will have application not only to high temperature materials, but also to the broader ceramic materials community.

2.5 Figures

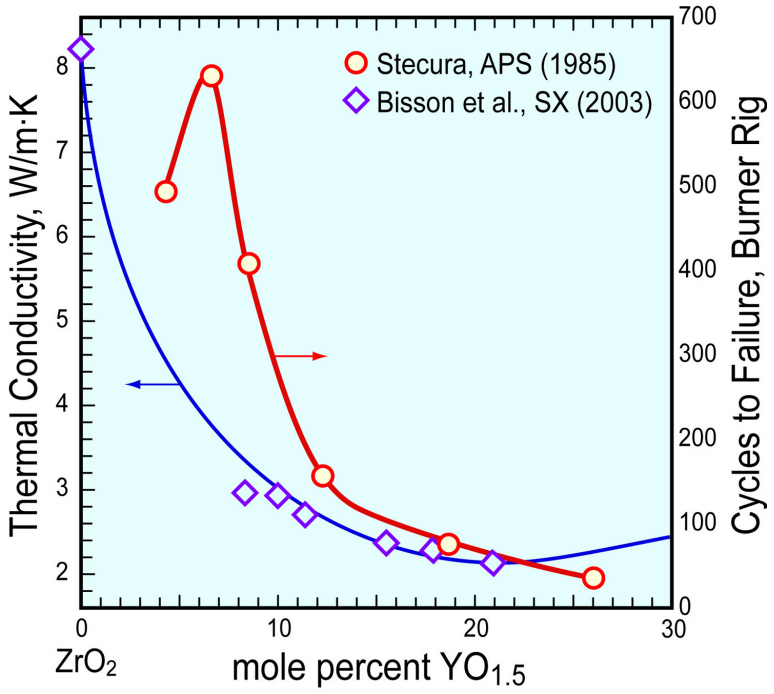

Figure 2.1 As yttria-content increases, thermal conductivity decreases but lifetime in a cyclic burner rig decreases. The debit in increased thermal conductivity associated with choosing 8YSZ is offset by its improved durability. Figure from C.G. Levi, adapted from [00Bis, 79Ste].

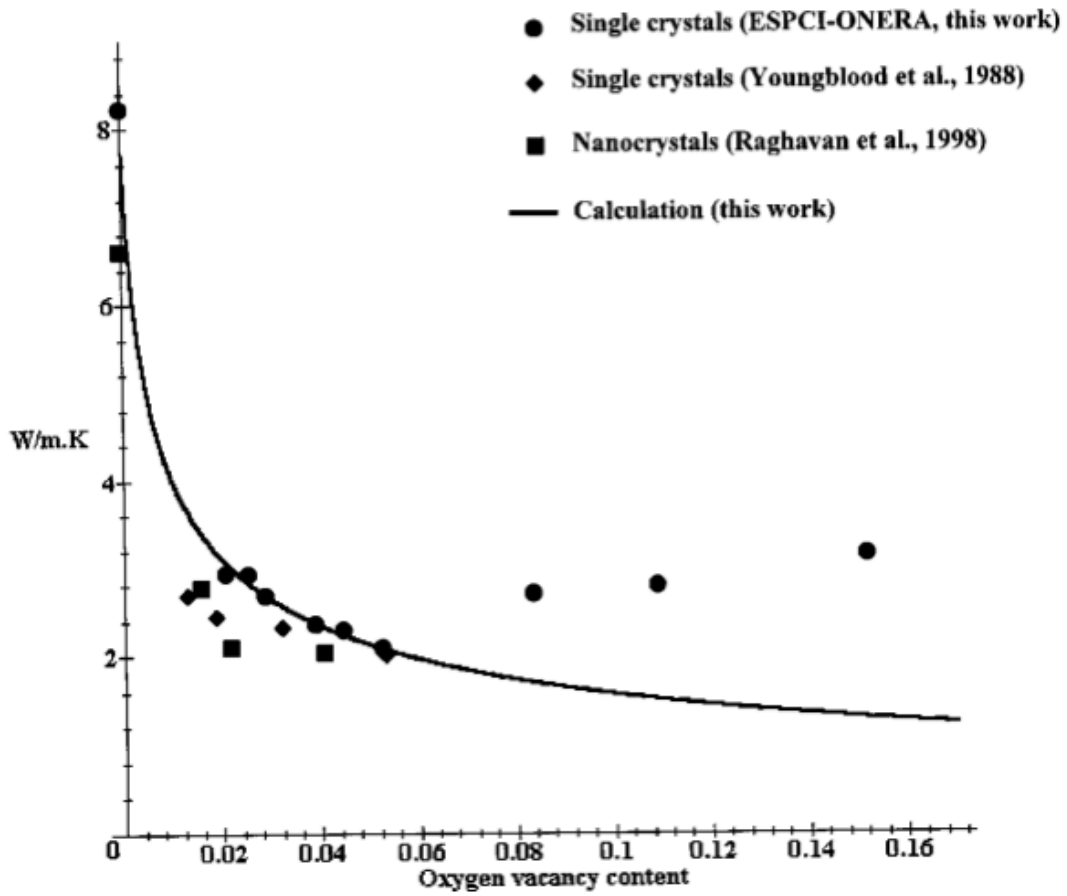

Figure 2.2 Thermal conductivity as a function of oxygen vacancy concentration [00Bis]. To obtain the corresponding $YO_{1.5}$ content (in mol%), multiply the oxygen vacancy content by 4.

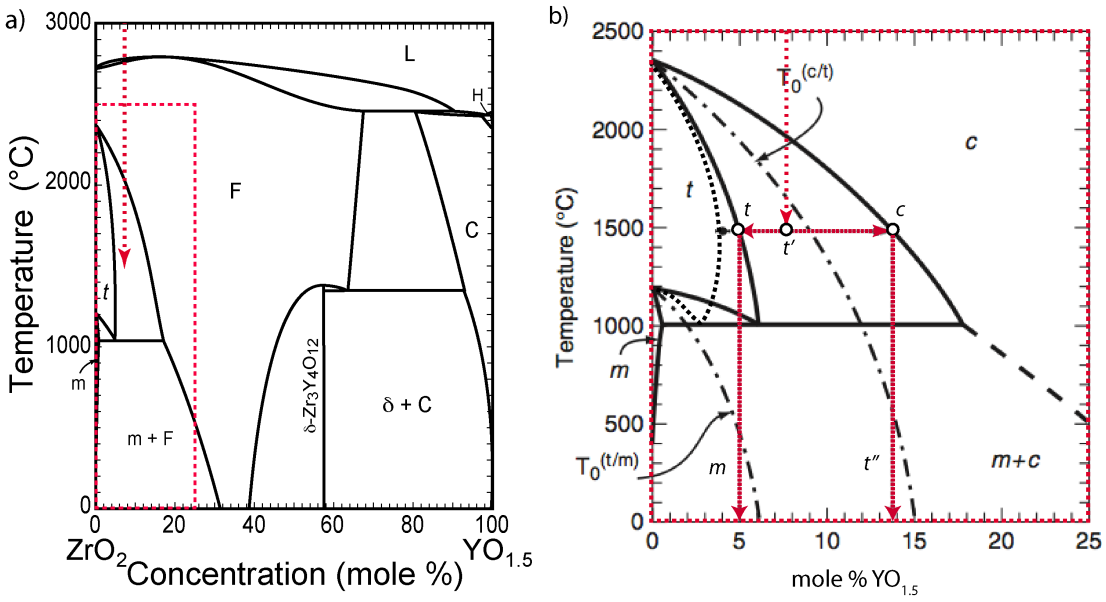

Figure 2.3 (a) The entire $YO_{1.5}$-ZrO_2 binary phase diagram with a red arrow indicating how *t'*-8YSZ is deposited. The relatively flat shape of the liquidus reduces the driving force for chemical segregation during coating deposition. (b) An inset of the ZrO_2-rich portion of the phase diagram adapted from [11Kro] to include the retrograde solvus of the *t* phase proposed by [13Lip]. Red arrows indicate the phase evolution of *t'* at 1482°C. The *c* phase in (b) is the *F* phase in (a).

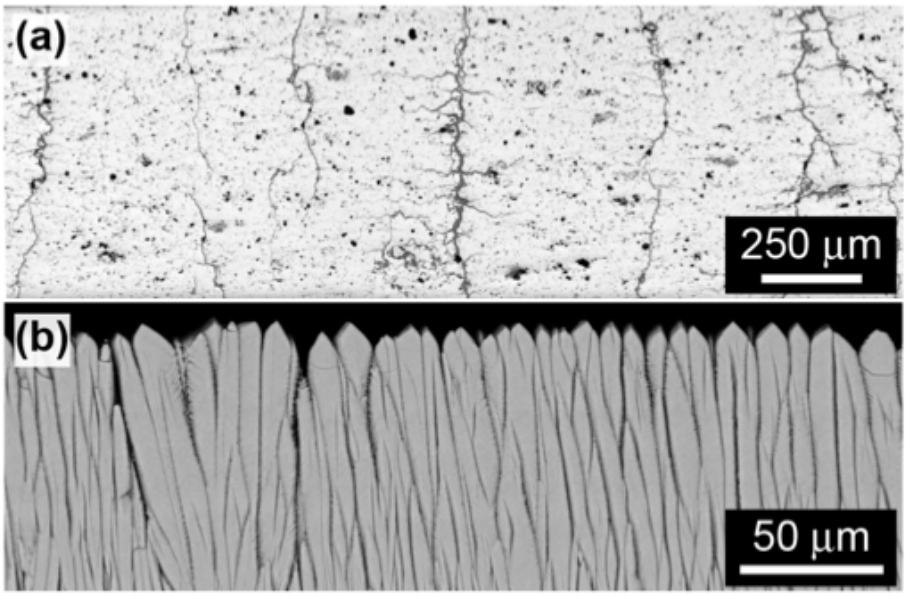

Figure 2.4 Typical coating microstructures deposited by (a) atmospheric plasma spray (APS) and (b) electron beam physical vapor deposition (EBPVD) from [13Zal].

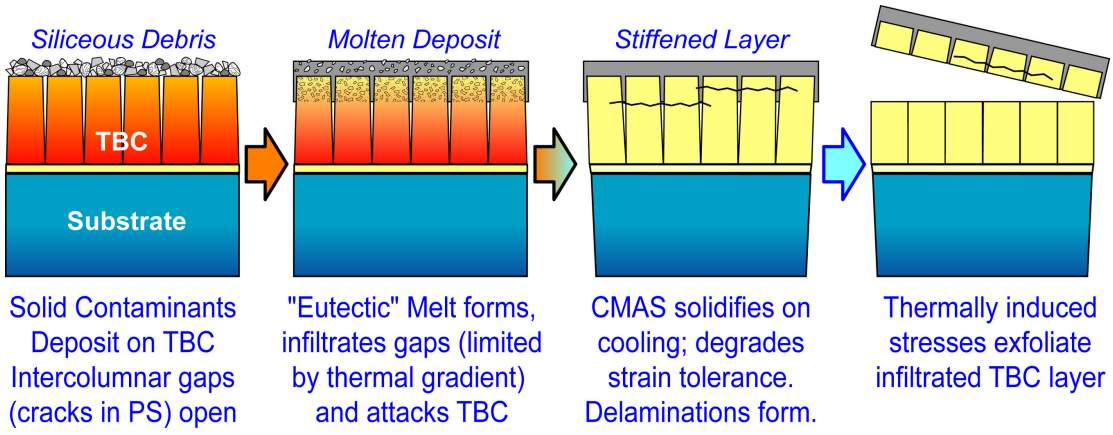

Figure 2.5 Schematic of TBC spallation due to infiltration by molten silicates. Figure courtesy of C. G. Levi, originally adapted from C. Johnson, GE GRC.

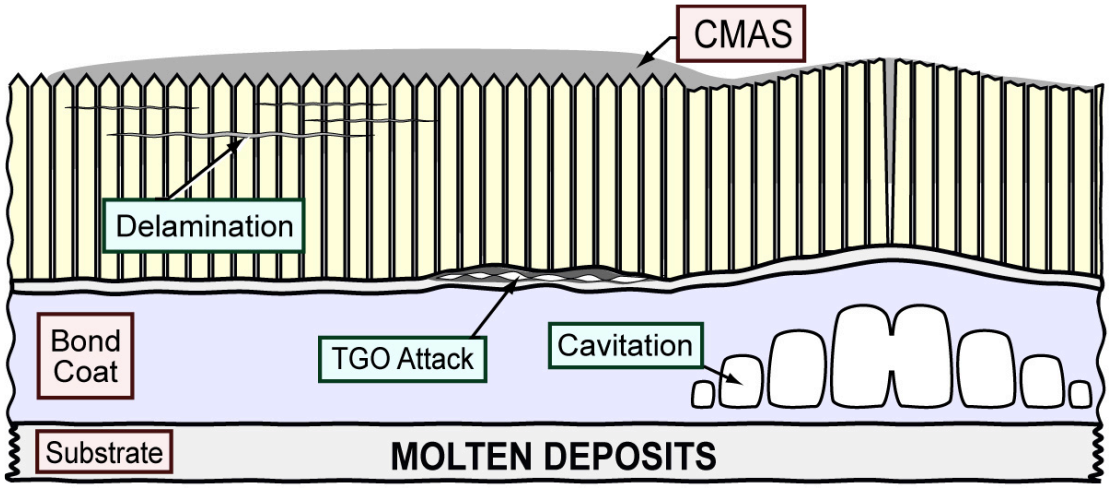

Figure 2.6 Failure mechanisms associated with the presence of CMAS in gas turbines [12Lev]

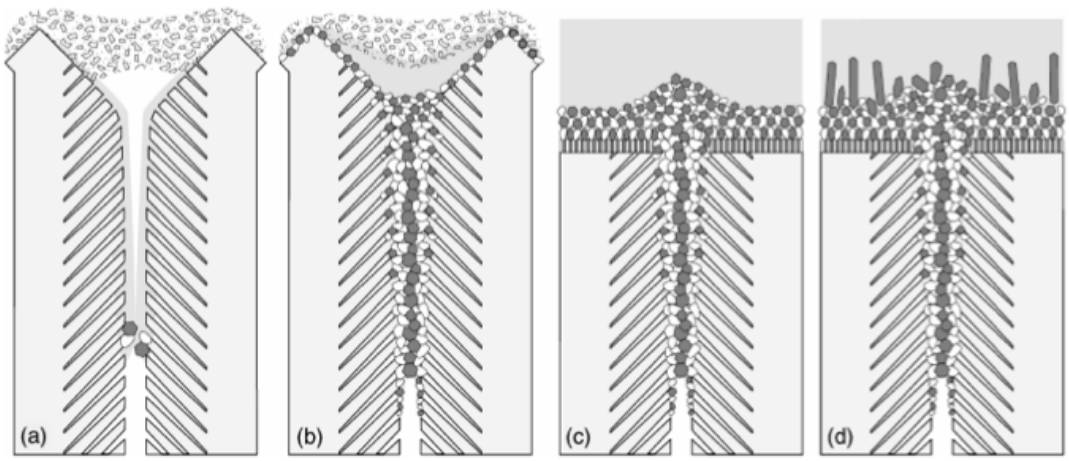

Figure 2.7 Schematic depiction of the interaction of gadolinium zirconate (GZO) with CMAS, as proposed by The molten silicates first (a) wick down the column sides but the intercolumnar gap is quickly filled by crystalline reaction products, (b). (c) The column tips are slowly attacked by the bulk molten silicate melt. (d) additional crystalline reaction products grow during cooling.

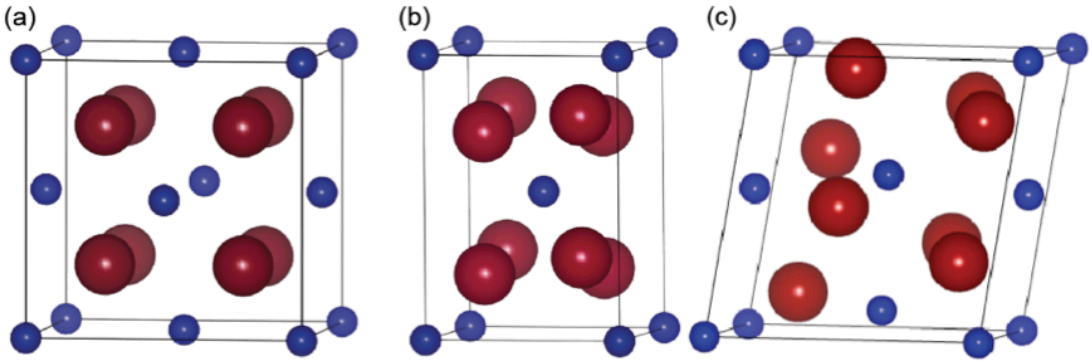

Figure 2.8 The cubic, tetragonal, and monoclinic crystal structures of pure ZrO_2 [12Kro].

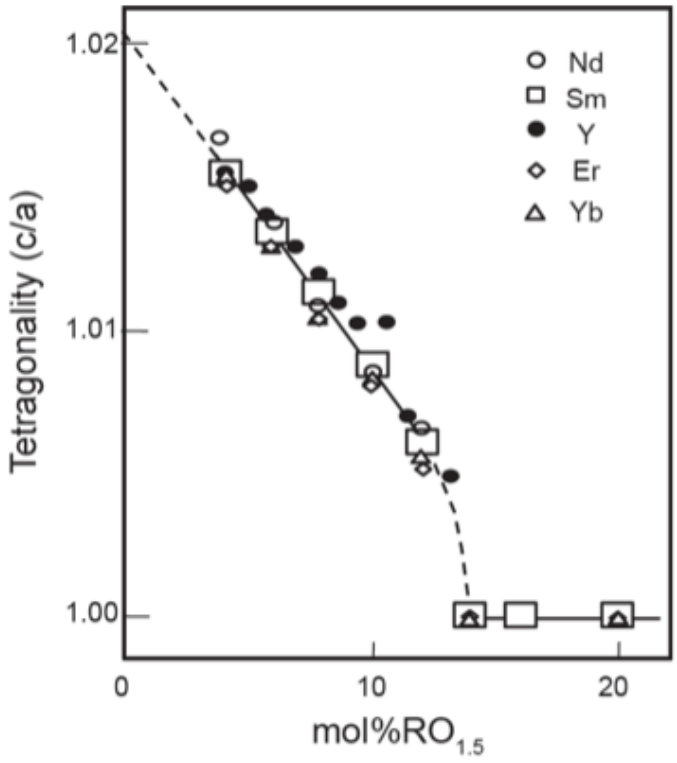

Figure 2.9 Tetragonality as a function of trivalent dopant content. From [12Kro, 88Yos].

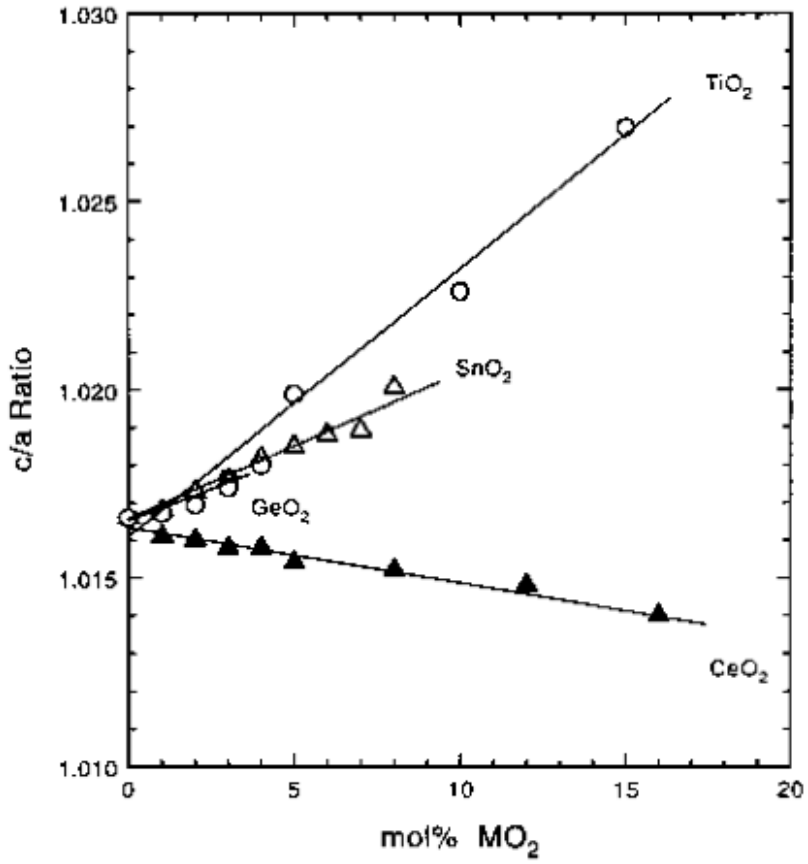

Fig. 11. Axial ratio *c/a* of 2Y-TZP that contains tetravalent dopants.

Figure 2.10 Tetragonality as a function of tetravalent dopant content [97Kim]

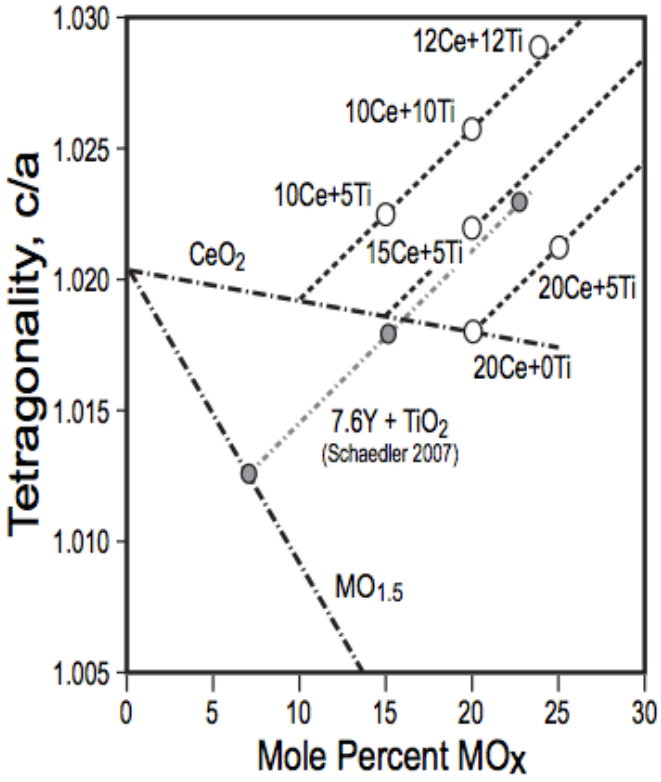

Figure 2.11 Tetragonality as a function of dopant content in the CeO_2-TiO_2-ZrO_2 (CeTiSZ) system [13Kro2]. The combination of oversized Ce^{4+} and undersized Ti^{4+} cations leads to a stable tetragonal phase with unprecedented levels of tetragonality.

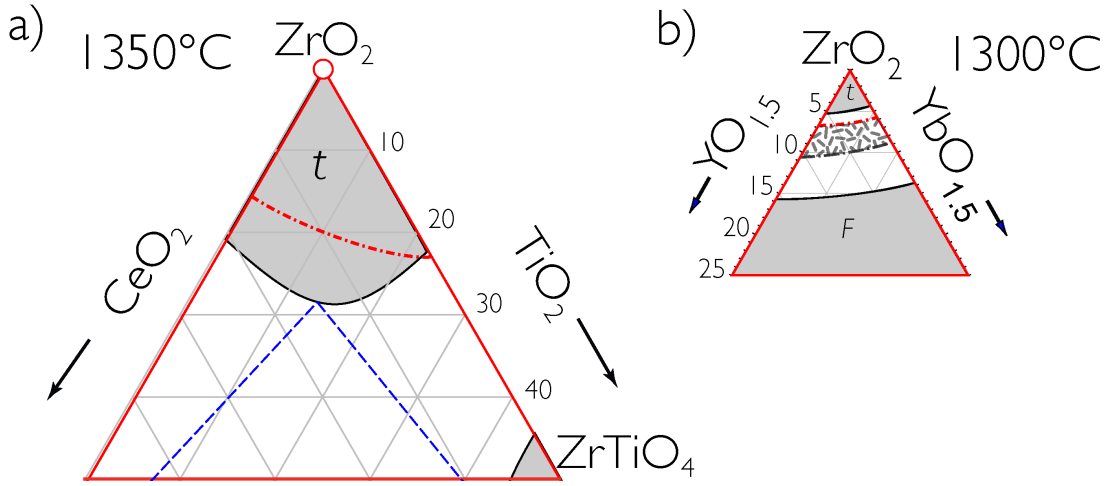

Figure 2.12 Due to the nature of the stabilization mechanisms the tetragonal phase field is significantly larger in (a) tetravalently stabilized zirconia systems such as CeTiSZ than it is in (b) zirconia stabilized by only trivalent dopants such as in the ZrO_2-$YO_{1.5}$-$YbO_{1.5}$ system.

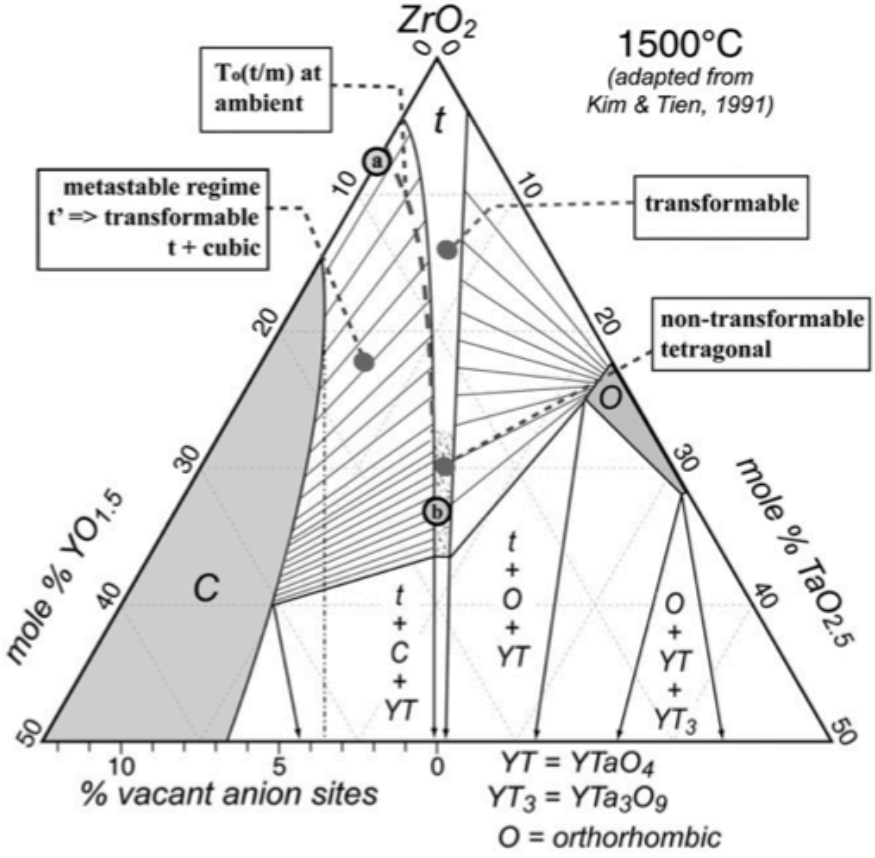

Figure 2.13 The tetragonal phase in the ZrO_2-$YO_{1.5}TaO_{2.5}$ (ZYTO) system is stabilized by equimolar concentrations of charge-compensating cations [07Pit].

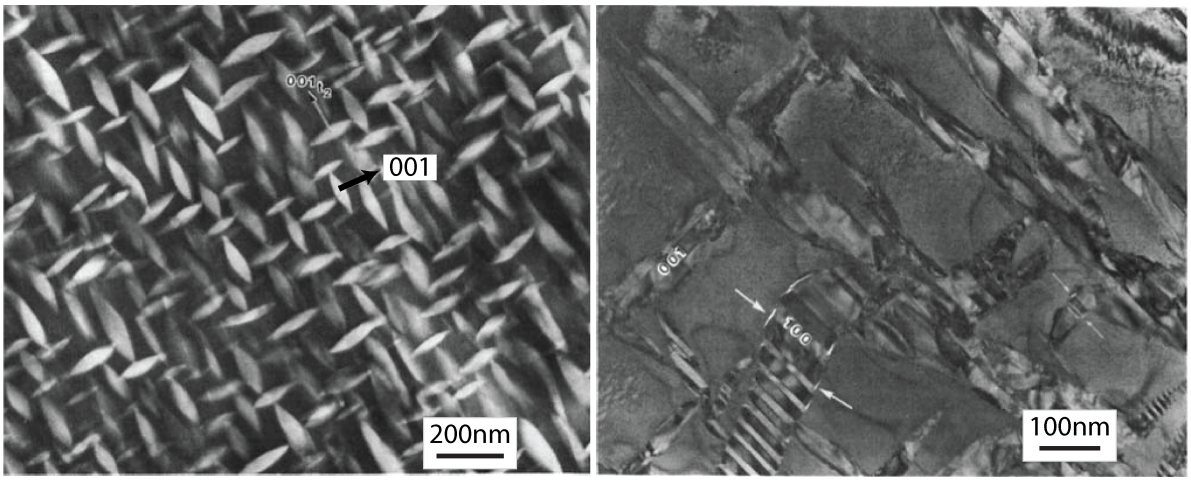

Figure 2.14 – Microstructure of partially stabilized zirconia (PSZ) (a) before and (b) after transformation toughening has occurred. Adapted from [87Heu].

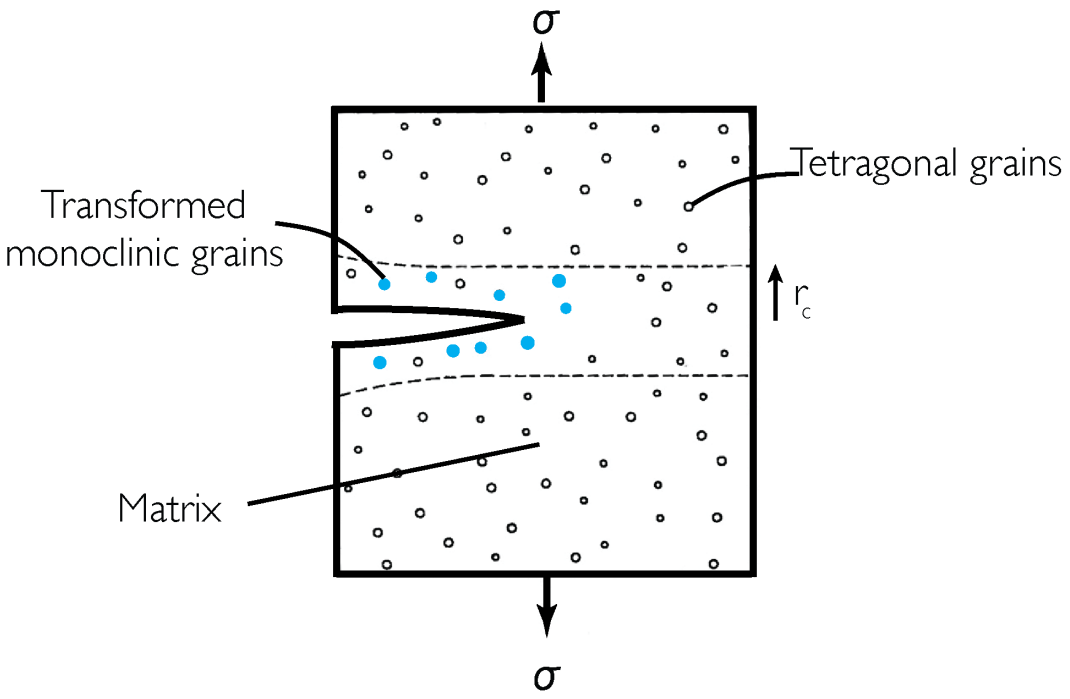

Figure 2.15 – Transformation toughening schematic, adapted from [00Cou].

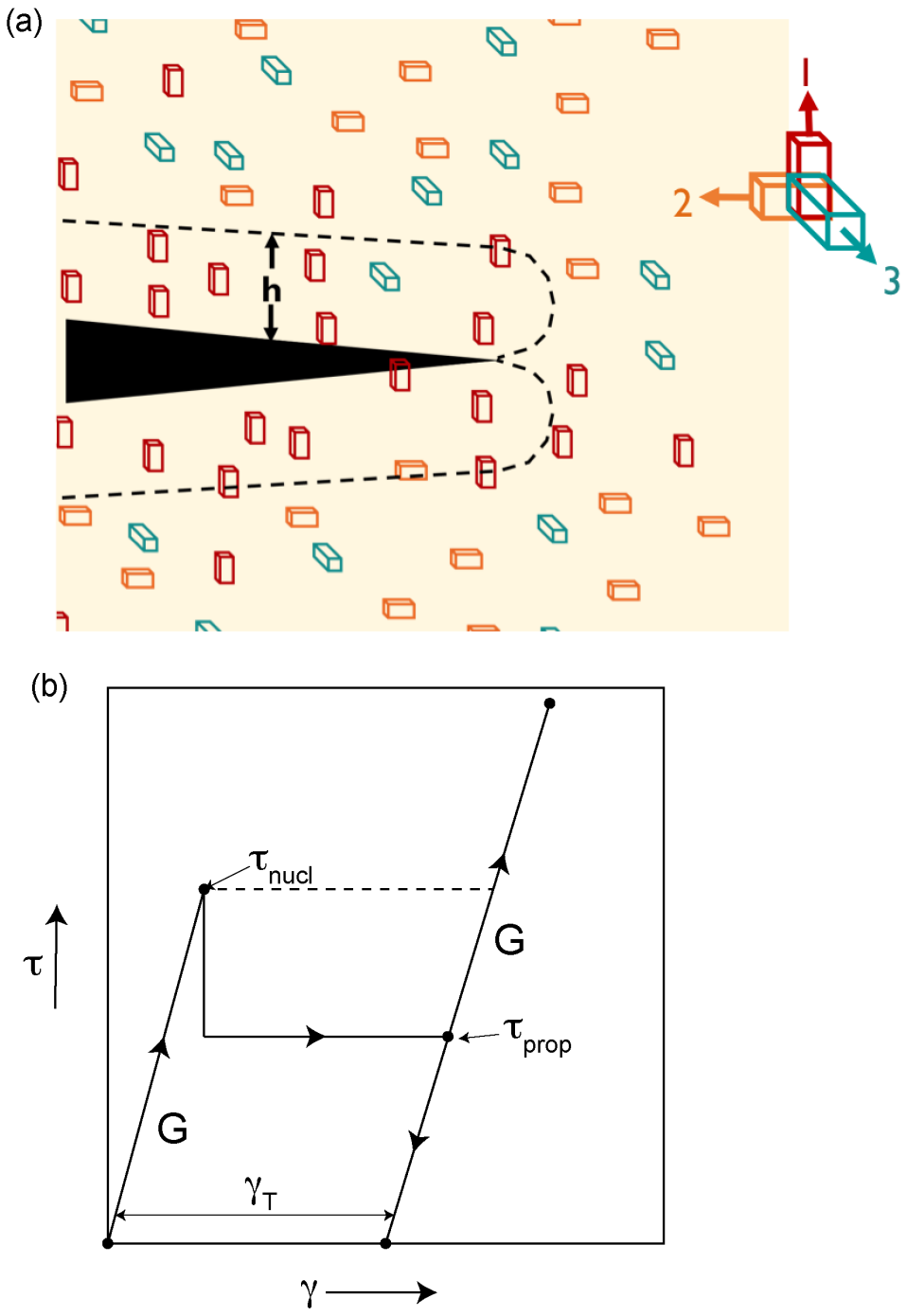

Figure 2.16 (a) Schematic of the process zone in ferroelastic (FE) switching. (b) Stress/strain curve of nucleation-controlled FE toughening. When shear stresses around the crack reach γ_{nucl}, FE switching is activated, resulting in a permanent shear strain, γ_T. Adapted from [12Kro, 07Mer].

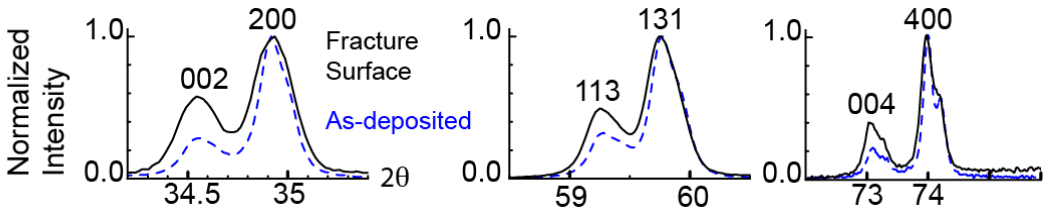

Figure 2.17 Increases in the intensity of out-of-plane peaks after a double cantilever beam fracture test are indicative of ferroelastic switching. Figure courtesy of E. Donohue [13Don].

CHAPTER 3: EXPERIMENTAL PROCEDURES

Understanding the phase equilibria and evolution in novel TBC systems is critical to identifying promising compositions for next generation TBCs. Given the various stabilization mechanisms discussed in Chapter 2, a multi-pronged approach was utilized to achieve this by first understanding the phase evolution of industrially sprayed coatings in an isovalent system, then investigating the phase equilibria and toughening mechanisms in a charge-compensated system. The experimental activities involved (i) material synthesis, (ii) high temperature treatments, and (iii) evaluation of samples using a combination of analytical techniques. This chapter describes the equipment and general methods for each type of experimental technique. If needed, additional pertinent information is provided in the description of experimental results in subsequent chapters.

3.1 Materials and Specimen Preparation

3.1.1 Atmospheric (air) Plasma Sprayed Coatings

In the CeO_2-TiO_2-ZrO_2 (CeTiSZ) system, powder with the composition 14Ce16Ti (14.5 mol% CeO_2, 15.8 mol% TiO_2, balance ZrO_2) was purchased from Saint Gobain (Thermal Spray Powders, Worcester, MA). The powder had been 'fused and crushed' and then plasma-spherodized to improve the flowability of the powder during spraying and also increase the homogeneity of the powders. Coatings, ~750μm thick, were deposited using air plasma spray (APS) on nickel alloy bars that had previously been coated with a porous MCrAlY bond coat. The specimens were fabricated at GE Power in Schenectady, NY using spray parameters similar to those used to deposit 8±0.5mole% ZrO_2 (8YSZ) coatings. After deposition the samples were heat treated in vacuum for 2 hours at 1120°C (2048°F) and then quenched in argon. Free-standing coatings were made by putting the samples in an acid bath to etch away the bondcoat, separating the ceramic from the substrate. After several days the

bond coat was etched away, leaving free-standing coatings. The coatings were cut into ~2.5cm x 2.5cm squares using a water jet at GE Global Research Center in Niskayuna, NY. Chemical composition of both the powder and resulting coatings was determined via inductively coupled plasma optical emission spectroscopy (ICP-OE) by Dirats Laboratories, Inc. (Westfield, MA). Samples were also manufactured in the full, multi-layered TBC system in which a superalloy (Inconel 718) was coated with a CoNiCrAlY bond coat followed by a thin layer of YSZ to prevent adverse reactions between CeTiSZ and the thermally grown oxide (TGO).

3.1.2 Air Plasma Sprayed Single Splats

To investigate segregation during the air plasma spraying process, "single splat" samples were fabricated by Dr. Vaishak Viswanathan in Prof. Sanjay Sampath's group at Stony Brook University. "Single Splat" samples were deposited on aluminum substrates by passing the air plasma gun over the substrate only once. Three different gun powers, 24kW, 35kW and 46kW, were used to investigate the influence of deposition conditions on the initial phases and microstructure. Typical "single splats" from a 46kW gun are shown in Figure 3.1. The splats were deposited with a spray distance of 100mm without pre-heating the aluminum substrate.

3.1.3 Synthesis of Powders and Consolidation of Pellets

Powders for thermal stability and phase equilibria studies were synthesized via reverse co-precipitation [90Cif, 93May].

Compositions in the ZrO_2-TiO_2-CeO_2 system, henceforth CeTiSZ, were synthesized as described in [12Kro] using Titanium iso-propoxide, cerium nitrate hexahydrate and zirconium n-butoxide (all Alfa Aesar) as precursors, which were mixed in ethanol due to

their water-sensitive nature. The solutions were assayed to determine the oxide yield and subsequently mixed in the appropriate proportions to yield the desired composition. The mixed solutions were then added drop-wise into ammonium hydroxide (NH_4OH) while the pH of the vigorously stirred solution was maintained above 10 to ensure the precipitation of all the cations mixed at the molecular level. The precipitates were filtered, rinsed once in acetone and a second time in ethanol before being allowed to dry. The samples were then pyrolyzed at 600°C for 4 hours in air.

For studies in the ZrO_2-$YO_{1.5}$-$TaO_{2.5}$ (ZYTO) system samples were synthesized in a similar manner using precursor solutions of zirconium oxynitrate hydrate, (<99%), yttrium nitrate hexahydrate (<99%), and tantalum chloride (<99%) (Alfa Aesar, Ward Hill, MA; 99.9% purity). Solutions of $ZrO(NO_3)_2$ and $Y(NO_3)$ in deionized (DI) water and $TaCl_5$ in ethanol were prepared and assayed using the gravimetric method. The precursors were mixed in the requisite proportions just before precipitation to prevent hydrolysis of the $TaCl_5$ by water that may lead to segregation. Similar to the CeTiSZ samples, the mixed ZrO^{2+}, Y^{3+}, Ta^{5+}-containing solutions were then added drop-wise into ammonium hydroxide, NH_4OH. Centrifugation was used to separate the solution and the hydroxide precipitates, which were washed with ethanol, dried and then ground with a hot (~90°C) alumina mortar and pestle to reduce agglomeration. With the exception of the $TaO_{2.5}$-rich compositions 10Y70Ta and pure $TaO_{2.5}$, which were calcined at 900°C to ensure complete conversion of Ta-rich hydroxides to oxides, all of the precipitates were then calcined for 4h at 650° C to remove the organic components and produce molecularly mixed metal oxides.

In each system the resulting oxide powders were subsequently ground with an alumina mortar and pestle. Powders were uniaxially pressed at 500MPa into pellets, ~10mm in diameter and ~3mm thick.

A limited number of ZYTO pellets in the $YO_{1.5}$-rich region were densified using current assisted densification (CAD, FCT Systeme, Rauerstein, Germany). Powder produced via co-precipitation, as described above, was placed in a 9.15mm graphite die lined with a grafoil liner, pressed lightly to produce a powder compact, and the die/pellet assembly was then loaded into the CAD system. The pellets were densified under pressure at either 1250°C or 1500°C. The powder was heated at a rate of 100°C/min in vacuum under 100MPa uniaxial pressure, held for 17min, and cooled to approximately 125°C. The current was not pulsed during these experiments. Following CAD experiments, the residual grafoil was removed from the pellets by grinding. Trace grafoil burn-off and re-oxidation occurred during subsequent heat treatments in air for 100h at 1250°C or 1500°C.

3.2 Heat Treatment

3.2.1 Isothermal Exposures of Coatings

The free-standing CeTiSZ samples were heat treated in air for various times at 1316°C (2400°F) and 1427°C (2600°F), as detailed in Chapter 4. Samples were heated at a rate of 20°C/min up to the hold temperature for the specified dwell time and then cooled in the furnace at a rate of 15°C/min.

The sintering behavior of the free-standing coatings is likely different then what would be expected from ceramic coatings on a bond coat/superalloy substrate. The thermal expansion of the substrate (15-17x10^{-6}/K, [06Pol]) is significantly higher than that of the ceramic (11x10^{-6}/K, [96Jon]) and thus during heating and at high temperatures the columns of the dense vertically cracked coatings would be held apart, preventing the columns from sintering together.

3.2.2 Isothermal Exposures of Pellets

Pellets were sintered in air for specific times and temperatures, as detailed in Chapters 4-6. For all heat treatments the pellets were placed on a piece of platinum foil in a covered alumina crucible. Some samples were removed from the furnace and quenched in air to minimize the amount of atomic-ordering that could occur during cooling but most samples were "furnace-cooled" at a rate of 10°C/min.

3.2.3 CMAS Composition and Infiltration

CMAS exposures were conducted following the approach in [07Gra, 10Gra]. A CMAS composition of 33 mol% CaO – 9 mol% MgO – 13 mol% $AlO_{1.5}$ – 45 mol% SiO_2 [06Kra] was used, as it was representative of deposits observed on engine components in desert environments (excluding Fe and Ni) [96Bor]. The constituent oxides (SiO_2 99.8%, MgO 99.5%, CaO, 99.95%, all from Alpha Aesar, and Al_2O_3 99.995%, Sumitomo Chemical) were mixed in the appropriate proportions by ball milling in DI H_2O, dried, and annealed just below the melting point for 24h. This partially reacted crystalline material was used for all experiments to study the interaction with pellets.

TBC pellets were sintered in air for 100h at 1500°C and then polished with diamond lapping films down to the 3μm film. Pellets, 6.6mm in diameter, of pre-reacted CMAS were sintered for 4h at 1200°C. To avoid over-shooting 1200°C, a heating rate of 2°C/min was used from 1180°C to 1200°C in each experiment. The CMAS pellets then mechanically thinned to achieve an average loading of 20mg/cm^2 over the specimen area. The CMAS pellets were placed on top of the polished ZYTO pellet and annealed in air for 4h at 1300°C in a covered alumina crucible. For the most part, heating and cooling rates of 10°C/min were used in the CMAS exposures.

3.2.4 Flowing Water Vapor

Experiments in high temperature steam environments were conducted at GE Global Research Center to investigate the stability of the ZYTO composition, 40Y33Ta, in high-water-vapor conditions for an extended period of time. The pellet was weighed before and after being exposed to flowing 90% water vapor, 10% oxygen for 500h at 1315°C.

3.3 Characterization

Samples were analyzed using X-ray diffraction, scanning electron microscopy and energy dispersive spectroscopy.

3.3.1 Specimen Preparation

Following the high temperature exposures to air, water vapor or CMAS, preliminary analyses using X-ray diffraction and Raman spectroscopy were conducted on the specimens prior to mounting and polishing the samples using standard metallographic techniques. Electron transparent foils were prepared by extracting lamellae from polished samples using focused ion beam (FIB, Helios 600, FEI, Hillsboro, OR).

3.3.2 X-Ray Diffraction

Standard powder X-ray diffraction techniques were used as a preliminary assessment of the crystalline phases presented in heat-treated specimens (XRD, Philips XPERT). Phases were identified by comparison to published powder diffraction data (ICDD PDF-4 Database), when possible.

3.3.3 Electron Microscopy

FEI XL30 and XL40 Sirion FEG (Hillsboro, OR) scanning electron microscopes using secondary electron (SE) and backscattered electron (BSE) imaging modes were used to observe specimen microstructure. Transmission electron microscopy (TEM) was performed using a FEI 200kV Tecnai G2 Sphera utilizing bright field (BF) and dark field (DF) imaging modes, energy dispersive x-ray spectroscopy (EDS, Oxford, Inca), and selected area electron diffraction (SAED). A FEI Titan 300 kV FEG TEM/STEM system was used for high angle annular dark field (HAADF) imaging and EDS linescans.

Equilibrium compositions to elucidate the phase diagram(s) were determined using a combination of TEM-EDS and wavelength dispersive electron probe microanalysis (EPMA, SX-100, Cameca, Madison, WI). While EPMA has improved energy resolution of the x-ray emission compared to EDS, the spatial resolution is still limited by the interaction volume between the beam and the sample. Therefore, TEM-EDS was used for samples with grain sizes below ~1μm.

Standards were used for both TEM-EDS and EPMA. A sample with composition 16.62 mol% $YO_{1.5}$, 16.59 mol% $TaO_{2.5}$ was analyzed by inductively coupled plasma optical emission spectroscopy at an external laboratory (Dirats Laboratories, Westfield, MA) and used to manually adjust the k-factors in the TEM/EDS and EPMA. Pure yttria and tantala specimens were also used as standards in EPMA. Typical variation in the measurement of identical materials was less than 1 atomic percent.

CeTiSZ lamellae were attached to copper (Cu) TEM grids. ZYTO lamellae were placed on molybdenum (Mo) TEM grids to avoid overlap of the principal emission lines of the Cu TEM grids and Ta in the samples. Any contributions of Ga (from FIB) or Mo (Cu) to the

EDS spectra were deconvoluted using the INCA software. The K series principal emission lines were used for Y and Zr while the L series lines were used to quantify Ta.

3.3.4 Raman Spectroscopy

Raman spectroscopy (Triple Monochromator Jobin-Yvon; 633nm excitation) was used due to its high sensitivity to anion displacements, especially those associated with the monoclinic ZrO_2 phase.

3.3.5 Thermogravimetric Analysis

To study the high temperature stability of CeTiSZ and ZYTO samples thermogravimetric Analysis (TGA) measurements were carried out in air using a Cahn Instruments TG 171 (previously Cerritos, CA). The CeTiSZ specimens were pre-sintered at 1300ºC for 12 h, while the ZYTO samples were sintered for 100 h at 1500°C prior to TGA. For the CeTiSZ samples, a heating rate of 10ºC/min to 1500ºC was followed by a 10-min dwell at the maximum temperature. Specimens were then cooled to room temperature at 10ºC/min. ZYTO samples were heated at 25°C/min up to 1500°C, held for an hour, and then cooled at 15°C/min.

3.4 Toughness Measurements

3.4.1 Micro-indentation

Micro-indentation with a Vickers indenter was used as a preliminary screen of specimen toughness [81Ans]. Loads of 2-10kgs were used. The dimensions of the cracks propagating from the corners of the indents and the indents themselves were measured by scanning electron microscopy (FEI XL30 and XL40, Hillsboro, OR). A typical indent is shown in Figure 3.2. The toughness (Γ, J/m^2) was then calculated from the equation

$$\Gamma = \frac{K_C^2}{E} = 2\zeta^2 P\left(\frac{d^2}{c^3}\right) \qquad 3.1$$

where K_c (MPa$\sqrt{m}$) is the fracture toughness, E (GPa) is Young's modulus, ζ=0.016 is a geometrical factor [81Ans], P is the load, $2a$ is the average diagonal of the indent and c is the average crack length, as measured from the corner of the indent.

The guidelines outlined in [81Ans] were followed to ensure the most accurate toughness values could be determined, within the limitations of the test. These guidelines included:

(i) Pellet thickness was a minimum of 10 times greater than the longest radial crack, c, in accordance with semi-infinite body analysis.

(ii) Radial crack length, c, was much greater than the length of the indent diagonal, $2d$.

(iii) Indentations were only made on free-standing pellets.

(iv) The grain size was less than 1% of the average crack dimensions.

3.4.2 Micro- 3-Point Bend Experiments

A micro-three point bending technique was developed in collaboration with Prof. Kevin Hemker, Dr. Jessica Krogstad and Dr. Binwei Zhang at Johns Hopkins University. Description of the sample preparation is provided in Chapter 7. In the experimental set-up, shown in Figure 3.3 and Figure 3.4(a) and (b), and described in detail in [15Zha], sintered specimen beams rest on two pins, approximately 3mm apart. For all experiments, the indentor was located at the mid-span of the beams and the fixture moved towards the indenter at a quasi-static rate of 90 or 150nm/s (specified for each sample in Chapter 6). Images were taken every 0.5s. Digital image correlation was used to calculate the mid-span deflection relative to the ends of the beam. Tracking grids, 8 pixels x 10pixels, were prescribed at the mid-span and the ends of the beam so the net displacement of the mid-span

could be determined. A 10x objective lens (1μm = 1.91pixels) was used for modulus experiments while a 20x lens (1μm = 3.81 pixels) was used for fracture toughness experiments. Force as a function of deflection plots for each test were obtained by patching the loading history with deflection using time as a common variable.

3.5 Figures

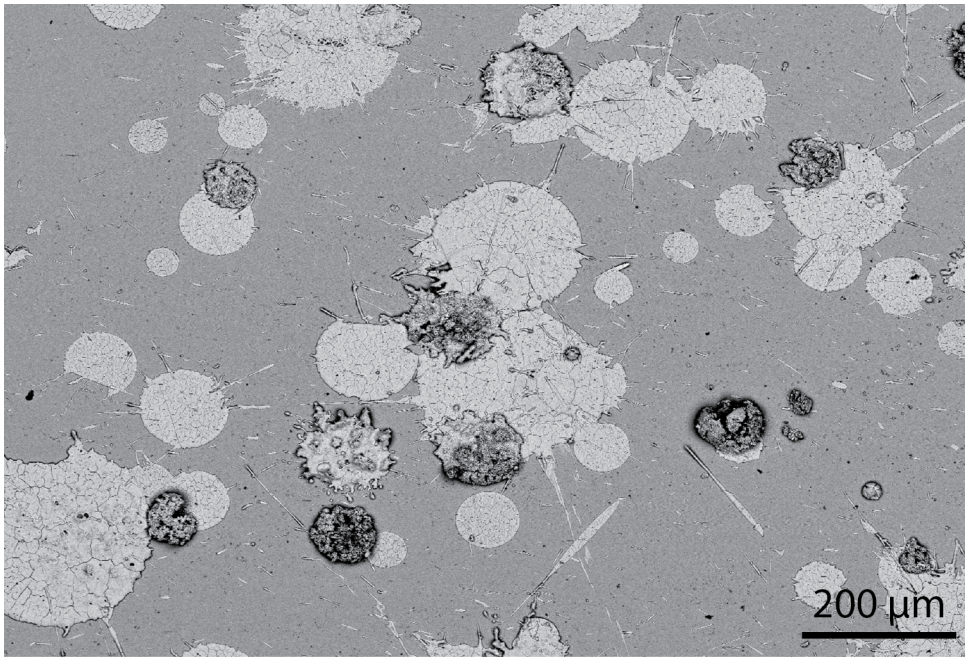

Figure 3.1 – SEM micrograph shows the typical microstructure of "single splats" deposited at Stony Brook University.

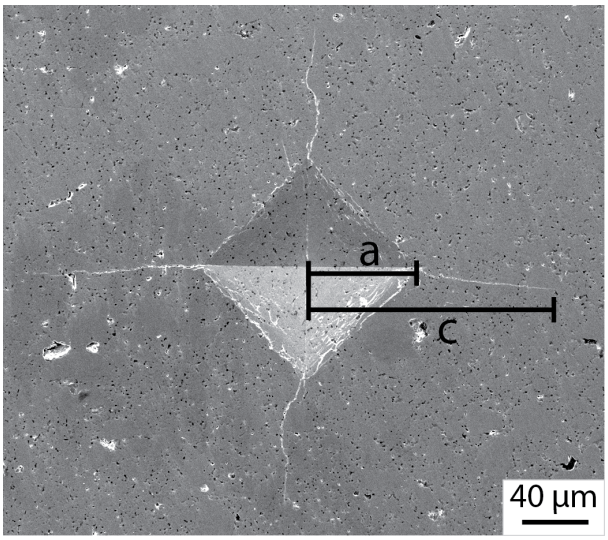

Figure 3.2 – Secondary electron image of a typical micro-indentation with the pertinent dimensions indicated according to [81Ans].

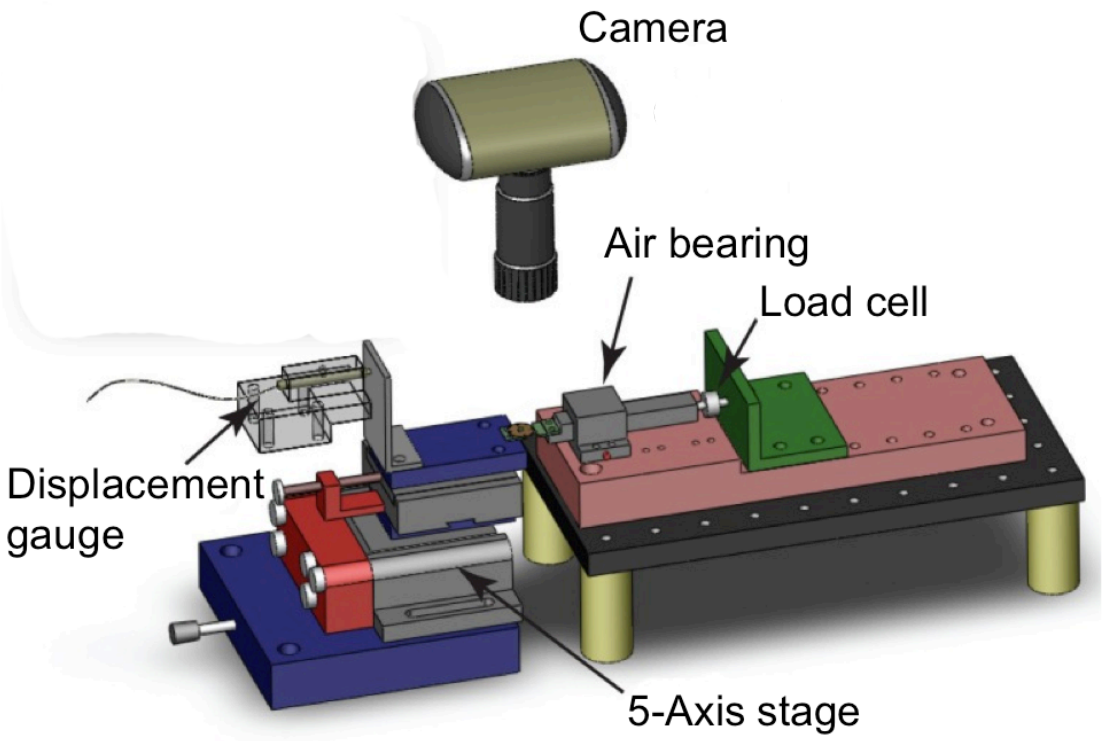

Figure 3.3 Schematic of the three-point bend experimental set-up at Johns Hopkins University. Image courtesy of Dr. Binwei Zhang.

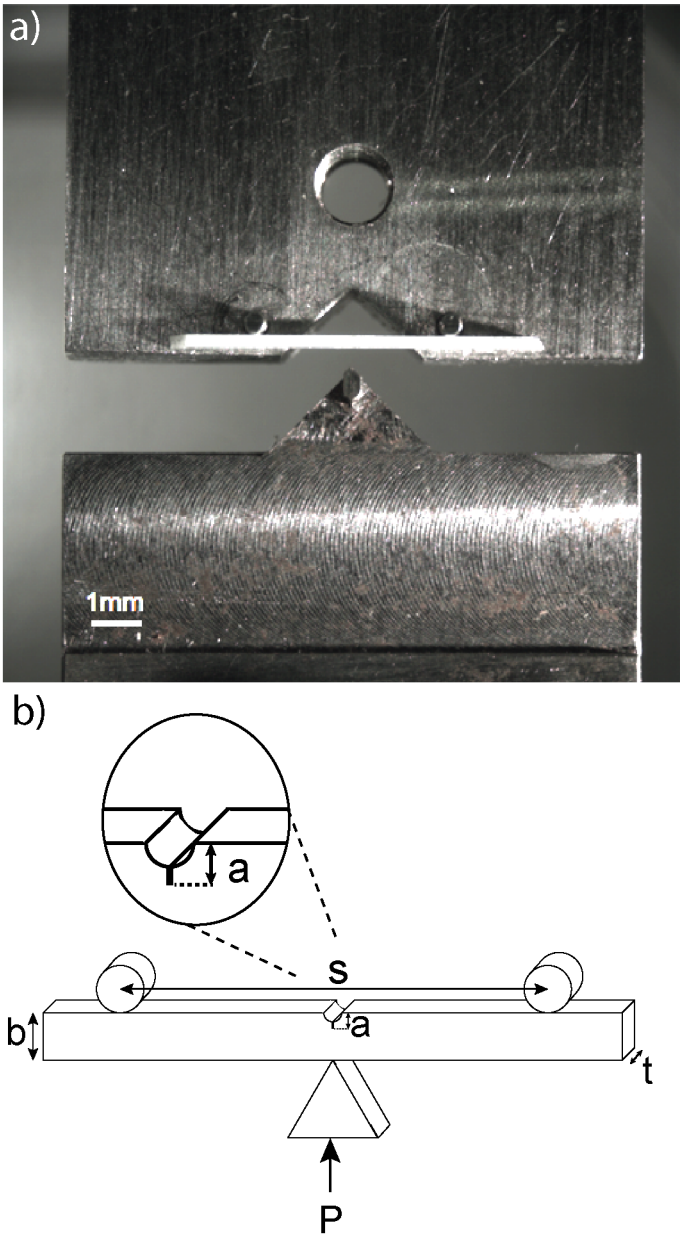

Figure 3.4 (a) Optical image showing typical set-up of 3mm span three-point bend experiment. (b) Schematic of the three-point bend set-up (not to scale) identifying the relevant variables and highlighting the pre-notch and pre-crack.

CHAPTER 4: NOVEL TBCS IN THE CERIA-TITANIA-ZIRCONIA SYSTEM

The CeO_2-TiO_2-ZrO_2 (CeTiSZ) system contains a relatively large, non-transformable tetragonal field with exceptional tetragonality at 1350°C [13Kro2]. It was suggested that the high tetragonality was responsible for the increased toughness values measured by micro-indentation. These results were sufficiently promising that coatings were fabricated using air plasma spray (APS). Unexpected phase and microstructure evolution is observed during subsequent heat treatments at 1316°C (2400°F) and 1427°C (2600°F). Segregation during solidification was proposed as a possible explanation for the presence of TiO_2-rich phases in the APS coatings. To study the influence of deposition parameters on segregation, 'single splats' were deposited. The extent of segregation observed in the splats was not sufficient to explain the microstructure and thus, precursor-derived powders were characterized. A reduction of at least one of the cations at high temperatures changes the phase equilibria and may explain the observed microstructures. This study illustrates the challenges associated with transitioning from lab-scale samples to industrial-scale coatings. When other novel thermal barrier coatings (TBCs) are proposed it is necessary to understand the liquidus and verify that cation oxidation state is stable up to high temperatures.

4.1 Background

The CeO_2-TiO_2-ZrO_2 (CeTiSZ) system was first investigated for TBC applications by Krogstad et al. [12Kro, 13Kro2]. The stabilization mechanism active in this system does not depend on the introduction of vacancies but rather the influence of differently sized cations. The oversized Ce^{4+} dilates the local structure around it, relieving the oxygen overcrowding [94Li2]. The undersized Ti^{4+} actually increases the distortion of the oxygen anions relative to their locations in pure ZrO_2 [94Li2]. The combination of these two effects results in unprecedented levels of tetragonality and stability of the solid solution at remarkably high

levels of co-doping [13Kro2]. The CeO_2-ZrO_2 and ZrO_2-TiO_2 binary phase diagrams had previously been investigated [83Tan, 10Wan], Figure 4.1. Krogstad was the first to attempt to experimentally determine the CeO_2-TiO_2 binary phase diagram [12Kro]. Using the information in the binary phase diagrams as well as experimental results of ternary compositions, a preliminary ternary phase diagram has been developed at 1350°C using co-precipitated powders, Figure 4.2, [12Kro, 13Kro2]. A relatively large non-transformable tetragonal phase field is present in the ZrO_2-rich portion of the diagram, [13Kro2]. Indentation toughness tests revealed that the sample with 10mol% CeO_2 and 10mol% TiO_2 (hereafter referred to as 10Ce10Ti) had a toughness of 42 J/m^2 after 1h at 1350°C [13Kro2], comparable to that of 8YSZ (41.8 J/m^2 [06Pit]). After 128h at 1350°C the measured toughness of 10Ce10Ti was even higher, 53 J/m^2, an effect ascribed to a larger grain size after the extended heat treatment.

4.2 Experimental Details

4.2.1 Manufacture of coatings and synthesis of powders

Given the phase stability and high toughness of CeTiSZ powder compacts it was of interest to assess their behavior when fabricated into coatings. The coatings were deposited on metallic substrates at GE Power in Schenectady, NY, via atmospheric plasma spray (APS) using parameters optimized for the deposition of 8YSZ. Powder feedstock with a nominal composition of 14.5 mol% CeO_2, 15.8 mol% TiO_2, balance ZrO_2 (14.5Ce16Ti) was manufactured by Saint Gobain. The composition was intentionally ordered with higher CeO_2 and TiO_2 contents to account for preferential loss of those compounds during the APS process. To minimize inhomogeneity, powders were fused and crushed prior to being agglomerated into hollow spheres (HOSP). Prior to spraying, the powder was dark maroon/brown in color, suggesting oxygen deficiency. After spraying the coatings were annealed under vacuum for 2hrs at <1100° C and quenched with argon. Similar to the HOSP

powder, the coatings were also maroon/brown in color. The coatings were then sectioned into 25 x 25 mm squares using a water jet followed by chemical removal of the metal substrate. Individual coupons were heat treated for 49 h at 1316° C (2400°F) and 6.5 h or 500 h at 1427° C (2600°F) with a heating/cooling rate of 10°C/min. Samples were also manufactured in the full, multi-layered TBC system in which a superalloy (Inconel 718) was coated with a CoNiCrAlY bond coat followed by a thin layer of YSZ to prevent adverse reactions between CeTiSZ and the thermally grown oxide (TGO).

To investigate the potential for segregation during deposition, single splat samples were fabricated from the same powders at Stony Brook University, in collaboration with Prof. Sanjay Sampath and Dr. Vaishak Viswanathan, as described in Chapter 3.

To verify the phase and microstructure evolution observed in air plasma sprayed samples was not an artifact of the processing conditions, powder samples were also synthesized via reverse co-precipitation, following the procedures described in Chapter 3. Two compositions, 14Ce14Ti and 12Ce12Ti, (again, compositions listed in mole percent of single-cation base oxide formulae) were heat treated at 1427°C for 6.5h.

4.2.2 Characterization

Phase evolution of the samples was studied using x-ray diffraction (XRD) at room temperature. Backscattered electron imaging (BS-SEM) was also used to characterize the phase constitution and microstructure of each sample. Lamellae for transmission electron microscopy (TEM) were extracted from samples using a focused ion beam (FIB). High angle annular dark field (HAADF) was used to characterize a coating that had not been exposed to high temperatures. Energy dispersive x-ray spectroscopy (EDS) in an SEM and a TEM was used for composition analysis. Some of the coating materials were sent to Dirats

Laboratories so that inductively coupled plasma optical emission spectroscopy (ICP-OES) could be performed.

Thermogravimetric analysis (TGA), described in Chapter 3, was performed on a precursor-derived sample of 14Ce14Ti that had been equilibrated for 12h at 1300°C.

4.3 Results

4.3.1 Air plasma sprayed coatings

As deposited the APS CeTiSZ coatings exhibited a dense vertically cracked (DVC) microstructure, Figure 4.3. By XRD, the 'as received' coatings are mostly tetragonal (*t*) ZrO_2 solid solution. ICP-OES results indicate the coatings have an average composition of 14.1Ce15.5Ti. Based on the ternary diagram in Figure 4.2, the coatings are just barely in the three-phase field, CeO_2 + $ZrTiO_4$ + *t*-ZrO_2. The coatings were maroon/brown in color, suggesting oxygen deficiency.

The phase stability of the CeTiSZ coatings was investigated for samples after exposures at 1316°C for 49 h and after 1427°C for 6.5 h and 500 h. The salient findings from the study are best summarized by the BSE images shown in Figure 4.4. After 49h at 1316°C, the vertical cracks initially present have nearly sintered together, Figure 4.4(a). Small amounts of $ZrTiO_4$ and CeO_2 were detected via XRD, EDX and BSE images such as the high magnification image in Figure 4.4(c). These phases were expected given the location of the coating composition in the 3-phase field, indicated in the ternary diagram in Figure 4.4(g). However, the extensive porosity seen in some regions of the coating was unexpected Figure 4.4(b). After 500 h at 1427°C, the microstructure is significantly different, Figure 4.4(d-f). Large ~30 μm pores are present throughout the well-sintered coating. The globular nature of the tetragonal grains, indicated with red circles, is suggestive of the presence of liquid phase during sintering, which is undesirable. While $ZrTiO_4$ and CeO_2 are present, as expected,

another Ti-rich phase is also present (darkest phase in (e)). The Ti-rich phase, which XRD indicates is likely rutile, is not predicted by the phase diagram at 1350°C for the composition of the coating.

To investigate if the presence of the non-equilibrium TiO_2-rich phase was a result of inhomogeneities present initially, the 'as-deposited' coating was characterized in more detail. Slight contrast variations are observed in BSE images, suggesting compositional fluctuations. Figure 4.5(a). BSE imaging of a lamella removed from a coating, Figure 4.5(b) also suggests the coatings are not homogeneous prior to heat-treatment. The extent and chemical compositions of the inhomogeneities are evident in the HAADF image in Figure 4.5(c). TEM-EDS of the phases present is plotted on the isothermal section shown in Figure 4.5(d), indicating non-equilibrium phases are present near the compositions of $CeTiO_4$ or $Ce_2Ti_2O_7$ and $CeTi_2O_6$. The presence of these phases supports the hypothesis that segregation is occurring during the coating deposition process. However, the microstructure of APS coatings is complex, involving many layers of splats, particles or parts of particles that were not melted and voids. To avoid the complexities of full coatings, single splats were fabricated to study the influence of processing conditions on segregation.

4.3.2 Air plasma sprayed single splats

Single-splats that were deposited using a plasma gun power of 24 kW were ~2 μm thick and ~80 μm in diameter, Figure 4.6. Directional solidification and grain growth are evident in the BF-TEM images in Figure 4.6(b) and (c). No evidence of segregation was observed at this scale.

Structures reminiscent of fine dendrites are present on the surface of the single splats deposited using a plasma gun power of 35 kW, Figure 4.7(a,b). The dendrites are depleted in CeO_2 and TiO_2 (c) based on TEM-EDS and are striated in BF-TEM images, suggesting the

transformation to monoclinic (*m*)-ZrO_2 has occurred. By TEM-EDS the composition of a region away from the dendrites is closer to the average coating composition.

The size of single splats deposited using a plasma gun power of 46 kW is significantly larger than that of other single splats investigated. Splat diameters range between 200-300 μm, Figure 4.8. Dendritic structures are evident on the splat surface. Based on SEM-EDS composition maps, the dendrites are again depleted in CeO_2 and TiO_2, Figure 4.9. Further TEM analysis, Figure 4.10, shows the dendrites also have striations, suggesting *m*-ZrO_2, (a,c). The bulk composition is slightly enriched in CeO_2 and TiO_2, based on TEM-EDS, (b).

Given the presence of inhomogeneities in both full coatings and single splats it was necessary to verify that the segregation was not already present in the powder used to produce the samples. The average composition of the HOSP powder was 14.5 mole% CeO_2 and 15.8 mole% TiO_2, as determined from ICP-OES. Further SEM-EDS characterization revealed compositional segregation in the powder, Figure 4.11(a-d). Contrast variation in BSE images supports these results, Figure 4.11(e,f) and dendritic structures are clearly present.

4.3.3 Precursor-derived powders

It was unclear if the phases and microstructures observed in coatings, single splats and HOSP powders were only a result of the processing conditions or if equilibrium thermodynamics also played a role. To investigate structures that had not evolved from the liquid, pellets of precursor-derived powders of 12Ce12Ti and 14Ce14Ti were heat treated for 6.5 h at 1427°C, Figure 4.12. Although only the equilibrium phases of CeO_2, $ZrTiO_4$ and *t*-ZrO_2 were identified by BSE images and XRD, the presence of globular grains is characteristic of liquid-phase sintering at high temperatures. Color gradients, especially in

the 14Ce14Ti sample, are apparent in optical photographs of the cross-sections of the pellets, Figure 4.12(c,d).

TGA measurements were carried out on the 14Ce14Ti precursor-derived composition. The results of these experiments, Figure 4.13, show that the sample slowly starts losing mass at T>1150°C. Above 1350°C, the rate of mass loss increases markedly. However the sample quickly regains the mass as it is cooled—Figure 4.13(b). As will be elucidated in Section 4.3.2, it is likely that the ~0.6 mg reversible mass change observed in the TGA experiments, which were repeated to ensure reproducibility, is directly correlated to the loss of oxygen associated with the reduction of Ce^{4+} to Ce^{3+}. As such, it can be roughly estimated that nearly 42% of the cerium cations have been reduced to a 3^+ oxidation state upon heating to and holding at 1500ºC.

4.4 Discussion

Salient findings in the study of CeTiSZ coatings pertain to (i) the suitable development of a DVC microstructure and associated compliance benefits, (ii) the unexpected accelerated sintering behavior of free-standing coatings, with evidence for the presence of a liquid phase during the densification process, (iii) the apparent segregation occurring during solidification of the studied compositions by APS, with attendant consequences to the stability of the ZrO_2 solid solution, and (iv) the consequences of the reduction of Ce^{4+} at high temperature in air.

4.4.1 Microstructure

The DVC microstructure observed in CeTiSZ coatings is promising, notwithstanding the use of spray parameters developed for 8YSZ, which suggests there are opportunities for further improvement by proper adjustment of the relevant process parameters, e.g. plasma gun power, powder feed rate, stand-off distance, etc. While some undesirable horizontal cracking

is observed in Figure 4.3, the DVC architecture has been successfully implemented. Such a structure is vital to enabling the coating to accommodate the thermomechanical strains that result from differences in thermal expansion between the metallic substrate and ceramic coating [01Eva]. Additionally, it has been shown that DVC CeTiSZ coatings exhibit toughness comparable to DVC 8YSZ using the DIC-instrumented double-cantilever-beam (DCB) test developed by Donohue [14Don].

The DVC microstructure of the CeTiSZ coatings, while suitable in the as-deposited condition, appears to experience excessive densification at high temperature, at variance with what would be expected in ceramic coatings on a bond coat/superalloy substrate. In the latter case the differential in thermal expansion of the substrate (~15-17x10^{-6}/K) [06Pol] and the ceramic (~11x10^{-6}/K for 8YSZ) [96Jon] would suggest that the vertical cracks would further open when heated, especially above the deposition temperature. This would hinder the tendency of the columns to sinter in spite of the likely presence of occasional local contacts between them. Conversely, freestanding coatings do not have such a constraint to sintering, which is consistent with the accelerated densification observed. There is, however, evidence of the presence of a liquid phase at the sintering temperature that may play an additional role in promoting densification.

4.4.2 Potential effects of segregation during solidification

In general, the phase and microstructure evolution of precursor derived powder compacts and APS samples differ significantly. Powder produced via reverse co-precipitation evolves in the solid state from nanocrystalline grains of metastable phases to larger grains of the equilibrium phases at high temperatures Figure 4.14(a). Coatings or splats deposited via APS solidify from the molten (or semi-molten state), Figure 4.14(b). Thus the solidification path and subsolidus cooling have an important effect on the phases present in ‘as-deposited’ coatings.

An experimentally determined ternary liquidus is not available but some initial insight can be derived from examination of the phase diagrams in Figure 4.1. It is first noted that in compositions with less than 20 mol% CeO_2 or 20 mol% TiO_2 the primary phase forming during solidification is the fluorite solid solution. However, the solute partition coefficient is much closer to unity in the ZrO_2-CeO_2 binary, reminiscent of the situation in ZrO_2-$YO_{1.5}$, than it is in the ZrO_2-TiO_2 binary. Hence, one would expect that for the compositions investigated the primary solidification phase is fluorite with a significantly lower solute content than the parent melt, in agreement with the experimental result in Figure 4.10. Moreover the shape of the binary diagrams suggests that the depleted fluorite solid solution would undergo the transformation to tetragonal phase, and then to monoclinic phase upon cooling in agreement with the observed presence of monoclinic phase in the single splat experiments.

Once it is established that the solidification path drives the liquid composition away from the ZrO_2 corner one can propose a tentative shape for the liquidus projection from the known temperatures and invariant transformations in the binary phase diagrams. The result of this exercise is presented in Figure 4.15, where it is shown that the liquidus surface is dominated by the primary crystallization field for fluorite, with tetragonal ZrO_2 solid solution, $ZrTiO_4$ and rutile TiO_2 extending from the ZrO_2-TiO_2 binary into the ternary, and a small brannerite ($CeTi_2O_6$) field extending from the CeO_2-TiO_2 binary. The scenario suggests that there is a ternary eutectic below 1390°C at the junction of the ZT, R and B crystallization domains. The implication is that if solidification proceeds away from the ZrO_2 corner toward the lower temperature TiO_2 corner one could have a small amount of the ternary eutectic that could re-melt and form a liquid phase that aids densification at the temperatures of interest. It is expected that this long solidification path is not present in the splats, consistent with the evidence, but there was evidence of $CeTi_2O_6$ and $CeTiO_4$ or $Ce_2Ti_2O_7$ in the as-received coating microstructures Figure 4.5.

It is also possible that composition variability in the fused and crushed, HOSP powders used in the APS deposition may give scenarios consistent with the solidification path ending near the TiO_2-rich corner. However, the compacts of precursor-derived powders also exhibit evidence for liquid presence after sintering at temperatures in the range 1350-1427°C Figure 4.12, which would be inconsistent with a solidification segregation argument as they were never fully molten, cf. Figure 4.14. This situation is explored in the next section.

4.4.3 High temperature stability of CeTiSZ coatings

An alternate scenario explaining the evolution of a minority liquid phase involves the potential change in the phase equilibria as a result of the reduction of Ce^{4+} to Ce^{3+} at high temperatures. The mass loss observed in the TGA experiments in Figure 4.13, as well as the extensive porosity in the coatings after exposures at 1316°C and 1427°C could therefore be attributed to the associated release of oxygen.

A thorough review of the literature supports the hypothesis of Ce^{4+} reduction. Several papers highlight the color change from yellow to maroon/brown as indicative of Ce^{4+} to Ce^{3+} in all samples containing Ce regardless of whether TiO_2 or ZrO_2 are present as well [13Gio, 00Kis, 08Mar, 04Ots, 94Pre]. The fact that the HOSP powder, as-deposited APS coatings, and the center of the 14Ce14Ti pellet in Figure 4.12 were maroon/brown suggests that Ce^{3+} is present. Color gradients in (1350°C) heat-treated pellets of precursor-derived 20Ce20Ti powder had previously been attributed to oxygen deficiency at the center of the pellet [10Lep]. Based on the TGA results, Ce^{3+} re-oxidizes quickly but it is possible that the oxygen diffusivity is such that the center of the pellet remains reduced at room temperature, Figure 4.12.

Review of the catalysis literature reveals that pure CeO_2 undergoes reduction at high temperatures and the presence of ZrO_2 or TiO_2 actually increase the reducibility of CeO_2.

While pure CeO_2 was initially investigated for solar thermochemical splitting of CO_2 and H_2O [02Sko] or catalysis [04Ots, 10Gao] it was found that the presence of ZrO_2 significantly increases the reducibility of Ce^{4+} [06Dut1, 14Hao, 03Hua, 11LeG, 12LeG, 11LeG2, 11LeG]. Theoretical calculations and experiments show that ~28% of the Ce (CeO_2 + $CeO_{1.5}$) in a 12 mole% CeO_2 stabilized ZrO_2 is present as Ce^{3+} at 1450°C in air [03Hua]. Compounding the problem for the stability of CeTiSZ coatings, the addition of TiO_2 also increases the reducibility of CeO_2 [06Dut2]. In compositions with a CeO_2:TiO_2 ratio of 1:1, Ce^{3+} is observed after exposure to 1200°C in air [08Mar].

Since Ce^{3+} is observed after heat-treating ZrO_2-CeO_2 and CeO_2-TiO_2 compositions in air but reducing environments are required to form Ti^{3+} compounds [08Mar], it is likely that Ce^{4+} is the cation being reduced in the compositions in this study. The ZrO_2-$CeO_{1.5}$ and $CeO_{1.5}$-TiO_2 binary phase diagrams would therefore be needed to accurately predict the isothermal section or liquidus projection for the CeTiSZ system. The ZrO_2-$CeO_{1.5}$ binary, Figure 4.16, differs greatly from that of ZrO_2- CeO_2. While the reduction of CeO_2 certainly influences the phase equilibria in the ZrO_2- CeO_2 binary, it is insufficient to explain the incipient melting observed in 14Ce14Ti without invoking ternary alloying effects in the CeO_2-TiO_2-ZrO_2 system. Unfortunately, the $CeO_{1.5}$-TiO_2 binary phase diagram has not been determined experimentally or via thermodynamic calculations in literature, inhibiting the estimation of higher temperature isothermal sections or the liquidus. While the shape of the liquidus would not influence solid-state phase evolution, if the reduction of CeO_2 to $CeO_{1.5}$ results in a liquid phase the shape of the liquidus would influence the phase segregation kinetics.

4.5 Conclusions

The CeTiSZ system showed promising phase stability and toughness results when investigated with precursor-derived powders at 1350°C [13Kro2]. Although APS coatings exhibit equivalent toughness to 8YSZ [14Don], the phases and microstructure after

equilibrating at 1316°C (2400°F) and 1427°C (2600°F) are not desirable. Segregation during solidification is proposed as a possible explanation for the presence of TiO_2-rich phases in the APS coatings. 'Single splats' were deposited to study the influence of deposition parameters on segregation. The extent of segregation observed in the splats is not sufficient to explain the coating microstructure. A change in the thermodynamic equilibrium is proposed based on the characterization of precursor-derived powders after exposure to T≥1427°C. The reduction of Ce^{4+} at high temperatures changes the phase equilibria and places an inherent temperature limit on CeTiSZ TBCs. Additional work is needed to explain the presence of a liquid phase at 1427°C.

This study illustrates the challenges associated with transitioning from lab-scale samples to industrial-scale coatings. When other novel thermal barrier coatings (TBCs) are proposed, it is essential to understand the liquidus and verify the stability of cation oxidation state up to high temperatures.

4.6 Figures

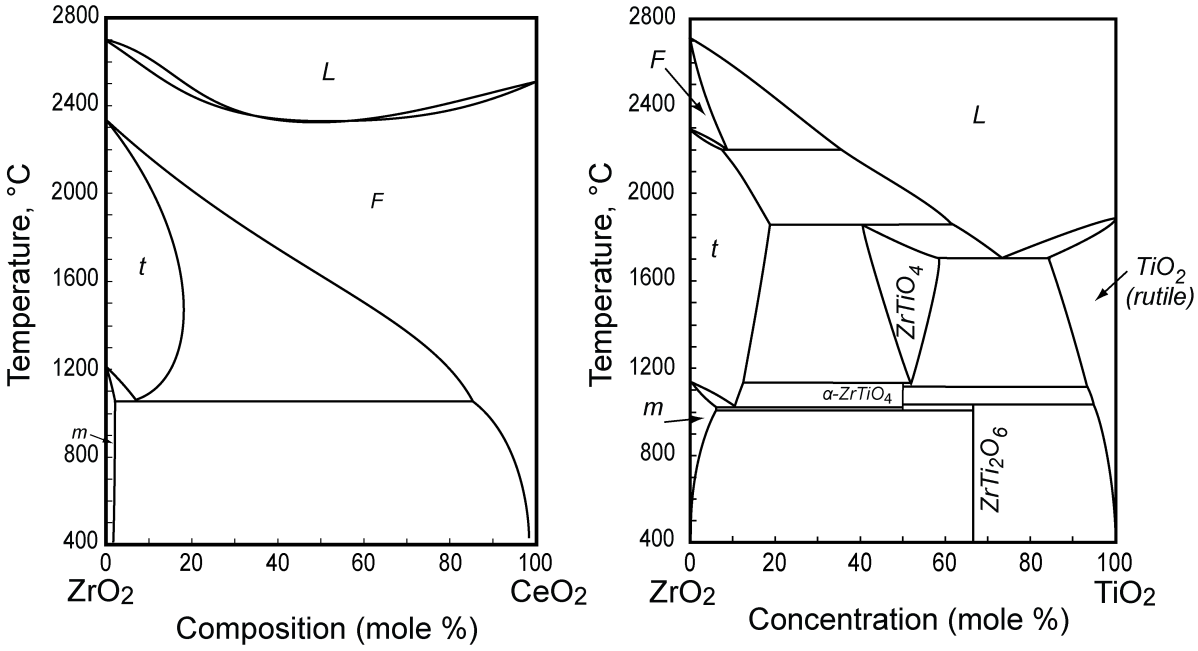

Figure 4.1Reported binary phase diagrams for the (a) ZrO_2-CeO_2 and (b) ZrO_2-TiO_2 phase diagrams, adapted from [83Tan] and [10Wan], respectively.

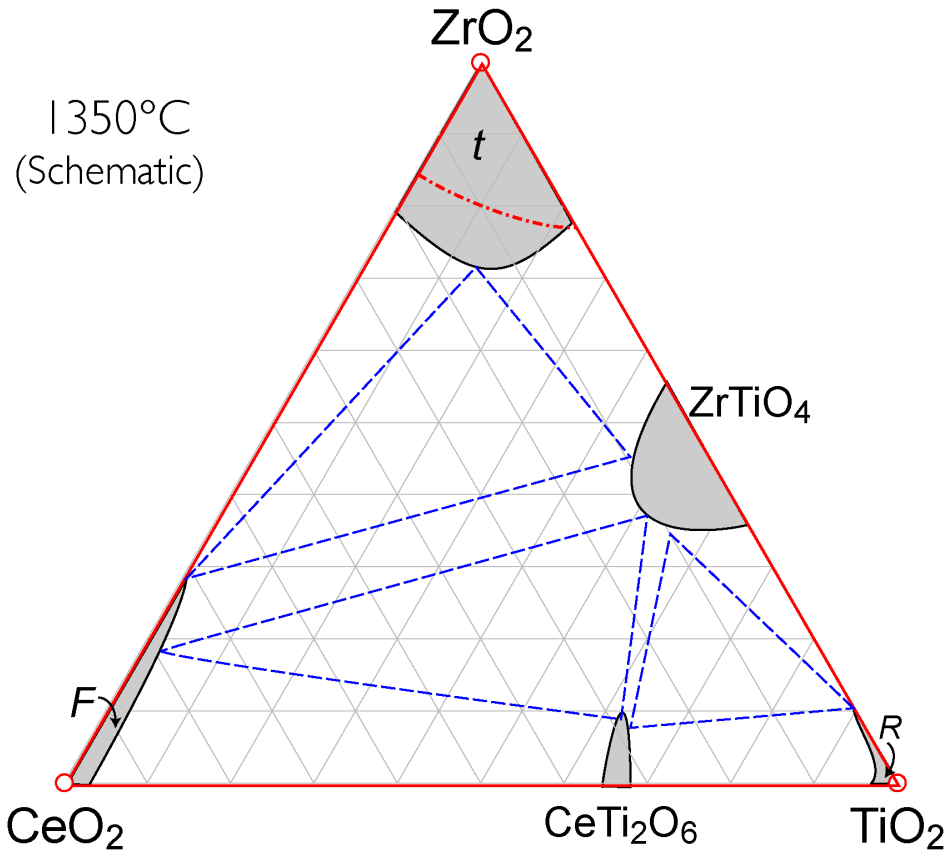

Figure 4.2 Pseudo-ternary CeO_2-TiO_2-ZrO_2 (CeTiSZ) 1350°C isothermal section originally published in [12Kro].

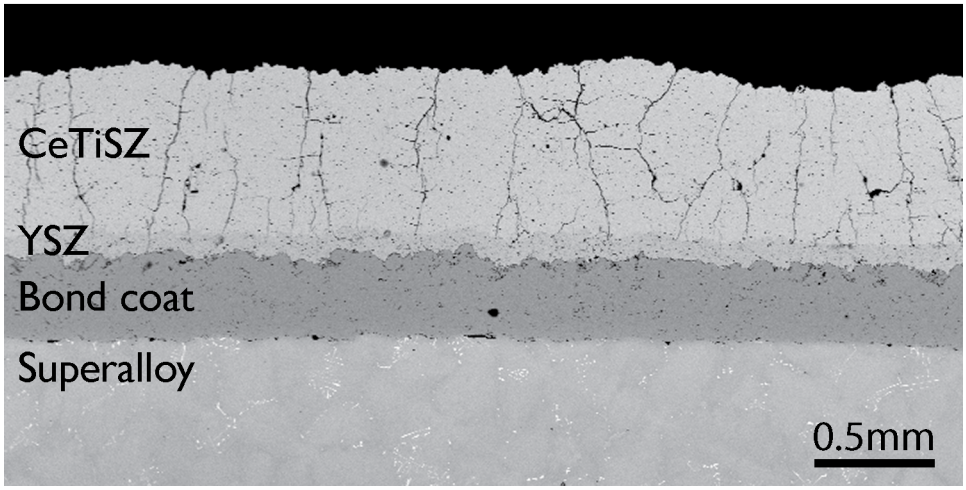

Figure 4.3 Air plasma sprayed (APS) CeTiSZ coatings initially exhibit a dense vertically cracked microstructure.

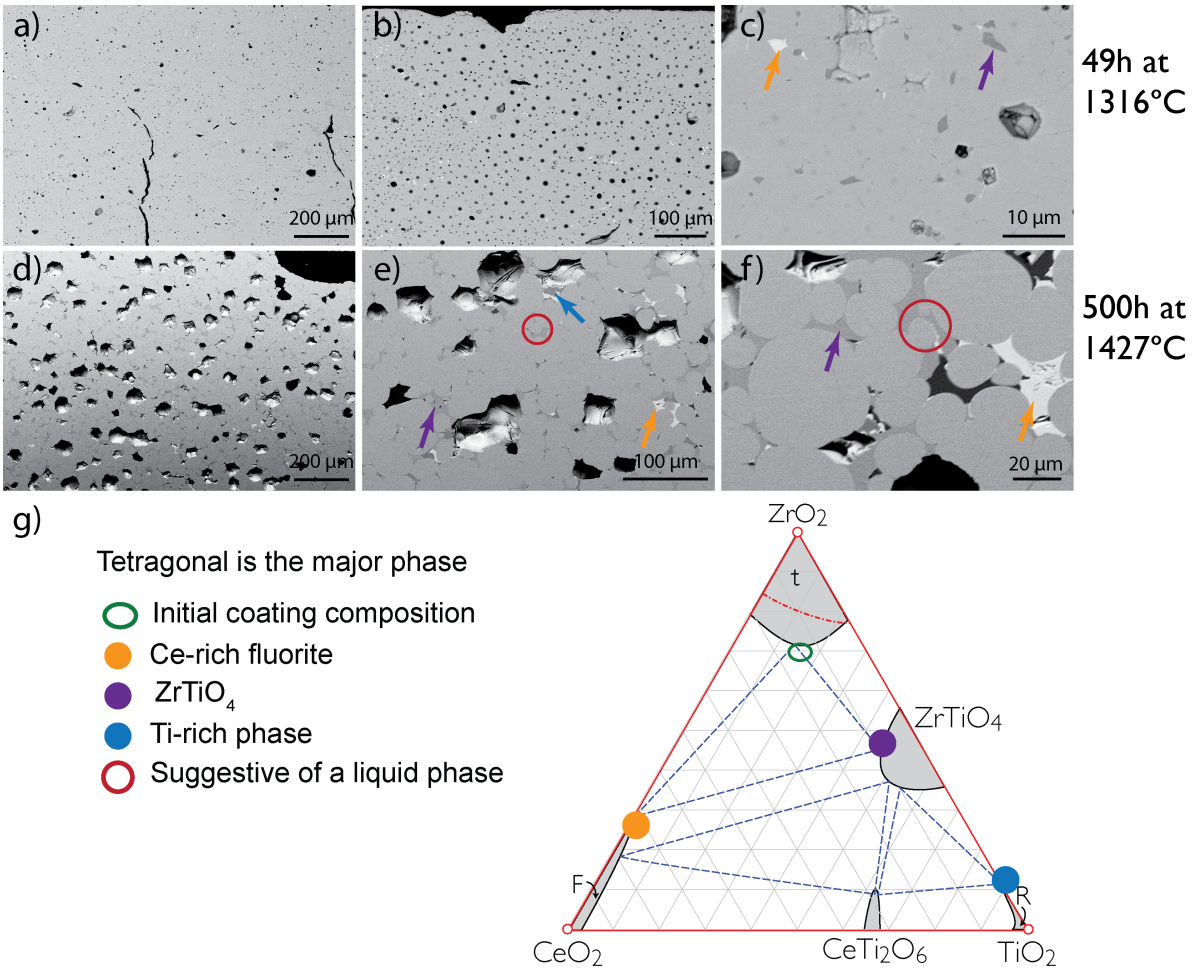

Figure 4.4 Cross-sections of CeTiSZ coatings heat treated for 49h at 1316°C (a, b, c) and 500h at 1427°C (d, e, f). Extensive porosity is present in both samples. The globular appearance of the grains in the sample heat treated at 1427°C indicates the presence of a liquid phase at high temperatures. Phases corresponding to the measured EDX compositions of regions marked with arrows in (c, e, f) are indicated in (g).

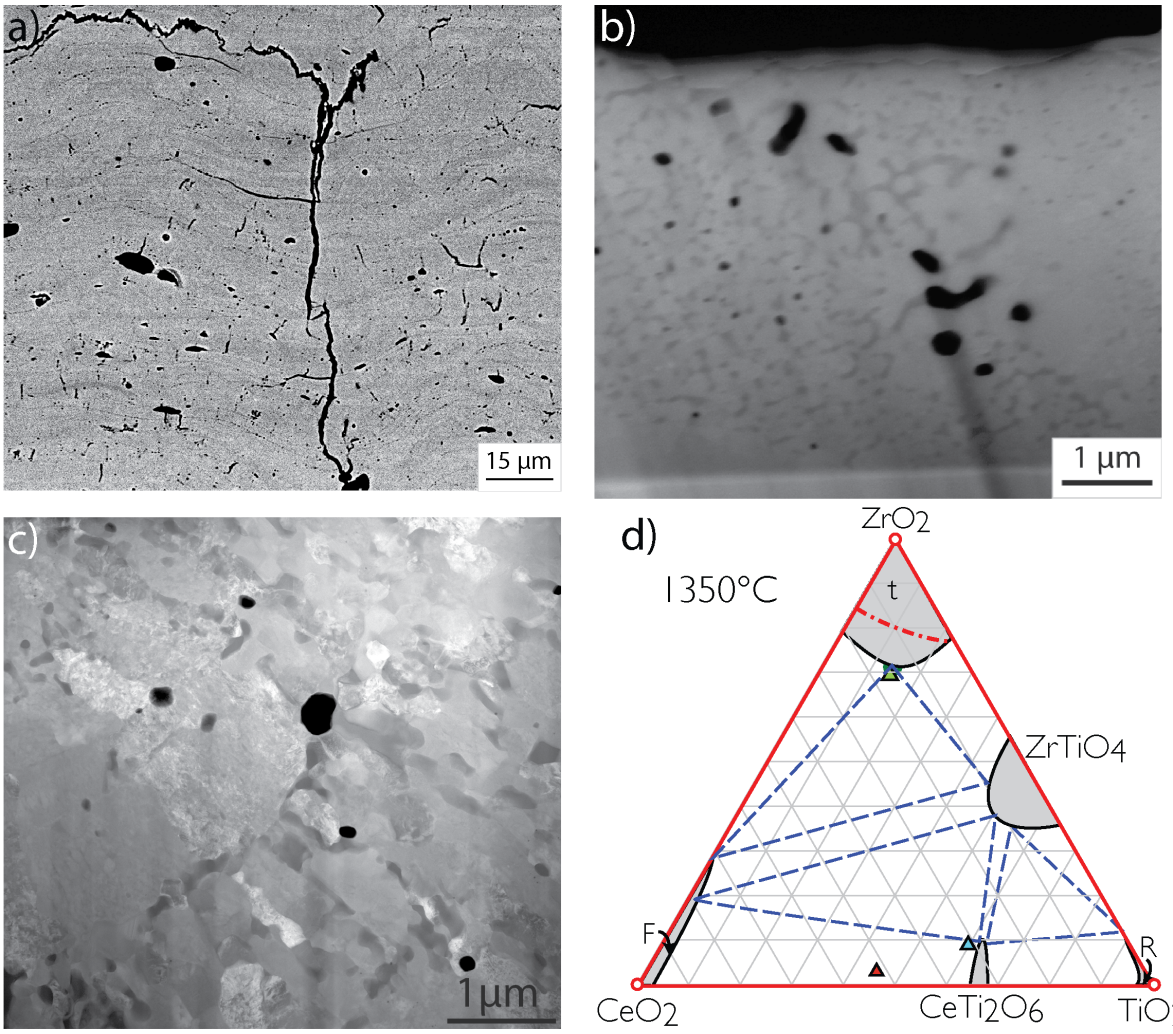

Figure 4.5 (a) High magnification BSE image of a CeTiSZ APS coating in which contrast variations can be attributed to changes in composition. (b) Segregation is apparent in BSE image of the TEM lamella in (c). (c) HAADF image from APS coating reveals microstructure is inhomogeneous. In order of decreasing grey level, the black regions are pores, followed by $CeTiO_4$ or $Ce_2Ti_2O_7$ (red triangle in d), then $CeTi_2O_6$ (blue triangle in d), with the bulk matrix corresponding to t-ZrO_2 (green triangle in d). (d) Isothermal section of the CeO_2-TiO_2-ZrO_2 phase diagram with TEM/EDS compositions of phases present in the 'as deposited' APS coating.

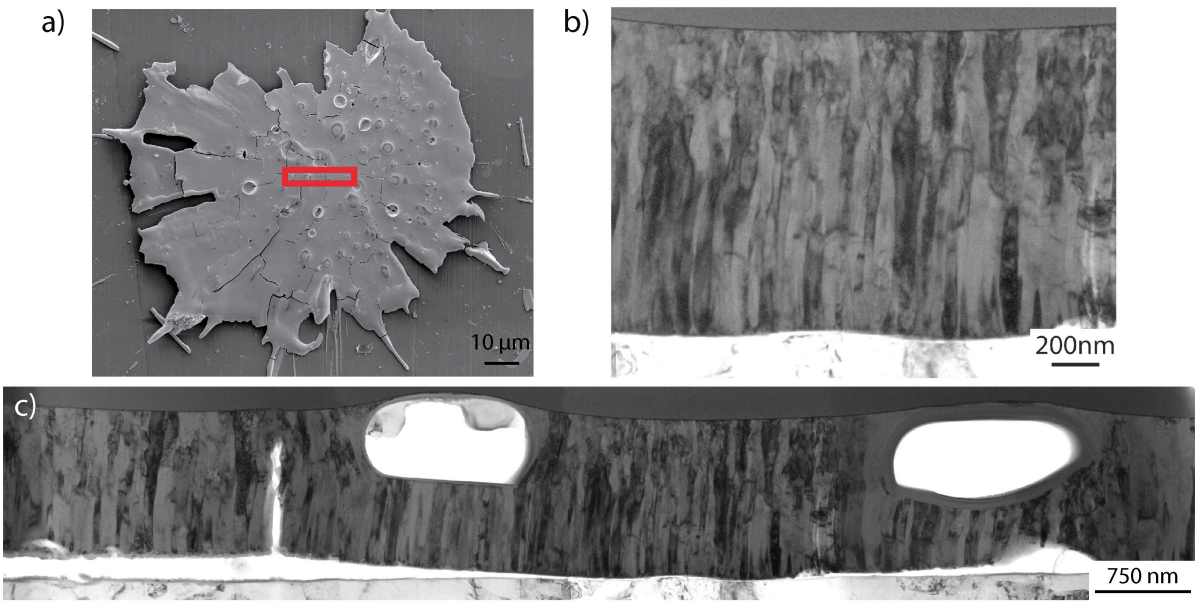

Figure 4.6 (a) BSE image of single splat deposited with a plasma gun power of 24kW. Location of TEM lamella is indicated with the red box. (b) BF-TEM image shows the splats are very thin (~2µm) and directional solidification/grain growth is evident. (c) BF-TEM image of the entire lamella indicates the presence of porosity but direct evidence of segregation is not observed.

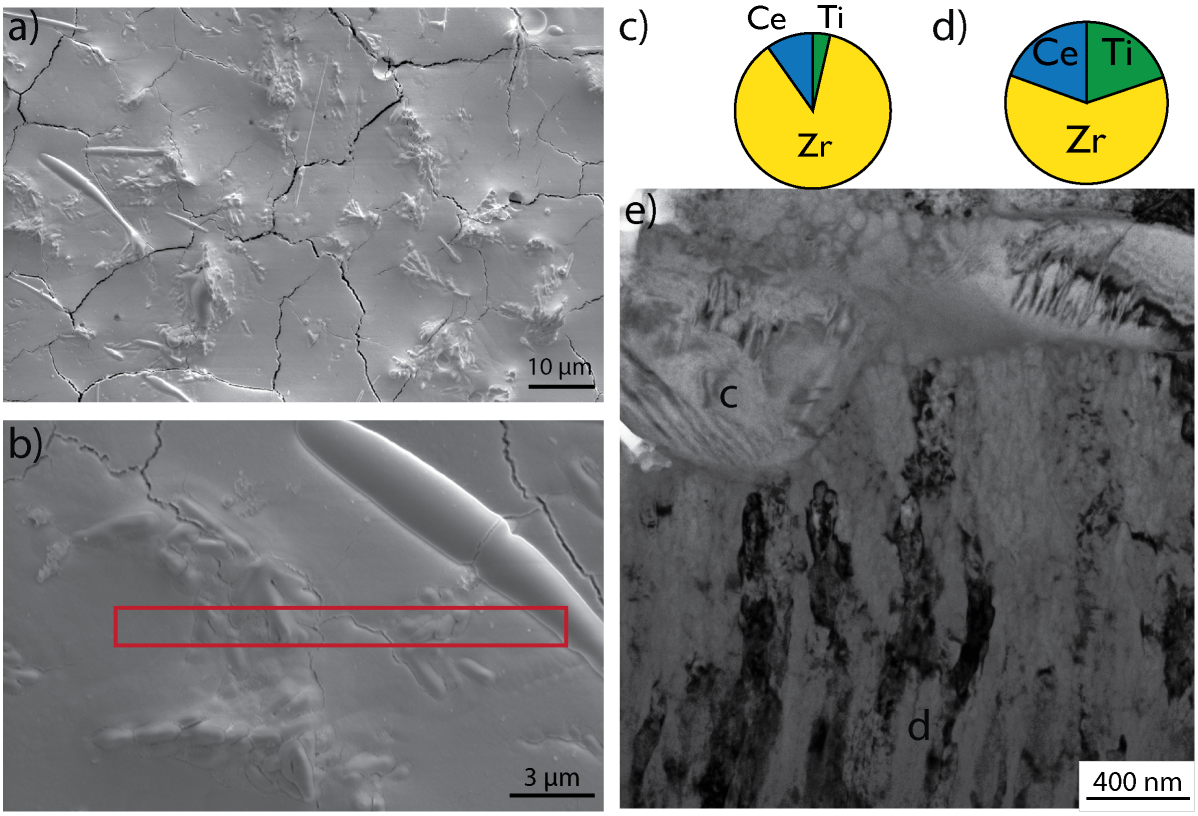

Figure 4.7 (a) BSE image of the surface of a single splat deposited with a plasma gun power of 35kW. (b) Location of TEM lamella is indicated with the red box in the BSE image. Based on unstandardized TEM-EDS the dendrites (c) are depleted in CeO_2 and TiO_2 (9.8mole% and 3.6mole%, respectively) and the bulk composition (d) is 19.4 mole% CeO_2 and 19.9mole%TiO_2. Locations of EDS-spectra are indicated in (e). Dendrites and directional solidification are observed in BF-TEM, (e).

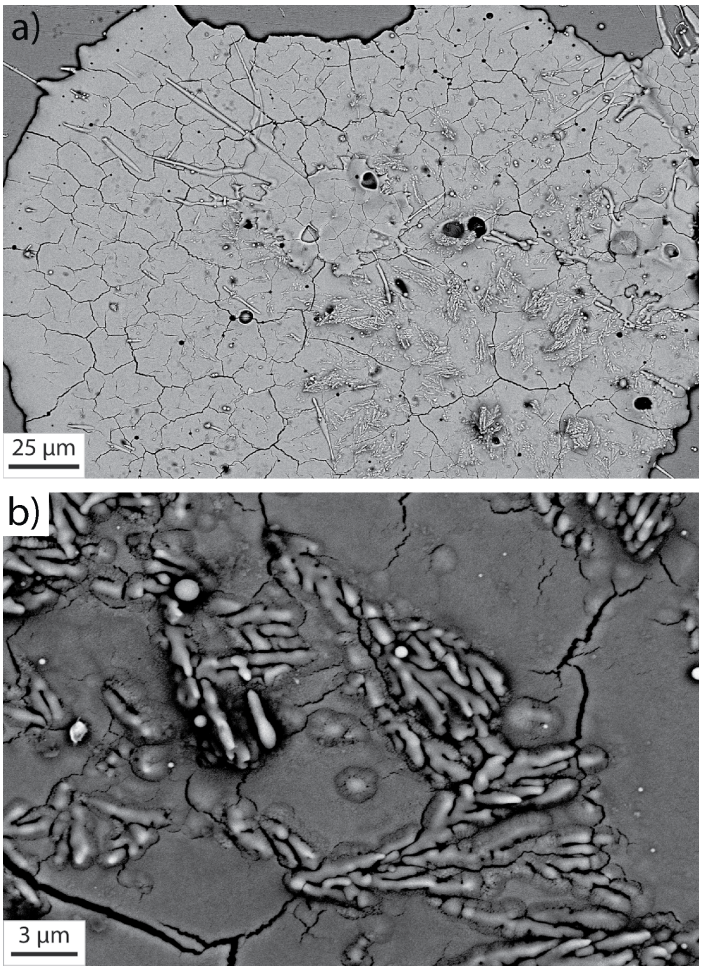

Figure 4.8 Low magnification (a) and higher magnification (b) BSE images of the dendrites observed in the single splats deposited with a plasma gun power of 46kW.

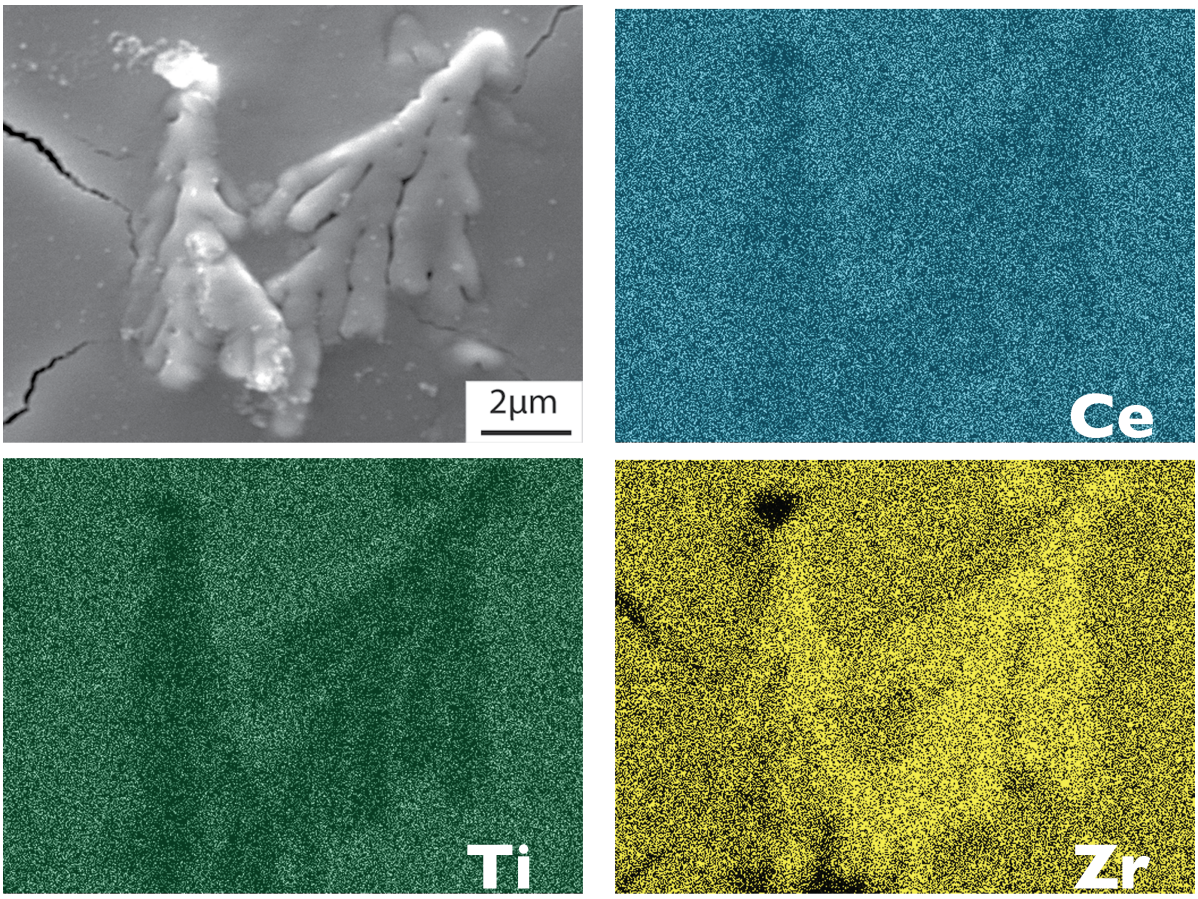

Figure 4.9 SEM-EDS map showing the dendrites in a single splat deposited with a plasma gun power of 46kW are rich in ZrO_2 and depleted in CeO_2 and TiO_2.

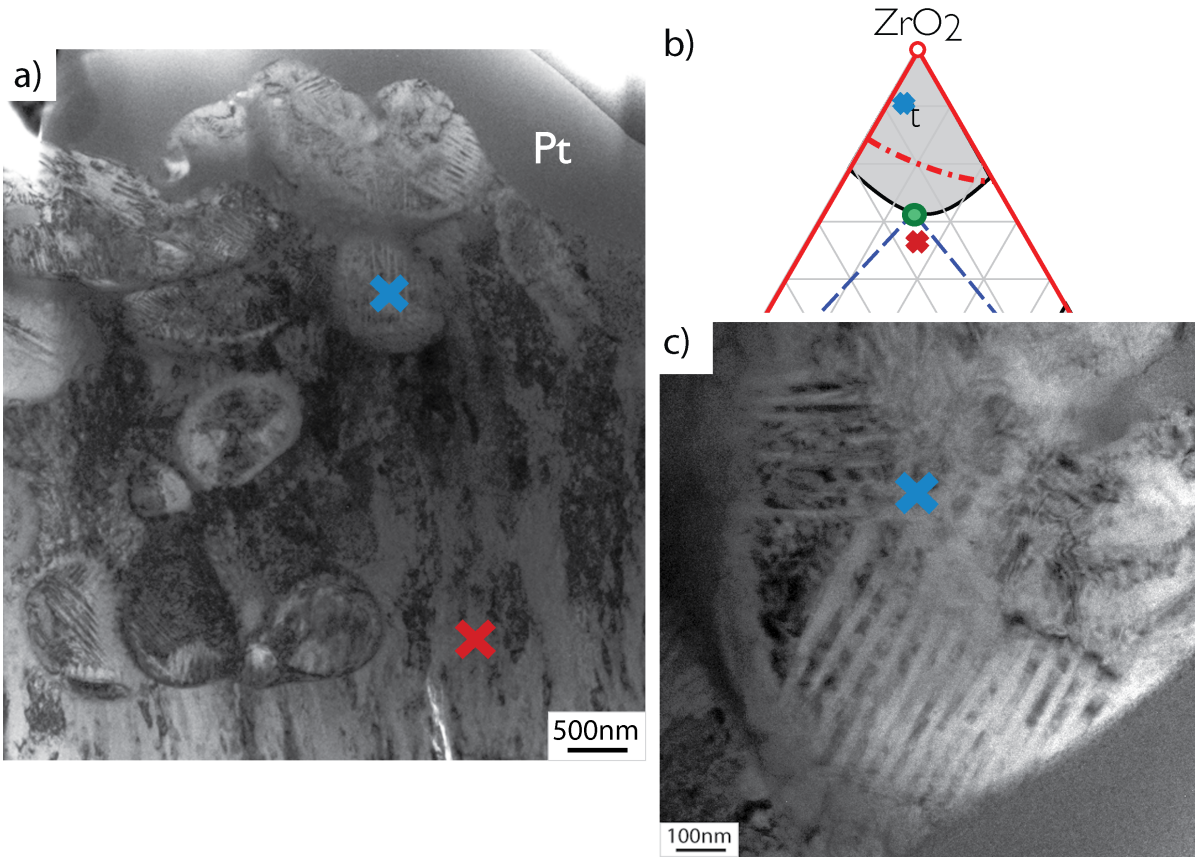

Figure 4.10 (a) and (c) BF-TEM images of the dendrites in single splats deposited with a plasma gun power of 46kW. (b) TEM-EDS results from the regions marked in (a) showing the dendrites are rich in ZrO_2 and depleted in CeO_2 and TiO_2 relative to the bulk.

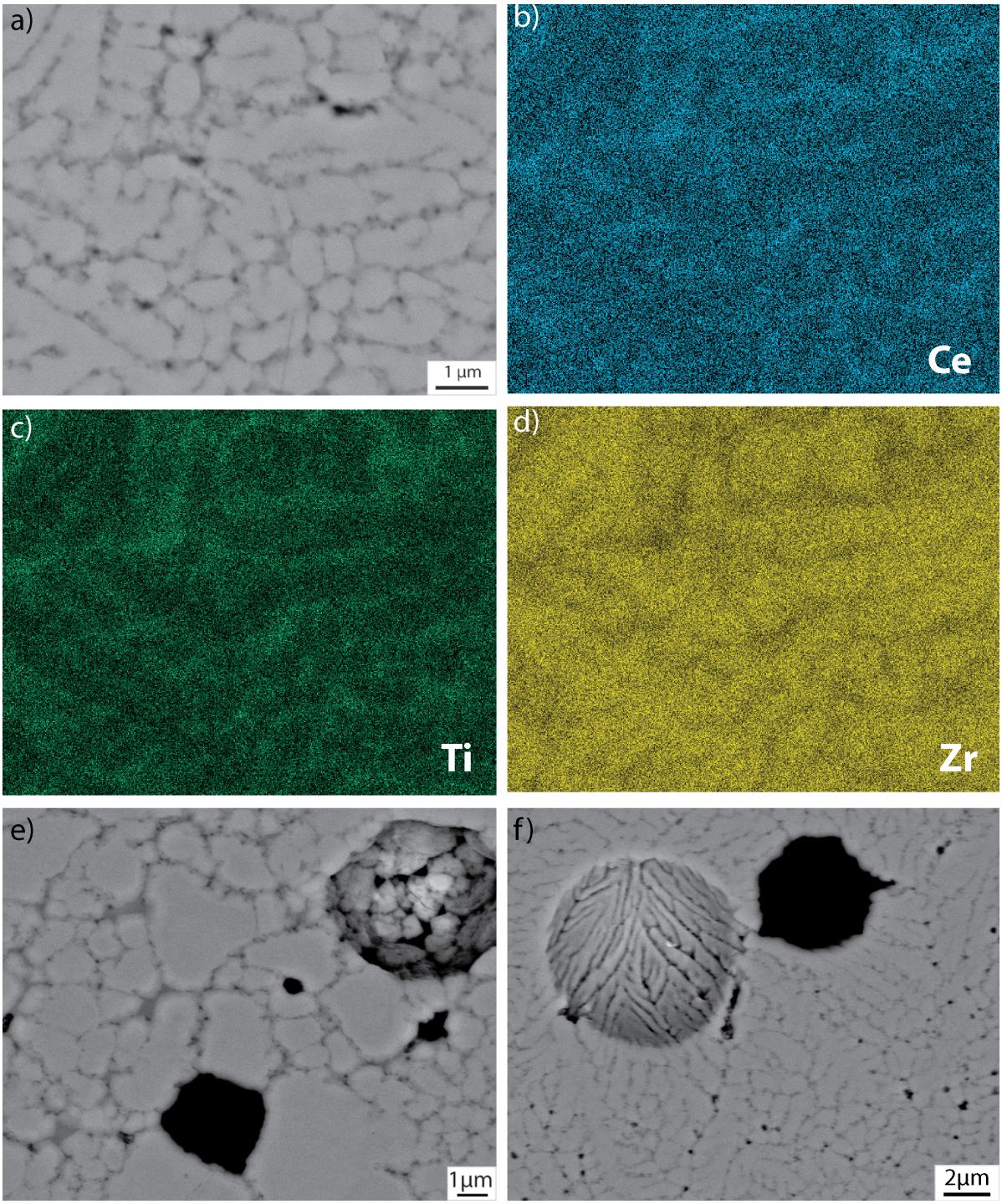

Figure 4.11 (a, e, f) Dendrites and segregation are observed in BSE images of the powder used to deposit the single splats and full coatings. (b, c, d) SEM-EDS composition maps show regions that are rich in TiO_2 or CeO_2 and depleted in ZrO_2.

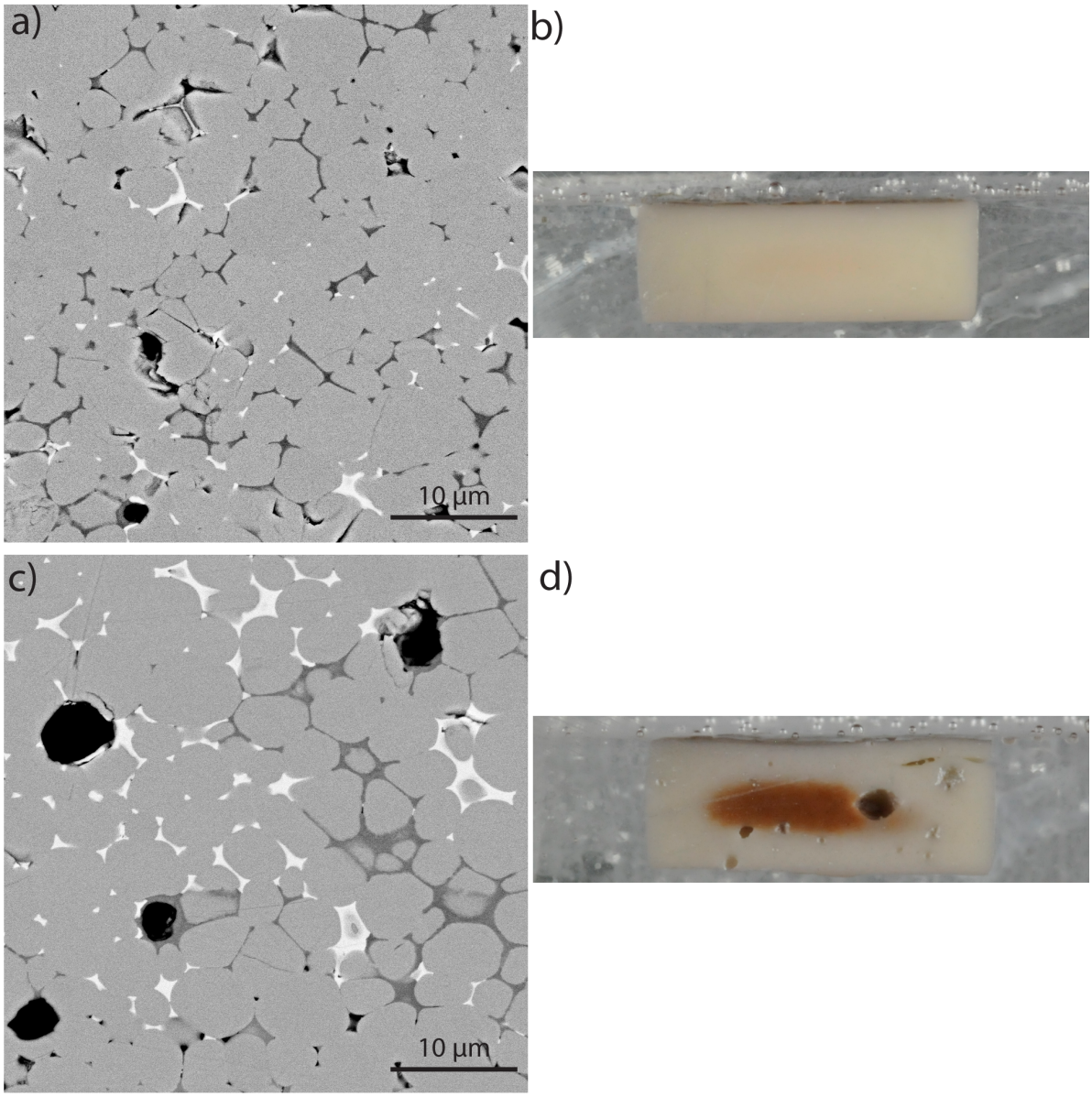

Figure 4.12 BSE images and corresponding photographs of the polished cross-section of (a and b) 12Ce12Ti and (c and d) 14Ce14Ti pellets made from precursor-derived powder after 6.5h at 1427°C (2600°F). Shot on an iPhone 5s.

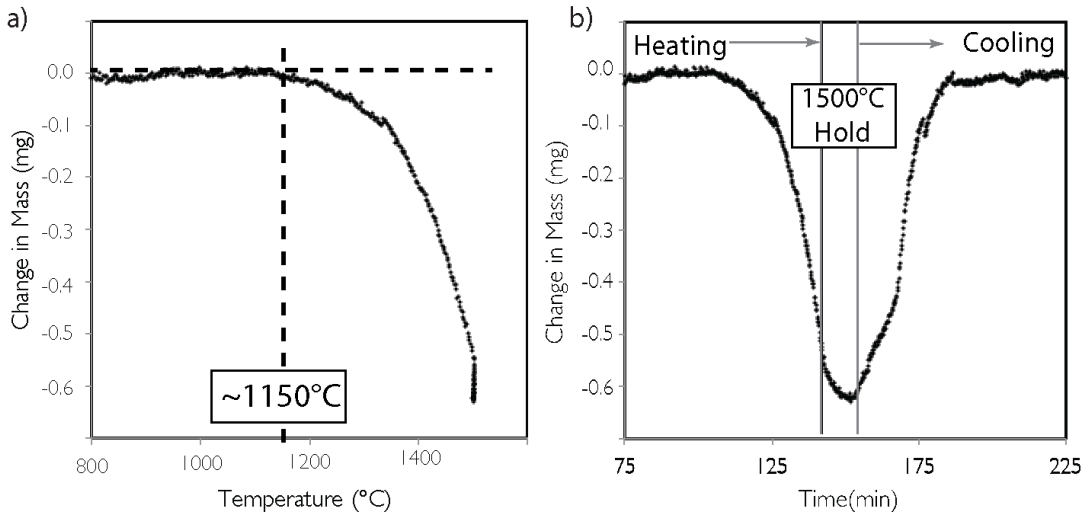

Figure 4.13 (a) TGA analysis shows that 14Ce14Ti loses mass above ~1150°C however that mass, which is presumably oxygen, is regained quickly during cooling (b).

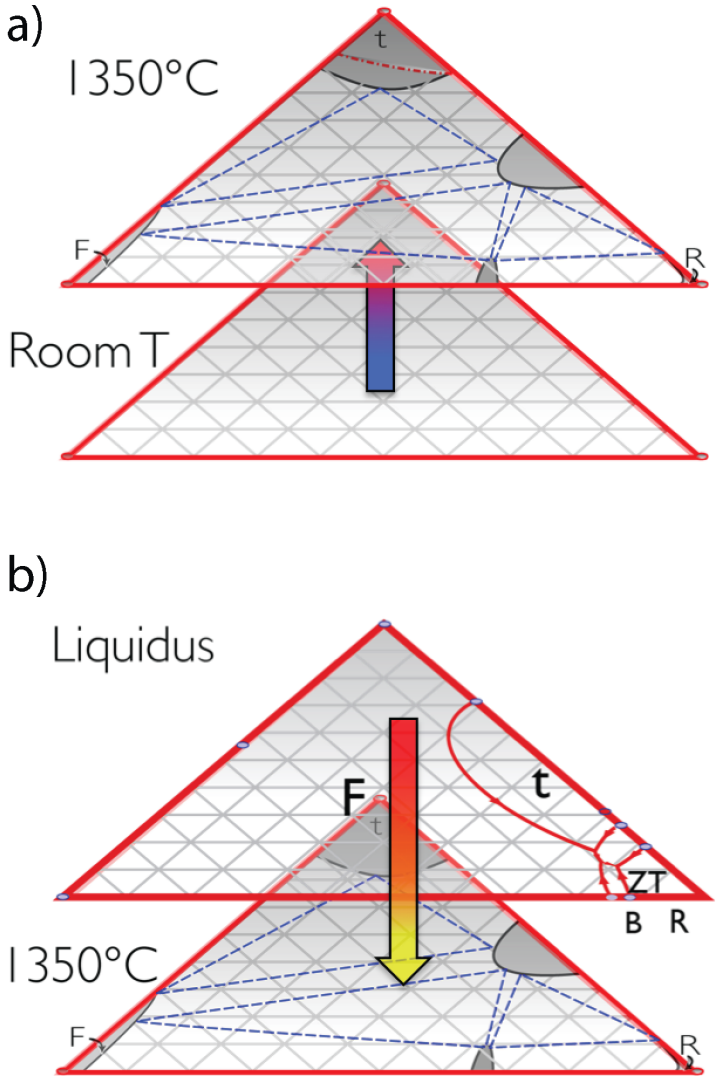

Figure 4.14 The phases and microstructure evolves differently in (a) pre-cursor derived ceramics and (b) in air plasma sprayed ceramics.

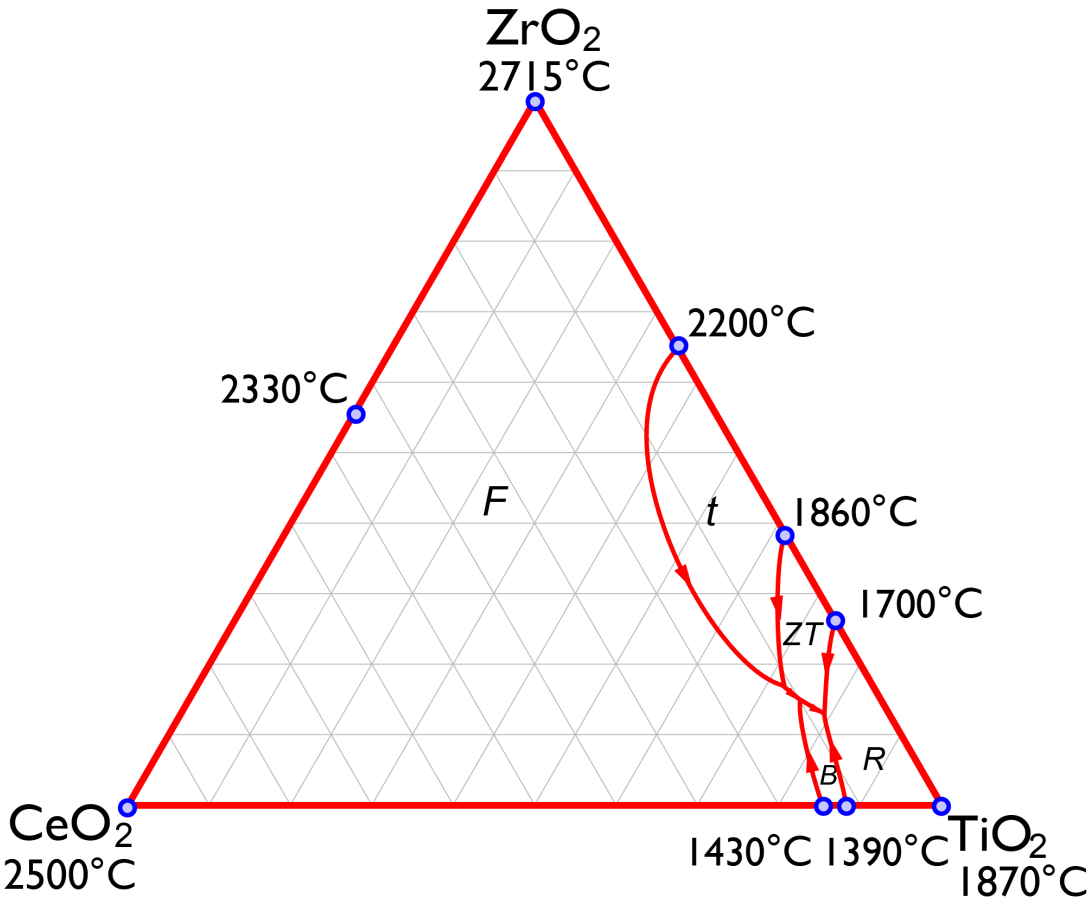

Figure 4.15 Estimation of the liquidus projection for the CeO_2-TiO_2-ZrO_2 ternary system based on melting temperatures of the end components [02Li, 70Rou] and invariant points in the available binaries [04Fab, 83Tan, 10Wan].

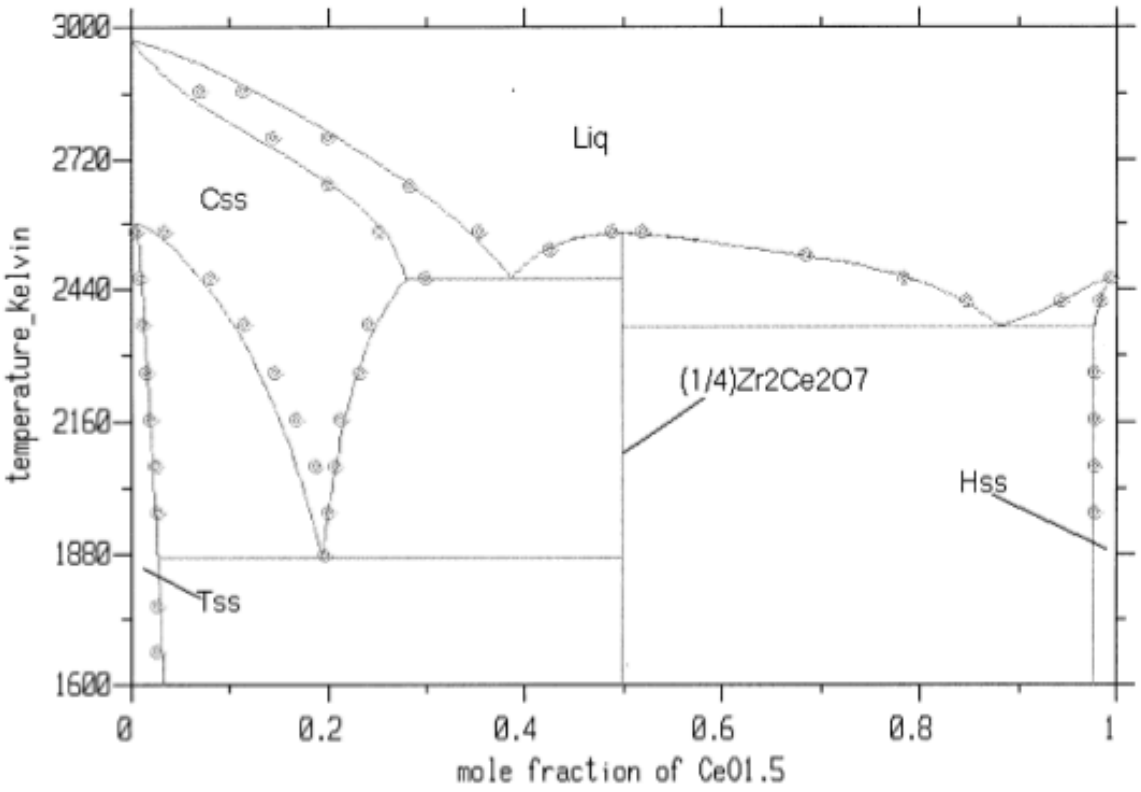

Figure 4.16 Thermodynamically calculated $CeO_{1.5}$-ZrO_2 binary phase diagram published in [03Hua].

CHAPTER 5: THE YTTRIA-TANTALA BINARY

The increased reducibility of Ce^{4+} at high temperatures limits the use of compositions in the CeO_2-TiO_2-ZrO_2 (CeTiSZ) system at temperatures above 1300°C. Given the possibility of temperature excursions in excess of 1300°C, CeTiSZ may not be a viable replacement for the industry-standard 8 ± 0.5mole% $YO_{1.5}$-stabilized zirconia (8YSZ). As described in Chapter 2, zirconia stabilized with charge compensating dopants such as Y^{3+} and Ta^{5+} also offers the possibility of a non-transformable, tetragonal phase with high tetragonality and low thermal conductivity [91Kim, 06Pit, 07Pit, 14Lim]. Additionally other phases in the ZrO_2-$YO_{1.5}TaO_{2.5}$ (ZYTO) system effectively mitigate damage caused by molten silicates ($YO_{1.5}$-rich fluorite) [14Kra2] and exhibit even lower thermal conductivity than the ZrO_2-rich tetragonal phase at 1000°C ($YTaO_4$) [14Lim]. To identify additional compositions with promising characteristics, it is essential to understand the phase equilibria at engine-relevant temperatures. Unfortunately, there is a paucity of phase equilibria information, especially in the ZrO_2-lean portion of the ZYTO system. While the ZrO_2-$YO_{1.5}$ binary has been studied extensively due to its technological importance in TBCs, fuel cells and sensors, very few groups have systematically studied the $YO_{1.5}$-$TaO_{2.5}$ binary. The investigations that have been completed are either limited in composition range ($TaO_{2.5}$<50 mole%) [91Yok] or in temperature range (T>1600°C) [73Bon].

To elucidate the phase relationships in the $YO_{1.5}$-$TaO_{2.5}$ binary and provide a foundation for investigations of the ZYTO ternary, compositions ranging from pure $YO_{1.5}$ to pure $TaO_{2.5}$ were synthesized via co-precipitation and heat treated at 1250-1600°C. X-Ray diffraction (XRD), Raman spectroscopy, selected area electron diffraction (SAED) and atomic resolution transmission electron microscopy (TEM) were used to determine equilibrium crystal structures. Equilibrium compositions were measured using electron probe microanalysis (EPMA) and energy dispersive x-ray spectroscopy via TEM (TEM-EDS). In

the $YO_{1.5}$-rich portion of the binary, fluorite (*F*, $Fm\bar{3}m$) is stable at ~80mole% $YO_{1.5}$ at T≥1500°C. While additional studies are ongoing, two structurally similar orthorhombic phases, Y_3TaO_7 (*W, Ccmm*) and $Y_7Ta_3O_{18}$ (*o*, *Cmmm*) are likely present at 75 mole% $YO_{1.5}$ and 70-72 mole% $YO_{1.5}$, respectively. There are two stable phases on the $TaO_{2.5}$-rich side of the binary, the orthorhombic perovskite YTa_3O_9 (*P*, *Cmmm*) from 1200-1800°C and hexagonal YTa_7O_{19} (*h*, $P\bar{6}c2$) from ambient to ~1550°C. For the first time, a complete phase diagram that includes temperatures below 1600°C is presented.

5.1 Background on $YO_{1.5}$-$TaO_{2.5}$ phase equilibria

Several compounds in the $YO_{1.5}$-$TaO_{2.5}$ binary are of interest as lasers (YTa_7O_{19}) [09Cav], phosphors ($YTaO_4$) [83Bri], ionic conductors (Y_3TaO_7) [91Yok] or thermal barrier coatings ($YTaO_4$) [14Shi]. Despite the technological applications, very few studies have systematically investigated the phase equilibria in this binary. There is no thermodynamic assessment of this binary system except for a simplified version in the context of the ternary ZrO_2-$YO_{1.5}$-$TaO_{2.5}$, which left out several phases [11Bha]. There are, however, two published experimental diagrams, one across the entire composition space but only for temperatures above 1600°C [73Bon] and the other covering only the $YO_{1.5}$ rich half but extending to lower temperatures [91Yok], as seen in Figure 5.1(a) and (b), respectively. Table 5.1 indicates the abbreviations for each phase as well as the structure (PDF) card used to identify most phases via XRD.

The terminal phases have some mutual solubility. Based on a study at 1410°C, more $TaO_{2.5}$ is soluble in $YO_{1.5}$ (~5mol%) than the amount of $YO_{1.5}$ soluble in $TaO_{2.5}$ (<1mol%) [79Vas]. $TaO_{2.5}$ is of technological interest for its optical [05Una], catalytic [03Che], dielectric [02Rob] and chemical properties [04Mol]. Despite being the subject of numerous studies over the last ~50years, the crystal structures of the high and low temperature phases of $TaO_{2.5}$ are still under debate because both structures transform to metastable phases on

cooling [68War, 70Rot2, 70Rot, 07Liu, 03Gre, 03Ask, 07Bre]. It is generally accepted that the high temperature (α) form is tetragonal ($I4_1/amd$) [07Liu], stable above ~1360°C up to the melting point of 1872°C [56Rei, 72Jeh], whereas the low temperature form (β) is orthorhombic (*Pna2*) [69Wol]. The first order transformation from β to α is sluggish [56Rei], unlike the unquenchable, reversible and likely displacive transformations to orthorhombic (~1000°C) and then triclinic (340°C) that α undergoes on cooling [07Liu, 68War, 07Bre]. These transformations complicate the interpretation of XRD, Raman or electron microscopy results acquired at room temperature and thus conclusions based on room temperature analyses should be considered with caution. *In situ* synchrotron XRD and Raman scattering experiments at high temperatures have been essential in disentangling thermal history artifacts and elucidating the actual equilibrium α-$TaO_{2.5}$ structure [07Bre]. Like α, the structure of β-$TaO_{2.5}$ has also been debated for over 50 years, in part because of transitions that occur on cooling. An excellent review of the β-$TaO_{2.5}$ literature is provided in [03Gre]. After reviewing the β literature, one clear conclusion is that the crystal structure, and more specifically the multiplicity, *m*, of superstructures along the b-axis, is highly dependent on synthesis technique, thermal history and cation impurities. The strongest XRD peaks from β can be indexed as orthorhombic but numerous weak peaks are present and depend on *m*. Similar to α-$TaO_{2.5}$, β undergoes at least one phase transition on cooling, complicating room temperature analyses [03Ask]. Unfortunately *in situ* XRD or Raman experiments have not been conducted on β-$TaO_{2.5}$, but would be critical to understand the actual low temperature structure.

At the other end of the binary phase diagram, the crystal structure and phase transitions of Y_2O_3 are well understood. Y_2O_3 is cubic (bixbyite, *C*, $Ia\bar{3}$), a defect form of fluorite in which the oxygen vacancies are ordered, from ambient to 2325°C. At that temperature Y_2O_3 transforms to a hexagonal structure (*H*, $P\bar{3}m1$) before melting at 2430°C [90Car].

It is generally acknowledged that there are several intermediate binary phases, all of which exhibit phase transformations. The equimolar composition $YTaO_4$ (YT) has a monoclinic fergusonite structure designated as *M'* (P2/a) at room temperature, which undergoes a reconstructive transformation to a tetragonal, scheelite-type structure designated as *T* ($I4_1/a$) at 1425°C [67Wol2, 83Bri, 14Fen, 59Kom, 14Shi, 74Gra, 95Mat]. Upon cooling, *T*-YT undergoes a displacive transformation to a metastable monoclinic fergusonite known as *M* (*I*2/a) which resists transformation to *M'*, which is considered to be the true equilibrium form at lower temperatures. The different crystal structures of $YTaO_4$ are important in the phosphor community because the luminescent efficiency of *M'* is twice that of *M* [83Bri]. A metastable disordered tetragonal form of $YTaO_4$ (*$P4_2/mnc$*) analogous to the t-ZrO_2 solid solution has been reported to form by sol-gel synthesis and pyrolysis at 700°C, which transforms to *M'* at 850°C [95Mat].

There are three different structures with approximate composition Y_3TaO_7 reported in the literature. Two of these are closely related orthorhombic phases stable at 1500°C and below, Y_3TaO_7 (Y_3T) at 25 mole%$TaO_{2.5}$ (*W, $C222_1$*) and $Y_7Ta_3O_{18}$ (Y_7T_3) from 28-30%$TaO_{2.5}$ (*o, Cmmm*) [79All, 91Yok, 79Ros, 79Ros2]. The former reportedly decomposes into the latter plus a fluorite phase at ~1600°C [79All], and the latter into *T*-YT and fluorite at ~1870°C [91Yok]. In contrast, other works report Y_3TaO_7 as a pyrochlore or defect fluorite structure above 1600°C [73Bon, 64Roo, 79Vas]. A recent study of many rare earth tantalates, RE_3TaO_7, (RE=lanthanide or Y) determined the space group *$C222_1$* for Y_3TaO_7 results in asymmetric Ta-O octahedra and unrealistic Ta-O bond distances, suggesting the correct space group is *Ccmm* [09Fu].

Two alternate structures exist on the $TaO_{2.5}$-rich side. YTa_3O_9 (YT_3) (also written as $Y_{0.33}TaO_3$) is reported to have an orthorhombic defect perovskite structure (*P, Cmmm*) [68Tru] above 1600°C and melts without decomposition at ~1800°C [73Bon]. The structure has been the subject of debate, with different reports identifying it as tetragonal (*P4/mmm*)

[67Iye] or monoclinic [73Bon, 65Roo, 79Vas]. Below a temperature between 1410°C and 1650°C the stable phase is hexagonal YTa_7O_{19} (YT_7, *h*, $P\bar{6}c2$) [09Cav, 07Leo, 79Vas].

While the crystal structures and other properties of several single phases in the $YO_{1.5}$-$TaO_{2.5}$ binary have been studied, there have been very few investigations of the phase relationships in the binary. In a systematic way, this study of the entire $YO_{1.5}$-$TaO_{2.5}$ binary elucidates the temperature and compositional ranges over which phases are stable.

5.2 Experimental Details

5.2.1 Synthesis

Equilibrium phase relations were determined by annealing the pure terminal oxides as well as samples of the following compositions: 85Y15Ta, 75Y25Ta, 72Y28Ta, 60Y40Ta, 40Y60Ta, 20Y80Ta, and 8Y92Ta. Powders were synthesized via reverse co-precipitation of precursor solutions as described in Chapter 3. The resulting powders were pyrolyzed at ≥650°C and ground to remove agglomerates before uniaxial compression into pellets 10mm in diameter. To ensure complete conversion of Ta-rich hydroxides into oxides, 40Y60Ta, 20Y80Ta, and 8Y92Ta were calcined at 900°C. Pellets were placed on platinum foil inside a covered alumina crucible and sintered under temperature and time conditions presented in Tables 5.2-5.6. Heating and cooling rates for all samples were 10°C/min, with the exception of 75Y25Ta and 72Y28Ta, which were quenched in air after the prescribed dwell. To better understand the ordering kinetics of $YO_{1.5}$-rich phases, powders of 85Y15Ta, 75Y25Ta, and 72Y28Ta were heat treated at 900°C (16h) and 1000°C (18h).

5.2.2 Characterization

XRD, BSE imaging on an SEM, and Raman were used to characterize the samples after each heat treatment. The grain size of the $TaO_{2.5}$-rich compositions was larger than the

electron beam interaction volume (>1μm), allowing electron probe micro analysis wavelength dispersive spectroscopy (EPMA-WDS) to be used to determine the equilibrium phase compositions. Pure $YO_{1.5}$ and $TaO_{2.5}$ were used as standards EPMA. $YTaO_4$, which was assumed to be a line compound, was used as an internal standard. Accounting for differences in porosity in the samples, the scatter in EPMA data was ~0.5 mole%, base on single cation. The $YO_{1.5}$-rich compositions had very small grains (<300nm) necessitating the use of TEM with EDS to determine equilibrium compositions with an accuracy of <1mole%. Given the similarity between the crystal structures of 75Y25Ta and 72Y28Ta and the need to understand the local structure, SAED and atomic resolution TEM were also conducted.

In-situ high temperature XRD was performed to study the equilibrium structure of 72Y28Ta at temperatures up to 1500°C. By directly characterizing the crystal structure at high temperature, artifacts caused by furnace cooling can be avoided. Powder that had been pre-equilibrated for 100h at 1500°C was used in the experiment. At a rate of 1°C/second, the temperature was raised to 1200, 1250, 1300, 1400 and 1500°C. The sample was held at each temperature for 25 minutes before a 25-minute XRD scan was collected. After the 1500°C measurement, the sample was cooled to 1250°C and a final XRD measurement was taken.

5.3 Results

5.3.1 Terminal Oxides

XRD and Raman spectroscopy indicate $YO_{1.5}$ exhibits the cubic bixbyite (*C*-type rare earth oxide) structure throughout the temperature range studied (1250-1600°C) Figure 5.2(a, b), consistent with previous literature [89Mar, 65Pat] The very strong peak at 380cm^{-1} in the Raman spectra is characteristic of *C* [09Wan, 14Abr] and is used to indicate the presence of *C* in other $YO_{1.5}$-rich samples in the binary. It was not possible to determine the maximum

$TaO_{2.5}$ solubility in $YO_{1.5}$ due to the small grain size and extensive porosity in 85Y15Ta, as will be shown in Section 5.3.4.

In contrast, the XRD and Raman spectroscopy results of pure $TaO_{2.5}$, Figure 5.3(a,b), indicate this oxide undergoes a phase transition but there is a discrepancy in the phase transformation temperature. As noted in section 5.1 the presence of displacive phase transitions on cooling from α- or β-$TaO_{2.5}$ complicates the analysis of measurements acquired at room temperature. Therefore the presence of a triclinic phase [68War] (PDF 01-075-9704, asterisks in Figure 5.3(a) implies α was present at the sintering temperature whereas the presence of an orthorhombic phase [70Rot2] (*Pmm2E*, PDF 00-025-0922, triangles in Figure 5.3(a) suggests β was stable at the temperature of interest [03Ask, 70Rot2, 69Wol]. XRD peaks associated with triclinic $TaO_{2.5}$ appear in samples heat treated at 1400°C and 1500°C but the Raman spectra do not change until after heat treatments at 1600°C. Raman spectra from 1350-1500°C match the spectra for orthorhombic (β) $TaO_{2.5}$ reported in [12Joe, 14Li]. Very little (<1mole%) $YO_{1.5}$ is soluble in $TaO_{2.5}$ at any of the temperatures studied, as indicated by the EPMA results from sample 8Y92Ta, Tables 5.2-5.6 and Figure 5.4.

5.3.2 Phases in the $TaO_{2.5}$-Rich Region

The XRD and EPMA results for the compositions 40Y60Ta, 20Y80Ta, and 8Y92Ta indicate that $YTaO_4$ (*M'*- or *T*-YT), YTa_3O_9 (*P)*, and YTa_7O_{19} (*h*) are stable in the $TaO_{2.5}$-rich region of the binary, as shown in Tables 5.2-5.6 and Figure 5.4. Each filled-in symbol indicates nominal compositions while the compositions of the equilibrium phases are depicted by open symbols.

EPMA measurements after heat treatments at 1350°C-1600°C indicate that *P* is a line compound at 75mole% $TaO_{2.5}$. From 83-87.5mol% $TaO_{2.5}$, *h* is stable in the temperature

range of at least 1250°C to 1500°C. At 1600°C, *h* is no longer observed in 8Y92Ta but is instead replaced by *P* + α, suggesting the maximum temperature at which *h* is stable is between 1500°C and 1600°C. The EPMA results are corroborated by changes in the XRD and Raman spectra of the composition 8Y92Ta, Figure 5.5. That composition contains *h* and $TaO_{2.5}$ from 1250-1500°C, however the XRD pattern changes significantly between 1400°C and 1500°C. EPMA confirms the transformation does not significantly impact the solubility of *h*, as chemical compositions of both phases in 8Y92Ta remain constant over the temperature range 1400-1500°C. The Raman spectra clearly indicate that *h,* which exhibits many more Raman active modes than α, β, or *P*, is no longer stable at 1600°C, Figure 5.5(b).

Grain coarsening and other microstructural changes are observed with increasing heat treatment temperatures in BSE images, Figure 5.6. In all images, the black regions are pores. With the exception of grain coarsening, no significant changes are observed in the microstructure of 40Y60Ta from 1350-1600°C as $YTaO_4$ (dark contrast) and *P* (light contrast) are stable throughout the temperature range. In agreement with EPMA and XRD data, the microstructure of 20Y80Ta and 8Y92Ta changes between 1500 and 1600°C. In 20Y80Ta, BSE images and EPMA indicate that small (~1μm) grains of *P* (dark contrast) and *h* (light contrast) are stable from 1350-1500°C. At 1600°C, large (~5μm) globular grains of $TaO_{2.5}$ (light contrast) are observed within a matrix of *P* (dark contrast), suggesting that *h* is no longer stable. In 8Y92Ta, the high aspect ratio grains with dark gray contrast, which are *h* by EPMA, are present with $TaO_{2.5}$ (light contrast) from 1350-1500°C but are no longer present at 1600°C. Instead, *P* (dark contrast) is in equilibrium with $TaO_{2.5}$ (light contrast) at 1600°C, in agreement with the EPMA results.

5.3.3 $YTaO_4$

While a single phase $YTaO_4$ (YT) composition was not synthesized in this study, the samples 60Y40Ta and 40Y60Ta each contain YT. XRD patterns from 40Y60Ta after heat treatments at 1250°C, 1350°C, 1400°C, and 1600°C clearly indicate that *M'*-YT is present at 1400°C and below, Figure 5.7(a). After heat treatments above 1400°C, *M*-$YTaO_4$ is observed, which is consistent with the displacive transformation of the high temperature tetragonal (*T*) equilibrium form of YT at 1425°C [94Bam, 83Bri, 59Kom, 14Shi], to the metastable monoclinic form (*M*) upon cooling. The $T \rightarrow M$ transformation results in the formation of twins in *M*-YT grains, as shown in the bright field, (BF), TEM image in Figure 5.8. These results are corroborated by Raman spectra of 60Y40Ta after sintering at 1250°C, 1500°C and 1600°C, Figure 5.7(b). All peaks in the Raman spectra after 1500°C and 1600°C correspond to *M*-YT [73Bla, 14Shi, 83Bri] while all peaks after the 1250°C heat treatment are accounted for by *M'*-YT [83Bri]. Furthermore, *M'* is also observed in 40Y60Ta via Raman spectroscopy after sintering at 1250°C and 1350°C. While the broad peak at 600cm^{-1} is likely due to *P*, all other peaks are accounted for by *M'*.

5.3.4 Phases in the $YO_{1.5}$-Rich Region

Compositions in the $YO_{1.5}$-rich portion of the binary exhibited small grains and extensive porosity, even after thermal exposure at 1500°C and 1600°C. In general, porosity increased and grain size decreased as $YO_{1.5}$ concentration increased, **Error! Reference source not found.**(a-d). These issues prevented the manufacture of lamellae with FIB for TEM analysis. As a result it was not possible to determine the composition of equilibrium phases in many of the $YO_{1.5}$-rich samples. With great care, lamellae from 72Y28Ta, and 60Y40Ta heat-treated for 100h at 1500°C were extracted using FIB and analyzed via TEM-EDS to determine the equilibrium compositions shown in Figure 5.4. While all grains analyzed in 72Y28Ta had the same composition (72.1mole% $YO_{1.5}$, 27.8mole% $TaO_{2.5}$), two phases

were present in 60Y40Ta (69.9mole% $YO_{1.5}$, 30mole% $TaO_{2.5}$ and 49.8mole% $YO_{1.5}$, 50.2mole% $TaO_{2.5}$), Table 5.3.

XRD patterns after heat-treatments at 1250, 1500 and 1600°C provide preliminary evidence of phase evolution, Figure 5.10, in $YO_{1.5}$-rich compositions. For convenience, the simulated XRD patterns of the accepted structures of *Ccmm* (*W*), *Cmmm* (*o*), and *F* calculated using the Vesta software package [08Mom] are also plotted. Note the $K\alpha_2$ peaks have not been removed; thus, peaks that should only be single peaks appear as doublets. After the 1250°C treatment, compositions 72Y28Ta, 75Y25Ta and 85Y15Ta all appear to contain fluorite instead of the expected orthorhombic phases, as evidenced by the lack of splitting in peaks near $2\theta \approx 80°$ and 82°. Small peaks associated with *C*-$YO_{1.5}$ are observed at ~79° and 81° in 85Y15Ta at all temperatures. After the 1500°C heat-treatment, peak splitting suggests that 72Y28Ta and 75Y25Ta are *Cmmm* and *Ccmm*, respectively, while 85Y15Ta contains *F* and *C*. After 1600°C, XRD peaks indicate that 72Y28Ta is still *Cmmm,* while the peaks in 75Y25Ta and 85Y15Ta suggest *F* is stable in those compositions.

To examine whether additional ordering was not occurring during cooling, XRD patterns from 72Y28Ta samples that had been furnace cooled (10°C/min) and cooled quickly over ~2 minutes in air were compared, Figure 5.11. Significant differences are not observed in the XRD peaks of furnace cooled or "quenched" 72Y28Ta. Given the possibility of oxygen ordering occurring, even during a "quench", *in situ* high temperature XRD was also employed for 72Y28Ta from room temperature to 1500°C, Figure 5.12. Although the data is noisy, it is possible to infer the peak shape, which differentiates the *Ccmm* (*W*) and *Cmmm* (*o*) structures. At all temperatures, the peak shape is more similar to that of *Cmmm* than *Ccmm* or *F*, suggesting that *Cmmm* is stable at 1500°C. The XRD peaks at high temperatures are shifted approximately -1° relative to the reference patterns due to the sagging of the platinum stage.

Complementary information on phase equilibria can also be derived from Raman spectroscopy. After 100h at 1500°C 85Y15Ta contains *C*, as evidenced by the strong peak at 380cm^{-1}, Figure 5.13. The peak near 800cm^{-1} in the spectra of 85Y15Ta, which is absent in pure $YO_{1.5}$, indicates that another phase is also present in 85Y15Ta at 1500°C. There are only slight differences in the Raman spectra of 72Y28Ta and 75Y25Ta, *o* (*Cmmm*) and *W* (*Ccmm*), respectively, suggesting the orthorhombic structures are very similar. The peaks of 72Y28Ta (*o*, *Cmmm*) are more broad then those of 75Y25Ta (*W*, *Ccmm*). There is also an additional peak in 72Y28Ta at 768cm^{-1}, which is not observed in 75Y25Ta.

The phase evolution of 75Y25Ta and 72Y28Ta was investigated further with Raman spectroscopy after heat treatments at 650, 900, 1000, 1250, 1500 and 1600°C, Figure 5.14. While broad peaks are observed in both compositions after sintering at 1000°C or below, more defined peaks are present after heat treatments at 1600°C. The position of all the peaks in 75Y25Ta and 72Y28Ta does not change from 1250-1600°C. However, the peaks in 75Y25Ta at 1250°C are more broad then those after the higher temperature heat treatments.

Raman and XRD characterize the average, bulk structure. To understand local ordering and microstructure, it was necessary to use electron microscopy. BF-TEM images of 72Y28Ta after 100h at 1500°C indicate that many grains have a striated microstructure, Figure 5.15(a) and (d). SAED patterns in (b) and (c) suggest that multiple domain orientations are present within each grain. The $[110]_{Ccmm}$ zone axis pattern in (b) was obtained from the grain labeled 'b' in (a). The SAED pattern in (c), which was taken from the grain indicated in (d), includes overlapping patterns from the $[001]_{Ccmm}$ and $[010]_{Ccmm}$ zone axes, suggesting that multiple domains are present within each grain. Further analysis of grain 'c', Figure 5.16, revealed that 4 different domains were present. Using the selected area aperture to obtain an electron diffraction pattern only from domain 1, the orientation was determined, which could be indexed as the $[111]_{Ccmm}$ zone axis or the equivalent $[112]_{Cmmm}$ zone axis. When the aperture positioned to isolate domain, 3, the location of all the diffraction spots could only

be explained by the presence of both the $[001]_{Ccmm}$ and $[010]_{Ccmm}$ zone axes, similar to the SAED pattern in Figure 5.15(c). When the aperture was over both domains 1 and 3, diffraction patterns from both domains are observed and a clear crystallographic relationship is evident. To better understand the boundaries between the domains, atomic resolution high angular annular dark field STEM was conducted by Dr. D. Park, a post-doctoral colleague. The atomic images of the boundaries between domain 1 and 3 as well as 1 and 2, suggest the domains are separated by coherent twin boundaries, Figure 5.17. Both images are taken along the $[111]_{Ccmm}$ zone axis, which is equivalent to the $[112]_{Cmmm}$ zone axis, and clearly show the mirror plane between the domains.

5.4 Discussion

Based on available information in the literature such as the liquidus in [91Yok] and results from this work, a revised $YO_{1.5}$-$TaO_{2.5}$ phase diagram is proposed in Figure 5.18. The salient findings regarding the terminal oxides are discussed first followed by conclusions from the $TaO_{2.5}$-rich region, $YTaO_4$, and $YO_{1.5}$-rich region. Possible explanations for the phase equilibria based on the crystal structures are proposed, though first principles calculations are needed to confirm the root energetic cause for the solubility limits of each phase.

5.4.1 Terminal Oxides

$YO_{1.5}$ is stable in the bixbyite structure in the entire temperature region studied, 1250-1600°C. The main Raman peak position at ~380cm^{-1} in rare earth (RE) oxides with the bixbyite structure is dependent on both RE ionic radius and the unit cell parameter [14Abr]. Heavier rare earth ions decrease the frequency of the characteristic peak while cations with smaller ionic radii decrease the unit cell parameter and thus increase the frequency. These mechanisms likely compensate for each other as Ta^{5+} is substituted on the $YO_{1.5}$ lattice. The average atomic mass increases but the unit cell parameter decreases and thus pure $YO_{1.5}$ and

$YO_{1.5}$ with some $TaO_{2.5}$ solubility have the same characteristic peak positions, as seen in Figure 5.2.

The structural transition between 1250°C and 1400°C implied by the XRD results of $TaO_{2.5}$, Figure 5.3(a), is in agreement with the proposed β→α transition temperature, 1360°C [56Rei, 72Jeh]. Additionally the sluggish nature of the first order β→α transition is evidenced by the presence of β, even after 100h at 1500°C. These orthorhombic peaks are notably absent after heat-treatment at 1600°C, which coincides with the change in the Raman spectra, Figure 5.3(b). The intensity of the Raman peaks from β-$TaO_{2.5}$ is three times higher than the intensity of the α-$TaO_{2.5}$ peaks, thus its presence, even as a minority phase after heat treatments at 1400°C and 1500°C, may overshadow the Raman active modes in α-$TaO_{2.5}$. This illustrates the importance of using complementary characterization methods to elucidate phase equilibria.

The asterisks in Figure 5.3 indicate peaks associated with the triclinic phase that results from the transformation from α upon cooling [68War] (PDF 01-075-9704). Similarly, β-$TaO_{2.5}$ also undergoes phase transitions on cooling. The triangles indicate the orthorhombic (*Pmm2E*, PDF 00-025-0922) structure [70Rot2], which has a multiplicity, *m*, of 14 and forms when β transforms on cooling [03Ask, 70Rot2, 69Wol].

5.4.2 $TaO_{2.5}$-Rich Region

The observation that *P*-YTa_3O_9 ($Y_{0.33}TaO_3$) is a line compound agrees with [73Bon] but contradicts findings by [79Vas] that suggest it has a significant solubility range. The lack of binary solubility in *P* can be understood by closely examining the crystal structure, Figure 5.19. As originally reported by [68Tru], the A-site deficient orthorhombic perovskite structure of *P* is stabilized by cation vacancies. Two-thirds of the A (Y)-sites are unfilled relative to the aristotype ABO_3 perovskite structure [73Bon, 68Tru, 08Zho]. The Ta^{5+}-

cations sit in the B-sites in the oxygen octahedra. Given the preferred coordination environment of Y (8-fold) and Ta (6-fold) in the perovskite structure, binary solubility is not expected as it would introduce cation or oxygen vacancies. Additionally, recent electron diffraction and synchrotron X-ray diffraction on the structures of $Ln_{1/3}TaO_3$ where Ln=La, Ce,…,Yb indicated that the A-cations/vacancies were ordered along the [001] [08Zho]. Although $Y_{0.33}TaO_3$ was not specifically studied, it is expected that it would have ordered cation vacancies similar to $Dy_{0.33}TaO_3$ given the similarities in ionic radius of Y^{3+} (1.019 Angstroms) and Dy^{3+} (1.027 Angstroms). This cation/vacancy ordering precludes the possibility of any significant binary solubility because substitution of excess Y^{3+} or Ta^{5+} would require introduction of oxygen or cation vacancies, respectively, destroying the cation/vacancy ordering of the perovskite crystal structure.

The binary solubility in the YT_7 structure can also be explained by examining the YT_7 crystal structure. YT_7 has a hexagonal crystal structure ($P\bar{6}c2$) [09Cav, 07Leo, 76Ros] similar to other $LnTa_7O_{19}$ compounds [90Sch]. In this structure, double layers of pentagonal TaO_7 bipyramids are along the c-axis. These double layers are intercalated by single layers of edge-sharing trigonal antiprisms that are alternatively occupied by Y^{3+} and Ta^{5+}, Figure 5.20. The YT_7 phase field extends from the stoichiometric 87.5 mole% $TaO_{2.5}$ to 83 mole% $TaO_{2.5}$ ($YTa_{6.64}O_{18.1}$). The additional Y^{3+} would likely substitute for the Ta^{5+} in the trigonal antiprisms. One oxygen vacancy is required for every substituted Y^{3+} to maintain charge neutrality. The YT_7 structure is therefore stable up to a $YO_{1.5}$ content of 17 mole%, which corresponds to an oxygen vacancy concentration of ~4.7%.

The changes in the XRD pattern of 8Y92Ta between 1400 and 1500°C are the result of the β to α transformation in $TaO_{2.5}$. However this transformation is expected to occur at 1360°C [56Rei, 72Jeh], suggesting i) the small (<1mole%) amount of soluble $YO_{1.5}$ increases the transformation temperature of $TaO_{2.5}$ by ~50°C or ii) the transformation requires an overheating of ~50°C to occur within the 100h heat treatment. It is widely known that small

amounts of dopants can alter the β→α transformation temperature. In general, cations that are equal to or larger than Ta^{5+} stabilize α [70Rot] while smaller cations stabilize β [70Rot2]. The influence of Y^{3+} on the transformation temperature has not explicitly been studied, however chemically similar species such as Sc^{3+} (0.745 Angstroms) and Lu^{3+} (0.861 Angstroms) have been investigated. While Sc^{3+} stabilizes α, Lu^{3+} does not [70Rot]. Since the ionic radius of Y^{3+}, 0.90 Angstroms, is similar to that of Lu^{3+}, it is likely that Y^{3+} will also not decrease the β to α transition temperature. Therefore it may be possible for small amounts of $YO_{1.5}$ to increase the β to α transition temperature.

5.4.3 $YTaO_4$

The results from compositions containing $YTaO_4$ are consistent with the accepted temperature, 1425°C, of the *M'*→*T* transformation [83Bri, 74Gra, 95Mat, 67Wol2]. The nature of the *M'*→*T* transition dictates if it must be depicted on the binary phase diagram.

To understand the nature of the phase transition, it is necessary to appreciate the differences between the *M'* and *T* structures. The *M'* structure was first reported by [67Wol2] and subsequently slightly revised by [83Bri]. The space group was identified as *P2/a* [67Wol]. Perhaps the most obvious difference between *M'* and *T* is that Y and Ta atoms are in separate layers parallel to the [001] axis in *M'*, and the atoms are mixed in each layer in *T* parallel to the [001] axis. Y is 8-fold coordinated in both *M'* and *T*, but Ta is octahedrally coordinated in *M'* and only tetrahedrally coordinated in *T*, Figure 5.21, [83Bri, 74Gra, 67Wol]. In *M'*, the Ta atoms have a distorted octahedral coordination with 4 shorter Ta-O bonds [83Bri].

The transition from *M'* to *T* has not been studied systematically and thus much about the transition is still unknown. [67Wol2] stated that the transformation is likely a sluggish, first order transition that depends on diffusion (nucleation and growth). Given the large

crystallographical differences between *M'* and *T*, [74Gra] and [83Bri] also concluded the transformation was likely reconstructive. Dilatometry or DTA/DSC experiments are needed to experimentally verify the first order nature of the *M'*→*T* transition; however, these preliminary studies suggest it is a reconstructive transformation. Despite this, all current $YO_{1.5}$-$TaO_{2.5}$ phase diagrams omit the *M'*→*T* transformation [73Bon, 79Vas, 91Yok]. Since it is likely a first-order (reconstructive) transformation, it must be depicted on the phase diagram and is included in the revised diagram in Figure 5.18.

Contrary to the *M'*→T transition, the *T*→*M* transformation is a continuous, second-order transition [67Wol2, 14Fen, 14Shi] and thus does not need to be represented in the binary phase diagram. The presence of *M* via XRD and Raman spectroscopy after sintering at temperatures greater than 1425°C, indicates that the displacive transformation is not suppressible and occurs in pure $YTaO_4$ on cooling. Twins observed in *M* via BF-TEM are further evidence of the diplacive nature of the *T*→*M* transformation [05Prytz, 14Shi]. Additionally it is widely accepted that *M* is in fact metastable and the true equilibrium phase at lower temperatures is *M'* [83Bri]. The transition from *T* to *M'* would require a mechanism that produces rotational twins spontaneously in a crystal, which is difficult and thus the metastable *M* phase is formed [74Gra]. For these reasons, *M* is not depicted in the revised $YO_{1.5}$-$TaO_{2.5}$ phase diagram.

5.4.4 $YO_{1.5}$-Rich Region

Determination of the phase equilibria in the $YO_{1.5}$-rich region, especially 70-80mole% $YO_{1.5}$, is complicated by several factors including i) the fact that the *C*, *W*, and *o* crystal structures are all ordered derivatives of *F*, and ii) their slow densification and grain coarsening kinetics, even at temperatures as high as 1600°C.

To understand the crystal structures in the $YO_{1.5}$ rich region, it is best to start with the fluorite structure, as it provides the template on which *C, W* and *o* are based. The defect fluorite structure, Figure 5.22, is one in which the cations are arranged in an f.c.c. array while the oxygen ions occupy the tetrahedral sites, (a). For the overall composition of 75Y25Ta, the Y and Ta will be disordered and one out of eight oxygen sites (12.5%) will be vacant to maintain charge balance. In stoichiometric MO_2 fluorite the cations are 8-fold coordinated but in a defect fluorite such as 75Y25Ta the cations are on average ~7-fold coordinated. In reality, the larger Y^{3+} would likely be 8-fold coordinated while the oxygen vacancies prefer to be near the smaller Ta^{5+}, resulting in TaO_6 octahedra [07Yas]. Such coordination environments result in regions of local order but an average structure that is still fluorite, as has been observed in similar systems such as $YbO_{1.5}$-$TaO_{2.5}$ [13Kin] and $YO_{1.5}$-$NbO_{2.5}$ [97Mii, 15Che, 13Lop, 13Siq]. Since such ordering is related to the location of oxygen vacancies, which are much more mobile than cations, it is likely that ordered domains could form during cooling from high temperatures, as is evident by the Raman peaks in 75Y25Ta after heat-treatments at 1600°C despite appearing fluorite by XRD.

The cubic bixbyite structure (*C*) of $YO_{1.5}$ is essentially a defect fluorite where 25% of the anion sites are vacant to maintain charge balance. The cations reside on the f.c.c. sites while the anion vacancies are ordered and the anions shifted from the nominal positions in F (ignored here for clarity), resulting in a doubling of the lattice parameters relative to fluorite as shown depicted in Figure 5.22 [65Pat]. Therefore the *C*-$YO_{1.5}$ only requires oxygen vacancy ordering. The mobility of anions is higher than that of cations and thus bixbyite orders quickly compared to cation-ordered fluorite-related phases. Despite the structural similarities, bixbyite is readily differentiated from *F*, *W*, or *o* as evidenced by the sharp peaks in XRD and Raman spectroscopy.

The orthorhombic Weberite-type Y_3TaO_7 (*W*) phase is a cation and oxygen vacancy ordered form of fluorite. The relationship between the Weberite-type phase and the fluorite phase is

shown in Figure 5.22(b). In *W*, Figure 5.24, Y^{3+} (green) and Ta^{5+} (blue) cations decorate the fluorite lattice in a 3:1 ratio such that corner sharing TaO_6 octahedra form one-dimensional chains parallel to the [001] direction of the orthorhombic structure, as depicted in (a) and (b). The tilting of the TaO_6 octahedra results in a doubling of the a-axis relative to the fluorite unit cell. As shown in (b), there is a TaO_6 chain at (0,0) and the next chain is at ½(a+b), in the *Ccmm* structure. Without octahedral tilting, the structure would be orthorhombic with lattice parameters of $2a_f$, $\sqrt{2}a_f$, and $2\sqrt{2}a_f$ and with the space group *Cmmm* [09Fu], Figure 5.25(a). Tilting of the TaO_6 octahedra doubles the c-axis relative to *Cmmm*, Figure 5.22(b). In Y_3TaO_7 the tilting of the TaO_6 at (0,0,0) is in phase with that of the TaO_6 at (0.5, 0.5, 0) and the tilting is along the [010] axis so the structure is orthorhombic with the space group *Ccmm* [09Fu]. In the *W* structure, there are two different Y^{3+} sites, one Ta^{5+} site, and 3 distinct oxygen sites, as shown in Figure 5.24(g). The YI sites are 8-fold coordinated (green polyhedra) while the YII sites (purple) have 7-fold coordination, (c) and (d), respectively. Ordered oxygen vacancies (white) are present within the chains of TaO_6 octahedra such that zigzag pairs of vacancies occur parallel to the [001] direction, i.e. to the $[00\bar{1}]_F$ direction of fluorite, (h) [79Ros]. This is similar to the configuration in the pyrochlore structure, where the vacancy chains run in all the <110> fluorite directions. The Ta-O-Ta angle, depicted in Figure 5.24(h), varies based on the size of the rare earth cation, ranging from 153.1° (La) to 135.9° (Ho) [04Wak].

The orthorhombic *Cmmm* is not observed in any RE_3TaO_7 (RE= lanthanide or Y) [09Fu]. For the RE_3TaO_7 stoichiometry with this structure, YII would only have 6 oxygen atoms coordinating it, resulting in a highly deformed YO_6 octahedron, Figure 5.25(c). Additionally, the OIII atom is coordinated by only two Ta^{5+} cations, causing insufficient charge compensation for that atom [09Fu]. Tilting of the TaO_6 octahedra brings the OIII atom closer to the YII atom, increasing the coordination of YII to 7 while also bringing two YII within the coordination sphere of OIII, Figure 5.24(d). However the introduction of excess

Ta^{5+}, as in 70Y30Ta results in the *o* (*Cmmm*) structure [79Ros2, 07Yas, 91Yok]. The excess Ta^{5+} (relative to Y_3TaO_7) occupy a fraction of the YII site, as may be expected based on the smaller ionic radius of Ta^{5+} relative to Y^{3+} and the reduced coordination of the YII site relative to the YI site. The increase in local disorder that occurs with Ta^{5+} substitution likely explains why the Raman peaks of 72Y28Ta (*Cmmm*) are more broad then those of 75Y25Ta (*Ccmm*), Figure 5.13. Oxygen must be introduced to maintain charge balance. Recent neutron diffraction showed that the oxygen vacancy prefers to be near the Ta cation [07Yas] and more specifically at the anion site connecting the chains of TaO_6 octahedra [79Ros2]. Therefore the oxygen atoms preferentially fill the vacancies in the *W* structure, destroying the [001] chains of alternately tilted TaO_6 octahedra, Figure 5.25(d). The average *o* structure for 70Y30Ta reported in literature is shown in Figure 5.25(e) and (f). Each partially filled anion site has an occupancy of 60%, as indicated by the white and red spheres. However, the two sites are only separated by ~1.2Angstroms. This separation is significantly smaller than the ~2.8Angstrom bond length. In reality, the oxygen vacancy would occupy one of sites, and the octahedral tilting would likely still be present but only over short distances [79Ros2]. The average structure, as investigated by X-ray or neutron diffraction, would appear to have octahedra that are not tilted [79Ros2, 07Yas]. Since *W* and *o* differ by slight movements of the YII site and oxygen atoms/vacancies, it is conceivable that 72Y28Ta has the *Cmmm* structure at high temperatures, but quickly transforms to multiple domains of *Ccmm* during cooling (even quenching). In other words, the cations are ordered up to at least 1600°C, as suggested by the high temperature XRD (Figure 5.12), but the oxygen vacancies move between the two sites freely. Therefore at high temperature, the TaO_6 octahedra are on average, not tilted. On cooling the oxygen vacancies order because they are much more mobile than cations. The oxygen vacancies would likely order in such a way as to optimize the coordination of YII sites and improve the charge compensation of OIII. The optimum arrangement would therefore result in slight shifts of the Y^{3+} cations and tilted TaO_6 octahedra as in *Ccmm*. However, these changes happened very quickly, producing domains

of *Ccmm,* Figure 5.16. Therefore the XRD pattern of 72Y28Ta after furnace cooling looks similar to the pattern after quenching the sample in air, Figure 5.11. Room temperature XRD again shows an average structure in which the TaO_6 octahedra are not tilted, however they may be tilted within each domain. The *Ccmm* domains came from the same parent *Cmmm* structure and therefore there are twin boundaries separating the domains, as seen in the atomic resolution images, Figure 5.17. Previous studies have relied solely on bulk characterization techniques [07Yas, 91Yok] and thus only reported the average structure.

Two scenarios regarding the region 25-30%$TaO_{2.5}$ are considered for the purposes of this discussion. In one case the *W (Ccmm)* and *o* (*Cmmm*) are two distinct phases, as proposed by Yokogawa [91Yok]. The second scenario examines the proposition that W and o are different degrees of order within the same field. If it is assumed that Y_3TaO_7 is a line compound and *o* has the solubility range of 28-30 mole% $TaO_{2.5}$, then the two-phase field is only ~3mole% wide. It is difficult to envision a free energy landscape wherein two closely related phases, one of which exhibits a solubility range, could actually be immiscible within the 25-28 mole% range. Alternatively, it is conceivable that the *Ccmm* structure gradually transforms to *Cmmm* as Ta^{5+} is added. Based on what is known about the structures, there is not a structural reason for the two-phase field to exist. The O-Ta-O angle would be a suitable order parameter to follow as the $TaO_{2.5}$ concentration increased. It is interesting to note that the *Cmmm* structure has not been observed above 30mole% $TaO_{2.5}$, which corresponds to 40% of the OIII sites being vacant and 10% of the YII sites being occupied by Ta^{5+}.

In addition to the structural similarities between the phases in the $YO_{1.5}$-rich region of the binary, sluggish ordering kinetics, coarsening, and sintering also complicate the determination of the phase equilibria. The presence of fluorite peaks in the XRD patterns of 85Y15Ta, 75Y25Ta and 72Y28Ta after 400h at 1250°C suggest that the average structure of those compositions is fluorite. The samples start with the disordered fluorite structure after

co-precipitation. Metastable extension of the fluorite phase field has been observed and explained in other $YO_{1.5}$-rich, precursor derived ceramics [98Lev]. However the presence of Raman peaks associated with the *Ccmm* and *Cmmm* structures in 75Y25Ta and 72Y28Ta indicates that ordered orthorhombic domains are present even though the average, bulk structure determined by XRD after heat-treatments at 1250°C is fluorite. The propensity of 75Y25Ta and 72Y28Ta to form locally ordered domains is evident in the Raman spectra recorded after heat-treatments at 650°C (4h), 900°C (16h), 1000°C (18h) and 1250°C (400h). Figure 5.14. Raman peaks after higher temperature heat-treatments are less broad than those after lower temperature exposures, indicating an increase in local order after the high temperature heat-treatments. With the exception of the additional peak at 768cm^{-1}, the Raman spectra of 75Y25Ta and 72Y28Ta are nearly identical after heat-treatment at 1250°C. This suggests that the cations and anions have similar bonding environments and have not yet reached the equilibrium arrangements of *Ccmm* and *Cmmm*, respectively. It is highly unlikely that compositions near Y_3TaO_7 and $Y_7Ta_3O_{18}$ would be fluorite at 1250°C, since the orthorhombic forms are known to be stable at 1500°C [91Yok]. Therefore it is assumed that *Cmmm* and *Ccmm* are the true equilibrium phases on the $YO_{1.5}$ -$TaO_{2.5}$ binary at 1250°C [91Yok].

The ordered nature of *C*, *W*, and *o* also results in reduced ion diffusion, which could contribute to the slow coarsening and sintering in the $YO_{1.5}$-rich region. In contrast to cation-ordered phases, bixbyite (*C*), which contains ordered oxygen vacancies, forms rather quickly from fluorite due to the high mobility of anions [77Ray]. Once formed however, the ionic conductivity of bixbyite is several orders of magnitude lower than that of fluorite [83And]. The drastic decrease in ionic conductivity is attributed to the highly ordered oxygen vacancies in bixbyite, which do not contribute to oxygen ion diffusion. It is possible that the slow oxygen diffusion may also suggest that cation diffusion is also reduced, which would inhibit coarsening and densification of $YO_{1.5}$.

When cation ordering is required in addition to oxygen vacancy ordering, as is the case for *W* and *o*, it is arguable that it would take longer for phases to fully order. The difficulty in forming these ordered phases is compounded by the sluggish kinetics at temperatures below 1300°C. For example, the onset of sintering in other $YO_{1.5}$-$TaO_{2.5}$ containing oxides was not observed until 1230°C [11Bha2]. Similar to the bixbyite structure, ionic conductivity is reduced by several orders of magnitude in *W* relative to disordered fluorite [90Iku, 93Kim]. Again the lack of 'mobile' oxygen vacancies in a perfectly ordered structure, which would require increasing the energy as their coordinating environment is changed, would be responsible for the significant decrease in ionic conductivity. Reduced ionic conductivities may also translate to decreased diffusion and coarsening in Y_3TaO_7-containing compositions,

5.5 Conclusions

The utilization of complementary characterization techniques proved invaluable to understanding the nature of the true equilibrium phases in the $YO_{1.5}$-$TaO_{2.5}$ system. Additional insights were gained by understanding the crystal structures. Results presented in this study agree with previous literature on the stability of the terminal oxides. The temperature and composition ranges of two phases on the $TaO_{2.5}$-rich portion of the diagram were determined; the perovskite line-compound, YTa_3O_9 (*P*, *Cmmm*) is stable from 1200-1800°C and hexagonal YTa_7O_{19} (*h*, $P\bar{6}c2$) is stable from at 83-87.5 mole% $TaO_{2.5}$, and from ambient temperature to ~1550°C. The reconstructive *M'*→*T*-$YTaO_4$ transition is included on the binary for the first time.

The close relationships between the phases in the $YO_{1.5}$-rich region and slow coarsening kinetics complicate the determination of the phase equilibria in that region. Fluorite (*F*, $Fm\bar{3}m$) is stable at ~80 mole% $YO_{1.5}$ at T≥1500°C. While additional investigations are ongoing, two structurally similar orthorhombic phases, Y_3TaO_7 (*W, Ccmm*) and $Y_7Ta_3O_{18}$ (*o*,

Cmmm), are likely present at 25 mole% $TaO_{2.5}$ and 28 mole% $TaO_{2.5}$, respectively. It remains to be determined if a two-phase region exists between *W* and *o* or if the structural change is represented by the development of local Cmmm domains as Ta^{5+} is added to Y_3TaO_7. Elucidating the phase equilibria in the binary provides a foundation needed to understand the phase equilibria of the ZrO_2-$YO_{1.5}$-$TaO_{2.5}$ (ZYTO) system, as shown in Chapter 6.

5.6 Tables and Figures

Table 5.1 Phase identification reference

Compound	Structure	Group	Abbr.	PDF number
$YO_{1.5}$ (Y)	Bixbyite (cubic)	$Ia\bar{3}$	*C*	00-041-1105
	hexagonal	$P\bar{3}m1$	*H*	
$TaO_{2.5}$	tetragonal	$I4_1/amd$	α	01-075-9704
	orthorhombic	*Pna2*	β	
$YTaO_4$ (YT)	Scheelite (tetragonal)	$I4_1/a$	*T*	
	met. Fergusonite (monoclinic)	*I2*	*M*	00-024-1415
	Fergusonite (monoclinic)	P2/a	*M'*	00-024-1425
Y_3TaO_7 (Y_3T)	Weberite –type (orthorhombic)	*Ccmm*	*W*	
	fluorite (cubic)	$Fm\bar{3}m$	*F*	00-038-1403
$Y_7Ta_3O_{18}$ (Y_7T_3)	orthorhombic	*Cmmm*	*o*	
YTa_3O_9 (YT_3)	Perovskite (orthorhombic)	*Cmmm*	*P*	01-072-2030
	tetragonal	*P4/mmm*	τ	
YTa_7O_{19} (YT_7)	hexagonal	$P\bar{6}c2$	*h*	00-030-1465

Table 5.2 Sample composition, length of heat treatment, phase constitution, and equilibrium compositions after 100h heat treatment.

1600° C

Nominal Sample Composition	Heat Treatment	Phase Constitution	Phase	Composition via EPMA or TEM* (cat. %)	
				$YO_{1.5}$	$TaO_{2.5}$
Y	48h/FC	*C*	--	--	--
85Y15Ta	100h/FC	*C* + *F*	--	--	--
75Y25Ta	100h/Q	*F*	--	--	--
72Y28Ta	100h/Q	*o*	--	--	--
60Y40Ta	100h/FC	*o* + *T*	--	--	--
40Y60Ta	100h/FC	*T* + *P*	*T*	51.9	48.1
			P	26.8	73.2
20Y80Ta	100h/FC	*P* + α	*P*	26.5	73.5
			α	0.1	99.9
8Y92Ta	100h/FC	*P* + α	*P*	26.0	74.0
			α	0.0	100.0
Ta	48h/FC	α	α	--	--

Table 5.3 Sample composition, length of heat treatment, phase constitution, and equilibrium compositions after 100h heat treatment.

1500° C

Nominal Sample Composition	Heat Treatment	Phase Constitution	Phase	Composition via EPMA or TEM* (cat. %)	
				$YO_{1.5}$	$TaO_{2.5}$
Y	48h/FC	*C*	--	--	--
85Y15Ta	200h/FC	*C* + *W*	--	--	--
75Y25Ta	100h/FC	*W*	--	--	--
72Y28Ta	100h/FC	*o*	*o*	72.1±0.4*	27.8±0.4*
60Y40Ta	100h/FC	*T* + *o*	*T*	49.8±1*	50.2±1*
			o	69.9±0.5*	30±0.5*
40Y60Ta	100h/FC	*T* + *P*	YT	50.2	49.8
			P	25.3	74.7
20Y80Ta	100h/FC	*P* + *h*	*P*	25.2	74.8
			h	17.0	83.0
8Y92Ta	100h/FC	*h* + α	*h*	12.6	87.4
			α	0.0	100.0
Ta	48h/FC	α	α	--	--

Table 5.4 Sample composition, length of heat treatment, phase constitution, and equilibrium compositions after 100h heat treatment.

1400° C

Nominal Sample Composition	Heat Treatment	Phase Constitution	Phase	Composition via EPMA or TEM* (cat. %)	
				$YO_{1.5}$	$TaO_{2.5}$
Y	48h/FC	*C*	--	--	--
85Y15Ta	--	--	--	--	--
75Y25Ta	--	--	--	--	--
72Y28Ta	--	--	--	--	--
60Y40Ta	--	--	--	--	--
40Y60Ta	300h/FC	*M′* + *P*	*M′*	50.0	50.0
			P	25.4	74.6
20Y80Ta	300h/FC	*P* + *h*	*P*	25.1	74.9
			h	16.8	83.2
8Y92Ta	300h/FC	*h* + *β*	*h*	12.5	87.5
			β	-0.1	100.1
Ta	48h/FC	*α* + *β*	--	--	--

Table 5.5 Sample composition, length of heat treatment, phase constitution, and equilibrium compositions after 100h heat treatment.

1350° C

Nominal Sample Composition	Heat Treatment	Phase Constitution	Phase	Composition via EPMA or TEM* (cat. %)	
				$YO_{1.5}$	$TaO_{2.5}$
Y	48h/FC	*C*	--	--	--
85Y15Ta	--	--	--	--	--
75Y25Ta	--	--	--	--	--
72Y28Ta	--	--	--	--	--
60Y40Ta	--	--	--	--	--
40Y60Ta	400h/FC	*M′* + *P*	*M′*	50.0	50.0
			P	25.6	74.4
20Y80Ta	400h/FC	*P* + *h*	*P*	--	--
			h	17.4	82.6
8Y92Ta	400h/FC	*h* + *β*	*h*	12.5	87.5
			β	-0.1	100.1
Ta	48h/FC	*β*	--	--	--

Table 5.6 Sample composition, length of heat treatment, and phase constitution after 100h heat treatment.

1250° C

Sample Composition	Heat Treatment	Phase Constitution	Phase	Composition via EPMA or	
				$YO_{1.5}$	$TaO_{2.5}$
Y	48h/FC	*C*	--	--	--
85Y15Ta	800h/FC	*C* + *W*	--	--	--
75Y25Ta	400h/FC	*W*	--	--	--
72Y28Ta	400h/FC	*o*	--	--	--
60Y40Ta	SPS+100h/FC	*M′* + *o*	--	--	--
40Y60Ta	400h/FC	*M′* +*P*	--	--	--
20Y80Ta	400h/FC	*P* + *h*	--	--	--
8Y92Ta	400h/FC	*h* + *β*	--	--	--
Ta	48h/FC	*β*	--	--	--

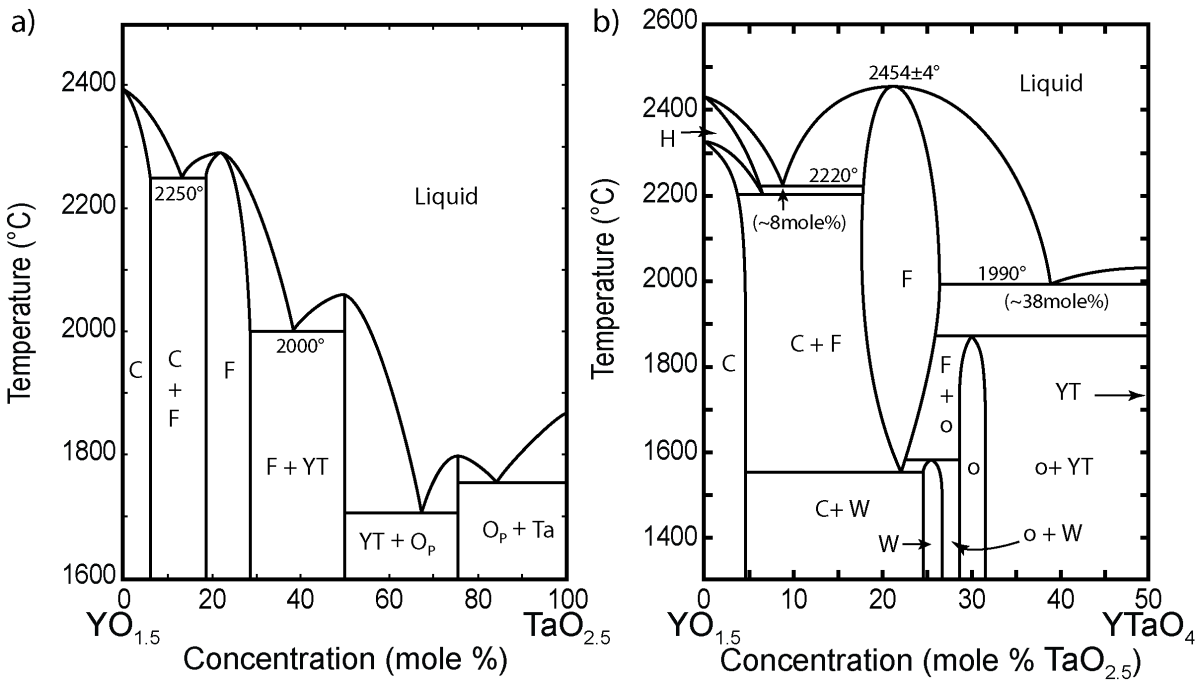

Figure 5.1 Earlier $YO_{1.5}$-$TaO_{2.5}$ phase diagrams reported by (a) [73Bon] and (b) [91Yok]. Phases are labeled according to Table 1 except W in (b) was originally identified with the space group $C222_1$ (Y_3TaO_7). $YTaO_4$ is labeled as YT because the transition from *M'* to *T* was not accounted for in the original diagrams. Similarly, $TaO_{2.5}$ is only labeled as "Ta" in (a) because the β to α transition was originally not considered.

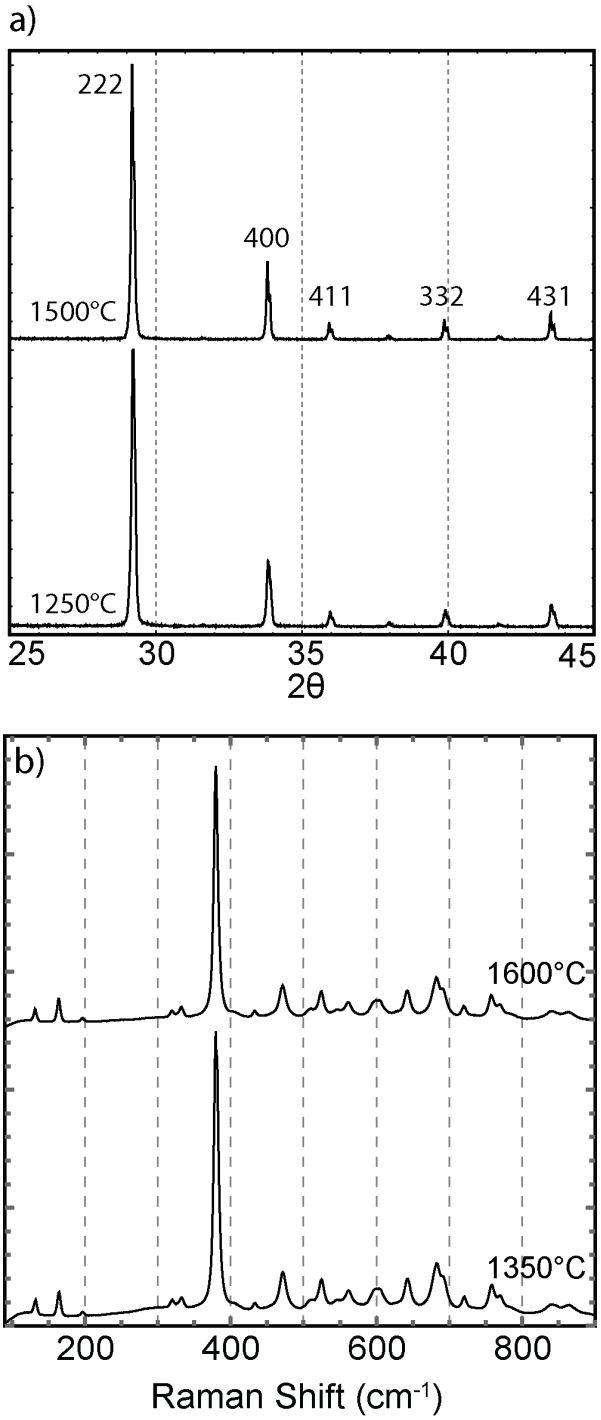

Figure 5.2 (a) XRD and (b) Raman of pure $YO_{1.5}$ shows that the cubic bixbyite structure is stable after prolonged heat treatments from 1250° to 1600°C, followed by air cooling.

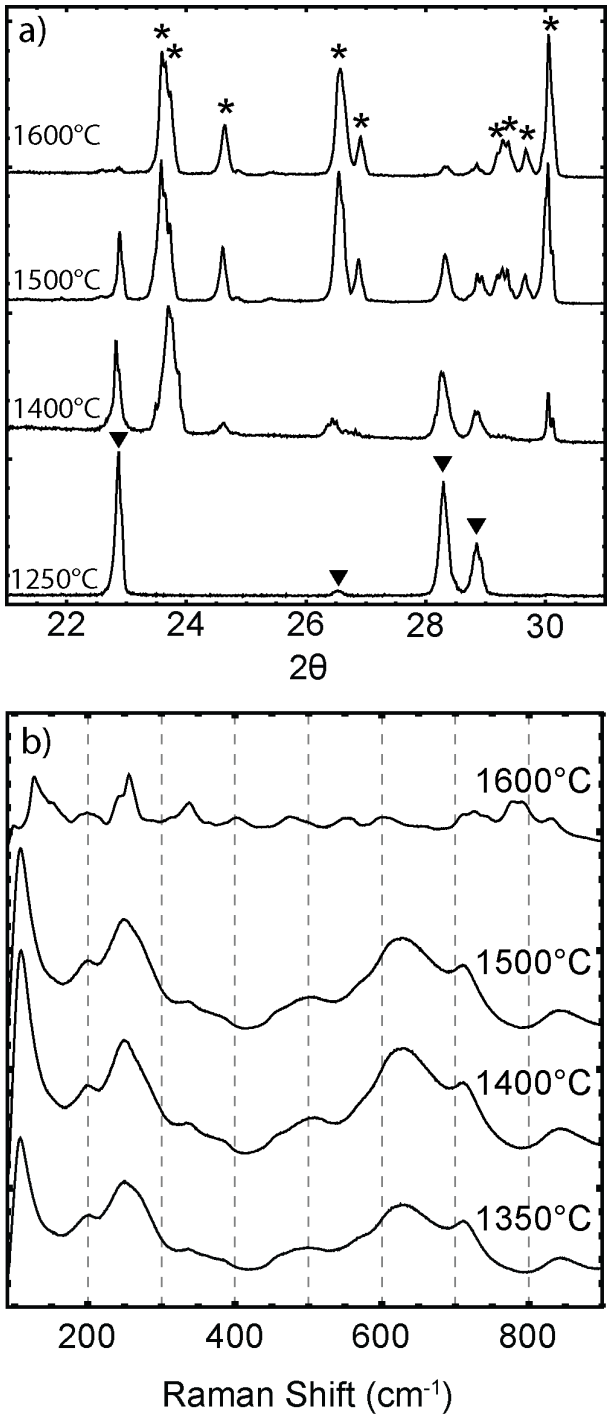

Figure 5.3 (a) XRD and (b) Raman of pure $TaO_{2.5}$ after various heat treatments for 48h. Asterisks in (a) indicate XRD peaks associated with the triclinic phase [68War] (PDF 01-075-9704) while triangles indicate the low temperature orthorhombic (*Pmm2E*, PDF 00-025-0922) structure [70Rot2]. Raman peaks from 1350-1500°C match those of β-$TaO_{2.5}$ [12Joe, 14Li].

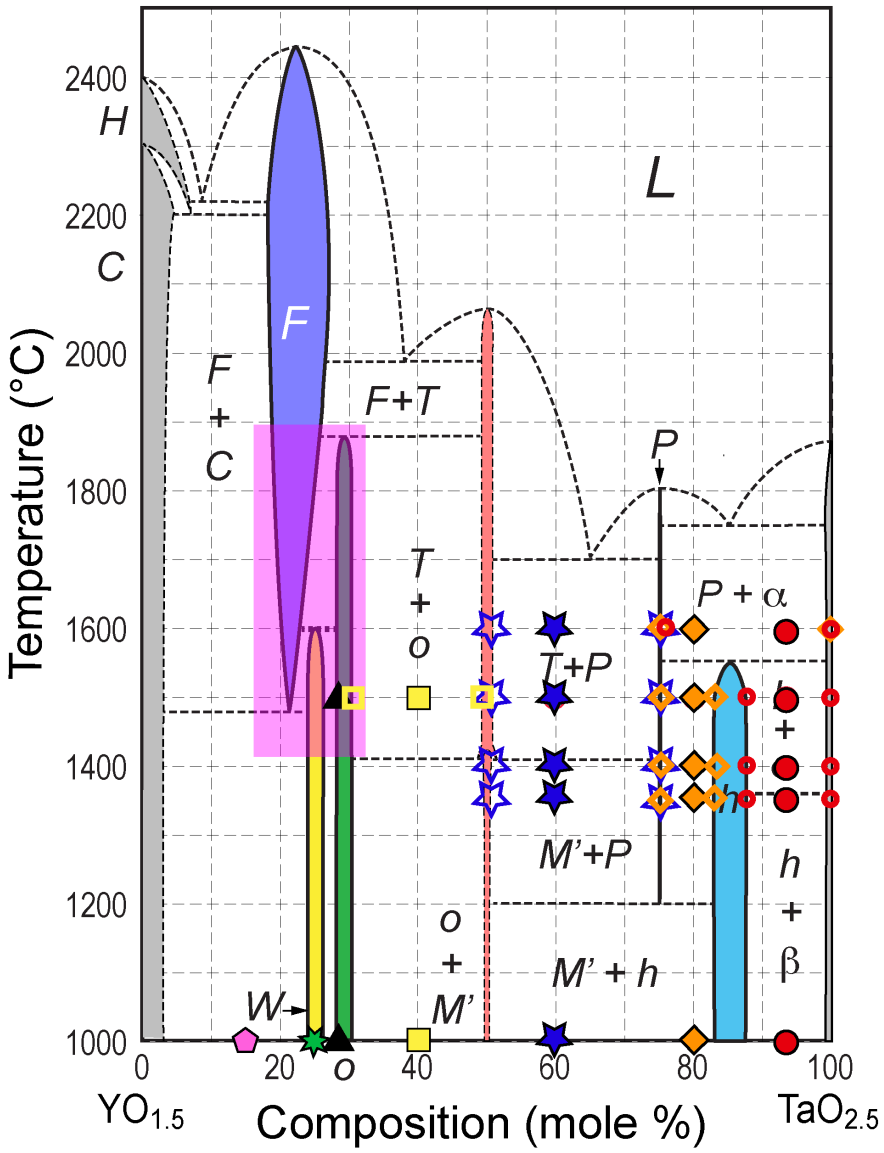

Figure 5.4 Binary phase diagram indicating nominal sample compositions and equilibrium composition determined via EPMA and TEM-EDS. Solid symbols indicate the nominal composition while unfilled symbols correspond to the measured equilibrium compositions. Pink highlighted region indicates a region where the similarity of the crystal structures complicates the determination of the phase equilibria. Phase equilibria between 1000°C and 1250°C were not studied in depth.

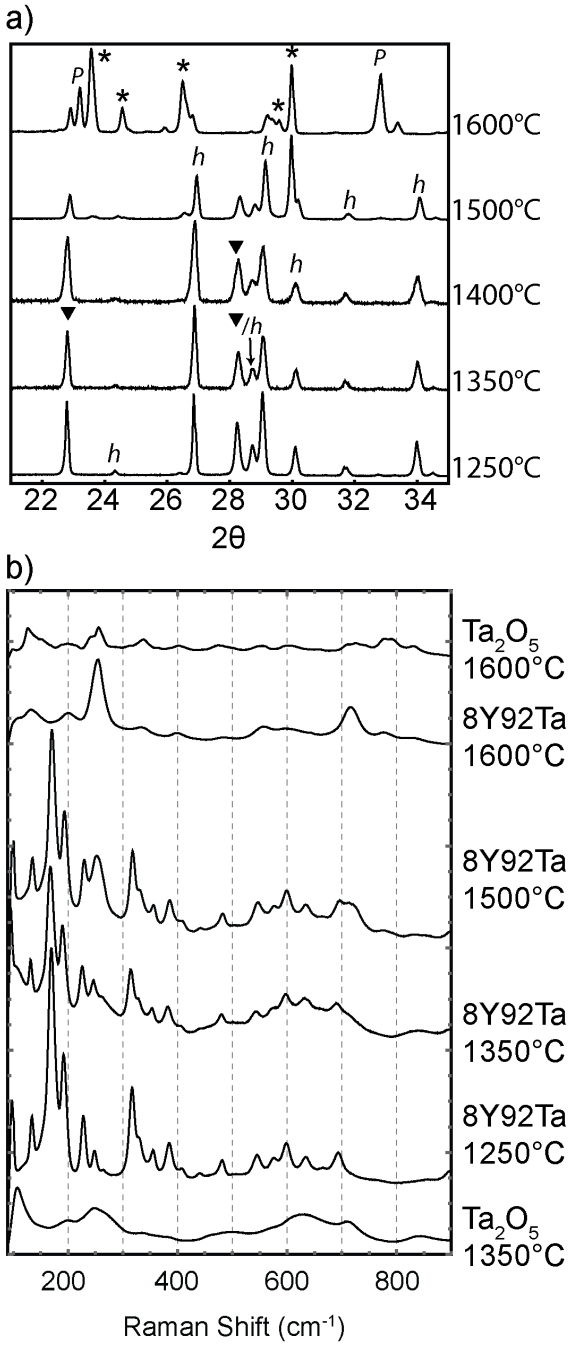

Figure 5.5 (a) XRD patterns for 8Y92Ta after heat treatments at 1250, 1350, 1400, 1500 and 1600°C indicate the phase evolution. At 1600°C, *P* and α are stable while *h* and β are stable at lower temperatures. (b) The stability range of *h* is evident in Raman spectroscopy since *h* has many more Raman active modes than α, β, or *P*. Asterisks in (a) indicate XRD peaks associated with the triclinic phase that transforms from α [68War] (PDF 01-075-9704) while triangles indicate the low temperature orthorhombic that transforms from β (*Pmm2E*, PDF 00-025-0922) structure [70Rot2].

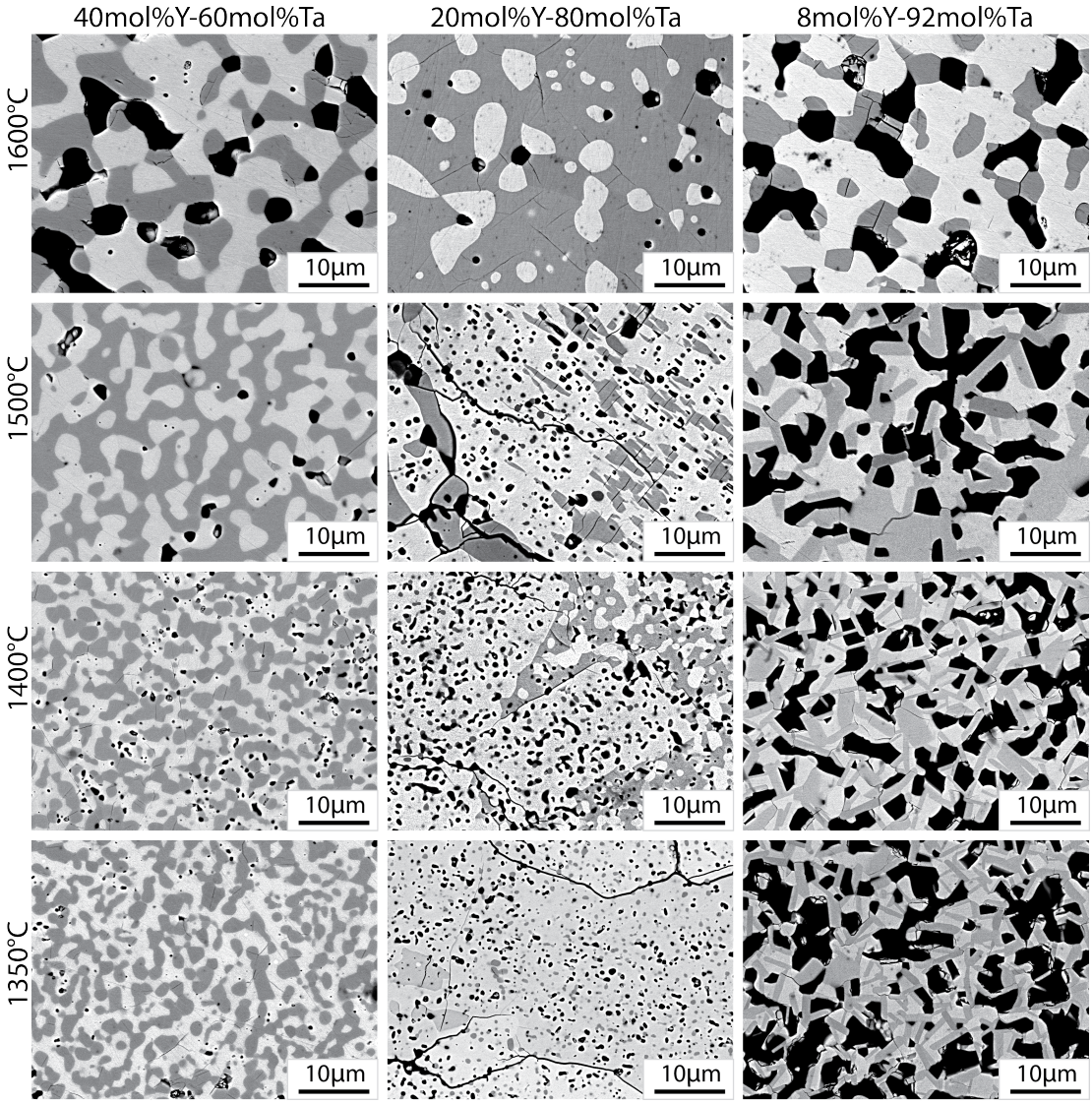

Figure 5.6 – BSE images of 40Y60Ta, 20Y80Ta, and 8Y92Ta after heat treatments at 1350, 1400, 1500, and 1600°C. Microstructure changes accompany changes in phase equilibria, such as YT_7 (high aspect ratio, dark contrast in 8Y92Ta) no longer being stable at 1600°C in 20Y80Ta and 8Y92Ta.

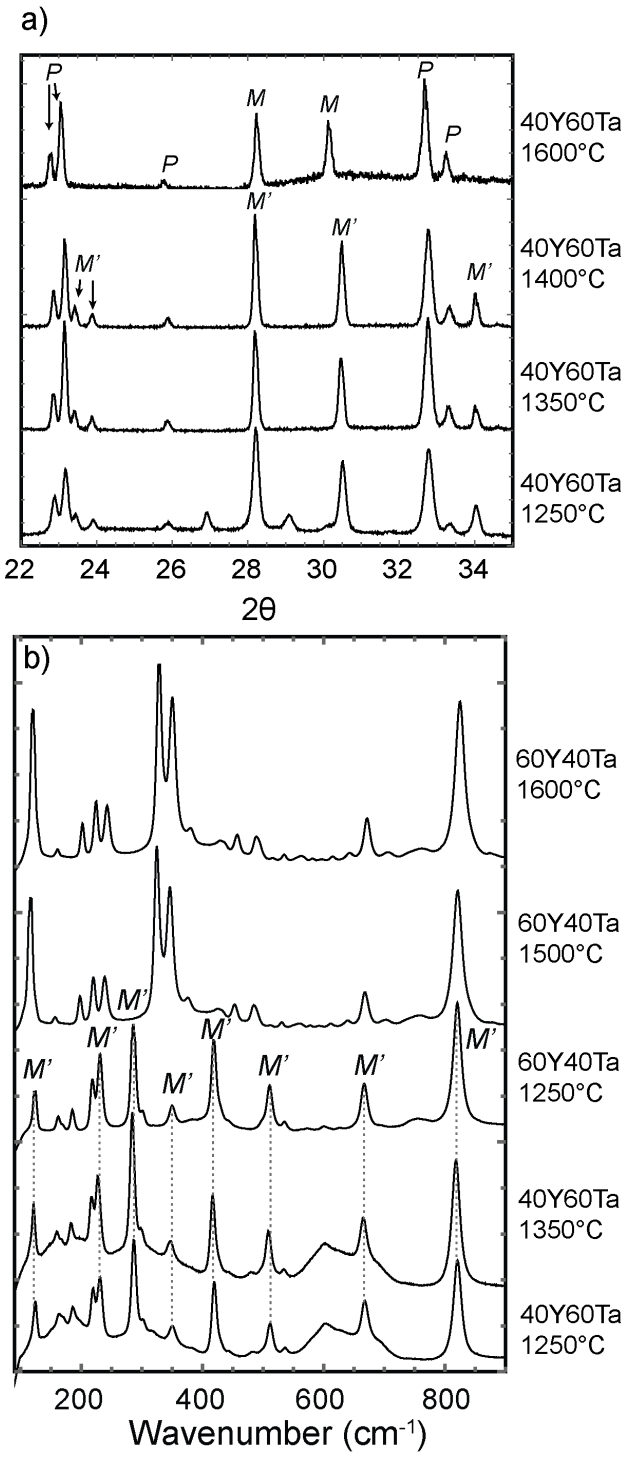

Figure 5.7 – (a) XRD of 40Y60Ta at 1250, 1350, 1400 and 1600°C indicates that *M'* is present up to 1400°C [83Bri]. (b) Raman spectroscopy of 40Y60Ta at 1250 and 1350°C and 60Y40Ta at 1250, 1500, and 1600°C confirms that *M'* is not stable at or above 1500°C but rather *M* forms from transformation of the high temperature T phase [73Bla, 83Bri, 14Shi].

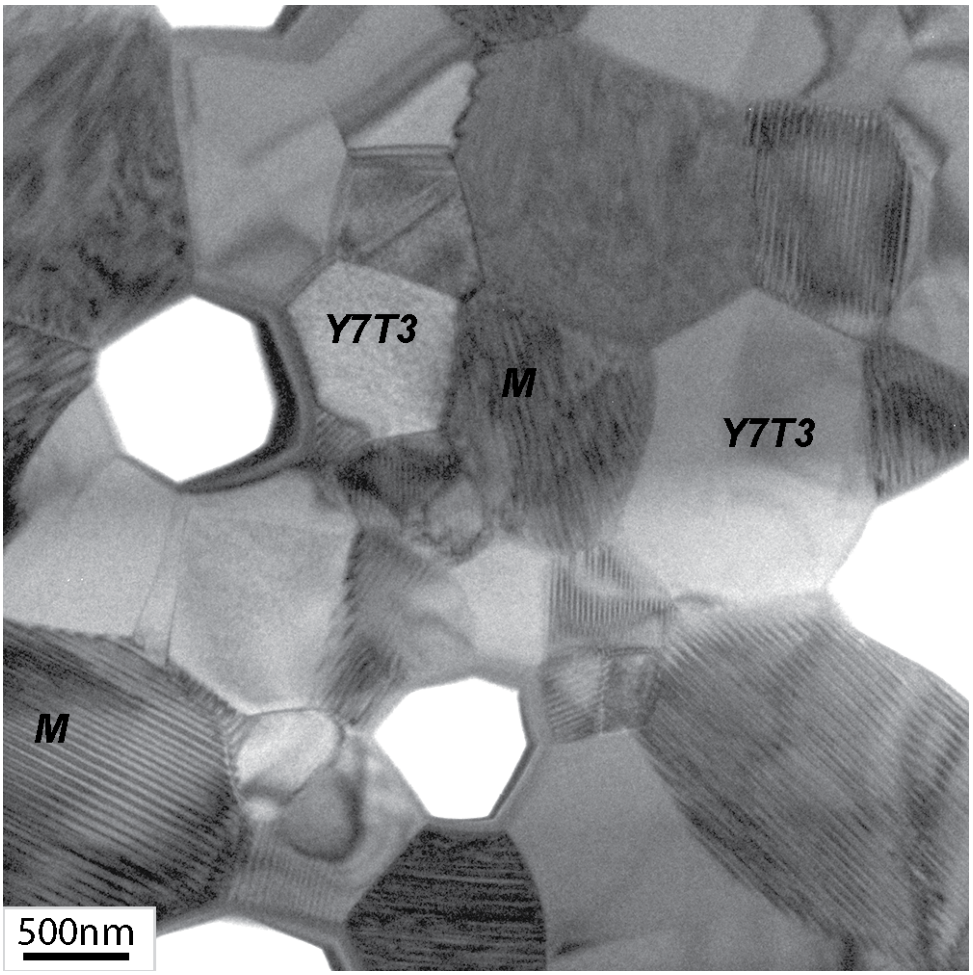

Figure 5.8 – BF-TEM image of 60Y40Ta after 100h at 1500°C shows the light contrast Y7T3 grains and the twinned microstructure of *M*-YT grains. The twins result from the displacive *T*→*M* transformation that occurs on cooling.

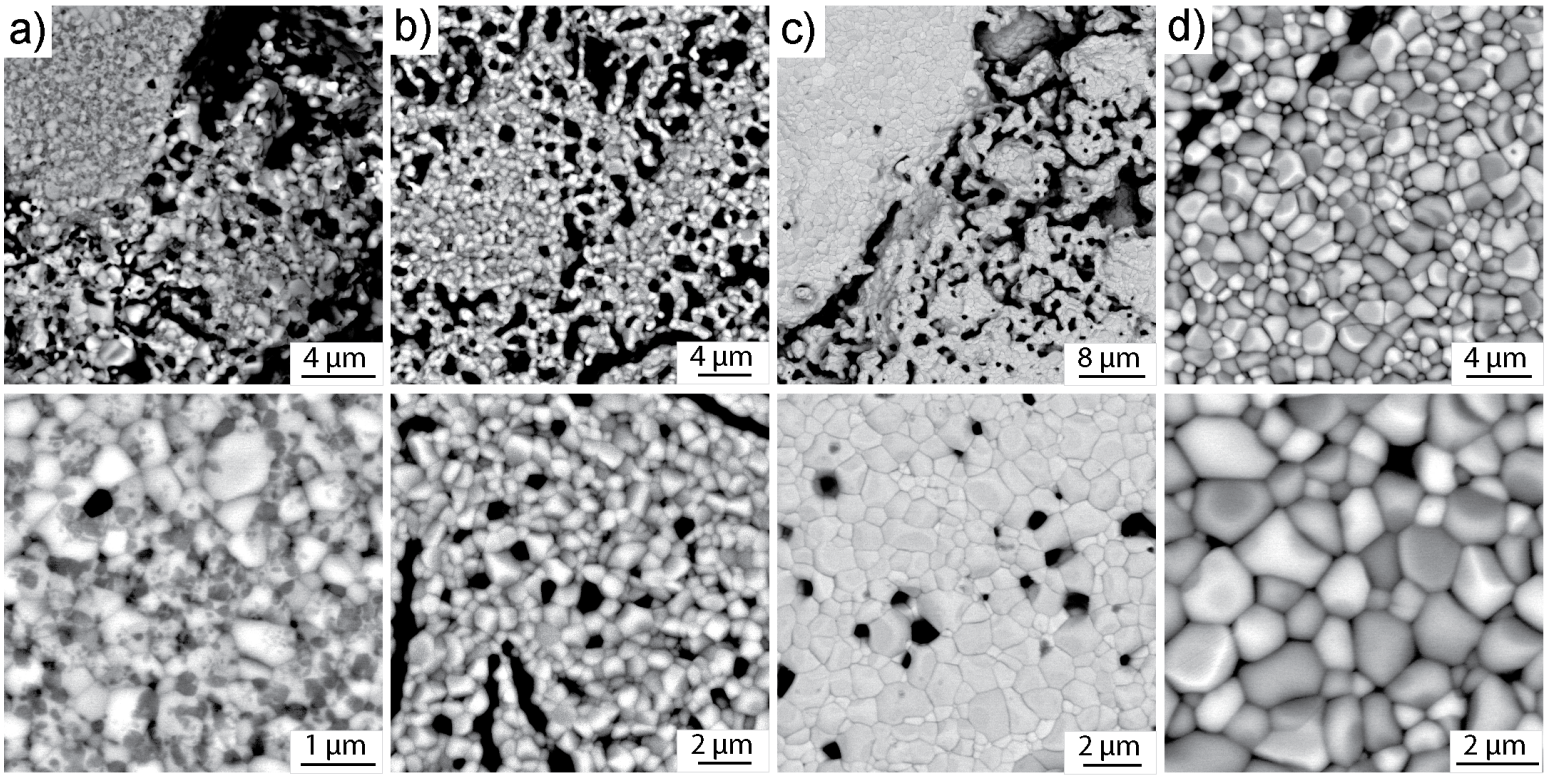

Figure 5.9– Low (top) and higher (bottom) resolution BSE images of (a) 85Y15Ta (200h), (b) 75Y25Ta, (c) 72Y28Ta, and (d) 60Y40Ta after 100h heat treatments at 1500°C. Samples containing more $YO_{1.5}$ exhibited smaller grains and more porosity than samples closer to $YTaO_4$. All black areas are pores.

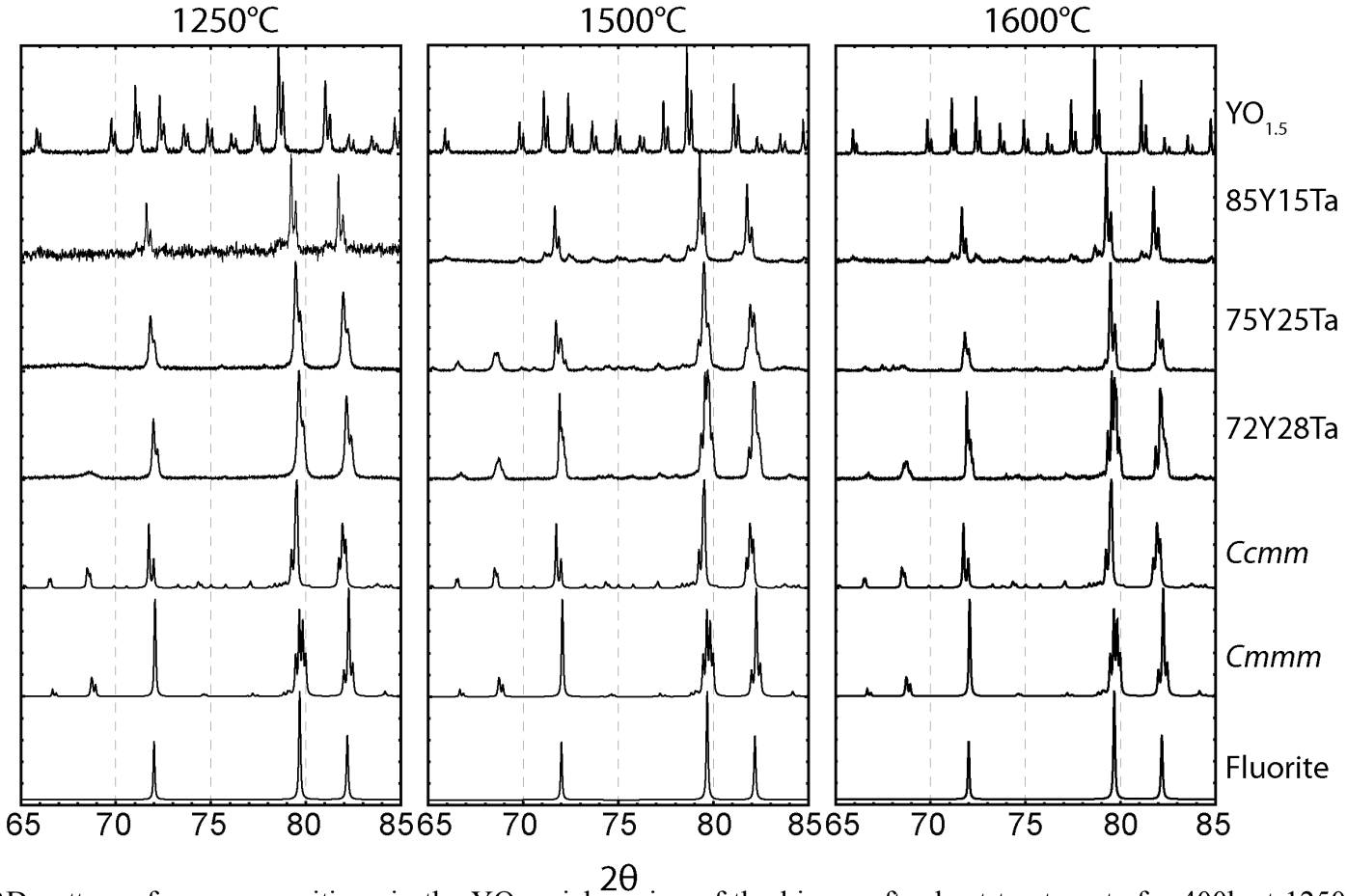

Figure 5.10 – XRD patterns from compositions in the $YO_{1.5}$-rich region of the binary after heat-treatments for 400h at 1250°C, 100h at 1500°C and 100h at 1600°C. The peak splitting of the peaks at 80° and 82° 2θ differentiate the XRD patterns of the average structures of *Ccmm* and *Cmmm*. Reference patterns for *Cmmm*, *Ccmm* and *Fluorite* are crystal structures from [79Ros2], [09Fu], and [07Yas], respectively, simulated using VESTA [08Mom].

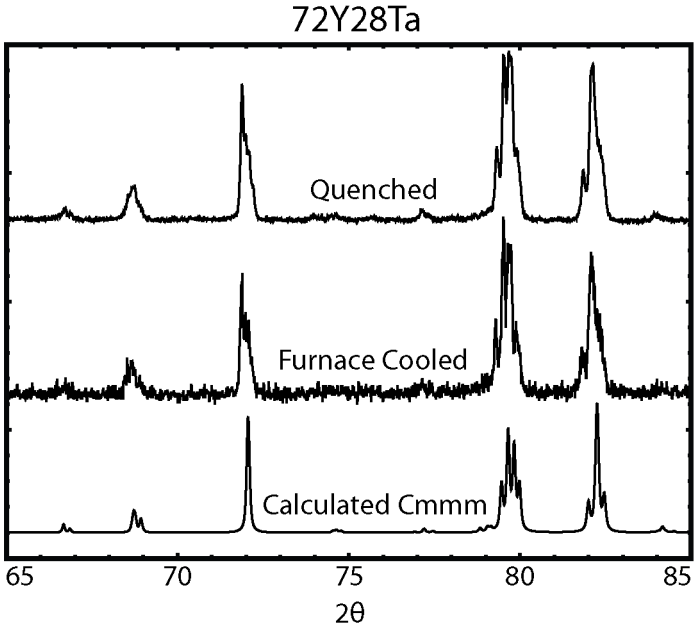

Figure 5.11 – XRD patterns of 72Y28Ta after furnace cooling (10°C/min) and quenching from 1500°C do not show significant differences in peak shape or location. Signal-to-noise difference between the furnace cooled and quenched patterns is due to detector parameters and does not reflect the crystallinity of the sample.

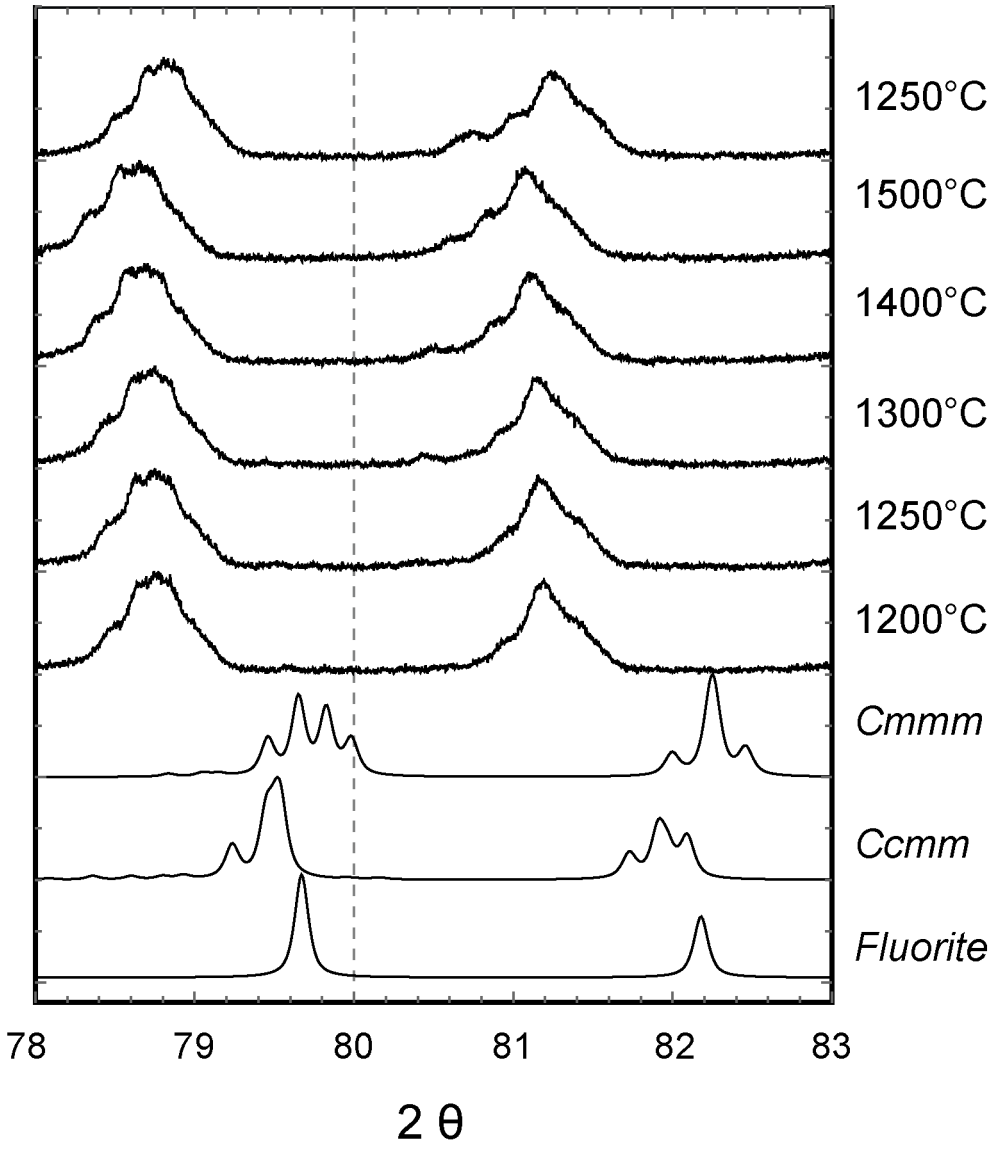

Figure 5.12 – High Temperature XRD patterns from 72Y28Ta. Reference patterns for *Cmmm*, *Ccmm* and *Fluorite* are from [79Ros2], [09Fu], and [07Yas], respectively. Peak shift of the patterns is due to the bowing of the platinum stage at high temperature.

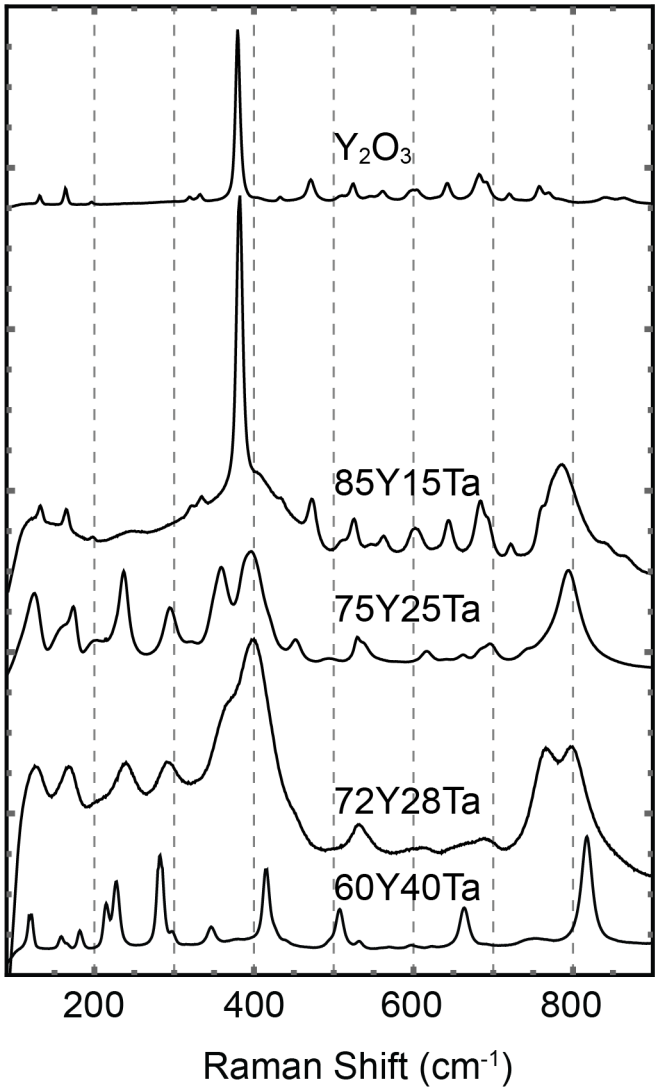

Figure 5.13 – Raman spectra (633nm excitation) of the compositions in the $YO_{1.5}$-rich portion of the phase diagram after 100h at 1500°C.

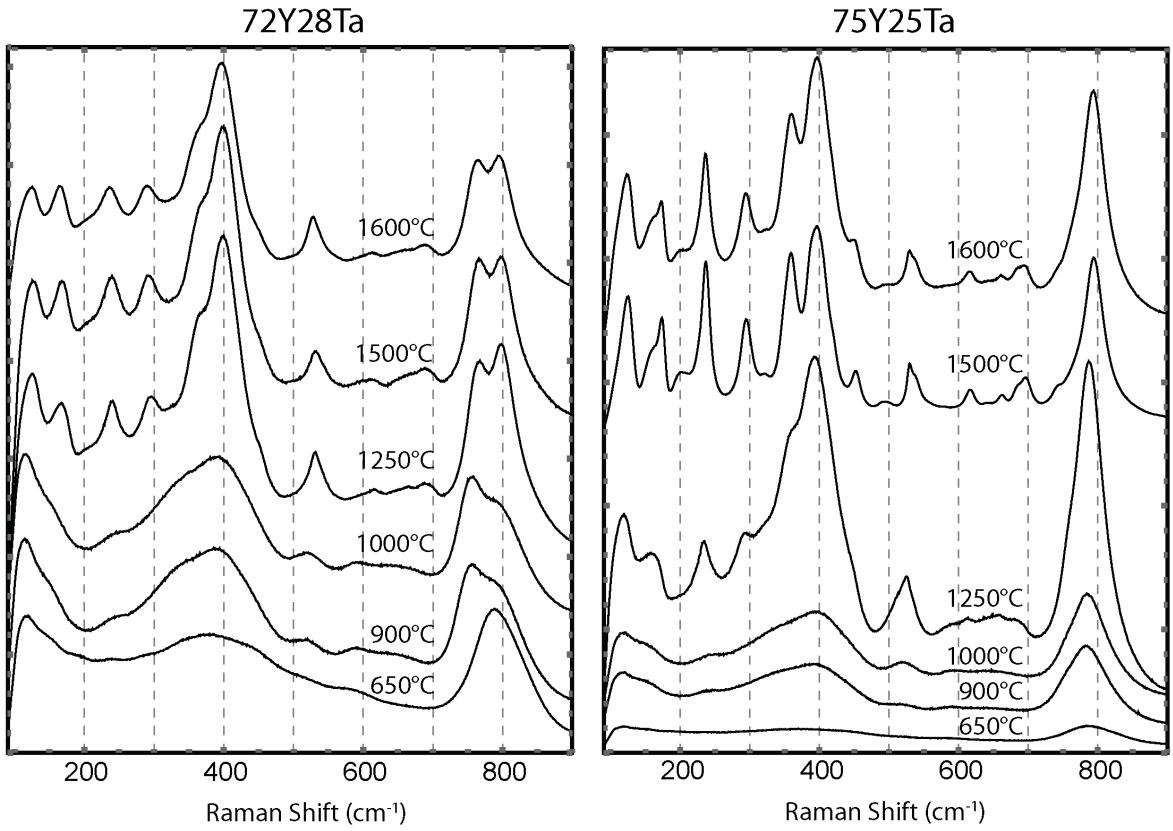

Figure 5.14 – Raman spectra of 72Y28Ta and 75Y25Ta after heat treatments at 650°C (bottom, blue), 900°C, 1000°C, 1250°C, 1500°C, and 1600°C (top, purple) indicate that neither undergoes a significant phase change in that temperature range.

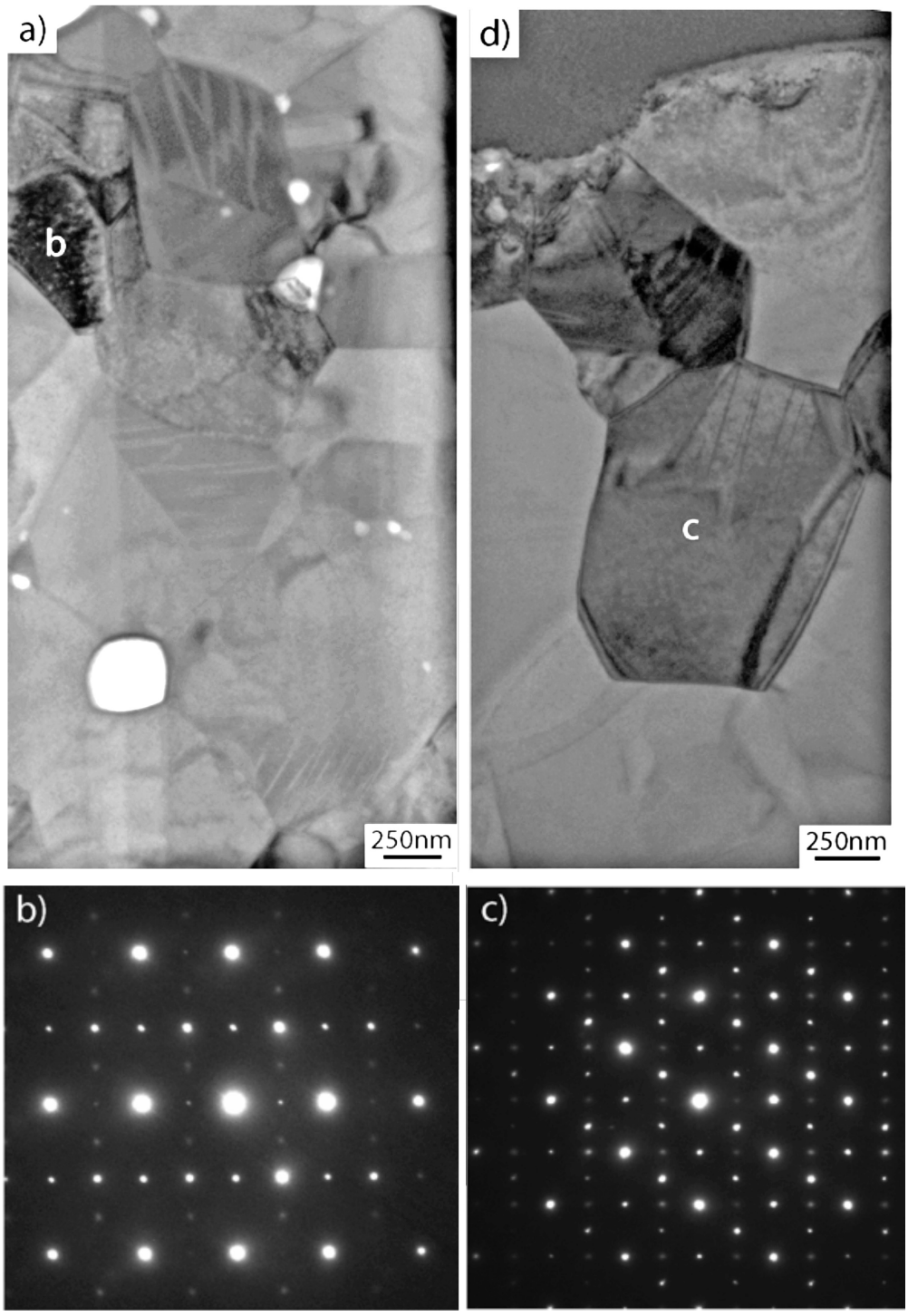

Figure 5.15 – Grains with striated microstructures are observed in 72Y28Ta in (a) and (d) bright field TEM images. Selected area electron diffraction (SAED) pattern along the $[110]_{Ccmm}$ zone axis from location 'b' in (a) is shown in (b). SAED pattern from location 'c' in (d) is shown in (c) and includes overlapping patterns of $[001]_{Ccmm}$ and $[010]_{Ccmm}$.

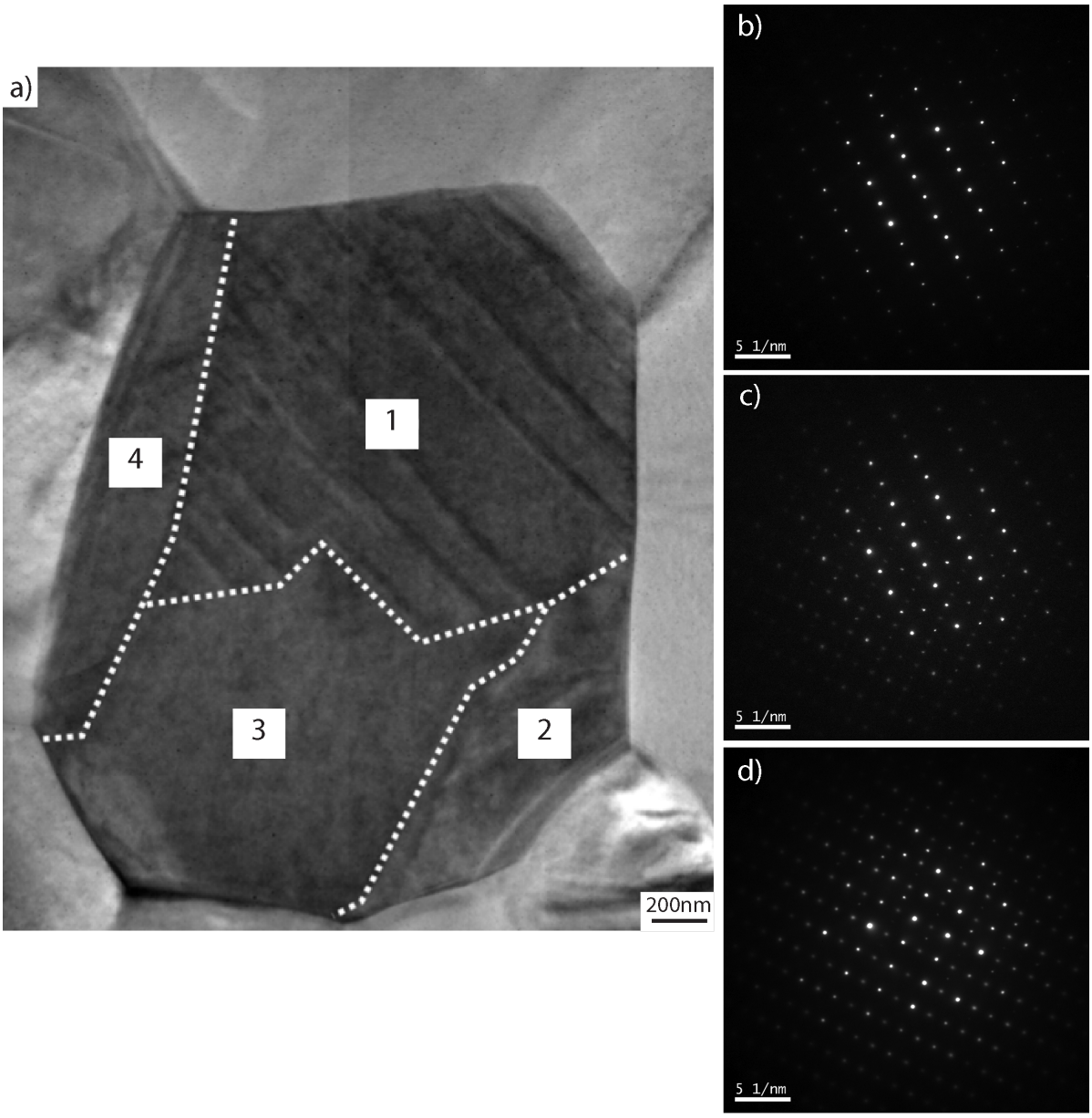

Figure 5.16 – (a) BF-TEM image illustrating the multi-domain structure observed in many grains in 72Y28Ta. (b) Domain 2 can be indexed as the $[112]_{Cmmm}$, which is equivalent to the $[111]_{Ccmm}$. (c) SAED pattern from both domain 1, 2 and 3, indicating the domains are crystallographically related. (d) SAED pattern from region 3 can only be explained by two variants of *Ccmm*, $[001]_{Ccmm}$ and $[010]_{Ccmm.}$ BF image courtesy of D. Park.

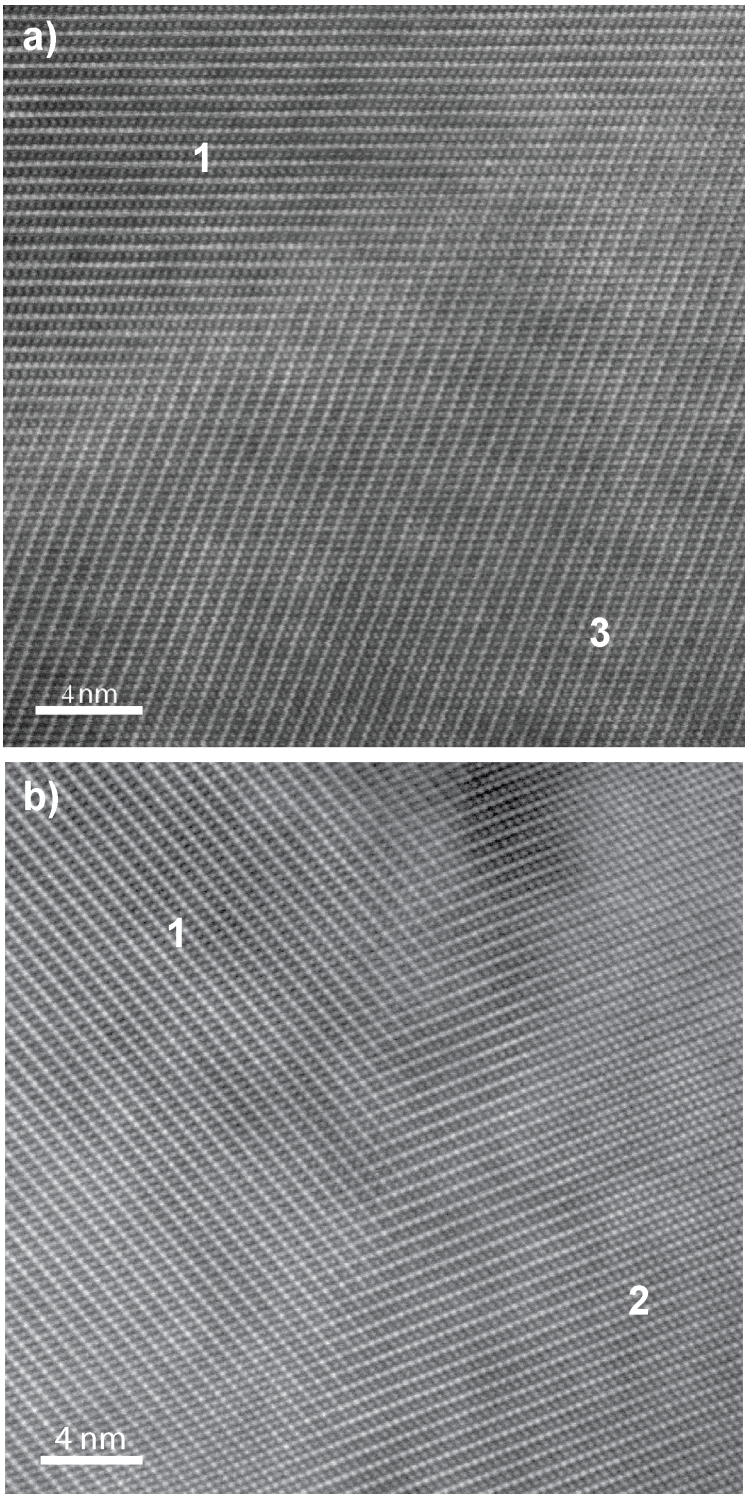

Figure 5.17 – (a) Atomic resolution HAADF-STEM images of the coherent twin boundaries between domain regions (a) 1 and 3 and (b) 1 and 2 in the grain shown in Figure 5.16. Both images are along the $[111]_{Ccmm}$ which is equivalent to the $[112]_{Cmmm}$. Images taken by D. Park.

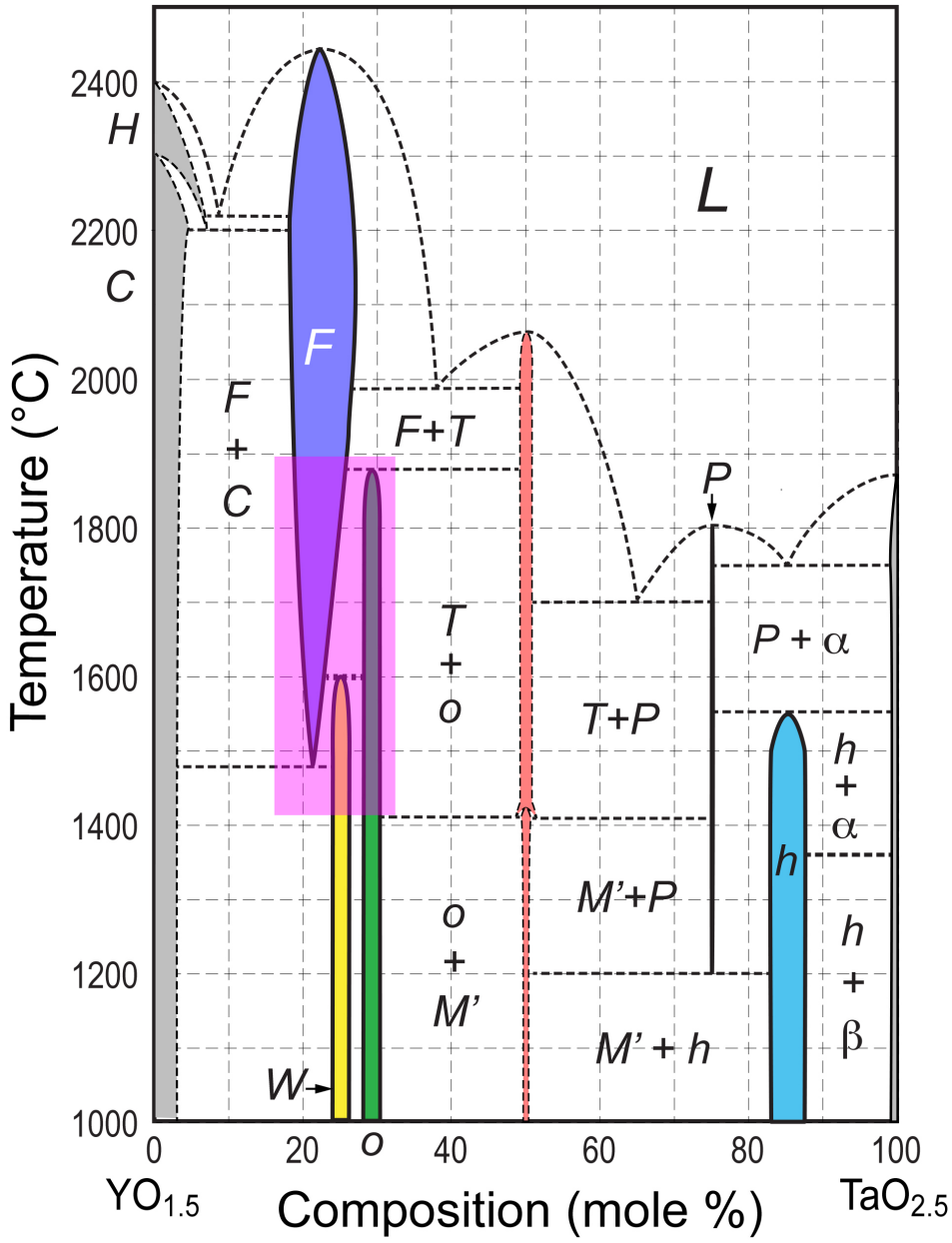

Figure 5.18 – Revised $YO_{1.5}$-$TaO_{2.5}$ binary phase diagram based on available literature and the results of this investigation.

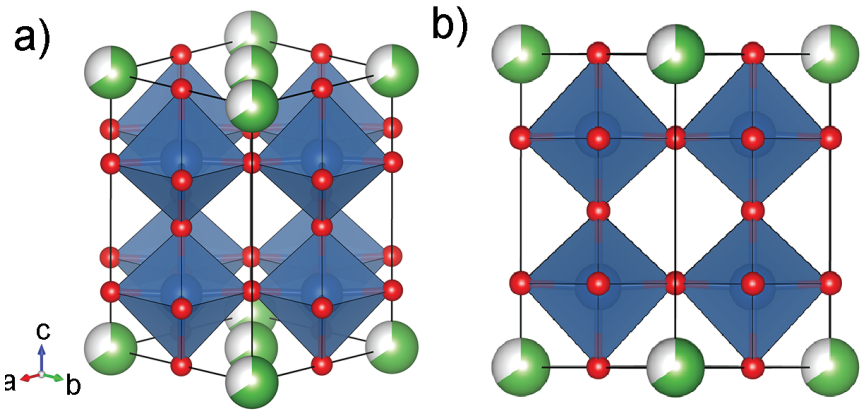

Figure 5.19 – Structure of the perovskite YTa_3O_9 [68Tru] simulated using VESTA [08Mom]. Ta ions (within octahedra) are blue, Y ions are green, and O ions are red. Vacancies or partially occupied sites are white. In reality, Y-vacancies are likely ordered as proposed by [08Zho].

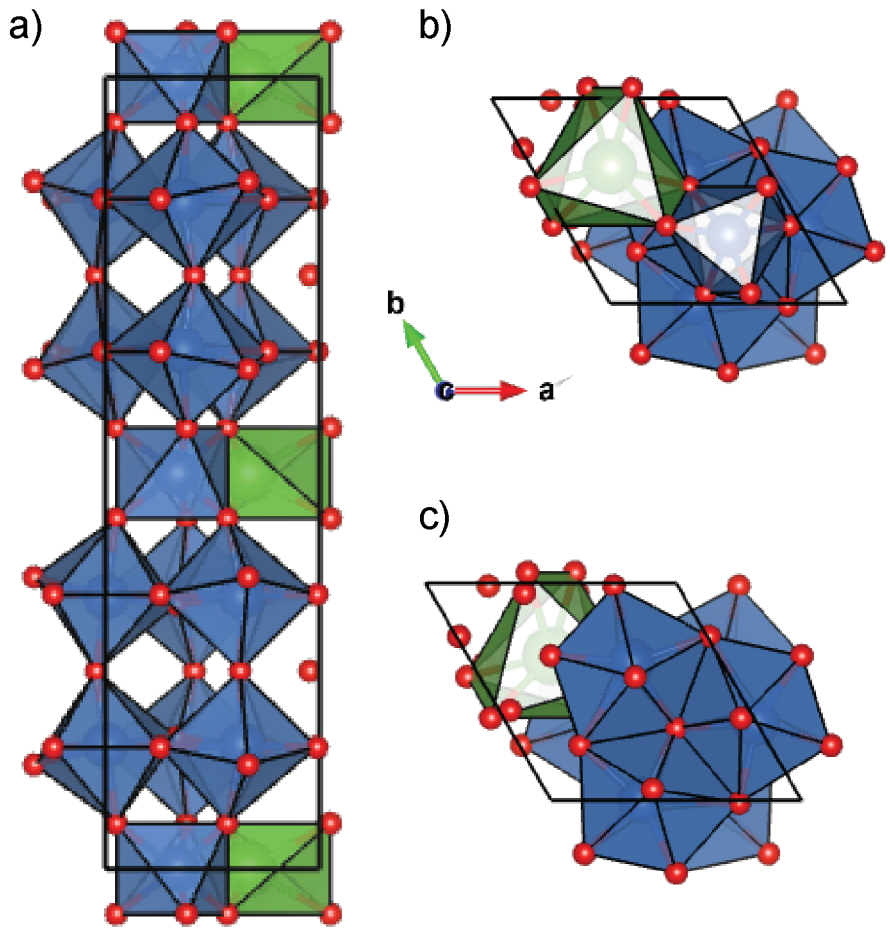

Figure 5.20 – Structure of *h*-YTa_7O_{19} [90Sch] simulated using VESTA [08Mom]. (a) projection along the a axis in which the c-axis is the long axis, (b) and (c) projections along the c-axis. The top layer of trigonal antiprisms is removed in (c) to highlight the pentagonal TaO_7 bipyramids (blue). YO_7 polyhedra are green.

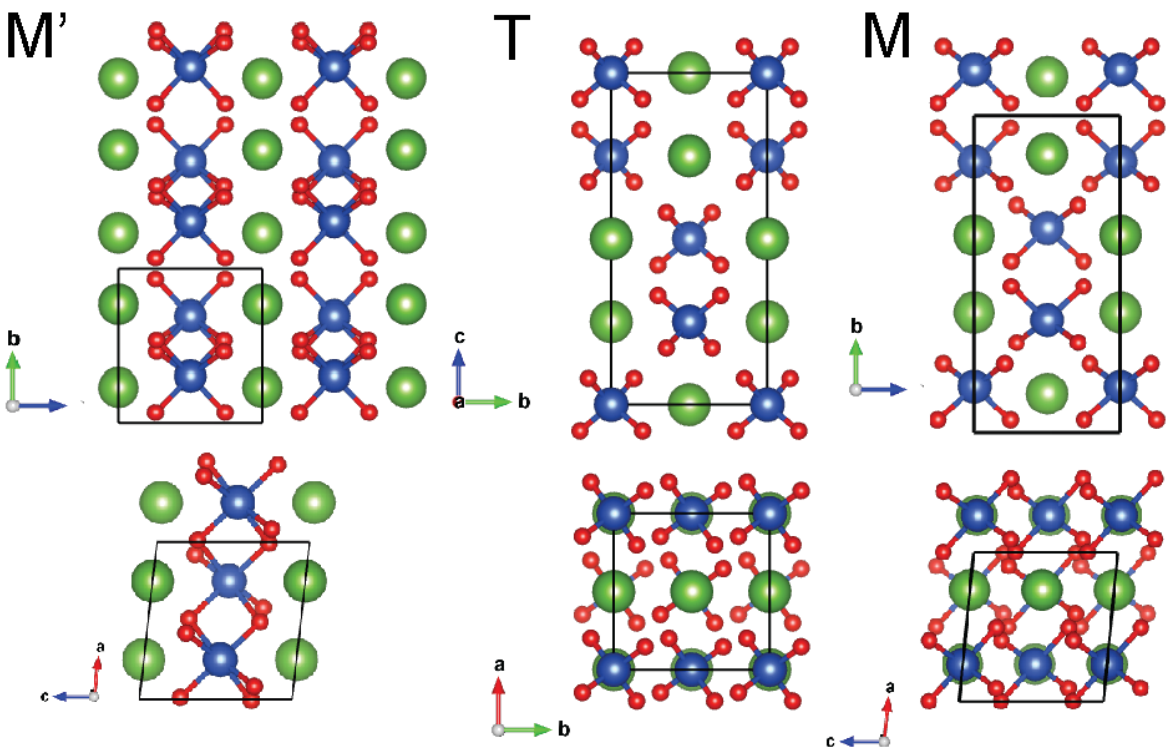

Figure 5.21 – Schematic illustrating the difference between the *M'* [67Wol], *T* [14Fen] and *M* [62Kel] crystal structures simulated using VESTA [08Mom]. Ta ions are blue, Y ions are green, and O ions are red.

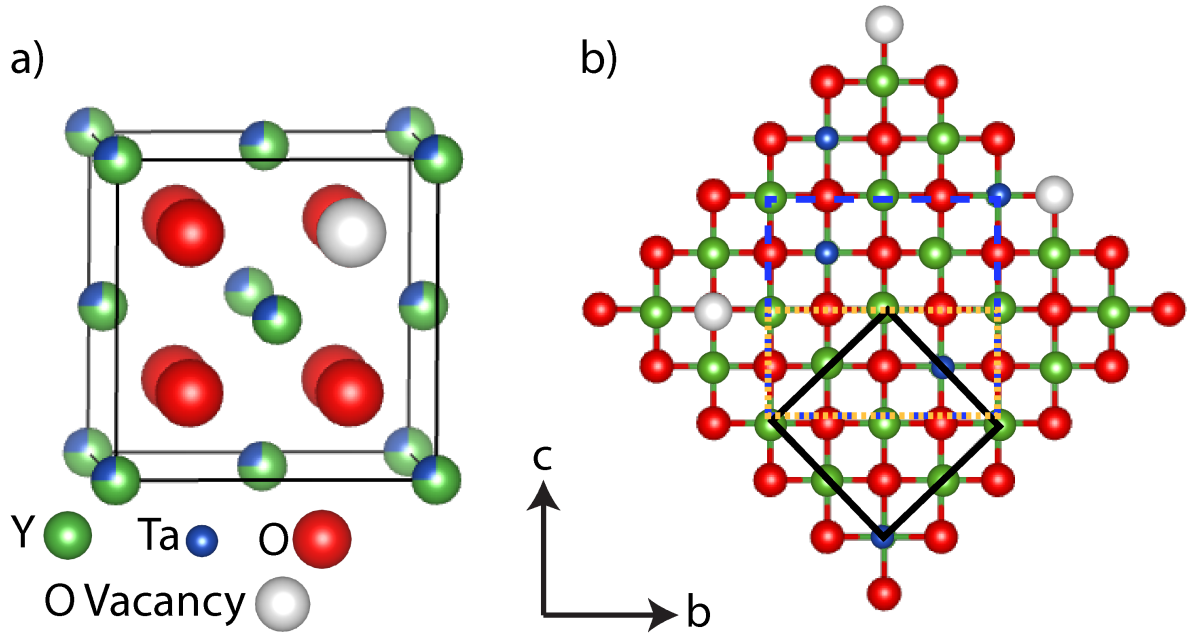

Figure 5.22 – The structure of *F* with a composition of 75Y25Ta. Y and Ta occupy the cation sites randomly and one out of every 8 oxygen sites is vacant. The unit cells of *F*, *o* (*Cmmm*) and *W* (*Ccmm*) are shown with the solid black, blue dashed and orange dotted lines, respectively.

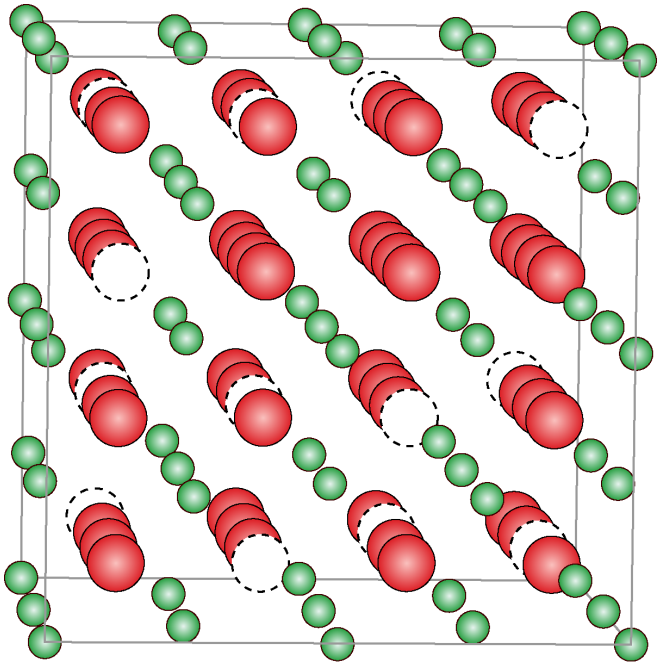

Figure 5.23 – The structure of *C* is similar to that of the defect fluorite, but a quarter of the oxygen sites are vacant and those vacancies are ordered. The ordering of vacancies causes the lattice parameter to double (i.e. $a_C=2a_F$).

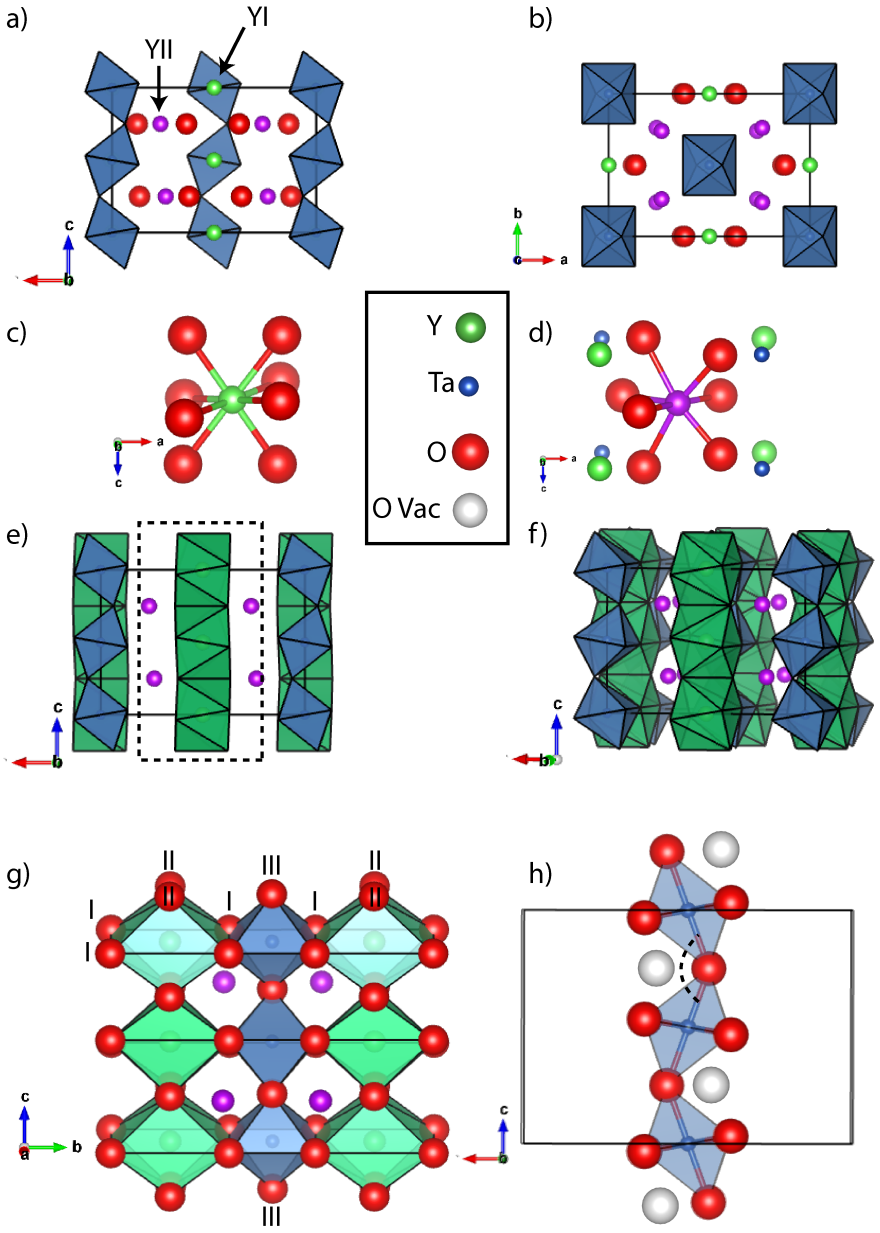

Figure 5.24 – The structure of *W* is a cation- and oxygen vacancy-ordered form of the fluorite structure, as shown in Figure 5.22(b). (a) Chains of corner sharing TaO_6 octahedra are parallel to the c-axis. The two distinct Y-sites are indicated. (b) Octahedra tilt about the 010 axis and the tilts are in-phase in the 010 direction. Cations in the YI (c) and YII sites (d) are 8 and 7-fold coordinated, respectively. Y1 polyhedra (green) are shown in (e) and (f). The slab outlined with a dashed line in (e) is shown along the a-axis, with the different oxygen sites labeled. Oxygen vacancies are ordered (h) and occur near OIII.

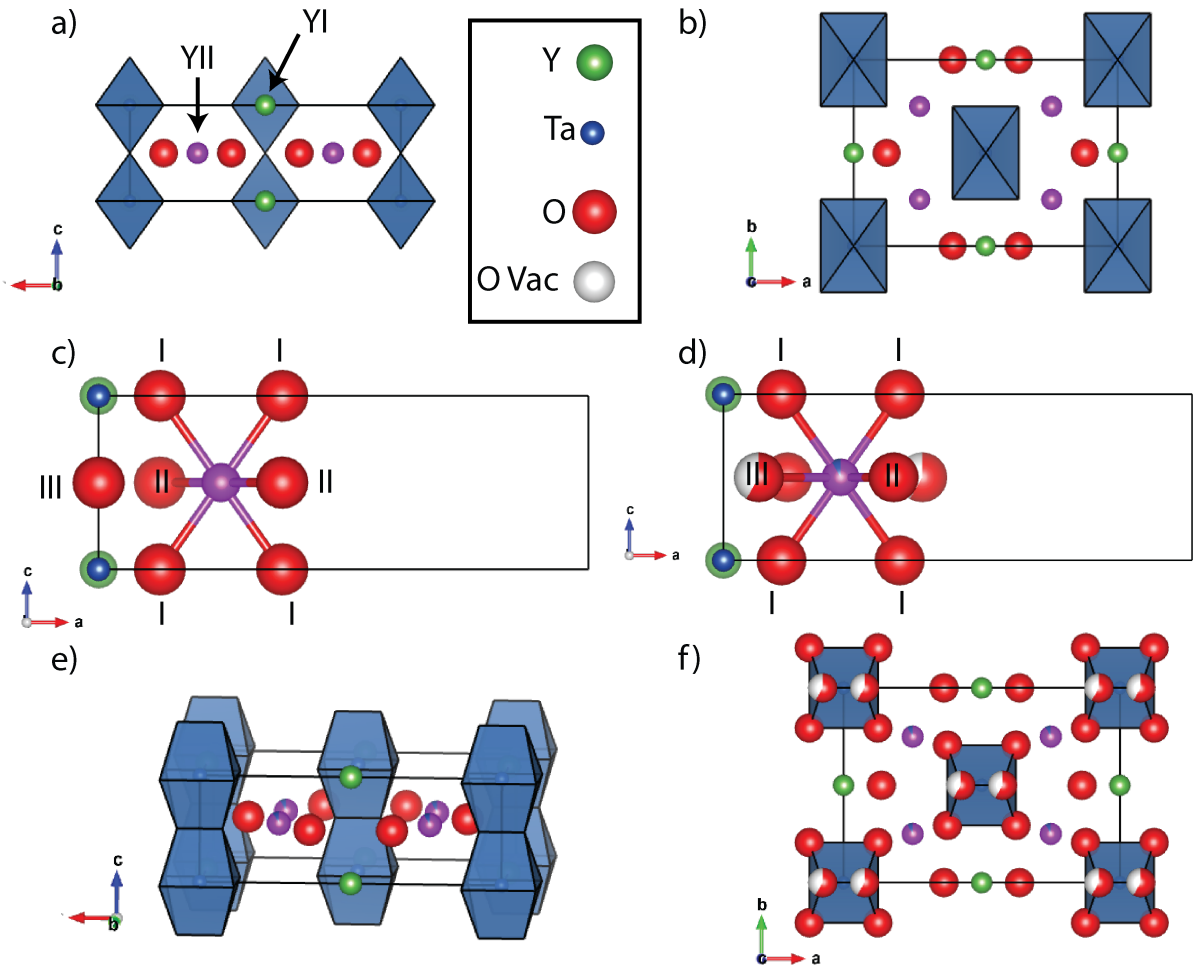

Figure 5.25 – The orthorhombic *Cmmm* Y_3TaO_7 structure is the parent structure to *Ccmm* Y_3TaO_7 in which the TaO_6 octahedra are not tilted, as seen along the (a) [010] and (b) [001] directions. (c) The YII cation would only be coordinated by 6 oxygens, as the OIII oxygen is outside (3.2Angstroms) the coordination sphere of YII. (d) When excess Ta^{5+} is added (i.e. 70Y30Ta), the additional oxygen atoms are located in formerly vacant sites in the *W* structure. The average *o* structure viewed near the (e) [010] and along the (f) [001] directions. Red and white spheres indicate partially (60%) occupied oxygen sites [79Ros2, 07Yas].

CHAPTER 6: PHASE EQUILIBRIA IN THE ZYTO SYSTEM

The ZrO_2-$YO_{1.5}$-$TaO_{2.5}$ (ZYTO) system contains several phases of interest for next generation thermal barrier coatings (TBCs). It is also of interest to the fields of phosphors, fuel cells, and photocatalysis. Despite the numerous applications, there is a paucity of information on the ternary phase equilibria, especially in the ZrO_2-lean region of the phase diagram. Precursor derived compacts of relevant ZYTO compositions were heat treated at 1250°C and 1500°C to establish the phase equilibria across the entire ternary system. Chemical composition and crystallographic information is used to deduce the isothermal section at 1250°C and 1500°C, which is found to vary significantly from previous estimates. Differences such as the extension of the fluorite field and solubility changes in the tetragonal ZrO_2, $YTaO_4$ and YTa_7O_{19} phase fields have important implications for the fields of TBCs and ionic/electronic conductors. By understanding the phase relations, especially within the ZrO_2-lean portion of the phase diagram, compositions with potentially attractive properties can be identified for further investigation.

6.1 Background on the phase equilibria

The constituent binary phase diagrams and available literature on the ternary system are reviewed first to provide context for the present study. The relevant phases and their shorthand notation are listed in Table 6.1. All compositions are listed as single cation.

6.1.1 Terminal oxide phases

All terminal oxides in the ternary system have multiple allotropes that may become stabilized or de-stabilized as their compositions are modified. Notably, ZrO_2 is tetragonal (*t*, $P4_2/nmc$) at 1500°C but transforms to a cubic form (fluorite, *F*, $Fm\bar{3}m$) above 2377°C, which melts at ~2710°C, and to the monoclinic form (baddeleyite, *m*, $P2_1/c$) below ~1205°C

[04Wan]. Y_2O_3 is cubic (bixbyite, C, $Ia\bar{3}$), an anion-ordered form of fluorite, from ambient to 2325°C, where it transforms to a hexagonal structure (H, $P\bar{3}m1$) before melting at 2430°C [65Pat, 90Car]. The structure of Ta_2O_5 has been the subject of more debate [07Bre]. It is generally agreed that the high temperature (α) form is tetragonal ($I4_1/amd$) [07Liu], stable above ~1360°C up to the melting point of 1872°C [72Jeh], whereas the low temperature form (β) is orthorhombic ($Pna2$) [69Wol].

6.1.2 $YO_{1.5}$-ZrO_2 binary

The ZrO_2-$YO_{1.5}$ binary is by far the most studied of the relevant binaries given its importance to high temperature ceramics such as thermal barrier coatings and solid oxide fuel cell electrolytes. The current phase diagram, Figure 6.1(a) and thermodynamic description are based on [04Fab], revised in [05Fab] and subsequently in [07Fab]. However, the general features are essentially the same, as the revisions were motivated for consistency with models for higher order systems. An earlier review [96Yas] suggested that the tetragonal phase boundary might exhibit retrograde solubility, at variance with the currently accepted diagram. However, recent work has found evidence consistent with a retrograde solvus [13Lip] with a maximum solubility of ~5 mole% $YO_{1.5}$ in ZrO_2. Approximately 4 mole% ZrO_2 is stable in $YO_{1.5}$ at 1500°C [05Fab]. In the binary at 1250°C the fluorite field extends from 50 to 84 mole% ZrO_2 [05Fab]. At 1500°C, the fluorite field extends from 13.5mole% $YO_{1.5}$ to 64mole% $YO_{1.5}$ [04Fab]. At lower temperatures (T<1300°C) rhombohedral δ-$Y_4Zr_3O_{12}$ ($R\bar{3}$) is stable. This phase can be viewed as an ordered derivative of fluorite [77Sco] and disorders congruently to fluorite at ~1384°C [05Fab]. To describe the ordering of fluorite to δ as "sluggish" would be an understatement as the δ phase has only been observed after heat treatments of 3-6 months at temperatures below 1300°C [83Pas, 77Sco]. Therefore is not expected to form δ in only 400h at 1250°C, however it is included in the isothermal section because it is a known equilibrium phase.

6.1.3 $TaO_{2.5}$-$YO_{1.5}$ binary

An extensive review of the available literature in the $TaO_{2.5}$-$YO_{1.5}$ binary was presented in Chapter 5. While experimental results from Chapter 5 were considered in the final isothermal sections at 1250°C and 1500°C, only the literature review (Figure 5.1) was used to predict the preliminary isothermal sections in Figure 6.2 and Figure 6.3.

6.1.4 $TaO_{2.5}$-ZrO_2 Binary

There is only one preliminary thermodynamic assessment and a rather schematic binary phase diagram for the $TaO_{2.5}$-ZrO_2 system, Figure 6.1(b) [56Kin, 11Bha]. The maximum solubility of $TaO_{2.5}$ in ZrO_2 at 1500°C was reported as 3.9mole% and that of ZrO_2 in $TaO_{2.5}$ as ~7mole% [91Zhe], however equilibrium solubility has not been rigorously studied at lower temperatures. Only one intermediate phase has been reported, orthorhombic $Ta_2Zr_6O_{17}$ (*O*, *Ima*2c), isostructural with $Nb_2Zr_6O_{17}$ [73Gal, 94Gri], with a solubility range at 1500°C reported as 20-29mole% $TaO_{2.5}$ [91Zhe] or 21.7-31.7mole% $TaO_{2.5}$ [91Kim]. This phase was not included in the preliminary thermodynamic assessment due to limited phase equilibria information. The solubility range at 1250°C is unknown, however the crystal structure of $Ta_2Zr_6O_{17}$ is stable above 750°C, and similar to its equilibrium form at 1500°C, is isostructural with $Nb_2Zr_6O_{17}$ [94Gri, 93Rus].

6.1.5 ZrO_2-$YO_{1.5}$-$TaO_{2.5}$ ternary diagram

The first experimental study of the ZrO_2-$YO_{1.5}$-$TaO_{2.5}$ phase diagram focused on the ZrO_2-rich portion [91Kim]. To date there is only a preliminary thermodynamic assessment of this system at 1200°C and 1500°C [11Bha]. However, $Ta_2Zr_6O_{17}$ and all binary $YO_{1.5}$-$TaO_{2.5}$ binary compounds, with the exception of $YTaO_4$, were not included in the optimization owing to insufficient data. In consequence, the shape of the tetragonal $Zr(Y,Ta)O_x$ phase

field resulting from that exercise is not consistent with the experimental observations [91Kim, 07Pit] or the model for zirconia stabilization using charge-compensating co-dopants [94Li3]. For example, it is well established that the composition ZrO_2-16.6$YO_{1.5}$-16.6$TaO_{2.5}$ is single phase tetragonal at 1500°C [06Pit, 07Pit] but the calculated diagram [11Bha] predicts a mixture of tetragonal Zr(Y,Ta)O_x solid solution and α-$TaO_{2.5}$.

There is no reported evidence of ternary phases in the ZYTO system, but all three terminal oxides and at least some of the binary phases are known to exhibit solubility of the other oxide(s). Most notably, the solubility of limit of the tetragonal ZrO_2 solid solution (*t*) is 18%$YO_{1.5}$-18%$TaO_{2.5}$, or approximately 22%$YTaO_4$ [91Kim, 07Pit]. Conversely, there is similarly high solubility of ~20%ZrO_2 in the tetragonal form (*T*) of $YTaO_4$ at 1500°C [14Shi]. Notably, the report of a disordered tetragonal form of $YTaO_4$ isostructural with tetragonal ZrO_2, noted earlier [95Mat], suggests the possible existence of a metastable extended tetragonal solid solution along the entire line of equimolar doping. Earlier work suggested the $Zr_{(1-x-z)}Y_xTa_zO_{2-(x-z)/2}$ fluorite field extends up to $z \approx 0.12$ at $x \approx 0.45$ [91Kim]. The solid solution phase *O*-$Ta_2Zr_6O_{17}$ has a maximum $YO_{1.5}$ solubility of 4.3mole% when there is 21.7mole% $TaO_{2.5}$ and a minimum $YO_{1.5}$ solubility when there is 31.7mole% $TaO_{2.5}$ [91Kim].

There is a paucity of ternary solubility information in the ZYTO system at 1250°C. In one of the few studies at temperatures below 1400°C it is clear that the *t*-ZrO_2 phase field does not have as much $YO_{1.5}$ and $TaO_{2.5}$ solubility as it did at 1500°C [07Pit]. After 600h at 1250°C, 16.7Y16.7Ta contains a large fraction of *m*-ZrO_2, suggesting the non-transformable *t* field observed at 1500°C is no longer present in the ZrO_2-$YTaO_4$ binary at 1250°C [11Bha2, 91Kim, 15Van]. The ternary solubility of the YT and F phase fields is expected to decrease relative to 1500°C however the true solubility at 1250°C has yet to be experimentally determined.

Relevant results from the published binary phase diagrams as well as ternary studies were used to construct preliminary isothermal sections at 1500°C (Figure 6.2(a)) and 1250°C (Figure 6.3(a)). Dashed lines, which encompass most of the diagram, indicate regions where the phase equilibria had not been studied rigorously and thus were still uncertain. The ternary solubility of the fluorite (*F*), $Ta_2Zr_6O_{17}$ (*O)*, and $YTaO_4$ (*M'*) phases was estimated based on the solubilities at 1500°C.

6.2 Experimental details

Equilibrium phase relationships at 1500°C and 1250°C were determined by heat treating pellets of the compositions listed in Table 6.2 and Table 6.3, respectively, and denoted by circles in Figure 6.2 and Figure 6.3. Sample compositions are listed in mole percent of single cation formula units, to provide a metric for the nominal level of substitution in the cation lattice. Compositions in two- and three-phase fields were chosen to minimize the number of samples required to determine the entire isothermal section.

All samples were produced by reverse co-precipitation as described in Chapter 3. With the exception of the $TaO_{2.5}$-rich composition, Sample 7, which was calcined at 900°C to ensure complete conversion of Ta-rich hydroxides to oxides, all of the precipitates were calcined for 4h at 650° C to remove the organic components and produce molecularly mixed metal oxides. Powders were uniaxially pressed into pellets, ~10mm in diameter and ~3mm thick, and these were sintered in air for at least 400h at 1250°C or 100h at 1500°C with a heating/ cooling rate of 10°C/min. For all heat treatments the pellets were placed on a piece of platinum foil in a covered alumina crucible. In an effort to reduce porosity, some samples were heat treated for 800h at 1250°C (Sample 1) or hot uniaxially pressed (Sample 4) for 18h at 1250°C with a load of 15MPa prior to sintering for at least 400h at 1250°C. For one composition (Sample 14), the pellet was consolidated using current assisted densification, as described in Chapter 3. To improve density and increase grain size, Sample 2 was heat-

treated for 100h at 1500°C before sintering for 400h at 1250°C. After the prescribed dwell at 1500°C, Samples 18, 19 and 20 were removed from the furnace and quenched in air to minimize the amount of atomic-ordering that could occur during cooling. To aid in Raman spectroscopy peak identification of *M'*-YT, *M*-YT, and *t*-ZrO_2, single phase samples of 45Y-45Ta-10Zr, 47.5Y-47.5Ta-5Zr, and 16Y-16Ta-68Zr were synthesized and sintered in air for 24h at 1250°, 100h at 1500°C and 100h at 1500°C, respectively. Additionally 11Y-8Ta-81Zr heat-treated at 1250° C for 400h was used to identify monoclinic peaks in the Raman spectra. Further details of the characterization methods are provided in Chapter 3.

6.3 Results

X-ray diffraction (XRD) and transmission electron microscopy with energy dispersive spectroscopy (TEM-EDS) results are summarized in Table 6.2 and Table 6.3. Each reported equilibrium composition is the average of TEM/EDS measurements obtained from at least 4 grains of each phase. The revised isothermal sections at 1500°C and 1250°C, which incorporate the results of the 21 compositions investigated, are shown in Figure 6.2(b), and Figure 6.3(b), respectively. The $C_0(t/m)$ line is depicted based on reference [16Van]. Dashed lines indicate three phase regions that are predicted based on previous studies but were not conclusively determined by this study. The proposed isothermal sections differ from the preliminary phase diagrams. The main differences are described in the remainder of this section, first focusing on the equilibria at 1500°C followed by the 1250°C isothermal section. With the exception of *P*, all phases have some solid solubility; however, they will be identified for simplicity by the shorthand notation in Table 6.1.

6.3.1 Ternary equilibria at 1500°C

6.3.1.1 Tetragonal ZrO_2 solid-solution-$YTaO_4$ quasi-binary

TEM/EDS results for samples 10, 11, 12 and 17 in the ZrO_2-rich region of the phase diagram identified the position of the phase boundaries for the solid solution fluorite (*F*), tetragonal zirconia (*t*), tetragonal yttrium tantalate (*T*), and orthorhombic tantalum zirconate (*O*), denoted in Figure 6.4(a). Nominal bulk compositions are denoted with filled-in symbols and the corresponding measured equilibrium compositions, shown in Table 6.2, are denoted with unfilled symbols of the same shape. The maximum ZrO_2 solubility in the YT phase was ~21.5mole%. BF-TEM of Sample 17, Figure 6.4 (b), shows *t* (light contrast) and *M*, which has a twinned microstructure with a well-developed array of twin domains of relatively uniform width, (c). The latter is consistent with the displacive transformation of the high temperature tetragonal (*T*) equilibrium form of YT at 1500°C [83Bri, 59Kom, 14Shi], to the monoclinic form (*M*) upon cooling.

The *t* phase field extends to ~18.5 mole% $YO_{1.5}$ + 18.5 mole% $TaO_{2.5}$. SAED patterns along the $[101]_t$ and $[100]_t$ zone axes, Figure 6.4 (d) and (e), respectively, confirm that *t* remains tetragonal within Sample 17. No monoclinic (*m*) ZrO_2 is observed in Samples 10, 11, 12, and 17, in agreement with [91Kim].

Raman spectroscopy was used to examine the stability of the *t* phase in the ZrO_2-rich region of the phase diagram owing to its high sensitivity to the *m*-ZrO_2 phase. Comparison with the reference Raman spectra of *M*-YT and in Figure 6.5 reveals that Samples 11 and 17 contain peaks corresponding to these two phases. Samples 10 and 12 contain additional peaks that are ascribed to the *O*-$Ta_2Zr_6O_{17}$ phase. The doublets at ~180cm^{-1} and ~650cm^{-1} characteristic of *m* are not observed in any of the ZrO_2-rich samples after equilibration at 1500°C, which agrees with the XRD results (not shown).

6.3.1.2 $YO_{1.5}$-rich compositions

An especially notable finding of this study is that the fluorite solid solution phase field extends to the $YO_{1.5}$-$TaO_{2.5}$ binary at 1500°C, as shown in Figure 6.2(b). The fluorite (*F*) boundaries are outlined based on TEM/EDS data collected from Samples 1, 2, 3, 4, 14, and 20 shown in Figure 6.6, Sample 11 in Figure 6.4, as well as information from the ZrO_2-$YO_{1.5}$ binary [04Fab]. The locations of Samples 18, 19, 20 and 21 are more clearly shown in the inset in Figure 6.6. Samples 2 and 20, depicted by the filled-in pentagon and diamond, respectively, in Figure 6.6, were expected to lie in two- or three-phase fields based on the phase equilibria suggested by previous work [91Kim, 91Yok]. However TEM/EDS of both samples, depicted with unfilled symbols, revealed that all grains measured had the same compositions as the nominal bulk, consistent with their location within a single-phase field. BSE images support these conclusions, as both samples do not exhibit significant Z contrast in the areas examined.

The extension of the fluorite field is corroborated by the TEM/EDS results from Samples 1, 4 and 14. Since Sample 1 is mostly *F* and the *C*-$YO_{1.5}$ grains were very small (~100nm), it was not possible to ascertain that there was only one yttria-rich grain through the thickness during TEM/EDS measurements. Therefore the TEM/EDS results for $YO_{1.5}$ in Sample 1 may be artificially high in ZrO_2 and $TaO_{2.5}$. The $YO_{1.5}$ phase boundary shown in the revised isothermal section is therefore based on the binary limits reported in the literature [05Fab, 79Vas].

As described in Chapter 5, Sample 13 (85Y15Ta) contains fluorite and *C* at 1500°C. Although the exact solubility range of *F* in the $YO_{1.5}$-$TaO_{2.5}$ binary is not known, it is suggested here to be in the range ~78-80 mole % $YO_{1.5}$, pending confirmation. The difference is not critical for the purposes of this work.

Figure 6.7(a) shows the main peaks in the XRD patterns of Samples 2, 15, 19, and 20 are all consistent with the fluorite crystal structure, albeit with slight peak shifts owing to changes in composition. Small reflections, identified with triangles, are observed in Samples 19 and 20 indicating a reduction in symmetry; however, the main *F* peaks are not split, suggesting the expected long-range orthorhombic symmetry has not been achieved. The main fluorite XRD peaks in Sample 21 are split, Figure 6.7(a), and match the peaks of *W*, space group *Ccmm* [09Fu], as noted in Chapter 5. Similarly, the main fluorite XRD peaks in sample 18 are also split and can be indexed based on the *o*-Y_7T_3 crystal structure (*Cmmm*) proposed by Rossell et al. [79Ros2].

There are significant differences in the Raman spectra, Figure 6.7(b), of samples near the $YO_{1.5}$-$TaO_{1.5}$ binary (Samples 18-21) compared to single-phase fluorite samples with higher Zr contents, e.g. Samples 2. Samples 18-21 have more Raman-active modes than Sample 2. Significant peak broadening occurs as ZrO_2 is added to Y_3TaO_7, (Samples 21, 19, 20, in order of increasing ZrO_2). There are only slight differences in the Raman spectra of Samples 18 and 21, as discussed in Chapter 5.

To probe more of the local structure, selected area electron diffraction (SAED) was performed on Samples 14, on the $YO_{1.5}$-$TaO_{2.5}$ binary, and Sample 20, in the ternary, Figure 6.8. SAED patterns from Sample 20 along the $[1\bar{1}0]_F$ and $[11\bar{2}]_F$ zone axes of fluorite, Figures 6(a) and (b), respectively, contain split spots and diffuse scattering. The main reflections correspond to the fluorite lattice. A pair of diffuse spots (split spots) occurs on both sides of the ½ ½ ½ reciprocal lattice point in the $[11\bar{2}]_F$ direction for the $[1\bar{1}0]$ pattern and in the $[1\bar{1}0]_F$ direction for the $[11\bar{2}]_F$ pattern. There is a diffuse-ring contour at the $^3/_2$ ½ ½ reciprocal lattice point in the $[11\bar{2}]_F$ pattern. The distance *D* (~0.45 nm^{-1}) between the split spots is the same as the diameter of the diffuse circles.

The SAED pattern in Figure 6.8 (c) could be indexed as the [116] zone axis of the *o*-Y_7T_3 (*Cmmm*) structure or the [113] zone axis of the *W* (*Ccmm*) structure since the two structures cannot be distinguished at that incidence. However the SAED pattern in Figure 6.8(d) can only be indexed by the $[\bar{1}10]$ zone axis of the *Cmmm* structure. Therefore the *Cmmm* phase reported by [79Ros2] is present on the $YO_{1.5}$-$TaO_{2.5}$ binary at 70mole% $YO_{1.5}$ after heating at 1500°C. The SAED pattern in Figure 6.8(e) contains two domains of the *Cmmm* structure on a $[1\bar{2}0]$ zone axis.

While the orthorhombic crystal structures may be present in the vicinity of Y_3T on the $YO_{1.5}$-$TaO_{2.5}$ binary, long-range orthorhombic symmetry is not observed when ZrO_2 is added. A bright field image of Sample 4, which contains 5 mole% ZrO_2, shows the presence of twinned *M*-YT and a second phase that is not twinned, Figure 6.9(a). TEM-EDX (Table 6.2) indicates the latter phase contains 61mole%$YO_{1.5}$, 27mole% $TaO_{2.5}$ and 12mole% ZrO_2. SAED patterns along the $[111]_F$ (b) and $[112]_F$ zone axes do not show the superlattice reflections that were observed in the orthorhombic phase in Sample 14, which did not contain ZrO_2. Therefore, the second phase in Sample 4 is fluorite, as indicated in Figure 6.6.

6.3.1.3 $TaO_{2.5}$-rich compositions

Both *P*-YT_3 and *h*-YT_7 are observed by TEM-EDS (Figure 6.10) along the $YO_{1.5}$-$TaO_{2.5}$ binary at 1500°C, as shown in Chapter 5. While *P*-YT_3 does not appear to have any detectable binary or ternary solubility at this temperature, ~8mole% ZrO_2 is soluble in *h*-YT_7 along a line of approximately constant Y. The hexagonal structure of *h*-YT_7 was confirmed by selected area diffraction patterns along the $[310]_h$ and $[210]_h$ zone axes, Figure 6.10(b) and (c), respectively. XRD in Figure 6.11(a) confirms that Sample 7 contains *O*, *h*-YT_7, and $TaO_{2.5}$ [90Sch, 71Ste, 68Tru, 68War], which have dark, medium and light contrast, respectively in the BSE image in Figure 6.11 (b). Long high-aspect ratio grains are observed for the O and *h*-YT_7 phases in Sample 7. Peaks from both the low (β) and high (α)

forms of $TaO_{2.5}$ are observed via XRD. Since these samples were furnace cooled over ~2 hours it is likely that $TaO_{2.5}$ partially transformed to the low temperature structure on cooling [07Bre, 07Liu].

XRD in Figure 6.11(a) indicates that only *M*-YT and *P*-YT_3, identified according to [68Tru, 08Zho] are present in Sample 6. This agrees with the 2-phase microstructure observed via BSE in Figure 6.11(c). Closer inspection with BF-TEM indicates striations suggestive of transformation twins that are likely a result of the 1st order transformation from *Cmmm* to *Pmma* that occurred on cooling [08Zho].

6.3.2 Ternary equilibria at 1250°C

6.3.2.1 Tetragonal ZrO_2 solid-solution-$YTaO_4$ quasi-binary

The TEM/EDS results for samples 11, 12, 16, and 17, Figure 6.12(a), indicate the position of the phase boundaries for the solid solution *F*, *t*, monoclinic yttrium tantalate (*M'*) and *O*. It is implicit that the phases are solid solutions however they will be referred to as *t*, *M'* and *O* for simplicity. Unlike at 1500°C, the maximum solubility of the *t* phase field differs depending on whether the bulk composition has more $YO_{1.5}$ or $TaO_{2.5}$, Figure 6.12(b). For example, *t* in Samples 11 or 16 contains ~15.4 mole% $YO_{1.5}$ and ~14.9 mole% $TaO_{2.5}$ while *t* only contains ~12.5 mole% $YO_{1.5}$ and ~12.6 mole% $TaO_{2.5}$ in Samples 12 and 17. The differences in solubility are larger than the standard deviation and experimental error (<1 mole%) in the EDS measurement.

Three phases are present in Sample 12 based on the contrast in the backscattered electron (BSE) image, Figure 6.12(d): *M'* (lightest contrast), *O* (medium contrast) and *t* (darker contrast). Some striations are observed in the *t* grains suggesting they have transformed to monoclinic (*m*) ZrO_2 on cooling. Black areas are pores. Excluding the pores, only two contrast levels are observed in Sample 11, Figure 6.12(e). Again the lightest contrast is *M'*.

Since the average atomic mass of the *F* and *t* phases is nearly the same, there is not a significant difference in contrast observed in BSE. One of the challenges of studying the ZYTO system at 1250°C is the minimal grain coarsening, which results in small grain sizes (<1μm) especially in multi-phase compositions such as Samples 12 and 11 in Figure 6.12(d) and (e), respectively. This hinders the microchemistry analysis by SEM/EDS or microprobe, and the residual porosity makes it difficult to extract suitable FIB specimens.

Based on the Raman spectroscopy, Figure 6.13, and XRD, Figure 6.14, *M'* is the equilibrium phase at 1250°C [83Bri]. *M* was not observed in any sample at 1250°C [73Bla, 14Shi]. Similar to the *t* phase, the *M'* phase exhibits different maximum solubility depending on the location of the bulk sample composition. TEM-EDS results from Sample 11 indicate ~18 mole% ZrO_2 is soluble in YT at 1250°C while the equilibrium YT in Samples 12 and 17 contains ~10 mole% ZrO_2, Figure 6.12(c).

Doublets associated with monoclinic-ZrO_2 (*m*) are observed at 182cm^{-1} and 191 cm^{-1} and near 650cm^{-1}, Figure 6.13, in Samples 12 and 17 [10She]. Additional peaks in the spectra of Samples 12 and 17 that are not attributed to *M'* or to *m* are attributed to *O*, as was observed at 1500°C. The presence of *m* in Sample 17 is also evident in the XRD pattern, Figure 6.14. All peaks in the Raman spectrum of Sample 16 are attributed to *t* while the spectrum of Sample 11 contains only *t* and *M'* peaks, in agreement with the XRD patterns in Figure 6.14 [83Bri, 10She, 15Van]. The presence of *m* was also confirmed using bright field (BF)-TEM, Figure 6.15(b) and (c). The transformation from *t* to *m* on cooling results in transformation twins, which are observed in Samples 17 and 12, Figure 6.15(b) and (c) respectively. Monoclinic ZrO_2 grains are notably absent from Sample 16, Figure 6.15(a). $YTaO_4$ grains in all samples do not contain the transformation twins that were observed via BF-TEM in *M*-$YTaO_4$ after heat treatments at 1500°C.

6.3.2.2 $YO_{1.5}$-rich compositions

Equilibrium compositions for Samples 3, 4 and 14 were measured by TEM-EDS and used to determine the phase boundaries in the $YO_{1.5}$-rich region, Figure 6.16. A selected area electron diffraction (SAED) pattern from one of the phases in Sample 4 can be indexed as the [100] zone axis of the fluorite structure, confirming the fluorite field extends to at least 12 mole% ZrO_2, Figure 6.17(a). XRD patterns from samples near Y_3TaO_7, Figure 6.17(b) suggest that Samples 18-21 do not contain an orthorhombic phase and instead match with the peaks of the fluorite phase.

TEM investigations on more samples in the $YO_{1.5}$-rich region were hampered by the very slow densification and slow grain coarsening of most $YO_{1.5}$-rich compositions, which hindered the extraction of suitable lamellae using the focused ion beam (FIB). For example, even after 800h at 1250°C small grains (<100nm) and extensive porosity (black contrast) persisted in Sample 1, Figure 6.18(a). The grain size and lower porosity were adequate to prepare lamellae from Samples 3 and 14, which are further from the pure $YO_{1.5}$ corner. Small (~500nm) grains of *F* and *M'*, which have grey and light contrast, respectively, are present in Sample 3, Figure 6.18(b). Larger (~1μm) grains of *M'* (lighter contrast) and *o*-Y_7T_3 are present in Sample 14, Figure 6.18(c).

The Raman spectra of Samples 2, 4, and 18-21, Figure 6.19, reveal that *M'* is present in Sample 4 and Samples 18-21 have more Raman-active modes than Sample 2, which is single-phase *F*. Peak broadening is observed as ZrO_2 is added to Y_3TaO_7, (Samples 19-21). Raman spectra from Samples 18 and 21, *Cmmm* and *Ccmm*, respectively, are only slightly different, suggesting the two orthorhombic structures are very similar, as discussed in Chapter 5.

6.3.2.3 $TaO_{2.5}$-rich compositions

At 1250°C, both YTa_7O_{19} (*h*) and YTa_3O_9 (*P*) are stable between *M'* and $TaO_{2.5}$. While *P* was not present in any of the samples investigated in this study, it has been observed via electron probe microanalysis and XRD at 1250°C as described in Chapter 5. Similar to *P* at 1500°C, it is expected that *P* at 1250°C would not have any binary or ternary solubility. TEM-EDS results from Samples 6 and 7, Figure 6.20(a), indicate that *h* is present and has a maximum ZrO_2 solubility of at least ~5.5 mole%. The binary solubility of *h* is depicted based on the results of Chapter 5. High aspect-ratio grains, which are characteristic of *h* are observed with the lightest contrast in the BSE images of Samples 6 and 7, Figure 6.20(b) and (c) respectively.

By comparing the XRD patterns of Sample 6 after heat treatments at 1250 and 1500°C, it is clear that for that composition, *M'* and *P* are not the equilibrium phases at 1500°C, Figure 6.21. In agreement with the literature, the crystal structure of pure $TaO_{2.5}$ changes between 1250°C and 1500°C, Figure 6.22. During cooling, α-$TaO_{2.5}$ undergoes two unquenchable, reversible phase transitions: from α to orthorhombic to triclinic [07Bre]. The asterisks in Figure 6.22 indicate peaks associated with the triclinic phase [68War] (PDF 01-075-9704). Similarly, β-$TaO_{2.5}$ also undergoes phase transitions on cooling. The triangles indicate the orthorhombic (*Pmm2E*, PDF 00-025-0922) structure [71Ste2].

6.4 Discussion

There are significant differences between the tentative and experimentally determined isothermal sections at 1250°C and 1500°C. There are several salient findings that merit detailed discussion beginning with the *t*-ZrO_2-$YTaO_4$ quasibinary followed by the similarities between the structures in the $YO_{1.5}$-rich portion of the ternary. Finally, the phase

equilibria of the $TaO_{2.5}$-rich compositions are discussed in the context of the crystal structures.

6.4.1 ZrO_2-$YTaO_4$ quasibinary at 1500°C

Both compounds in the quasi-binary exhibit a large homogeneity range at 1500°C. The shape and extent of the *t* field agrees with earlier experimental studies [91Kim, 06Pit, 07Pit]; however, there is a discrepancy with the recent thermodynamic assessment [11Bha]. The *t* field in the computed diagram curves toward the $YO_{1.5}$-rich corner of the phase diagram, at variance with the experimental findings. The shape of the *t* field in Figure 6.2 and Figure 6.4 results from the nature of cation substitution and is consistent with the model of tetragonal ZrO_2 stabilization by charge compensating dopants [94Li3].

The presence of tetragonal ZrO_2 in the SAED patterns, Figure 6.4(d) and (e), and in the Raman spectra, Figure 6.5, and the notable absence of monoclinic ZrO_2 indicate that compositions near the tip of the *t* region are non-transformable. All *t* grains observed in BF-TEM, e.g. Figure 6.4 (b), do not have twins, which are associated with the transformation to monoclinic ZrO_2. The stability of tetragonal ZrO_2 near the tip of the *t* field had been observed previously [91Kim, 07Pit, 01Rag, 16Van]. Again, the tetragonal phase in equilibrium with fluorite within the hashed region of the 2-phase, $t + F$ field in Figure 6.4(a), does not transform to monoclinic, as observed at 1250°C and in [91Kim, 07Pit, 01Rag, 16Van]. Given the difficulty associated with depositing coatings in the relatively small compositional space of the *t* phase field, the two-phase, $t + F$ region offers a more realistic opportunity for phase stable TBCs in the ZYTO system. There are, however, implications for the toughness, which will be discussed in Chapter 7.

The shape of the YT phase field and its notable lack of a solubility range within the $YO_{1.5}$-$TaO_{2.5}$ binary, suggest that pairs of Zr^{4+} are substituting for both Y^{3+} and Ta^{5+} in the *T*-YT

crystal structure, as has been proposed elsewhere [14Shi]. Such substitution is arguably consistent with the similarity between the ionic radius of Zr^{4+} (0.084 nm) and the average radius (0.88 nm) of Y^{3+} (0.102nm) and Ta^{5+} (0.074) [76Sha]. This nearly 5% difference, however, does induce some lattice distortion that is evident when comparing the Raman peaks of Samples 10, 11, and 17, which contain $YTaO_4$ + 21.5% ZrO_2, to the Raman peaks of $YTaO_4$ + 10% ZrO_2, Figure 6.5. The peak broadening observed indicates an increased disorder of the local structure as ZrO_2-content is increased [14Shi].

The low temperature *M'*-$YTaO_4$ structure observed at 1250°C, which has been characterized by [83Bri] was expectedly not observed at 1500°C. Although *T*-YT is expected to be the equilibrium phase at 1500°C, only *M*-YT is observed. The Raman peaks observed most clearly in Samples 11 and 17 (Figure 6.5) match those of *M*-YT reported by [14Fen, 14Shi].

There are several implications of the phase equilibria results reported in the quasibinary region at 1500°C. With the exception of the terminal oxides, the quasibinary is the only region in the isothermal section that nominally does not contain oxygen vacancies. The lack of oxygen vacancies along the ZrO_2-$YTaO_4$ quasibinary may result in slower diffusion and thus reduced coarsening of compositions in that region. Perhaps more importantly, the lack of oxygen vacancies results in an increase of the c/a axial ratio (tetragonality) with increasing $YO_{1.5}$ and $TaO_{2.5}$ [91Kim, 94Li3, 07Pit] with potential effects on the toughness, as discussed in Chapter 7.

The ZrO_2 solubility in $YTaO_4$ also has important implications for its use as a possible TBC. The $T \rightarrow M$ transformation temperature is highly dependent on the ZrO_2 concentration [14Shi]. Pure YT is reported to transform at 1426 ±7°C while $Y_{0.9}Ta_{0.9}Zr_{0.2}O_4$ transforms at 821±47°C [14Shi]. Extrapolating from this trend, YT with 21.5mole% ZrO_2, which is the maximum solubility measured at 1500°C, would transform at ~792°C. The equilibrium $YTaO_4$ in any composition within the F + *t* + YT or O + *t* + YT_3-phase fields or the *t* + YT

quasibinary would contain 21.5mole% ZrO_2 and would thus be tetragonal at turbine operating temperatures. Thus the ferroelastic transformation from *T*- to *M*-YT would not be a relevant toughening mechanism for those compositions at high temperature, at variance with the suggestion in [14Shi]. However, *T*-YT may be able to experience ferroelastic switching at high temperatures, and if retained within a tetragonal or cubic matrix upon cooling it could enable transformation toughening at lower temperatures.

Unlike compositions in the *F* + *t*-Z + YT or *O* + *t*-Z + YT_3-phase fields or the *t*-Z + YT quasibinary, compositions within the F + YT_3-phase field contain YT with less ZrO_2, (see Samples 3 and 4 in Figure 6.6 and Table 6.2). Compositions in the F + YT 2-phase region would therefore have higher $T \rightarrow M$ transformation temperatures. In these compositions, the ferroelastic *T*-→*M*-YT transformation may be a viable toughening mechanism at engine relevant temperatures.

6.4.2 ZrO_2-$YTaO_4$ quasibinary at 1250°C

There is a region in the *t* + *F* phase field at 1250°C, indicated by grey dashes in Figure 6.12, in which *t* is non-transformable, which has important implications for mechanical properties and potential ZYTO-based TBCs. Raman spectroscopy, XRD and BF-TEM images indicate that the *t* phase in Sample 16 does not transform to *m* on cooling. This is in agreement with Pitek's conclusions at 1500°C [06Pit, 07Pit] [06Pit, 07Pit] and Raghavan's at 1400°C [01Rag]. Additionally, the tetragonal phase within the three phase region, *t* + *F* + *M'*, also appears to be non-transformable, as *m* is not detected in Sample 11 via Raman (Figure 6.13), XRD (Figure 6.14), or in BF images (not shown). Non-transformability of the *t* phase in this region after 600h at 1250°C was initially alluded to in [11Bha2]. Combined with the non-transformable region in the *t* + *F* phase field, this conclusion opens a large compositional space at 1250°C in which the *t* phase does not transform to *m*. This conclusion is promising

for the ZYTO system since most current turbine engines rely on *t*-ZrO_2 based ceramics for TBCs due to their superior toughness, and 1250°C is a more realistic surface temperature than 1400°C or 1500°C.

While compositions in the entire *t* + *F* + *M'* region and part of the *T* + *F* region do not transform to *m* on cooling, compositions within the ZrO_2-$YTaO_4$ quasibinary at 1250°C do transform, as indicated by the presence of *m* in the XRD, Raman and BF-TEM images of Sample 17. This is in agreement with [11Bha2], who determined that 16Y-16Ta, which is located in the ZrO_2-$YTaO_4$ quasibinary at 1250°C, transformed to monoclinic on cooling.

Possible stabilization mechanisms can be deduced based on the shape of the *t* and *M'* phase fields. Unlike many of the other crystal structures in the ZYTO system, the *t* and *M'* phases lack oxygen vacancies. Both extend into the ternary, while maintaining constant and nominally null oxygen vacancy concentrations. Therefore the stabilization mechanisms of each phase are related to the ordering of the charge-compensating cations. At the maximum ternary solubility of each phase, it is clear that more $YO_{1.5}$ than $TaO_{2.5}$ is soluble in *t* and excess ZrO_2 is stable in slightly $YO_{1.5}$-rich *M'*, as seen in Figure 6.12(c) and (b). The shapes of both phase fields provide insight into the stabilization mechanisms for each crystal structure.

Excess $YO_{1.5}$ is likely stable in *t* because it introduces oxygen vacancies, which are known to stabilize the tetragonal phase in YSZ [02Fab, 94Li1]. The synergistic combination of the increased distortion from the smaller Ta^{5+} cation and the lattice dilation from the oversized Y^{3+} stabilizes much of the *t* field. However near the maximum ternary solubility of the phase, the presence of oxygen vacancies due to excess $YO_{1.5}$ also likely contributes to the stabilization of the *t* phase. The *t* phase field shape has been suggested before by [11Bha, 11Bha2]. The location of the non-transformable region on the $YO_{1.5}$-rich side of the *t* field,

and its noted absence on the $TaO_{2.5}$-rich side, is further evidence of the importance of oxygen vacancies in stabilizing *t* near its maximum solubility at 1250°C.

The explanation for the shape of the tip of the *M'* field is less clear. Up to ~10mole% ZrO_2 in $YTaO_4$ at 1250°C, two Zr^{4+} cations substitute for a Y^{3+} and a Ta^{5+} cation, as suggested by [14Fen, 14Shi]. Beyond 10 mole% ZrO_2, the rationale for additional Zr^{4+} substituting for Ta^{5+}, which is octahedrally coordinated in M', is not clear.

The fact that YT is only present as *M'* at 1250°C for all zirconia contents indicates that, the temperature at which *M'* transforms to *T* is above 1250°C, regardless of ZrO_2 content. Raman spectroscopy, XRD and BF-TEM images indicate that YT is present as M' when it contains 5.5 mole% ZrO_2 (Sample 6) as well as when it contains 10 mole% ZrO_2 (Samples 12 and 17) at 1250°C. Therefore the transformation from M' to T-YT occurs above 1250°C for those compositions, in agreement with Chapter 5. Precluding vapor or liquid phase deposition which may bypass the *M'* phase entirely, it is expected that YT remains *M'* until above at least 1350°C (Chapter 5), regardless of ZrO_2 content [83Bri, 14Shi].

6.4.3 $YO_{1.5}$-rich compositions at 1500°C

In agreement with XRD results from Sample 13 (85Y15Ta) in Chapter 5, the fluorite phase is present at 1500°C along the $YO_{1.5}$-$TaO_{2.5}$ binary. The prominence of the fluorite peaks in the XRD of Samples 2, 19 and 20, Figure 6.7(a), suggest the average structure of those compositions is fluorite. Similar extension of the fluorite field has been observed by XRD in the ZrO_2-$YO_{1.5}$-$NbO_{2.5}$ (ZYNO) system [98Fag, 97Irv]. Given the chemical similarities between $TaO_{2.5}$ and $NbO_{2.5}$ it is not surprising that the fluorite region also covers a large compositional space in the ZYTO system. In both systems, the fluorite field extends from F-$Zr_xY_yO_z$ toward Y_3MO_7 (M=Ta or Nb).

In RE_3TaO_7 compounds (RE=rare earth), the fluorite phase is stabilized at high temperatures or by smaller RE cations. A combination of these factors as well as similarities in crystal structure support the extension of the fluorite field. At temperatures above 1600°C Y_3TaO_7 is reported to either have a defect fluorite (*F*) structure or phase separate into *F* and Y_7T_3 [79All, 09Fu, 64Roo, 79Ros2, 91Yok, 87Yok]. It is worth noting that *F*-Y_3TaO_7 and *F*-$Y_2Zr_2O_7$ have similar defect structures and both contain 12.5% vacant anion sites. By progressively replacing pairs of Zr^{4+} in *F*-$Y_2Zr_2O_7$ with Y^{3+} + Ta^{5+} pairs, the concentration of oxygen vacancies remains constant, eventually resulting in Y_3TaO_7. Fluorite RE_3TaO_7 can also be obtained by decreasing the size of the RE cation, as was demonstrated by [04Wak] at 1400-1600°C (RE=Ho, Er, Tm, Yb, Lu). By introducing Zr^{4+}, the increased disorder favors the fluorite structure. It is unclear where Zr^{4+} would substitute in the Y_3TaO_7 structure. If it substitutes on the YI or YII sites it would reduce the average radii of the RE cations [76Sha], favoring the fluorite structure. If Zr^{4+} substitutes on the octahedrally coordinated Ta^{5+}-site, oxygen vacancies would need to be introduced to maintain charge neutrality. Based on the known structure of *o* and *W*, those oxygen vacancies would likely occupy the OIII site connecting the TaO_6 octahedra [07Yas, 79Ros]. Similar to the effect of adding additional Y^{3+} to Y_3TaO_7, the TaO_6 chains would therefore no longer be continuous, favoring the fluorite structure. The increase in local disorder caused by even modest Zr-substitution is evidenced by the broadening of the Raman peaks when comparing the additions of 1 and 5 mole% ZrO_2 (Samples 19 and 20) to Y_3TaO_7 (Sample 21) in Figure 6.7(b), as well as in the identification of the ZrO_2 containing samples as fluorite in XRD, Figure 5(a, b). Perhaps more convincingly, the fact that Zr-substitution favors the fluorite structure could explain why SAED patterns (Figure 6.9, (b), (c)) show fluorite with a composition of 61mole%$YO_{1.5}$, 27mole% $TaO_{2.5}$ and 12mole% ZrO_2 is present in Sample 4.

It is clear that both orthorhombic structures, *Ccmm* and *Cmmm,* are likely present on the $YO_{1.5}$-$TaO_{2.5}$ binary and the fluorite field extends to near the binary. However it is unknown

if the transition from disordered fluorite near $Y_2Zr_2O_7$ to cation/oxygen-vacancy ordered Y_3TaO_7 occurs continuously. The extension of the fluorite region does not provide a complete picture of the local structure of Samples 19, and 20, as the tiny peaks in the XRD pattern in Figure 6.7(a), peaks in the Raman spectra in Figure 6.7(b) and the additional reflections in the SAED patterns in Figure 6.8(a), (b) cannot be accounted for by the fluorite structure. Work in references [00Irv, 00Gar] suggests that the transition from $Y_2Zr_2O_7$ to Y_3NbO_7 is gradual as composition is varied. They observe short-range ordering of the oxygen vacancies as Y_3NbO_7 is approached. Neutron diffraction has been used to determine that ordered domains are present within a bulk fluorite matrix of Y_3NbO_7 [00Irv] and Yb_3TaO_7 [13Kin] despite both compounds being identified as fluorite by XRD. Therefore some degree of local ordering is likely present in several of the compositions within the fluorite field in the ZYTO system.

To understand if such ordering is present, it is important choose characterization techniques that are complementary to average structure techniques like XRD. Since Raman is sensitive to structural symmetries at smaller length scales than XRD and is also more sensitive to oxygen displacements, the Raman spectra provide additional insights into the local structure. The Raman spectra of Samples 19 and 20 clearly indicate that the anion lattice is not that of fluorite, Figure 6.7(b). It is worth noting that Raman peaks observed in Samples 19, 20 and 21 are similar to those for Y_3NbO_7 [97Yas]. Although the Raman peaks in that study were attributed to the fluorite structure based on XRD results showing fluorite peaks, electron diffraction was not conducted. It is likely, based on subsequent electron diffraction studies of Y_3NbO_7 [00Gar, 13Lop, 97Mii] that microdomains of an ordered phase were present and responsible for the strong Raman signal.

Perhaps the best probe of local structure is electron diffraction. SAED patterns similar to those in Figure 6.8(a) and (b) had previously been observed in Y_3TaO_7 [79All], Y_3NbO_7

[00Gar, 00Irv, 97Mii], other RE_3NbO_7 [13Lop] and even CaO and Tb_4O_7-stabilized zirconias [94Mii]. In each of these studies, the split spots and diffuse rings were attributed to the presence of antiphase domains of an ordered phase in the fluorite matrix. The domains were verified by high resolution (HR) TEM [13Lop].

According to [97Mii] the distance in reciprocal space between the split spots and the diameter of the diffuse rings, *D*, is related to the size of the ordered domains present in the fluorite matrix. For Sample 20, $D = 0.045 Å^{-1}$, similar to what was reported for Y_3NbO_7 [97Mii]. This corresponds to a domain size of ~22 Angstroms. The miniscule size of the domains implies that they formed on cooling. If the domains were present at 1500°C, they would have coarsened to significantly larger sizes. This information combined with knowledge of the Y_3TaO_7 crystal structure indicates that the fluorite structure is the actual equilibrium structure to ~1mole% ZrO_2 of the $YO_{1.5}$-$TaO_{2.5}$ binary.

There are various engineering implications of the $YO_{1.5}$-rich corner of the revised 1500°C isothermal section. The extension of the fluorite phase field to near the $YO_{1.5}$-$TaO_{2.5}$ binary results in a large two-phase region of fluorite and YT. This may have important implications for TBCs. Rare-earth-rich compositions such as $Y_2Zr_2O_7$, which is fluorite, have been shown to mitigate damage caused by molten silicates [14Kra, 13Zal]. Unfortunately, these fluorite-related phases have significantly lower toughness values compared to 7YSZ [06Lec]. It may be possible to improve the toughness of fluorite-based TBCs by adding $YTaO_4$, as discussed in Chapter 7.

The extension of the fluorite region to the $YO_{1.5}$-$TaO_{2.5}$ binary is also relevant to the fields of fuel cells, sensors and other ionic/electronic conductors. The large compositional space of the fluorite field allows the ionic and electrical conductivities to be optimized by tailoring the relative concentrations of Y and Ta [98Fag, 97Irv, 00Irv]. The presence of ordered domains within compositions near Y_3TaO_7 has implications for the fields of photocatalysis

and fuel cells since the local structure (on the same length scale as molecules) influences catalytic efficiency [13Kin] and ordered domains drastically reduce ionic conductivity [98Fag].

6.4.4 $YO_{1.5}$-rich compositions at 1250°C

Similar to what was observed in the $YO_{1.5}$-$TaO_{2.5}$ binary, the ordering kinetics, coarsening and densification in the $YO_{1.5}$-rich portion of the ZYTO ternary at 1250°C are sluggish. All compositions near Y_3TaO_7 are fluorite by XRD (Figure 6.16) after a 1250°C treatment, similar to the results of the $YO_{1.5}$-TaO_5 binary. However the presence of Raman peaks associated with the *Ccmm* and *Cmmm* structures in Samples 18-21 (Figure 6.19) indicates that although the average, bulk structure determined by XRD is fluorite, ordered orthorhombic domains are present. Additionally, compositional effects within the orthorhombic phases are observed in the Raman spectra. Broadening of Raman peaks, which occurs as $TaO_{2.5}$ (Sample 18) or ZrO_2 (Samples 19 and 20) is added to Y_3TaO_7 (Sample 21) at 1250°C, is an indication of increased disorder and is consistent with results at 1500°C. The additional peak (*) in the spectra of Sample 18 as been ascribed to the new Ta-O bonds and bonding environment on the YII sites relative to pure Y_3TaO_7, Figure 6.19 [14Fra].

When cation ordering is required in addition to oxygen vacancy ordering, as is the case for δ, *W*, and *o*, it takes significantly longer for phases to fully order [77Ray]. The difficulty in forming these ordered phases is compounded by the sluggish kinetics at temperatures below 1300°C. The combination of reduced diffusion due to oxygen vacancy and cation ordering and decreased kinetics at 1250°C may result in compositions near Y_3TaO_7 not reaching equilibrium during the 400h heat treatment. In agreement with Chapter 5 it is assumed that the phases proposed by Yokogawa *et al*. are the true equilibrium phases on the $YO_{1.5}$ -$TaO_{2.5}$

binary at 1250°C [91Yok]. It is still unclear if a two-phase field, $W + o$, is present or if the symmetry gradually changes from W to o as Ta^{5+} is added.

Slow diffusion and coarsening in $YO_{1.5}$-rich compositions is advantageous for their potential use as TBCs. The current industry-standard TBC, 7mole% $YO_{1.5}$ stabilized zirconia (7YSZ) suffers from significant sintering during thermal exposures above 1000°C, resulting in an undesirable increase in thermal conductivity and loss of coating compliance [09Tan]. $YO_{1.5}$-rich compositions in the ZYTO system would not only have low thermal conductivity [14Lim], but they could retain that thermal conductivity over longer periods of time due to the reduced densification rate.

6.4.5 $TaO_{2.5}$-rich compositions at 1500°C and 1250°C

There are no significant differences in the types of phases present in the $TaO_{2.5}$-rich region at 1250°C and 1500°C [16Mac]. The maximum ZrO_2 solubility in h is slightly lower at 1250°C (~5.5mole%) compared to at 1500°C (~8mole %) [16Mac]. As described in Chapter 5, the equilibrium structure of $TaO_{2.5}$ is different at 1250°C, in agreement with the $\alpha \rightarrow \beta$ phase transformation temperature of 1360°C [56Rei].

When constructing the preliminary isothermal section, YT_7 was omitted because previous studies at 1500°C [91Kim]and 1600°C [73Bon] showed that only the line compound YT_3 was stable between YT and $TaO_{2.5}$. However, it was shown in Chapter 5 that YT_3 and YT_7 are both stable at 1500°C, in agreement with the $YO_{1.5}$-$TaO_{2.5}$ binary, and both had been reported earlier at lower temperatures, e.g. at $1250 \leq T \leq 1410$°C by [79Vas] and at 1300-1450°C by [76Ros].

Similar to the lack of binary solubility of YT_3 described in Chapter 5, the lack of ternary solubility in the YT_3 phase can be explained by its crystal structure. YT_3 is a cation/vacancy

ordered, A-site deficient orthorhombic perovskite (*Cmmm*) [73Bon, 68Tru, 08Zho]. The cations and cation vacancies are ordered along the [001] direction. This cation/vacancy ordering precludes the possibility of any significant ZrO_2-solubility because substitution of aliovalent Zr^{4+}, which could occur on the Y-site, would require introduction of Y-vacancies, destroying the cation/vacancy ordering of the perovskite crystal structure. If the Zr^{4+} substitution occurred on the Ta^{5+} site, oxygen vacancies would be needed and it is unclear how their presence would change the structure.

On cooling, YT_3 undergoes a transformation from *Cmmm* to *Pmma* at ~525°C [08Zho]. This first-order transformation involves a reorientation of the tilts of the TaO_6 octahedra. Using Glazer notation [72Gla] the tilts change from $a^-b^0c^0$ (*Cmmm*) to $a^-a^-c^0$ (*Pmma*). The twinned microstructure observed in the YT_3 grains in the BF-TEM image (Figure 6.11(d)) is likely a result of this transformation.

The ternary solubility in the YT_7 phase can also be explained by examining the YT_7 crystal structure. As described in Chapter 5, YT_7 has a hexagonal crystal structure ($P\bar{6}c2$) [76Ros] similar to other $LnTa_7O_{19}$ compounds [90Sch]. In this structure, double layers of pentagonal TaO_7 bipyramids are along the c-axis. These double layers are intercalated by single layers of edge-sharing trigonal antiprisms that are alternatively occupied by Y^{3+} and Ta^{5+}. The YT_7 phase field extends roughly along constant $YO_{1.5}$ concentration, implying that the Zr^{4+} cations are substituting on the Ta^{5+} sites. Oxygen vacancies are required to maintain charge neutrality. The YT_7 structure is stable with the number of oxygen vacancies needed to accommodate ~8mole% ZrO_2 or ~2.7% of the oxygen sites.

6.5 Conclusions

Significant differences exist between the revised isothermal sections and those based on previous literature. One important conclusion is that there are regions at 1500°C and 1250°C

in which the tetragonal phase, *t*, does not transform to monoclinic on cooling. Compositions within the *F* + *t*, YT + *t*, and *F* + *t* + YT regions contain non-transformable *t* at 1500°C. Precluding compositions in the YT + *t* quasibinary, non-transformable *t* is also stable in those regions at 1250°C. The ternary solubilities of YTa_3O_9 (YT_3) and YTa_7O_{19} (YT_7) were elucidated for the first time. The ~8mole% ZrO_2 solubility in YT_7 is in contrast to the negligibly ternary or binary solubility in YT_3.

Diffusion and subsequent grain coarsening in compositions in the $YO_{1.5}$-rich portion of the diagram are remarkably slow at 1250°C, likely inhibiting the formation of the true equilibrium phases near Y_3TaO_7. At 1500°C, the fluorite phase field extends to the $YO_{1.5}$-$TaO_{2.5}$ binary at ~78-80mole% $YO_{1.5}$. This results in a large compositional space in which fluorite and $YTaO_4$ are stable. This phase field is promising because YT could improve the toughness of the $YO_{1.5}$-rich *F* phase, which has the potential to effectively mitigate molten silicate attack.

6.6 Tables and Figures

Table 6.1 Phase Identification Reference

Compound	Structure	Group	Abbr.	PDF number
$YO_{1.5}$ (Y)	Bixbyite (cubic)	$Ia\bar{3}$	*C*	00-041-1105
	hexagonal	$P\bar{3}m1$	*H*	
$TaO_{2.5}$	tetragonal	$I4_1/amd$	α	01-075-9704
	orthorhombic	*Pna2*	β	
ZrO_2 (Z)	fluorite (cubic)	$Fm\bar{3}m$	*F*	01-077-2115(6)
	tetragonal	$P4_2/nmc$	*t*	00-043-0308
	baddeleyite (monoclinic)	$P2_1/a$	*m*	00-037-1484
$YTaO_4$ (YT)	scheelite (tetragonal)	$I4_1/a$	*T*	
	met. fergusonite (monoclinic)	*I2*	*M*	00-024-1415
	fergusonite (monoclinic)	P2/a	*M'*	00-024-1425
Y_3TaO_7 (Y_3T)	Weberite (orthorhombic)	*Ccmm*	*W*	
	Fluorite (cubic)	$Fm\bar{3}m$	F_W	00-038-1403
$Y_7Ta_3O_{18}$ (Y_7T_3)	orthorhombic	*Cmmm*	*o*	
YTa_3O_9 (YT_3)	Perovskite (orthorhombic)	*Cmmm*	*P*	01-072-2030
	tetragonal	*P4/mmm*	τ	
YTa_7O_{19} (YT_7)	hexagonal	$P\bar{6}c2$	*h*	00-030-1465
$Ta_2Zr_6O_{17}$	orthorhombic	*Ima*2c	*O*	00-042-0060
$Y_4Zr_3O_{12}$	rhombohedral	$R\bar{3}$	δ	

Table 6.2 Sample compositions used to determine the ternary 1500° C isothermal section

Sample #	Nominal Composition (cat. %)	Anneal time (h)	Constitution[a]	Composition[b] (cat. %)		
				Phase	Y	Ta
1	75Y-10Ta-15Zr	100	*F*, *C*	*F*	71.9±0.5	12.0±0.5
				C	90.4±4	2.1±2
2	60Y-15Ta-25Zr	100	*F*	*F*	59.2±0.5	16±0.5
3	50Y-25Ta-25Zr	100	*F*, T	*F*	50.9±0.5	20.0±0.5
				T	47.8±1	47.7±1
4	55Y-40Ta-5Zr	100	*F*, *T*	*F*	60.6±1	26.7±1
				T	48.5±0.5	49.7±0.5
5	37Y-41Ta-22Zr	24+76	*O, T*, *h*	*O*	3.3±0.5	30.1±1
				T	39.9±0.5	41.9±1
				h	15.9±1	75.6±1
6	40Y-55Ta-5Zr	100	*T, P*	*T*	45 ±1	47.8±1
				T	24.7±1.2	73.9±1
7	10Y-70Ta-20Zr	100	O, α, *h*	*O*	1.7±0.5	32.3±0.5
				α	0.3±0.2	89.4±1
				h	14.2±1	77.7±0.5
8	40Y-33Ta-27Zr	24+76	*F, T*	-	-	-
9	44.5Y-15Ta-40.5Zr	100	*F*	-	-	-
10	17.5Y-28.5Ta-54Zr	100	*O, t, T*	*O*	2.9±0.5	29.3±0.5
				t	17.9±0.5	18.5±0.5
				T	39±1	39.5±1.5
11	27.5Y-22.5Ta-50Zr	100	*F, t, T*	*F*	29.2±0.5	13.7±0.5
				t	18.5±0.5	18.9±0.5
				T	37.9±0.5	39.6±1
12	13Y-20Ta-67Zr	100	O, *t*	*O*	2.9±0.5	29.4±0.5
				t	17.2±0.5	17.9±0.5
13	85Y-15Ta-0Zr	100	*C, F*			
14	60Y-40Ta-0Zr	100	*T, o*	*o*	69.9±0.5	30±0.5
				T	49.8±1	50.2±1

15	45Y-5Ta-50Zr	24+76	*F*	-	-	-
16	22Y-13Ta-65Zr	100	*t, F*	-	-	-
17	27.5Y-27.5Ta-5Zr	100	*t, T*	*t*	18.3±0.4	19.9±0.4
				T	38.0±0.4	41.1±0.5
18	72Y-28Ta-0Zr	100	*o*	*o*	72.1±0.4	27.8±0.4
19	74.5Y-24.5Ta-0Zr	100	*W, F*			
20	72.5Y-22.5Ta-0Zr	100	*F*			
21	75Y-25Ta-0Zr	100	*W*			

[a] Phase abbreviations introduced in Table 6.1 are used to report the phases present, as determined by XRD.

[b] Composition measured by TEM-EDS and reported as a cation percent Y and Ta. The reported error represents the standard deviation of at least 4 grains measured for each phase.

Table 6.3 Sample compositions used to determine the ternary 1250° C isothermal section

Sample #	Nominal Composition (cat. %)	Anneal time (h)	Constitution[a]	Composition[b] (cat. %)		
				Phase	Y	Ta
1	75Y-10Ta-15Zr	800	*C, W*		-	-
2	60Y-15Ta-25Zr	100h/1500C+400	*F*	*F*	58.7±0.3	16.3±0.2
3	50Y-25Ta-25Zr	400	*F, M′*	*F*	50.8±0.6	20.1±1
				M′	47.8±1.3	46.2±1.1
4	55Y-40Ta-5Zr	HUP +400	*F, M′*	*F*	61.2±0.8	26.3±0.5
				M′	49.1±1.1	49.2±0.9
5	37Y-41Ta-22Zr	400	*O, t, M′*	-	-	-
6	40Y-55Ta-5Zr	400	*M′, h*	*M′*	47.7±1	46.8±1
				h	14.9±1.1	79.5±2.2
7	10Y-70Ta-20Zr	400	O, *h*	O	2.4±1.2	32.2±0.7
				h	12.7±0.6	85.2±0.6
8	40Y-33Ta-27Zr	400	*F, M′*	-	-	-
9	44.5Y-15Ta-40.5Zr	400	*F*	-	-	-
10	17.5Y-28.5Ta-54Zr	400	*O, t, M′*	-	-	-
11	27.5Y-22.5Ta-50Zr	400	*F, t, M′*	*F*	30.6±0.3	11.1±0.2
				t	14.9±0.6	14.6±0.3
				M′	40.5±1.2	40.9±1.3
12	13Y-20Ta-67Zr	400	*O, m, M′*	*O*	2.8±1.1	26.0±0.4
				m	12.7±0.4	12.7±0.3
				M′	45.3±0.9	44.8±1.1

13	85Y-15Ta-0Zr	400	*C, W*		-	-
14	60Y-40Ta-0Zr	SPS+100h	*o, M′*	*o*	68.6±0.7	31.1±0.6
				M′	49.3±1.8	50.5±1.6
15	45Y-5Ta-50Zr	400	*F*	-	-	-
16	22Y-13Ta-65Zr	400	*t, F*	*t*	15.9±0.5	15.2±0.3
				F	31.1±0.8	11.6±0.4
17	27.5Y-27.5Ta-5Zr	400	*m, M′*	*m*	12.2±0.5	12.5±0.2
				M′	43.9±1.7	45.5±1.6
18	72Y-28Ta-0Zr	400	*o*	-	-	-
19	74.5Y-24.5Ta-1Zr	400	*W +F*	-	-	-
20	72.5Y22.5Ta-5Zr	400	*W +F*	-	-	-
21	75Y25Ta-0Zr	400	*W*	-	-	-

[a] Phase abbreviations introduced in Table 6.1 are used to report the phases present, as determined by XRD.

[b] Composition measured by TEM-EDS and reported as a cation percent Y and Ta. The reported error represents the standard deviation of at least 4 grains measured for each phase.

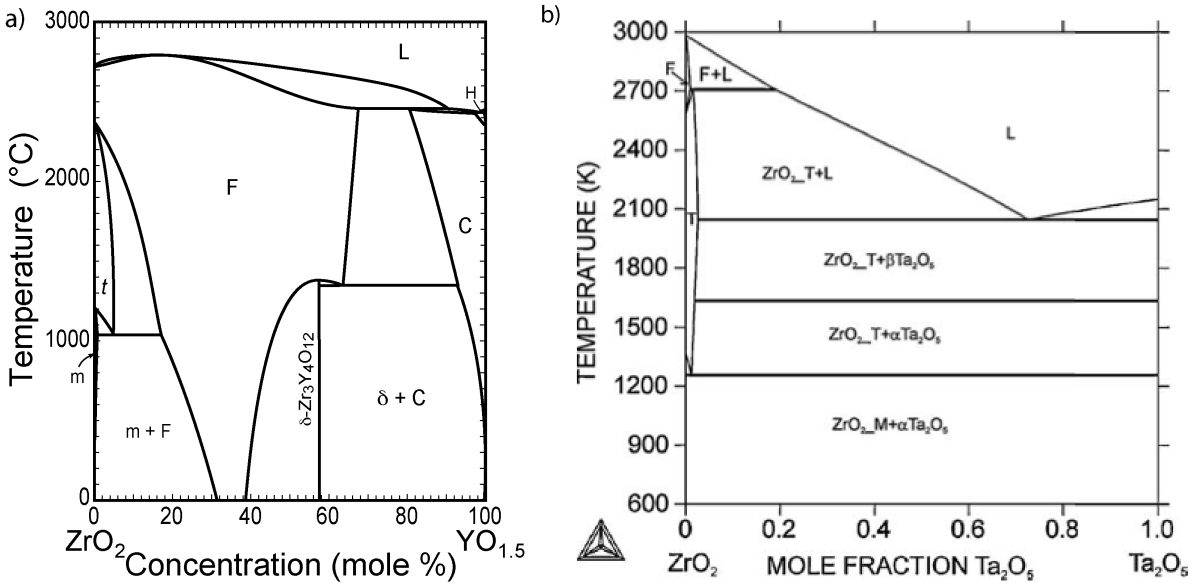

Figure 6.1 Reported ZrO_2-$YO_{1.5}$ (a) [05Fab] and ZrO_2-Ta_2O_5 (b) [11Bha] binary phase diagrams. The ZrO_2-Ta_2O_5 binary, which is calculated, is missing orthorhombic $Ta_2Zr_6O_{17}$, is not based on single cation $TaO_{2.5}$ and the temperature is in Kelvin.

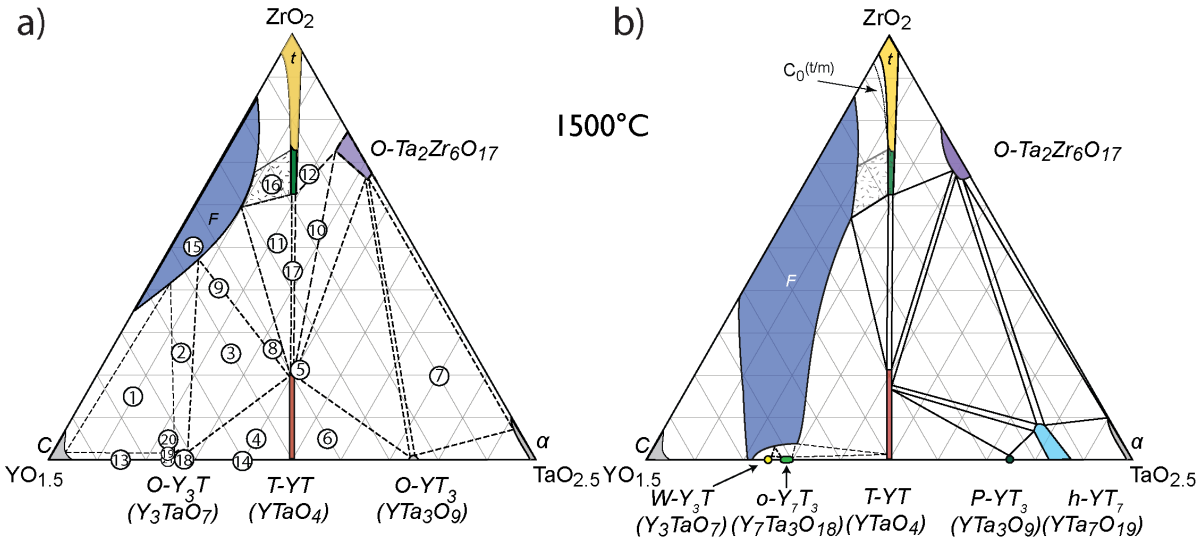

Figure 6.2 (a) The preliminary isothermal section of the ZrO_2-$YO_{1.5}$-$TaO_{2.5}$ (ZYTO) system at 1500°C based on current literature [91Kim, 06Pit, 07Pit, 91Yok]. Sample compositions reported in Table 2 are also indicated in (a). (b) The proposed ternary isothermal section that has resulted from this work.

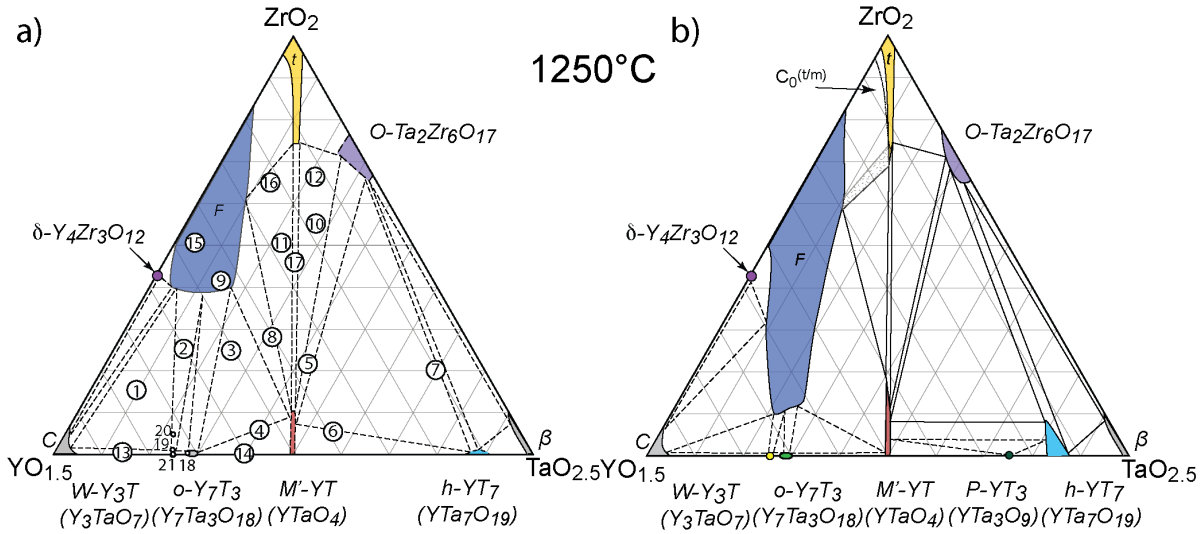

Figure 6.3 (a) The preliminary isothermal section of the ZrO_2-$YO_{1.5}$-$TaO_{2.5}$ (ZYTO) system at 1250°C based on current literature [91Kim, 06Pit, 07Pit, 91Yok]. Sample compositions reported in Table 2 are also indicated in (a). (b) The proposed ternary isothermal section that has resulted from this work.

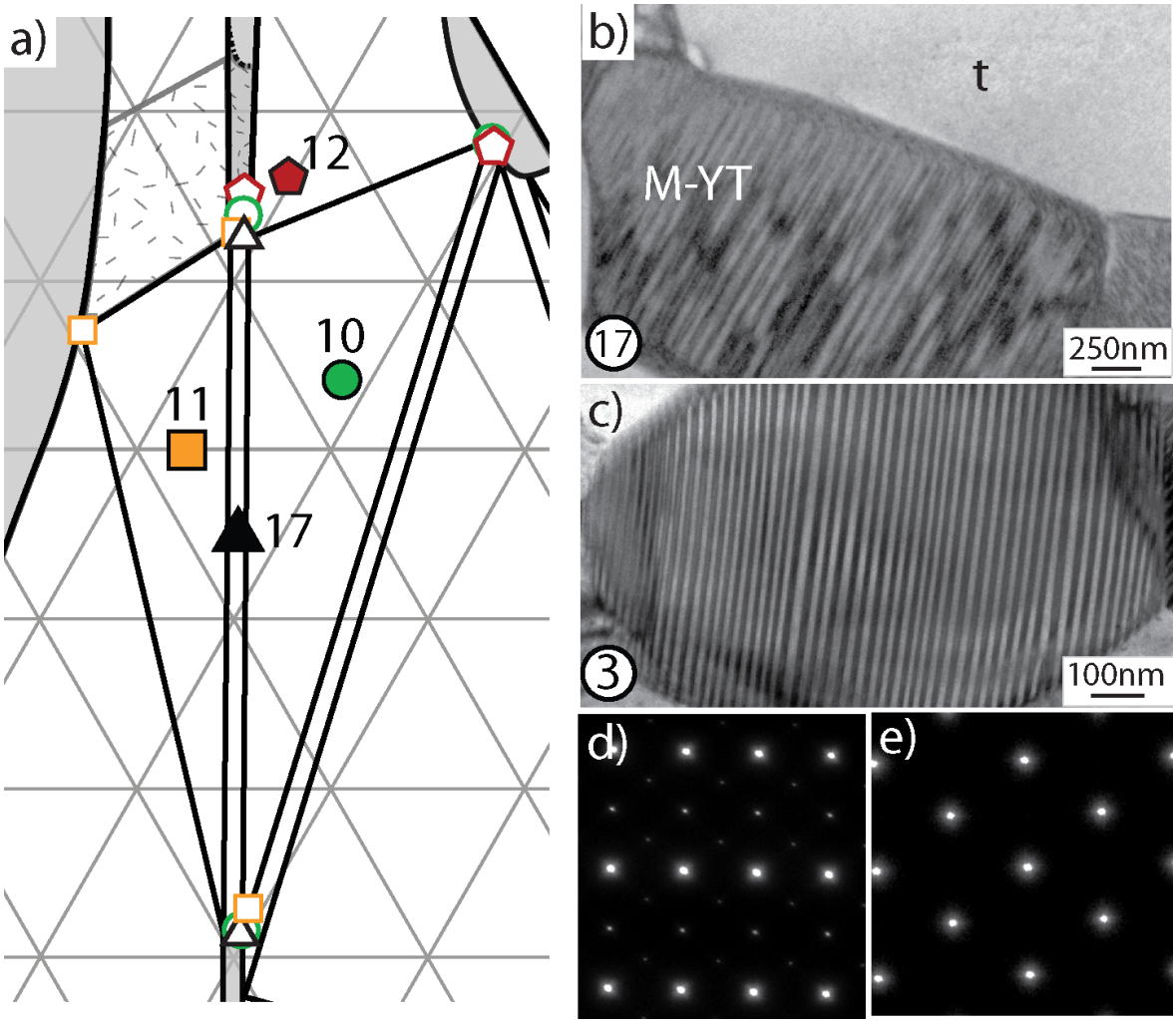

Figure 6.4 (a) TEM/EDS analysis of Samples 10, 11, 12 and 17 indicate the extent of the t-ZrO_2 (*t*) and $YTaO_4$ (YT) phase fields at 1500°C. The TEM-BF image (b) shows the light contrast, *t*- solid solution grains and the twinned microstructure of M-YT. The twins result from the T-YT to M-YT phase transition that occurs on cooling and can be observed more clearly in (c). SAED patterns along the (d) $[101]_t$ and (e) $[100]_t$ zone axes (subscript "t" indicates indices based on the tetragonal unit cell) that the ZrO_2-rich solid solution grains are tetragonal.

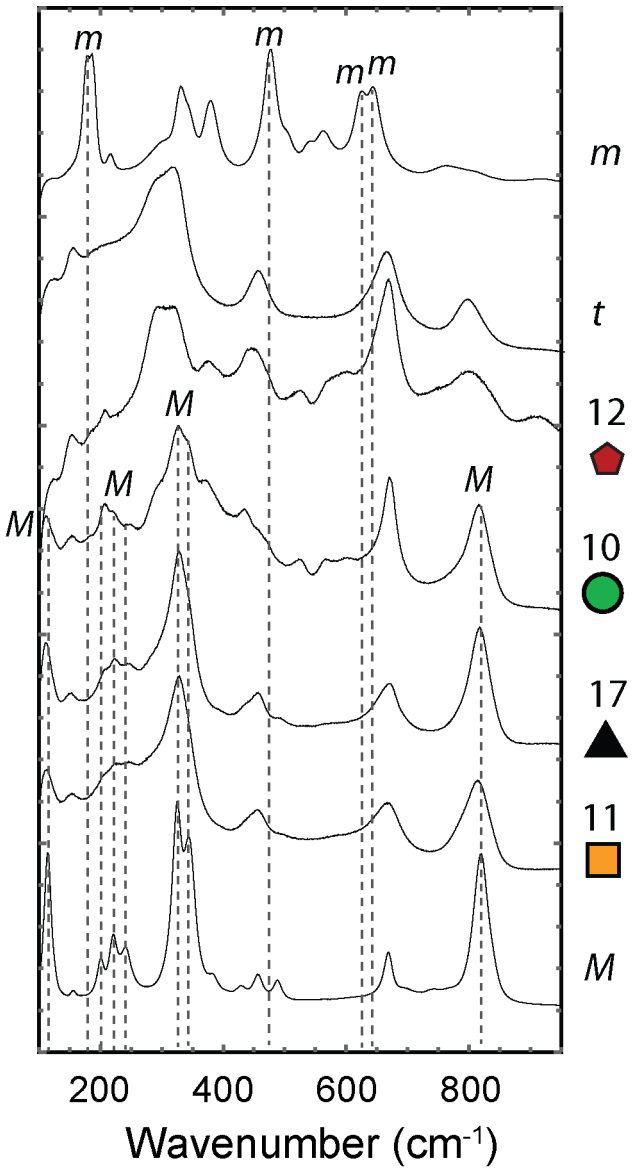

Figure 6.5 Raman spectra of Samples 11, 17, 10 and 12 after 100h at 1500°C. For reference, Raman spectra from single phase *M*-$YTaO_4$ (composition: 45Y-45Ta-10Zr), single phase *t*-ZrO_2 (composition:16Y-16Ta-68Zr) and *m*-ZrO_2 (composition: 11Y-8Ta-81Zr) are shown. *M* and *t* are observed for Samples 11 and 17. The significantly different spectra of Sample 10 is due to the *O*-$Ta_2Zr_6O_{17}$ phase. Monoclinic-ZrO_2 peaks are not observed in Samples 10, 11 or 17.

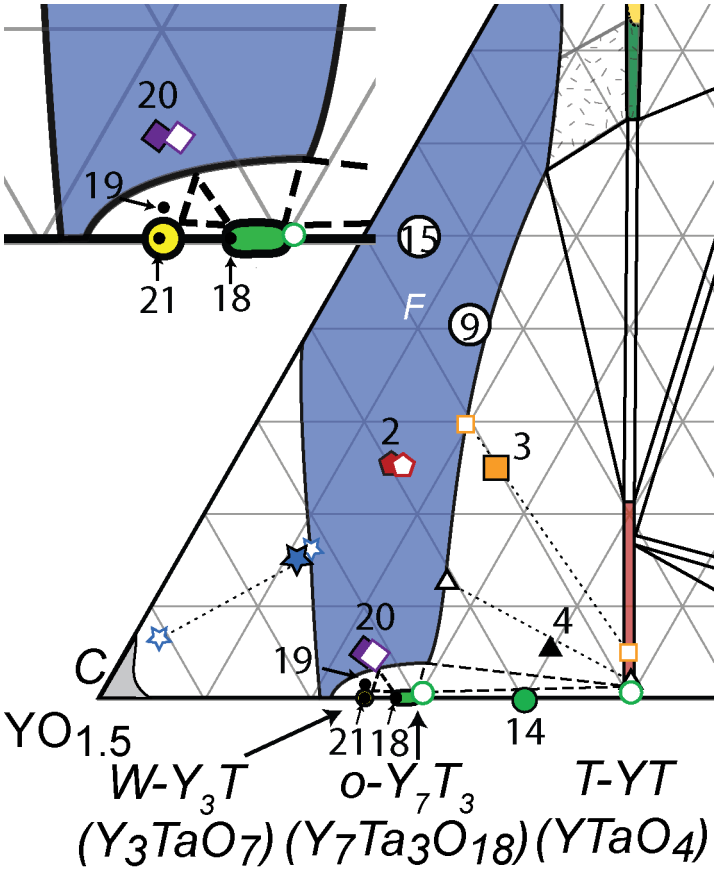

Figure 6.6 TEM/EDS results for samples 1, 2, 3, 4, 14 and 20 indicate that the fluorite field extends to the $TaO_{2.5}$-$YO_{1.5}$ binary at ~80mole% $YO_{1.5}$ at 1500°C. Additionally *W* and *o* are present at 75mole%$YO_{1.5}$ and 70-72 mole% $YO_{1.5}$, respectively.

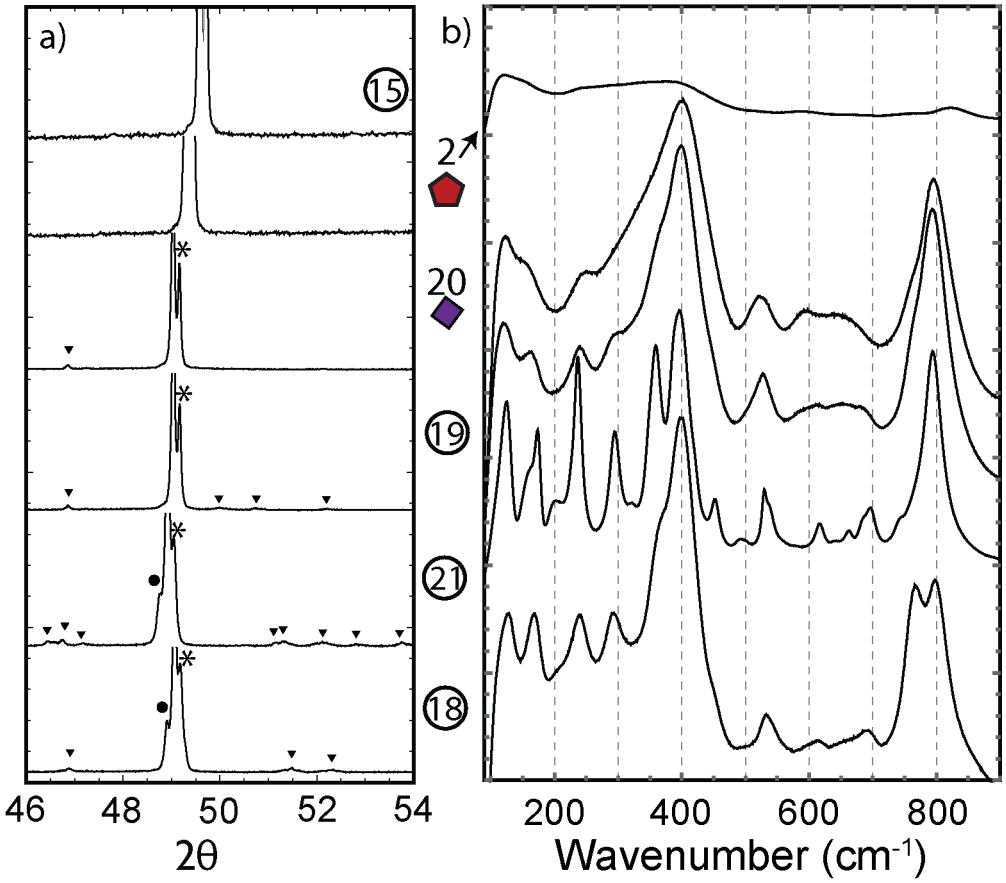

Figure 6.7 (a) The main XRD peaks of Samples 2, 15, 19 and 20 are not split, indicating the samples are fluorite after heat-treatment at 1500°C [84Hor]. The slight peak shifts are due to changes in composition. b) Peak splitting, indicated with •, and small additional reflections, indicated by triangles, are evident. Samples 18 and 21 are orthorhombic crystal structures in the space groups *Cmmm* and *Ccmm*, respectively [09Fu, 79Ros2]. Peaks caused by the Kα-2 X-rays are indicated with asterisks. b) Raman spectra indicate that there is additional ordering in Samples 18, 19, 20 and 21 that is not present in Sample 2.

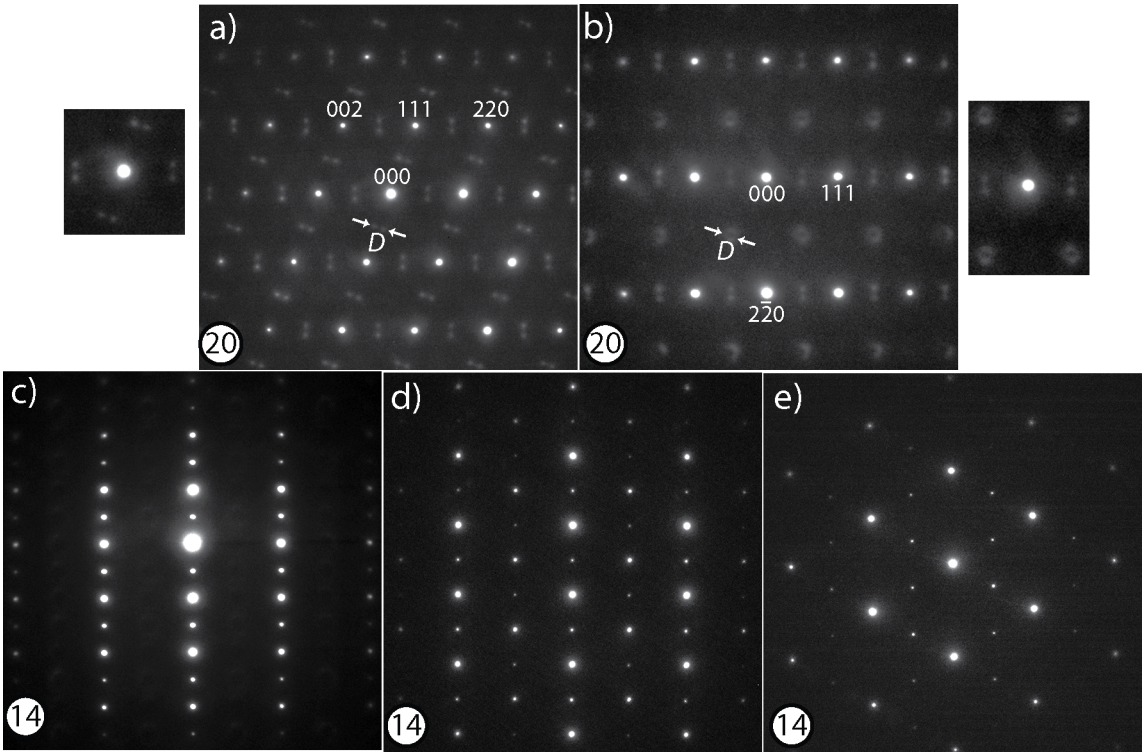

Figure 6.8 Split spots and diffuse scattering suggestive of local ordering are observed in the SAED patterns along the (a) $[1\bar{1}0]_F$ and (b) $[11\bar{2}]_F$ in the ternary Sample 20 after heat-treatment at 1500°C. (c) SAED pattern from an orthorhombic grain in Sample 14 can be indexed as the $[116]_{Cmmm}$ or $[113]_{Ccmm}$ zone axis. The SAED pattern in (d) can only be indexed as the $[110]_{Cmmm}$, confirming that orthorhombic *Cmmm* is present at ~$Y_7Ta_3O_{18}$. The SAED pattern in (e) can be indexed as the $[120]_{Cmmm}$ zone axis, assuming that 2 domain orientations are present.

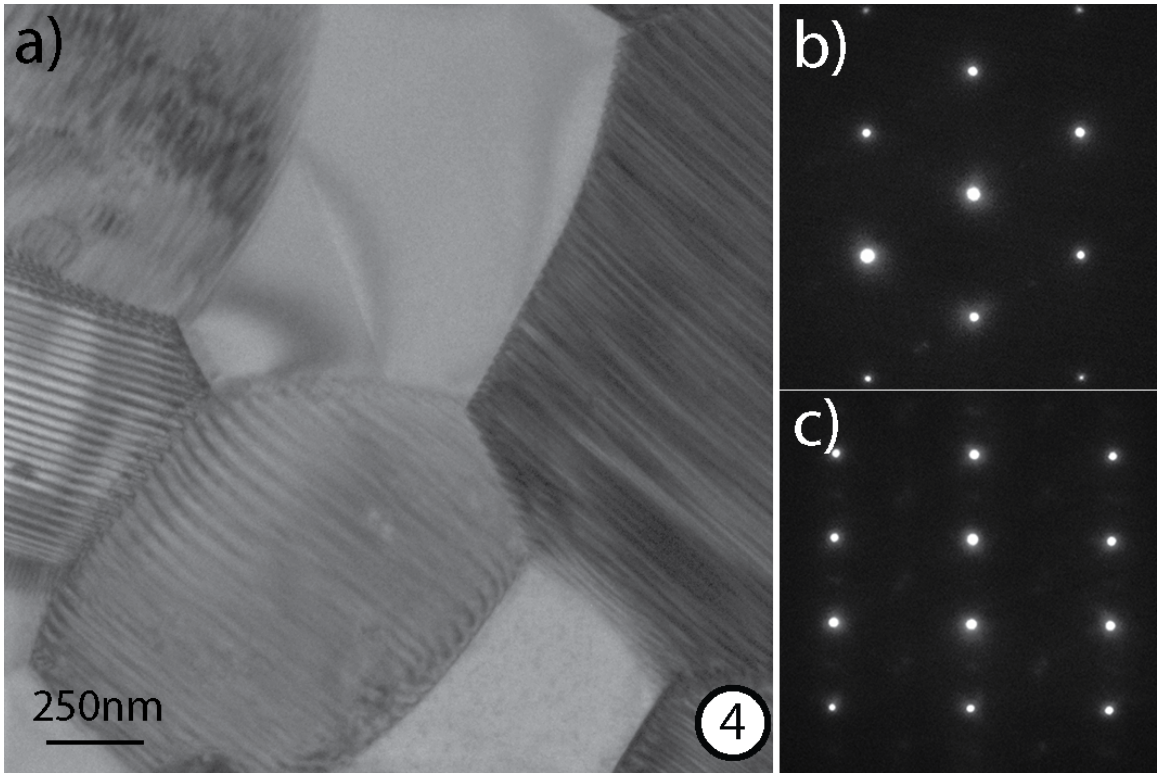

Figure 6.9 a) Bright field TEM image of Sample 4 shows twinned grains characteristic of *M*-$YTaO_4$ after heat-treatment at 1500°C. SAED patterns from the b) $(111)_F$ zone axis and c) $\{112\}_F$-type zone axis indicate the grains without twins have the fluorite crystal structure.

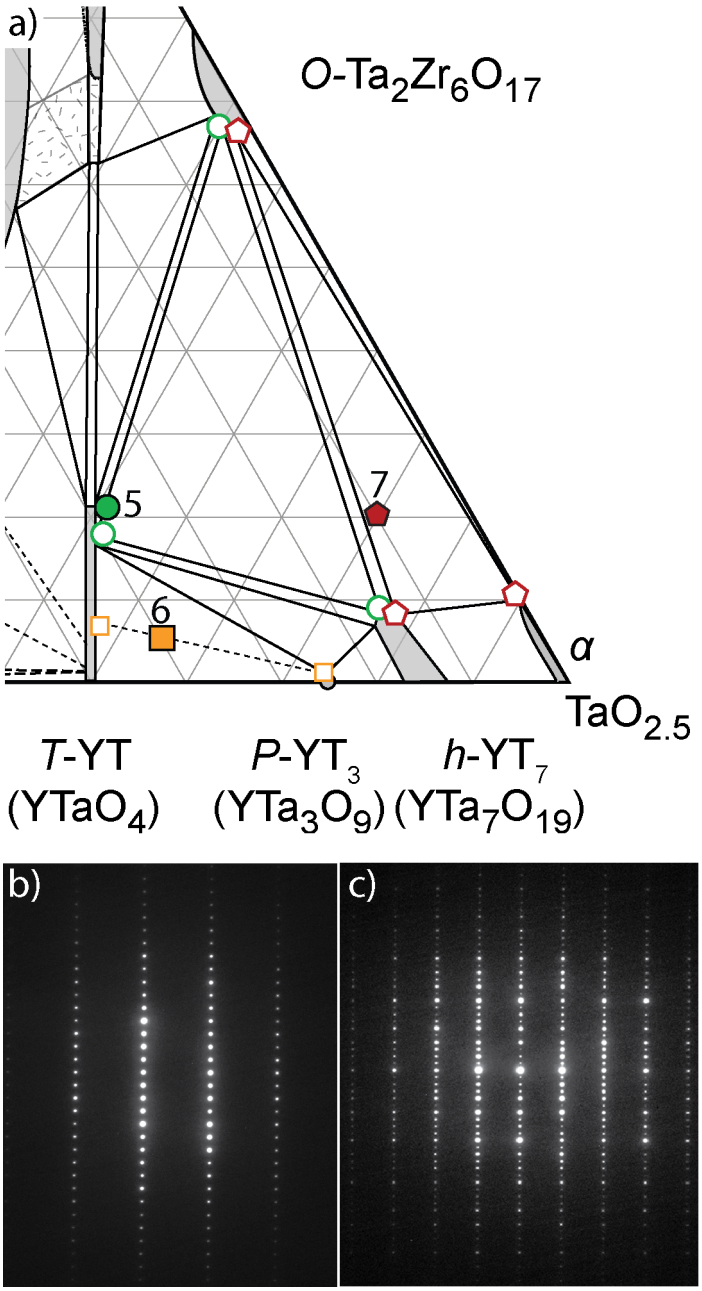

Figure 6.10 (a) TEM/EDS results from Samples 5, 6 and 7 outline the phase fields in the $TaO_{2.5}$-rich corner after heat-treatment at 1500°C. Selected area diffraction patterns along the b) {310}-type or {5 $\bar{1}$ $\bar{4}$ 0}-type and c) {210}-type or {10$\bar{1}$0}-type zone axes confirm the hexagonal structure of *h*-YT_7 is present in Sample 7.

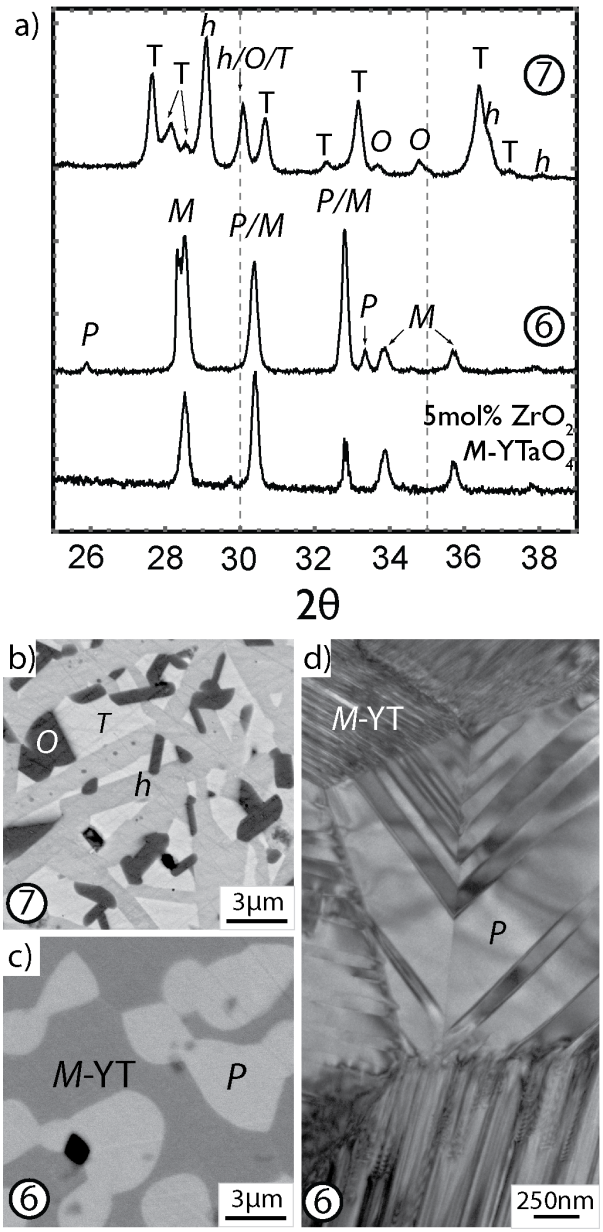

Figure 6.11 (a) *M*-$YTaO_4$ (*M*) and YTa_3O_9 (*P*) are present in Sample 6 and Ta_2O_5 (T) YTa_7O_{19} (*h*), and *O*-$Ta_2Zr_6O_{17}$ (*O*) are present in Sample 7 by XRD after heat-treatment at 1500°C. (b) BSE images show medium contrast, *h* with needle-like grains, dark contrast *O*, and light contrast $TaO_{2.5}$ (*T*) in Sample 7. (c) Sample 6 contains dark *M*-YT and light *P*. In both images pores have the darkest contrast. (d) BF-TEM of Sample 6 reveals the striated microstructure of *P* grains, which is suggestive of transformation twins that are a result of the 1st order transformation from *Cmmm* to *Pmma* that likely occurred on cooling [08Zho].

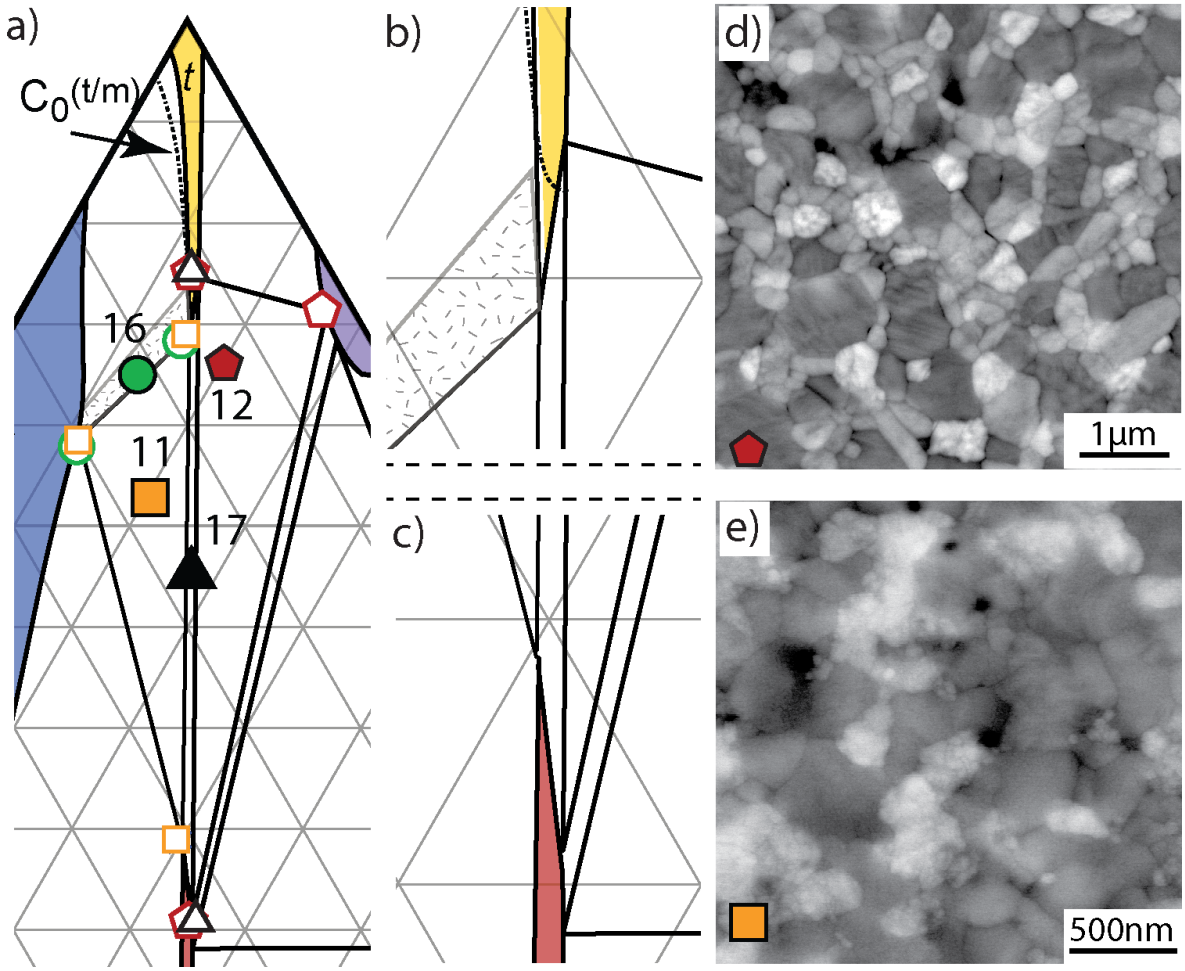

Figure 6.12 (a) TEM-EDS results of Samples 11, 12, 16, and 17 in the ZrO_2-rich region after heat treatment at 1250°C. Regions around the tips of the (b) *t* and (c) *M'* phase fields are magnified to more clearly show their unique shape. Sample 12 in the BSE micrograph in (b) contains ZrO_2, *O*, and *M'*. Sample 11, (c), contains *M'*, *t* and *F*, however *t* and *F* grains have the same contrast.

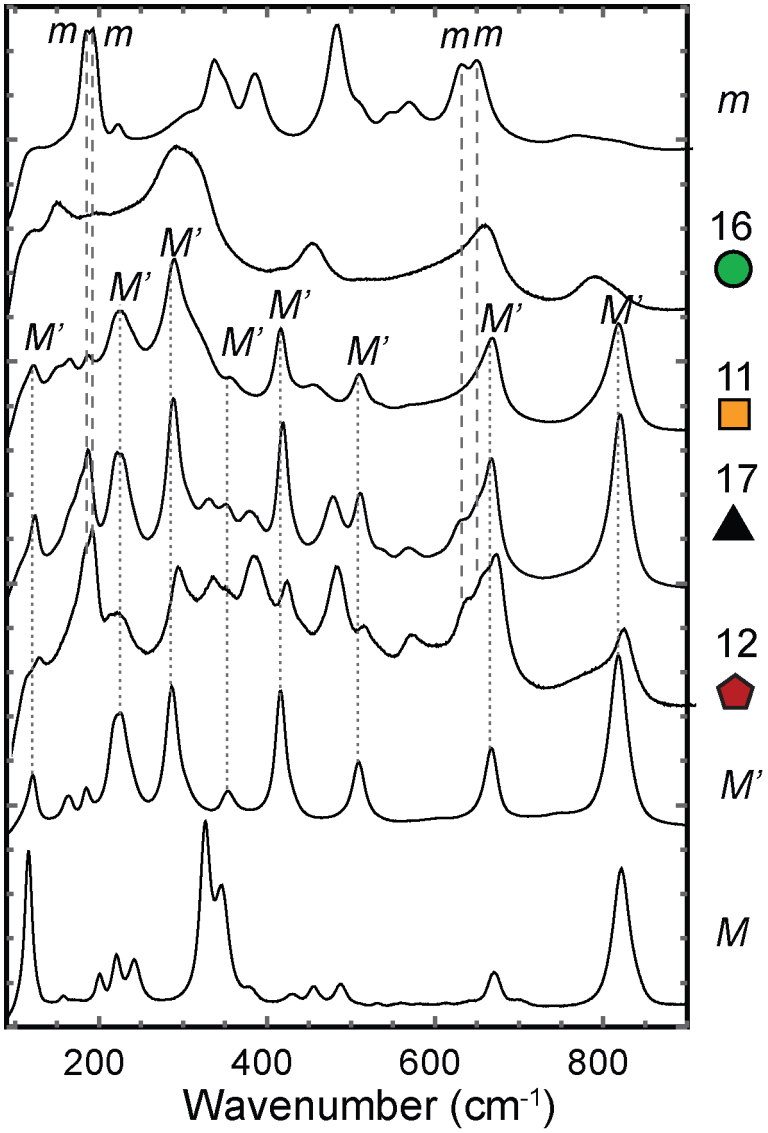

Figure 6.13 Raman spectra from Samples 12, 16 and 17 indicate *m* is present in the ZrO_2-$YTaO_4$ quasibinary and in 3-phase samples along the Ta-rich side of the *t* phase field after 1250°C. Peaks associated with *m* are identified based on [10She]. *M* (100h/1500°C) and *M'* (24h/1250°C) peaks match those reported in [73Bla, 14Shi] and [83Bri], respectively. The 2-phase (*F*+*t*) samples do not transform to monoclinic, but instead the Raman spectra is similar to that of *t*. $YTaO_4$ is present as *M'* instead of *M*, as the Raman spectra are easily distinguishable.

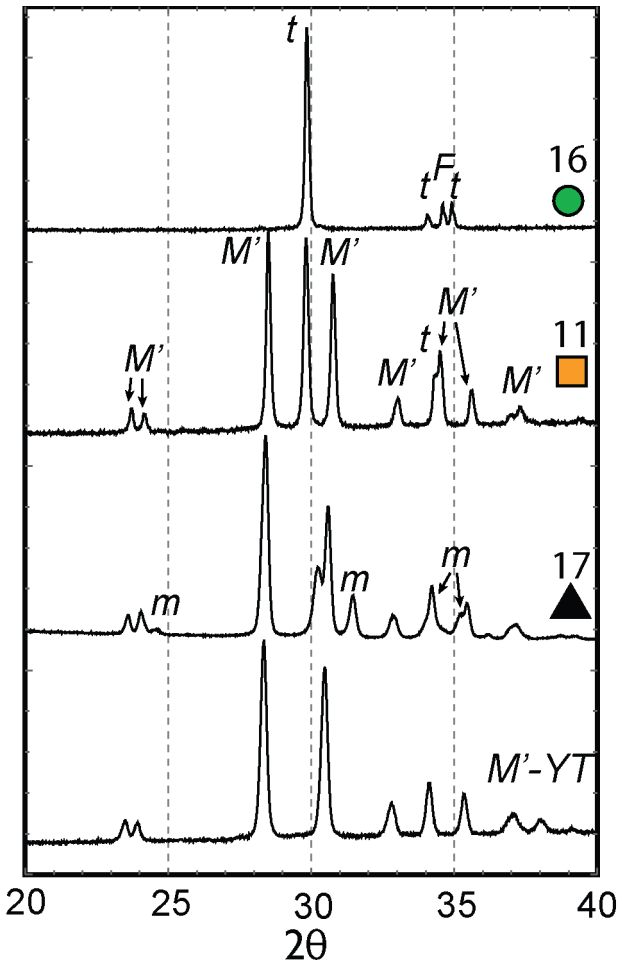

Figure 6.14 XRD of samples in the ZrO_2-rich region indicate that *m*-ZrO_2 is present in Sample 17 but is notably absent from Samples 11 and 16 after heat-treatment at 1250°C. *M'* is present in Samples 17 and 11.

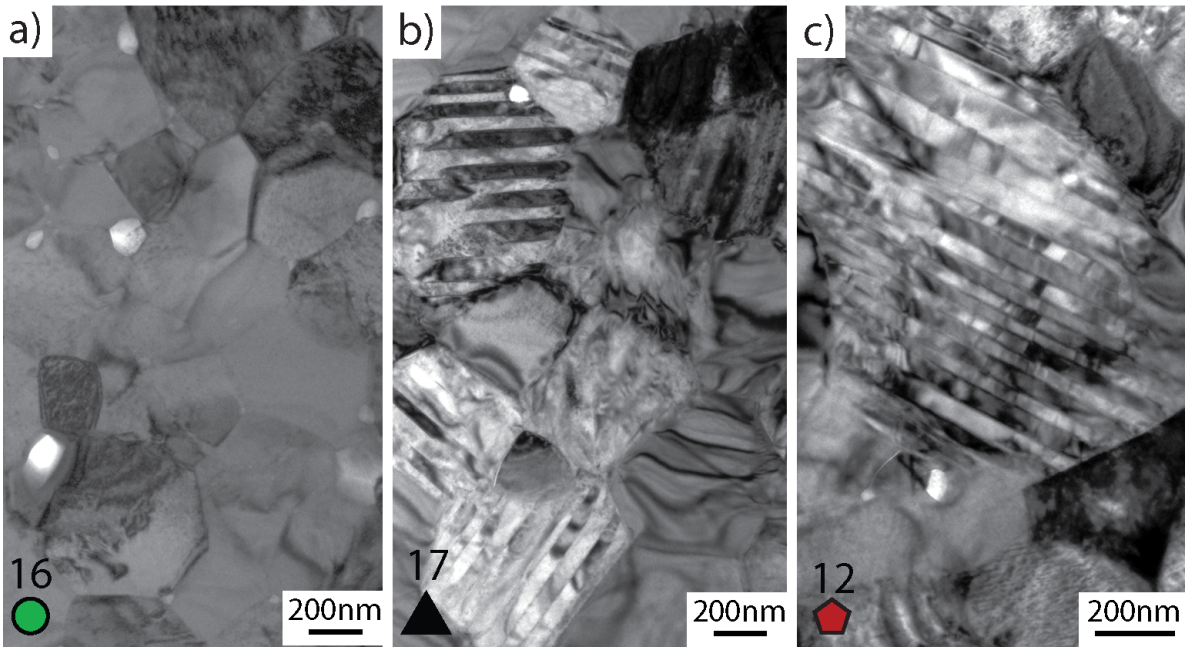

Figure 6.15 BF-TEM images of (a) Samples 16, (b) 17, and (c) 12 show that twinned monoclinic-ZrO_2 is present in Samples 12 and 17 but not in Sample 16 after heat-treatment at 1250°C. In agreement with the Raman spectra, the ZrO_2 in Sample 16 (a) does not transform to monoclinic. As evidenced by the presence of twins, monoclinic-ZrO_2 is present in Samples 17 (b) and 12 (c).

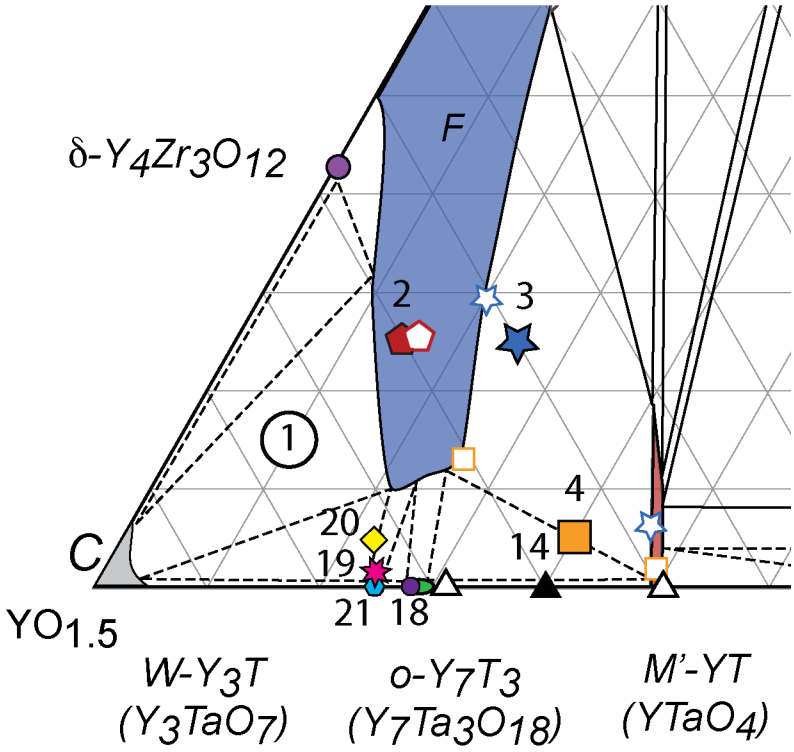

Figure 6.16 TEM-EDX results indicate the position of the phase boundaries. (b) SAED pattern from the [100] zone axis of a fluorite grain in Sample 4 proves the fluorite field extends to 12 mole% ZrO_2 at 1250°C. (c) XRD patterns from compositions in the Y-rich region suggest that compositions near Y_3TaO_7 have not yet ordered to any orthorhombic structure. XRD patterns of *Cmmm* and *Ccmm* are simulated using VESTA [08Mom] based on crystal structures provided in [79Ros2] and [09Fu], respectively.

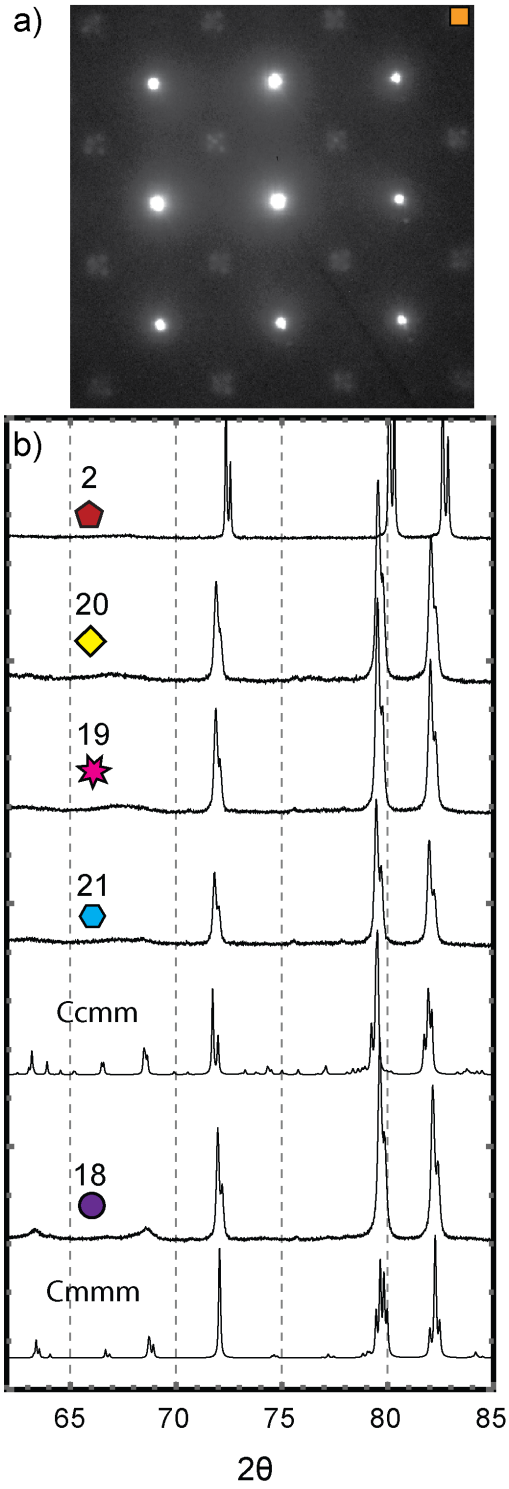

Figure 6.17 (a) SAED pattern from the [100] zone axis of a fluorite grain in Sample 4 proves the fluorite field extends to 12 mole% ZrO_2 at 1250°C. (b) XRD patterns from compositions in the Y-rich region suggest that compositions near Y_3TaO_7 have not yet ordered to any

orthorhombic structure. XRD patterns of *Cmmm* and *Ccmm* are simulated using VESTA [08Mom] based on crystal structures provided in [79Ros2] and [09Fu], respectively.

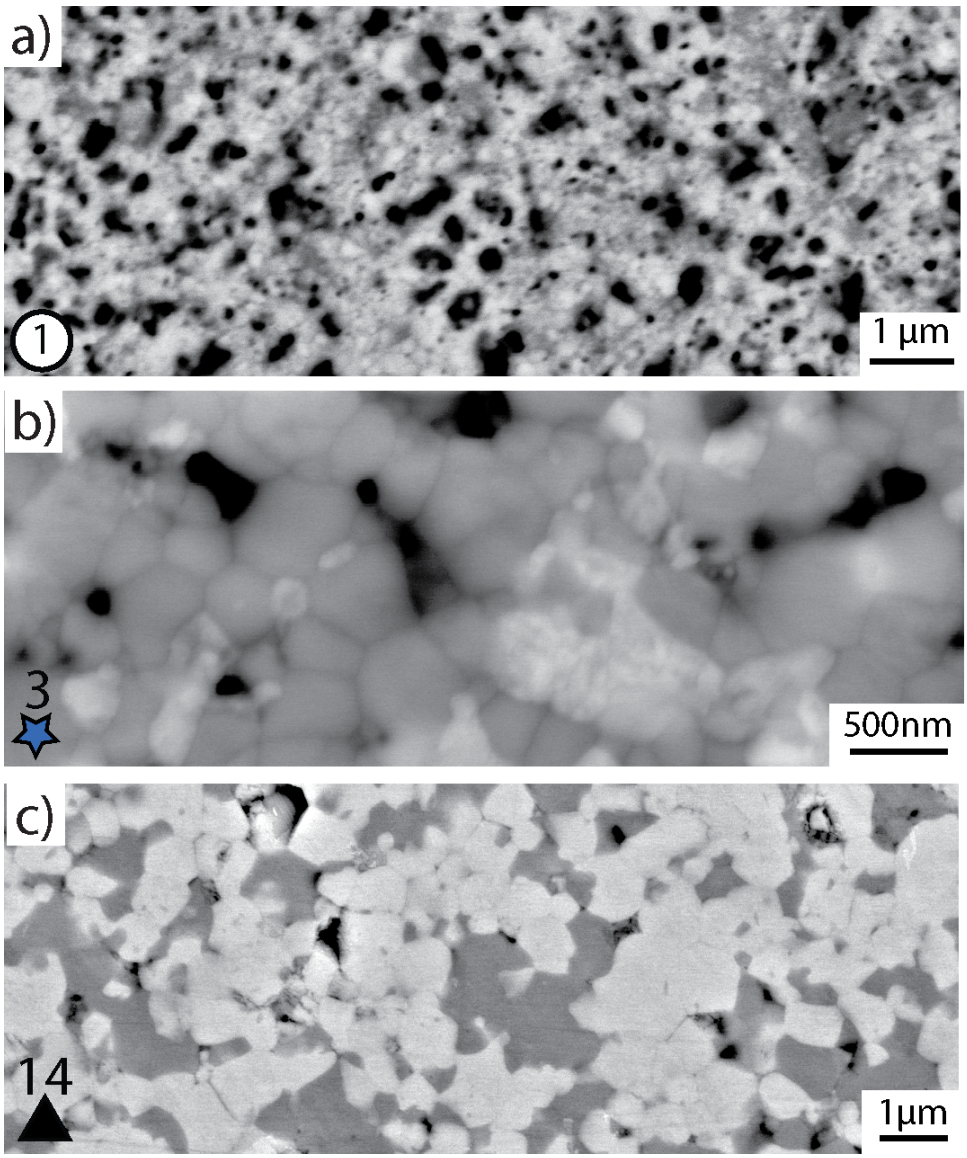

Figure 6.18 SEM micrographs of Samples (a) 1, (b) 3 and (c) 14 show the very small grains and significant porosity (black contrast) present in $YO_{1.5}$-rich compositions at 1250°C. Even after 800h at 1250C (a) grains are still <100nm in size.

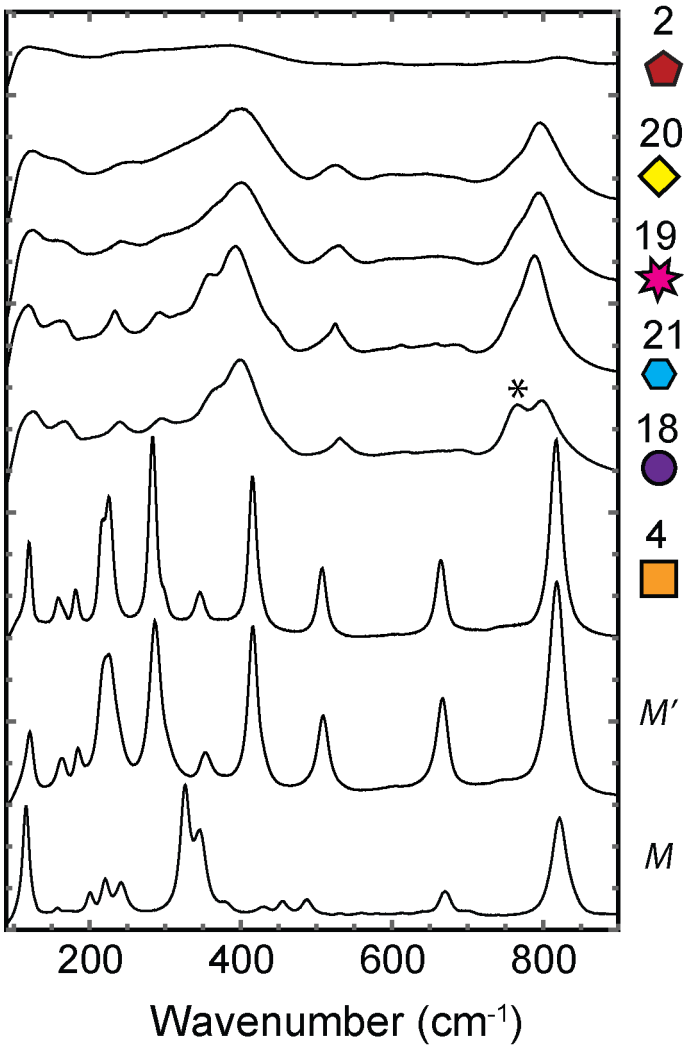

Figure 6.19 Raman spectra (633nm incidence) of compositions in the $YO_{1.5}$-rich region after heat-treatment at 1250°C suggest that M'-YT is present in Sample 4. With the exception of the additional peak observed at 768nm^{-1}, there are not significant differences between the Raman spectra of the samples near Y_3TaO_7 (18, 19, 20, 21) suggesting they have similar structures. Peak broadening as ZrO_2 is added to Y_3TaO_7 suggests that such substitution increases local disorder.

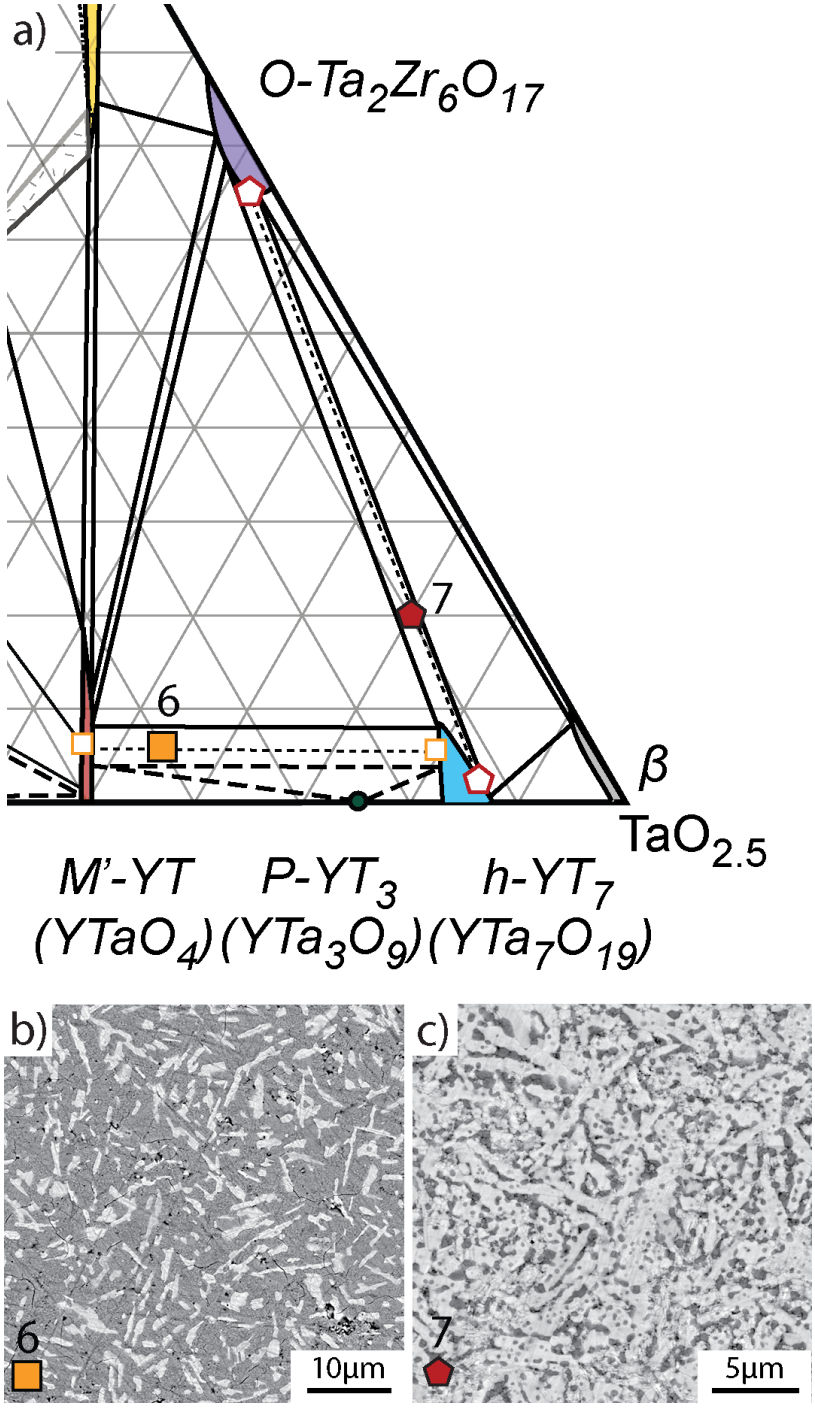

Figure 6.20 (a) Locations of the *M'*, *h*, and *O* phase fields were determined via TEM-EDS of Samples 6 and 7 after heat-treatment at 1250°C. On the binary, *P* is present based on Chapter 5. *h*-YT7, which has high aspect ratio grains, is observed with the lightest contrast in the BSE images of Sample 6 (b) and 7 (c). Although initially intended to be in the three-phase *h*+*T*+*O* phase field, only two phases (*h* and *O*) were observed in Sample 7.

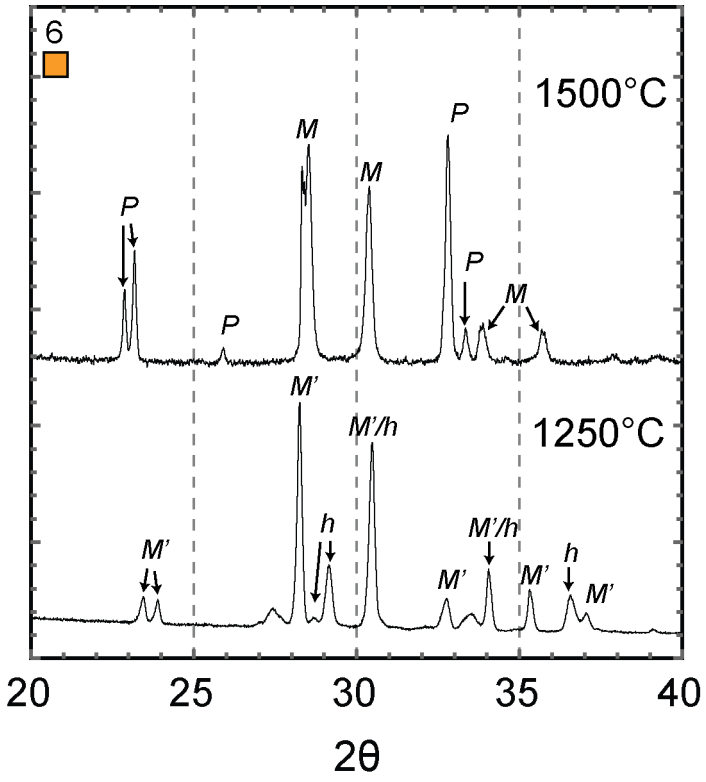

Figure 6.21 XRD patterns from Sample 6 after heat treatments at 1500 and 1250°C give clear evidence that *h* and *M'* are present at 1250°C while *P* and *M* are present at 1500°C.

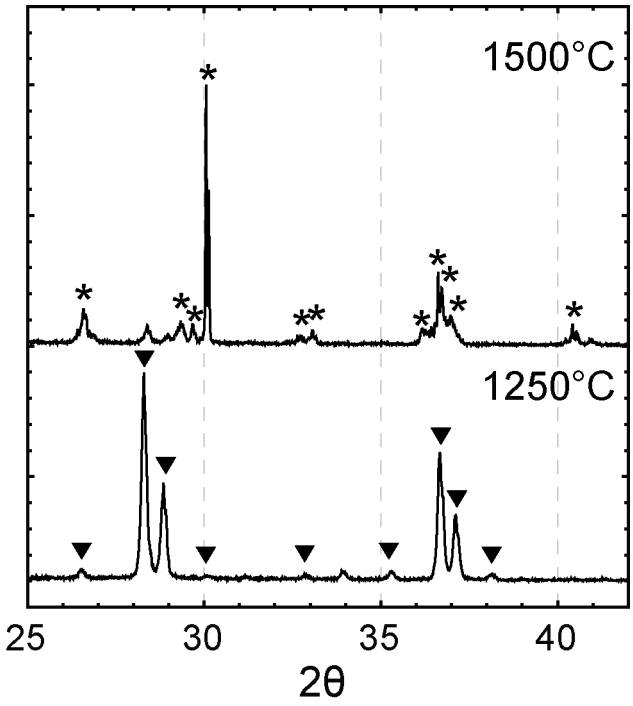

Figure 6.22 XRD of pure $TaO_{2.5}$ indicates the crystal structure changes between 1250°C and 1500°C. Asterisks indicate peaks associated with the monoclinic phase [68War] (PDF 01-075-9704) while triangles indicate the orthorhombic (*Pmm2E*, PDF 00-025-0922) structure [71Ste2].

CHAPTER 7: EVALUATING TOUGHENING MECHANISMS IN NOVEL TBC COMPOSITIONS

The elucidation of the complete isothermal sections of the ZrO_2-$YO_{1.5}$-$TaO_{2.5}$ (ZYTO) system at 1250°C and 1500°C revealed the presence of a large two-phase field in which fluorite (*F*) and $YTaO_4$ (YT) are stable. Such a large compositional space is promising because fluorite, with sufficient rare earth content, can mitigate damage caused by molten calcium magnesium alumino-silicates (CMAS) and the toughness of *F* may be able to be increased using $YTaO_4$ as a second phase. Additionally there is a narrow field in which solid solutions of tetragonal zirconia (*t*) and YT are both stable. Preliminary results provided in Appendix A indicate that compositions rich in $YTaO_4$ (YT) react with molten CMAS to form a crystalline reaction product with potential to help reduce CMAS penetration. While the details are still under investigation, they have motivated the synthesis of two-phase combinations between YT and either the nominally more CMAS resistant *F* phase or the nominally tougher *t* phase. Incorporating YT as a second phase has the potential to improve the CMAS resistance of phase stable *t* compositions. Thus multi-phase compositions offer the possibility of achieving combinations of properties that are not currently available in single-phase thermal barrier coatings (TBCs)

While investigation of the CMAS mitigation properties of $YTaO_4$ is ongoing, much is still unknown about the toughness and toughening mechanisms of compositions in the ZrO_2-lean portion of the phase diagram. This chapter presents two approaches to assessing the fracture toughness and elucidating the toughening mechanisms of single- and multi-phase compositions in the ZYTO system. First, micro-indentation measurements are used to compare the toughness of multiphase compositions. Given the ease of preforming micro-indentation tests and the small amount of material required, it is commonly used in the literature to determine toughness. However, as described in Chapter 2, the technique is not

without disadvantages. Other accepted toughness techniques such as 3-point bend require large amounts of material and synthesis of that material via co-precipitation is prohibitively slow. Thus, a micro-3-point bend technique was developed and utilized to determine the modulus and study the fracture behavior of three compositions within the ZYTO system relative to 8 ± 0.5 mole% $YO_{1.5}$-stabilized ZrO_2 (8YSZ). In addition, the micro-3-point bend technique enables characterization of the fracture surface and subsequent analysis provides insight into the fracture mechanisms. The three crystal structures investigated: metastable tetragonal 8YSZ (*t'*), monoclinic (*M*) YT and (*F*) fluorite exhibit significantly different fracture behavior. Samples containing the fluorite crystal structure show fracture surfaces characteristic of brittle fracture while samples containing YT have features suggestive of domain wall motion, a toughening mechanism analogous to ferroelastic switching.

7.1 Experimental details

7.1.1 Micro-indentation

Multi-phase compositions of *t* + YT (28Y28Ta) and *F* + YT (40Y33Ta) were synthesized and consolidated into pellets, as described in Chapter 3. All sample compositions are in mole percent of single cation formula units, balance ZrO_2, and are shown on the 1500°C ZYTO isothermal section in Figure 7.1. The 28Y28Ta sample (orange triangle in Figure 7.1) was heat-treated 100h at 1350°C, 1400°C, 1450°C, 1500°C, and 1550°C. To produce $YTaO_4$ precipitates, the same sample was subsequently heat treated at 1350°C for 100h. Samples were characterized after the 1500°C exposure and after re-equilibrating at 1350°C.

Samples of 40Y33Ta (blue/red square in Figure 7.1) were investigated after three different heat treatments, Table 7.1. After sintering at 1500°C for 100h and 1700°C for 100h, a pellet of 40Y33Ta was subjected to a long term anneal (500h) in a high water vapor environment at 1315°C, as described in Chapter 3. The primary purpose of the water vapor exposure was

to verify the stability of 40Y33Ta in combustion-like conditions. However the microstructure that was produced made an interesting comparison to 28Y28Ta and thus was investigated using micro-indentation.

At least 10 indents were measured for each sample at various loads. Backscatter electron (BSE) images obtained using a scanning electron microscope (SEM) and transmission electron microscopy (TEM) were used to characterize the microstructure of the samples. X-ray diffraction (XRD) and Raman spectroscopy were used to analyze the crystal structures present.

7.1.2 Micro-3-point bend

7.1.2.1 Powder Preparation

The toughening mechanisms associated with tetragonal (*t'*), fluorite (*F*), and $YTaO_4$ (YT) were studied by making compositions of 8YSZ, 45Y5Ta, and 47.5Y47.5Ta, respectively. A two-phase *F*+YT composition, 40Y33Ta, was also produced. Powders were synthesized via co-precipitation [90Cif, 93May], pyrolyzed for 4h at 650°C and then consolidated into pellets with a hydraulic press. With the exception of 8YSZ, samples were sintered in air for 100h at 1500°C and 48h at 1700°C. To mitigate the phase separation in 8YSZ, an alternative processing route was followed. The hydraulically pressed pellet was sintered using current assisted densification (CAD) (FCT Systeme, Rauerstein, Germany) at 1200°C for 10 minutes with a load of 65MPa. Following CAD the 8YSZ was sintered in air for 4h at 1100°C and then 50h at 1300°C. Relative densities were determined by measuring the mass and volume of the pellets as described in Chapter 3. These procedures resulted in relative densities ranging from 88-96% of the theoretical values as calculated from the number of atoms per unit cell (Table 7.3).

7.1.2.2 Bend Specimen Preparation

Pellets were thinned into disks with a thickness of ~300μm. The thin disks were mounted on a sacrificial piece of metal and then a 300μm diamond wire saw was used to cut the disks into bars, ~300μm x ~300μm x 5mm. Some of these bars were used for modulus testing. For toughness tests, a notch was cut into the bars using a 100μm diamond wire saw. A sharp pre-crack was put in the pre-notch using a focused ion beam (FEI, Helios, 21nA current, 30kV), Figure 7.2.

7.1.2.3 Loading Configuration

The loading geometry of the micro-3-point bend experiments was described in Chapter 3; the figure of the experimental set-up is provided in Figure 7.3 for convenience and understanding the equations that follow.

7.1.2.4 Analysis Methods

Modulus values were calculated based on the equations for a beam supported at both ends with a single load at the center. The equation for modulus is

$$E = \frac{\mathrm{F}s^3}{48\delta I} \qquad 7.1$$

where F is the applied load [N], s is the span between the two pins [m], δ is the beam deflection [m], and I is the moment of inertia [m^4] for a rectangular beam defined as

$$I = \frac{\mathrm{t}b^3}{12} \qquad 7.2$$

where t is the thickness [m] and b is the height of the beam [m], as depicted in Figure 7.3(b).

Toughness values were calculated using single edge notched beam (SENB) equations in [73Tad]. Relevant variables for the equations are depicted in Figure 7.3(b). The beam bending equations used were:

$\sigma = 6M/b^2$ where $M=Ps/4$, $P=F/t$ [N/m] and s is the span [m] between the two pins.

$$K_1 = \sigma f(\mathrm{a/b})\sqrt{\pi a} \qquad 7.3$$

where $f(a/b)$ is an empirical function that depends only on the crack length (a) and specimen height (b). $f(a/b)$ has been experimentally determined for s/b=8 and s/b=4. In these experiments s/b~10 and therefore the empirical formula for s/b=8 for $f(a/b)$ was used [73Tad].

$$f\left(\frac{a}{b}\right) = 1.106 - 1.552\left(\frac{a}{b}\right) + 7.71\left(\frac{a}{b}\right)^2 - 13.53\left(\frac{a}{b}\right)^3 + 14.23\left(\frac{a}{b}\right)^4 \qquad 7.4$$

To calculate the energy release rate (G), the measured modulus (E) and critical stress intensity factor (K_{1C}) were used in Griffith's equation:

$$G = \frac{K_{1C}^2}{E} \qquad 7.5$$

7.1.2.5 Characterization Methods

Prior to fracture, XRD was used to determine phases present in each sample. Phases were identified by comparison to published powder diffraction data (ICDD PDF-4 Database). Raman spectroscopy (633nm excitation) was used before and after fracture due to its high sensitivity to anion displacements, such as those associated with monoclinic ZrO_2 or tetragonal ZrO_2.

An FEI XL30 FEG SEM using secondary electron (SE) and BSE imaging modes was used to characterize the specimen microstructure before and after fracture. Fracture surfaces were also imaged by optical profilometry using the vertical scanning interferometry (VSI) mode of a Veeco WYKO NT1100 profiler.

Prior to fracture, the domain structure of $YTaO_4$ (YT) was investigated using transmission kikuchi diffraction (TKD), which was performed in collaboration with Dr. Patrick Trimbly and Prof. Julie Cairney at the University of Sydney. To better understand the evolution of the domain structure of YT as a result of fracture, it was necessary to perform TEM. Lamellae were extracted from the various specimens using a focused ion beam (FIB). TEM was conducted utilizing bright field (BF) and dark field (DF) imaging modes and selected area electron diffraction (SAED). A FEI Titan 300 kV FEG TEM/STEM system was used for high angle annular dark field (HAADF) imaging of 40Y33Ta.

7.2 Results

7.2.1 Micro-indentation

Given the importance of the *t* structure in enabling toughening mechanisms, the micro-indentation toughness measurements as a function of *t* content for 28Y28Ta and 40Y33Ta are shown in Figure 7.4. For comparison, additional results from the work of [06Pit, 07Pit] and S. Heinze (unpublished) are shown. Compositions corresponding to the symbols are plotted on the ZYTO isothermal section in Figure 7.1. The baseline is provided by the diamond symbols, which represent the single-phase *t* and *F* toughness values [06Pit, 07Pit]. The multiple values for *t* are the result of different dopant concentrations, within the single-phase *t* range in Figure 7.4. The *F*+YT samples showed an indentation toughness of ~15 J/m^2 after the higher temperature treatment, but upon re-equilibrating at 1315°C, the toughness increased to ~27 J/m^2. Similarly, the *t*+YT composition showed a toughness

ranging from 22-25 J/m^2 in Heinze's work (black triangle near the orange triangle in (Figure 7.4), but a similar sample with a subsequent lower temperature treatment had a higher toughness of ~30 J/m^2 in this work.

Examples of the *t*+YT (28Y28Ta) and *F*+YT (40Y33Ta) microstructures are depicted in Figure 7.5(a-c) and (d-f), respectively. These microstructures contain YT in two distinct size scales, one corresponding to the assemblage developed under a higher temperature treatment (>1500°C), evident in Figure 7.5(a,d) and the other resulting from precipitation of nano-scale YT from the counterpart phase at a lower temperature (T≤1350°C), e.g. Figure 7.5(c,f). The results will be discussed for each multi-phase sample below.

7.2.1.1 Tetragonal and $YTaO_4$ compositions

As expected, grains of YT (light contrast) and *t* (dark contrast) are observed after the 100h heat treatment at 1500°C (which followed 100h exposures at 1350, 1400, and 1450°C). Interestingly, long relatively planar boundaries are present between some *t* and YT grains. BF-TEM of the same sample indicates the YT grains (dark contrast) contain twins and are thus *M*-YT, Figure 7.6. The *t* grains do not contain twins, revealing they have not transformed to *m*. This is supported by Raman spectroscopy, Figure 7.7(b), which indicates that *M* and *t* are present but not *m*.

After re-equilibrating at 1350°C, fine scale YT precipitates form within the *t* grains, Figure 7.5(b). HAADF images Figure 7.5(c) and Figure 7.8(b) indicate the $YTaO_4$ precipitates are plate-like and parallel to each other. There is a ~200nm region within the *t* grain near the boundary with the large YT grain in which there are no YT precipitates, Figure 7.8(b). The Raman spectra of 28Y28Ta with the precipitates is nearly identical to the spectra after the 1500°C heat treatment, Figure 7.7(c). The measured toughness of 28Y28Ta with this type of

microstructure, i.e. containing two size distributions of YT as shown in Figure 7.5(c), was 30.2 J/m^2 (±5 J/m^2).

7.2.1.2 Fluorite and $YTaO_4$ compositions

After 100 h at 1700°C, long boundaries are present between *F* (dark contrast) and YT (light contrast) in 40Y33Ta, similar to the boundaries observed in 28Y28Ta, Figure 7.5. These boundaries are not as obvious after only 24 h at 1500°C, Figure 7.7.9, due to the small (750 nm) grain size. After 100 h at 1700° the measured toughness was 15.2 J/m^2 (2.8 J/m^2) while after 24 h at 1500°C the measured toughness was 26.4 J/m^2 (±4.2 J/m^2).

The water vapor exposure of a sample of 40Y33Ta, which had previously been exposed to 1500°C for 100h and 1700°C for 100h, did not result in a significant mass change even after 500h at 1315°C[†]. The long heat treatment allowed the sample to re-equilibrate at 1315°C, resulting in YT precipitates within the *F* grains, Figure 7.5(e) and Figure 7.10. The precipitates in 40Y33Ta are plate-like, similar to the precipitates in 28Y28Ta, but the plates are not parallel and occur at approximately 90° angles to each other. The measured toughness of this sample was 27.4 J/m^2 (±5.1 J/m^2).

The toughness as a function of grain size is plotted in Figure 7.11 for the different 40Y33Ta samples. While limited, the results suggest the measured toughness decreases as grain size increases for the samples after 24h at 1500°C (purple square) and 100h at 1700°C (red square). Interestingly, the measured toughness of the 40Y33Ta with the precipitates (after 500h at 1315°C, blue square), shows a toughness equivalent to the smaller grained material.

[†] The lack of significant mass change indicates that compositions similar to 40Y33Ta would be stable in the combustion environment. While this is important for the use of ZYTO compositions as TBCs, it will not be discussed further in this chapter.

7.2.2 Micro-3-point bend

The *t'*, *F*, and $YTaO_4$ crystal structures serve as case studies to exhibit the advantages of using the micro-3-point bending test to investigate fracture behavior. To identify crystallographic changes that occurred during fracture, it is necessary to rigorously study the samples both before and after fracture. Thus, this section is divided into characterization results before and after the 3-point bend experiments were conducted.

7.2.2.1 Prior to Fracture

The modulus values of 8YSZ, 40Y33Ta and 47.5Y47.5Ta were measured using the three-point bend technique. Unfortunately the modulus of 45Y5Ta was not measured. Differences in elastic moduli are evident in the load displacement curves, Figure 7.12 and summarized in Table 7.2. It is important to note that the influence of porosity was not accounted for in the modulus calculations. Each colored curve for 8YSZ and 40Y33Ta contains overlapping loading and unloading data in Figure 7.12. Both 47.5Y47.5Ta samples broke during the experiments shown in the figure, so only the loading curves are shown. Additional tests on 47.5Y47.5Ta were conducted at lower loads to more accurately determine the modulus. The measured modulus of 8YSZ, 208 GPa, agrees well with the accepted value of ~200 GPa [87Swa]. The measured moduli of 40Y33Ta (152GPa) and 47.5Y47.5Ta (184GPa) are lower than the expected values. This discrepancy is likely attributed to the presence of pores that crush during the modulus experiments.

Approximate grain sizes and phase constitution of the samples prior to fracture can be ascertained from BSE images, Figure 7.13 and are summarized in Table 7.3. As expected from the shorter heat treatments at lower temperature, 8YSZ has the smallest grains (100-500nm), Figure 7.13(a). In contrast, grains are two orders of magnitude larger (10-30μm) in single phase *F* and YT samples, 45Y5Ta and 47.5Y47.5Ta, respectively, Figure 7.13(c, d).

The two-phase (*F* + YT) sample, 40Y33Ta, contains 35% fluorite (dark contrast) and 65% $YTaO_4$ (light contrast) and the grains are smaller, (2-5μm), Figure 7.13(b). Similar to the microstructure observed in the micro-bending samples, some single "grains" in 40Y33Ta are composed of *F* and YT separated by long, presumably low energy, boundaries (higher magnification available in Figure 7.19). The YT sample, 47.5Y47.5Ta, contains a small percentage of YTa_3O_9, which has the lightest contrast in Figure 7.13(d). The presence of this phase is not entirely unexpected since $YTaO_4$ is essentially a line compound in the binary, thus any slight deviations from stoichiometry result in small amounts of a second phase.

$YTaO_4$ is present as *M*-YT after cooling to room temperature from 1700°C, as indicated by the twins present in the HAADF image, Figure 7.14(a) of 40Y33Ta. The twins have an orientation relationship of 85° around the $0\bar{1}0$ zone axis, as determined by TKD, Figure 7.14(b). In some regions of the sample, SAED patterns from the $(111)_F$ and $(\bar{2}12)_{MYT}$ zone axes, Figure 7.14(c and d), respectively, suggest there is an orientation relationship between *F* and YT. In several of the grains in (a) long grain boundaries are present between *F* and YT.

The 8YSZ sample has phase separated into the equilibrium *t* and *F* phases, as observed via XRD, Figure 7.15(a). Only *t* is observed with Raman spectroscopy, [09Mil] Figure 7.15(b), which is expected based on the weak Raman scattering intensity of the *F* phase. Raman is more sensitive to the anion displacements associated with the transformation from *t* to *m*-ZrO_2. As evidenced by the lack of peaks at 182cm^{-1}, 191 cm^{-1} and near 650cm^{-1} [10She], *m*-ZrO_2 is not present in 8YSZ before fracture.

7.2.2.2 After Fracture

Measured toughness values for the different samples are summarized in Table 7.3. Measured modulus values were used to calculate the energy release rate, *G*. Since the modulus of

45Y5Ta was not measured, the published modulus for fluorite with the composition ZrO_2 + 12.2 mol% $YO_{1.5}$ was used to calculate *G* [97Ada]. While modulus values were measured from multiple samples, each toughness value in Table 7.3 is a result of only one experiment. Given the variation in defect distribution from sample to sample, the measured toughness values are not statistically significant. However, the micro-3-point bend technique enables the characterization of the fracture surface from which valuable insights can be gained regarding the mechanical behavior of each sample. By characterizing the fracture surfaces, possible toughening mechanisms can be elucidated. The rough pre-notch is visible on the bottom of Figure 7.16(b) and (d), followed by the smooth FIB pre-crack and subsequent fracture surface.

Optical profilometry, Figure 7.17 and BSE images indicate that the fracture surface roughness varies significantly between the different compositions. The z-height of the surface is indicated by the color scale, defined in micrometers. The surface roughness values of 8YSZ, 40Y33Ta and 45Y5Ta only vary from ±5μm, while the fracture surface of 47.5Y47.5Ta varies by ±25μm. Higher magnification BSE images suggest the samples fracture differently, Figure 7.18. In each image, the crack is propagating upward. Unfortunately the small grain size of 8YSZ prevents fractographic analysis of 8YSZ in the SEM, Figure 7.18(a). In 40Y33Ta, (Figure 7.18(b) and higher magnification images in Figure 7.19), the *F* grains exhibit transgranular cleavage, resulting in smooth fracture surfaces. The fracture surface of YT grains is significantly more rough and contains signs of both inter- and transgranular fracture, Figure 7.19(b). Only transgranular fracture is present in the single phase, *F* sample 45Y5Ta, Figure 7.18(c). The nominally single phase $YTaO_4$ sample, 47.5YY47.5Ta, exhibits surface relief within regions of transgranular fracture on the same length scale as the twins in *M*-$YTaO_4$, Figure 7.18(d). On a whole, SEM images indicate the fracture surface of 47.5Y47.5Ta is rougher than the other samples, Figure 7.20(a), in agreement with profilometry data. The rough fracture surfaces suggest energy

dissipating mechanisms may be active during fracture. Striations are visible in $YTaO_4$ grains exposed by intergranular fracture, Figure 7.20(b and c). The striations are the same length scale as the twins in *M*-$YTaO_4$, however they vary in width, suggesting that regions of one domain orientation are larger than regions of the other domain orientation. Unlike the other samples that fractured catastrophically, the fracture of 47.5Y47.5Ta occurred more stably, such that the crack could be imaged propagating through the sample. A plot of the stress as a function of image number for the fracture test of 47.5Y47.5Ta shows a change in slope at ~38MPa, which could correspond to the introduction of microcracks.

To further investigate the fracture behavior of $YTaO_4$, a TEM lamella was extracted from a grain that had undergone transgranular fracture on the surface of 47.5Y47.5Ta. BF-TEM images reveal the domain structure of $YTaO_4$ far from the fracture surface, Figure 7.22(a) as well as near the fracture surface, (b-d). In all BF images the fracture is occurring from in the direction of right to left. Far from the fracture surface the domain walls are continuous while domain walls are jagged near the fracture surface. Most of the twins away from the fracture surface are approximately 200nm wide. The two domains of *M*-$YTaO_4$ are evident and a SAED pattern indicates the domains with dark contrast (e) are oriented along the [111] zone axis. A SAED pattern from a domain with light contrast is shown in (f) but unfortunately the zone axis could not be determined.

7.3 Discussion

Salient findings in the investigation of toughness in the ZYTO system include (i) the observation that YT is a useful addition to the toughness of the fluorite or tetragonal solid solution compositions, (ii) the development of a micro-3-point bend technique, (iii) the confirmation that fluorite containing $YO_{1.5}$- and $TaO_{2.5}$ lacks appreciable toughening mechanism, and (iv) the first-reported evidence of domain motion under stress in YT. Finally by studying samples that contain $YTaO_4$ in micrometer- (1-5μm) and nanometer-

sized grains, it is possible to hypothesize about the possible toughening mechanisms that may be active at the different length scales.

7.3.1 $YTaO_4$ positively contributes to toughness

Although none of the multi-phase compositions in this study exhibit toughness values greater than that of 8YSZ, compositions containing $YTaO_4$ had higher indentation toughness values than would be expected based on the experience of two phase combinations between tetragonal and fluorite solid solutions. It is clear from Figure 7.4 that YT-containing compositions have higher indentation toughness values than single-phase fluorite, especially when compared with similar volume fractions of tetragonal solid solution added to the fluorite. Additionally compositions that contain YT and *t* exhibit higher indentation toughness values than would be expected by assuming *t* was the only phase contributing to the toughness. Based on these results it is evident that at least one toughening mechanism is active in YT, as will be elaborated later. This is promising because the introduction of YT could (i) improve the toughness of CMAS resistant *F* compositions or (ii) improve the CMAS resistance of phase stable *t* compositions.

7.3.2 Development of a micro-3-point bend technique

The micro-3-point bend technique developed and utilized in this study offers the possibility to measure modulus and toughness and enables the characterization of the fracture surface. In addition to serving as a benchmark for compositions in the ZYTO system, the 8YSZ composition can be used to verify that the micro-3-point bend technique is accurate and appropriate for dense ceramic samples. The measured modulus of 208GPa for 8YSZ samples agrees well with the accepted value of ~200GPa [87Swa], confirming the bending of micro-scale beams produces accurate results in the elastic regime.

To accurately measure toughness using a SENB set-up, it is critical that the pre-notch and pre-crack act as a single sharp crack. Analysis of the required dimensions for homogeneous linear elastic material was performed in [05Bos]. As defined in Figure 7.23, c is the depth of the pre-notch and ρ is the pre-notch radius. A critical length of pre-crack, a_c, was determined such that if $a < a_c$ fracture is controlled by the nominal stress intensity factor. For the case of c/b=0.5 (where b is the height of the bar), the critical value is $a_c/\rho \approx 0.2$. The average c/b ratio in the samples in this study was 0.15 and all samples investigated met the requirement for a_c/ρ. Therefore the pre-notch and pre-crack act as a single sharp crack and valid toughness values can be calculated. The measured toughness of 8YSZ of 34.5J/m^2 agrees with the value of 39 J/m^2 determined by micro-indentation [07Sch]. The lower toughness measured in this study may be due to the fact that 8YSZ has phase separated into t and F. If F is incoherent it constrains switching in the tetragonal phase. On the other hand, if t and F are still coherent, the coercive stress increases and the volume of switchable material decreases, reducing the work of fracture. While the accurate modulus values determined by micro-bending indicate the technique generates valid modulus results, the number of toughness tests per sample were not enough to provide statistically significant toughness results. Additional samples will enable the validation of the micro-3-point bend technique for the measurement of fracture toughness of ceramic samples using significantly less material than the traditional 3-point bend test.

7.3.3 Fluorite lacks appreciable toughening mechanisms

Another key outcome of this work was the confirmation that the fluorite phase containing ZrO_2, $YO_{1.5}$ and $TaO_{2.5}$ does not have any significant toughening mechanisms and exhibits similar fracture behavior to other fluorite compounds. Transgranular cleavage fracture in the fluorite composition, 45Y5Ta, results in a fairly smooth fracture surface, as evidenced in BSE images and optical profilometry. The presence of “river marks”, Figure 7.18, which are

characteristic of brittle fracture [93Law, 48Tip], suggest that the incorporation of Ta in solid solution does not fundamentally incorporate any new toughening mechanisms relative to the YSZ fluorite. First coined by Constance Tipper in her pioneering work on the brittle fracture of steels, river patterns are so characteristic of brittle fracture that images of them grace the covers of fractography textbooks [99Hul]. River marks form when the crack traverses a twist grain boundary, as depicted in Figure 7.24. As the crack crosses a twist boundary from grain 1 (blue) to grain 2 (green), it must separate into partial fronts, connected by cleavage steps, to stay on its preferred cleavage plane. Like other fluorite materials such as CaF_2, cleavage in ZrO_2-containing fluorite structures is most favorable along the {111} planes [83Mic]. Thus river patterns are formed as the crack stays on {111} planes as it traverses the twist grain boundary in Figure 7.18(c).

7.3.4 Domain motion in *M*-$YTaO_4$

Non-linearity of the load-displacement curves of 47.5Y47.5Ta, Figure 7.12, combined with analysis of the fracture surface also reveals, for the first time, evidence of domain motion in *M*-$YTaO_4$, a mechanism underpinning ferroelastic toughening. The striated structure observed in the grains on the fracture surface of 47.5Y47.5Ta Figure 7.20 has previously been observed in *M*-$LaNbO_4$ and attributed to the twin domains [77Bri]. Although additional crystallographic analysis is required, the BSE and BF-TEM images suggest the *M'* domain boundaries are mobile during the fracture event. $YTaO_4$ has not been studied previously but domain motion in isostructural $LaNbO_4$ has been studied extensively. Similar to $YTaO_4$, $LaNbO_4$ is a ferroelastic material that is tetragonal at high temperatures and undergoes a second order transformation to monoclinic at low temperature (T<~500°C) [97Jia, 80TsuI]. The two domains present in *M*-$LaNbO_4$ are related by a ~95° rotation around the monoclinic (010) axis [96Jia, 05Prytz, 80TsuI]. Non-linear load-displacement curves during compression experiments of $LaNbO_4$ single crystals [76Tsu] and polycrystalline samples

[09Mok, 96Jia2] have clearly shown the domains can move in response to applied stress. As little as 0.588 MPa is required to move one domain wall in a single crystal of $LaNbO_4$ at room temperature [76Tsu], which is three orders of magnitude less than the stress required to initiate ferroelastic switching in tetragonal ZrO_2-5.8 mole% $YO_{1.5}$ single crystals at 500°C [01Bai]. Presumably, the domain walls would move such that the domain oriented most favorably to reduce the stress will grow in size while the unfavorably oriented domain will shrink. Similar to domains in tetragonal ZrO_2, the switching of domains in $LaNbO_4$ is influenced by temperature and strain rate [80Tsu2, 09Mok]. While $LaNbO_4$ domains switch when a stress is applied, the amount that switches back after the stress is removed is dependent on the strain rate [80Tsu2]. In $LaNbO_4$, the slower the strain rate, the less 'back-switching' occurs once the external stress is removed. The 'new' domains observed to the right of the presumably pre-existing domains near the fracture surface of 47.5Y47.5Ta are domains that did not switch back after the crack front passed. $YTaO_4$ has a larger monoclinic distortion (β=95.75°) [14Shi] than $LaNbO_4$ (β=94.1°) [77Bri] potentially increasing the stress at which domain motion occurs. It is interesting to note that the addition of ZrO_2 to $YTaO_4$ decreases β to ~95° [14Shi], which could make it easier to move domain walls in $YTaO_4$-20mole%ZrO_2, for example.

The formation of new domains in addition to the movement of pre-existing domain boundaries has also been proposed as a possible explanation of the yielding behavior of $LaNbO_4$ [96Jia2, 77Bri]. Evidence of domain formation in $YTaO_4$ is observed in Figure 7.22(c) as a 'blade' of the dark contrast domains is observed, unassociated with any other dark contrast domains near the center of the image. The combination of domain motion and formation of new domains has the potential to be beneficial for the toughness of $YTaO_4$ containing compositions.

Based on the amount of surface area generated during fracture of $YTaO_4$ and the evidence of domain motion/formation, it is surprising that the only toughness value measured was very low (7.6 J/m^2). Given the low density (87% theoretical) and presence of porosity in 47.5Y47.5Ta as well as 45Y5Ta, it is possible that the pores act as stress concentrators, resulting in artificially low toughness values. It is evident that further experimentation is required to determine accurate toughness values.

7.3.5 Length scale of $YTaO_4$ may dictate toughening mechanisms

$YTaO_4$ is present in two different length scales in the micro-indentation and micro-3-point bend samples. Although additional research is required, it is possible that different toughening mechanisms are active on each length scale.

Domain motion is probably favored in larger (1-5μm) grains of *M*-$YTaO_4$, as discussed earlier. In two-phase samples such as 28Y28Ta (*t* + YT) and 40Y33Ta (*F* + YT), the grains are large enough to study the orientation relationships between *t* or *F* and YT. While these orientation relationships may not influence the mechanical behavior of large-grained materials, they could play a critical role in enabling toughening mechanisms in materials with nano-scale YT precipitates. Several microstructural features of large-grained samples suggest there is an orientation relationship between *t* or *F* and YT. The long *t*/YT and *F*/YT grain boundaries, Figure 7.5(a,d), present after the higher temperature exposures suggest a low energy boundary between the two phases. The SAED patterns on either side of the boundary between YT and *F*, Figure 7.14, are further evidence of an orientation relationship, however additional work is needed to confirm the coherent nature of the boundary.

The microstructure of the nano-scale YT precipitates is very similar to tetragonal ZrO_2 precipitates in partially stabilized zirconia (PSZ) and may be amenable to exploiting the $T \rightarrow M$-YT transition to activate transformation toughening. In both cases, samples are first

heat-treated at high temperatures at which the dopant solubility in ZrO_2 is high. Subsequent re-equilibration at lower temperatures results in formation of dopant-rich precipitates due to the lower dopant solubility. Specifically for the case of 28Y28Ta, the $YO_{1.5}$ and $TaO_{2.5}$ solubility in *t* decreases at lower temperatures, Figure 7.8, resulting in YT precipitates in *t*. This microstructure evolution is promising for the formation of YT precipitates from vapor deposited, super saturated solid solutions, as has been observed in electron beam physical vapor deposited (EB-PVD) coatings [15Van].

Understanding the fundamental reasons underpinning the size and spatial distribution of precipitates is central to activating the transformation toughening mechanism. The YT domain structure within *F* (Figure 7.10) is strikingly similar to that of tetragonal ZrO_2 domains within partially stabilized zirconia, see Figure 2.14. In PSZ, lenticular plates of *t*-ZrO_2, ~250nm in diameter and with an aspect ratio of 5:1, form parallel to the $\{100\}_F$ planes in the fluorite matrix [78Han, 00Han]. The orientation relationship between the lattices is such that the principal axes of the *t* and *F* unit cells are parallel, and for each of the three precipitate variants observed in a given matrix orientation, the c_t-axis is always perpendicular to the habit plane [00Han]. A similar orientation relationship has been proposed in the ZYTO system [15Van], explaining why the YT precipitates are arranged differently in 40Y33Ta (*F* matrix) than they are in 28Y28Ta (*t* matrix). In both PSZ and ZYTO compositions, lattice mismatch between the precipitates and matrix dictate precipitate shape and are critical to maintaining the coherency of the boundaries [78Han, 15Van].

The orientation relationship between YT and *t* or *F* is important for the activation of transformation toughening in YT-containing compositions. For transformation toughening to be effective, *T*-YT must be constrained by the *t* or *F* matrix below its transition temperature. Additional work is needed to verify if the YT precipitates are *T* or *M*. Coherent boundaries have proven to be critical in maintaining metastable phases [78Han, 11Kro, 13Kro], thus

coherent or semi-coherent boundaries between the YT precipitates and the matrix may preserve *T*-YT at room temperature. The stress-activated transformation to *M*-YT would create a compressive strain field about the crack tip to oppose crack propagation, increasing the effective toughness of the material. The system would be, in principle, analogous to a dispersion of metastable tetragonal zirconia in cubic zirconia, opening a path for exploitation of transformation toughening at high temperatures. Furthermore, the presence of large (2-5μm) grains of *M*-YT and nano-scale (50-150nm) possibly *T*-YT precipitates may enable both domain motion and transformation toughening to contribute to the measured indentation toughness.

7.4 Conclusions

While the toughness results for multi-phase compositions are preliminary and not yet at the levels characteristic of 8YSZ, they suggest a path for development of two-phase compositions that may resolve the toughness penalty to CMAS resistant compositions. If successful, this would represent not only a major contribution to thermal barrier coating technology but also add to the understanding of toughening mechanisms in ceramics.

Indentation toughness results of two phase compositions containing YT + *t* and YT + *F* suggest that the addition of $YTaO_4$, especially as nanoscale precipitates, produces higher toughness than would be expected if the second phase did not exhibit any toughening mechanisms (such as *F*). To further explore the possible toughening mechanisms in $YTaO_4$ and attempt to obtain more accurate toughness results from a standardized test, micro-3-point bend experiments were conducted. Analysis of the fracture surfaces indicates that fluorite in the ZYTO system does not display any appreciable toughening mechanisms. Evidence of domain wall motion in *M*-$YTaO_4$ was reported for the first time. The mechanism underpins ferroelastic switching, which is the main toughening mechanism in 8YSZ, and may contribute to the toughness of $YTaO_4$-containing compositions.

7.5 Tables and Figures

Table 7.1 Summary of multi-phase samples investigated with micro-indentation.

Composition	Heat treatment	Grain size (approx) [μm]	% tetragonal	Toughness [J/m^2]	Standard Deviation [J/m^2]
28Y28Ta	100h 1350°C after 100h at 1350, 1400, 1450, 1500, 1550°C	5	57	30.2	4.9
40Y33Ta	24h 1500°C	0.75	0	26.4	4.2
40Y33Ta	100h 1700°C	4	0	15.2	2.8
40Y33Ta	100h 1500°C+100h 1700°C + 500h 1315°C	4	0	27.4	5.1

Table 7.2 Experimentally determined modulus values as well as modulus values available in the literature.

Phase	Measured Modulus [GPa]	Previously reported modulus [GPa]	Source
t'	208	200	[87Swa]
F + *YT*	152	190*	
F	--	222	[97Ada]
YT	138	184	[14Fen]

* Calculated based on phase fractions of *F* and YT in 40Y33Ta and previously reported moduli values for *F* and YT.

Table 7.3 Sample names, relative theoretical densities, anticipated and measured toughness values, and grain size.

Sample Composition	**Phases present**	**% theoretical density**	**Grain size [μm]**	**Anticipated toughness (based on indentation results)**	**Actual toughness, K_{1C} (G) MPa$\sqrt{m}$ [J/m^2]`**
8YSZ	*t'*	~98%	<1	higher (40J/m^2)	2.68 (34.5)
40Y33Ta27Zr	*F* + YT	~96%	~2	moderate (15-30J/m^2)	1.18 (9.2) 1.52 (15.1)
45Y5Ta50Zr	*F*	~88%	~20	low (~10J/m^2)	1.61 (11.6)
47.5Y47.5Ta	YT	~87%	~20	unknown	1.03 (7.6)

Measured modulus values in Table 7.2 were used to calculate the energy release rate, *G*. The previously reported value for fluorite (ZrO_2 + 12.2 mol% $YO_{1.5}$) was used to calculate *G* for 45Y5Ta.

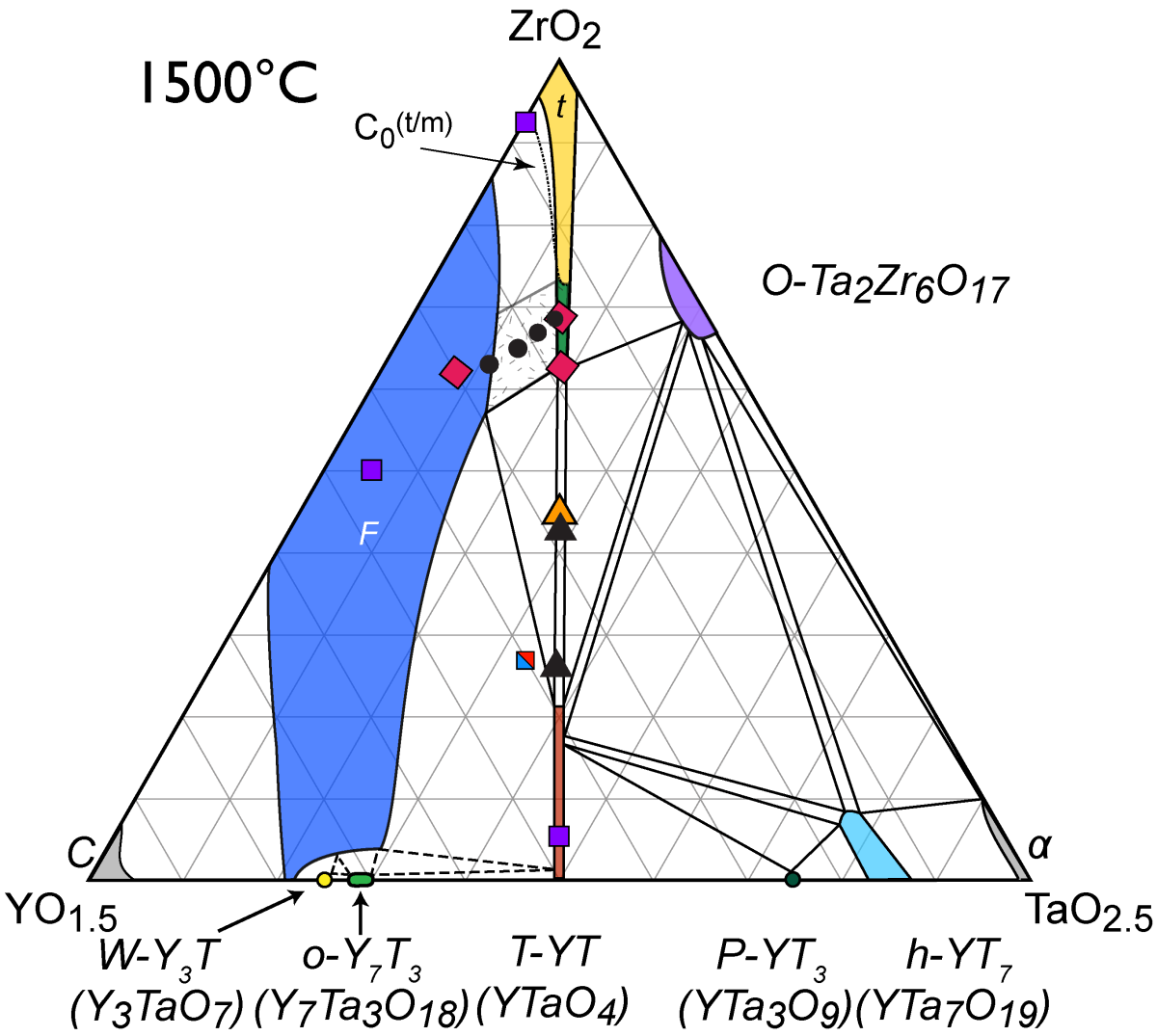

Figure 7.1 Compositions in the ZYTO system investigated with either micro-3-point bend (purple squares and blue/red square) or micro-indentation (orange triangle and blue/red square) in this work. Additional symbols are compositions investigated by S. Heinze (to be published) or F. Pitek [07Pit].

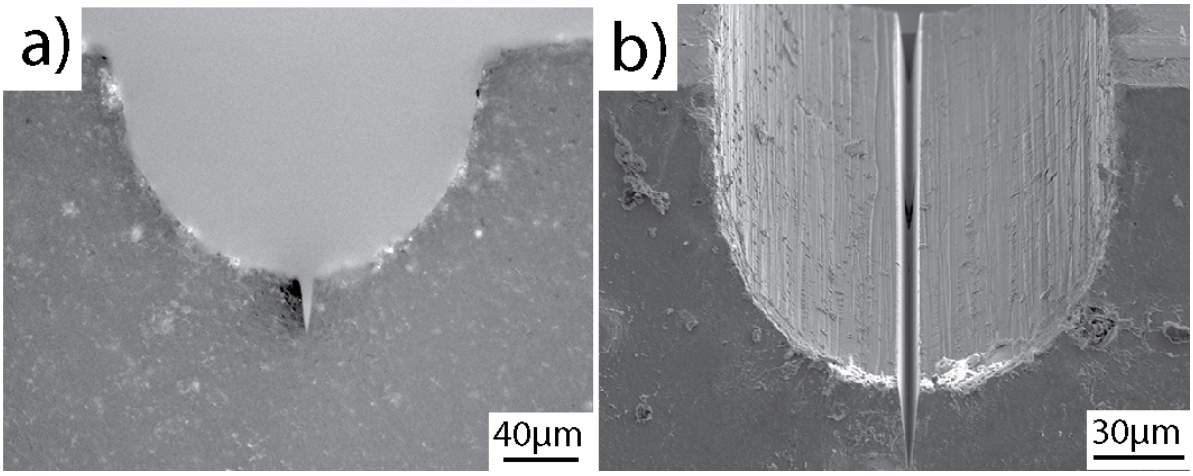

Figure 7.2 SEM images show pre-notch and pre-crack viewed (a) from the side and (b) at an angle of 52°.

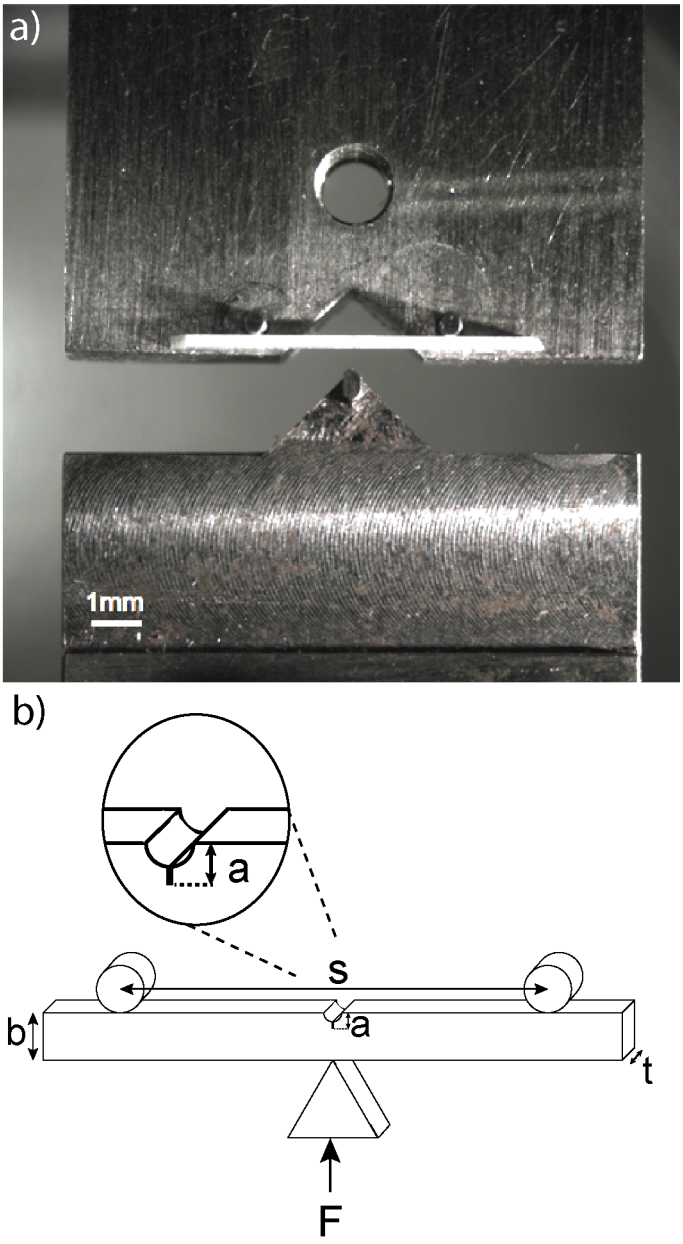

Figure 7.3 Photograph of a sample in the experimental set-up. (b) Schematic of the micro-bend experiment, including relevant variables. Schematic not drawn to scale.

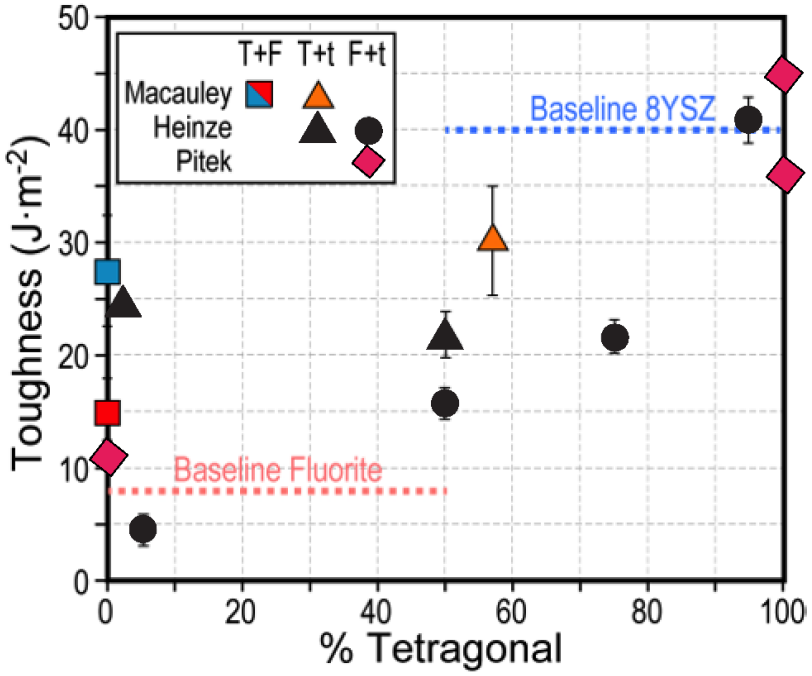

Figure 7.4 Toughness results for different two-phase combinations, except for the diamonds, which represent single-phase baselines. The squares at 0% tetragonal correspond to two-phase *F* + YT compositions, while the triangles are primarily YT + *t*, with a small amount of fluorite. Symbols correspond to the compositions shown in Figure 7.1.

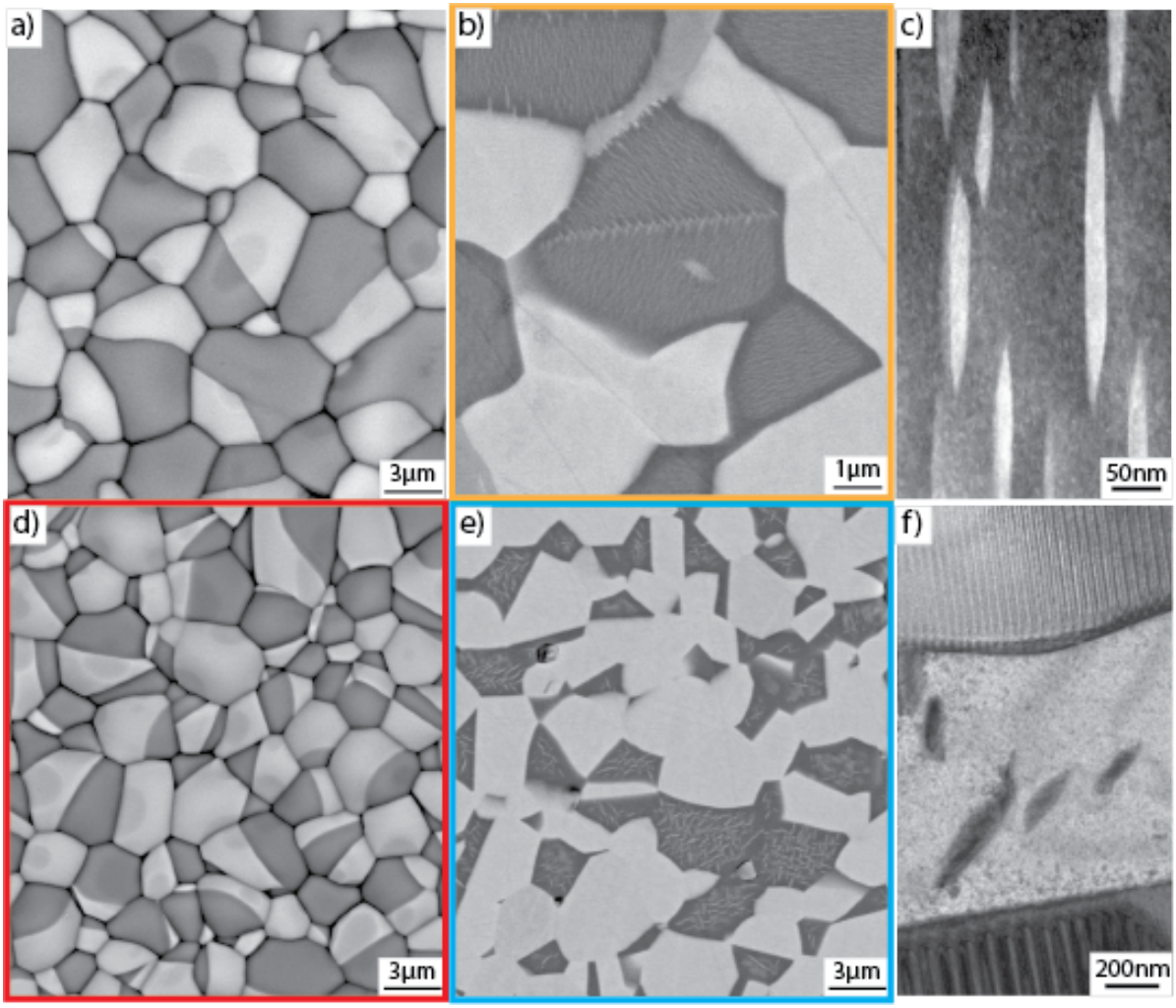

Figure 7.5 BSE images show *t*-ZrO_2 (dark) and $YTaO_4$ (light) are present in a sample at 28Y28Ta that was first heat treated for (a) 500h at T≤1550°C and then (b) at 1350°C for 100h. HAADF image along the $[100]_t$ in (c) clearly shows aligned precipitates of $YTaO_4$ in a matrix of *t*-ZrO_2. $[001]_t$ is to the right in the HAADF image. Similarly, BSE images indicate fluorite (dark) and $YTaO_4$ (light) are present in a sample of 40Y33Ta that was treated for (d) 100h at 1700°C followed by (e) 500h at 1315°C. (f) $YTaO_4$ precipitates in fluorite grains are present base on BF-TEM images.

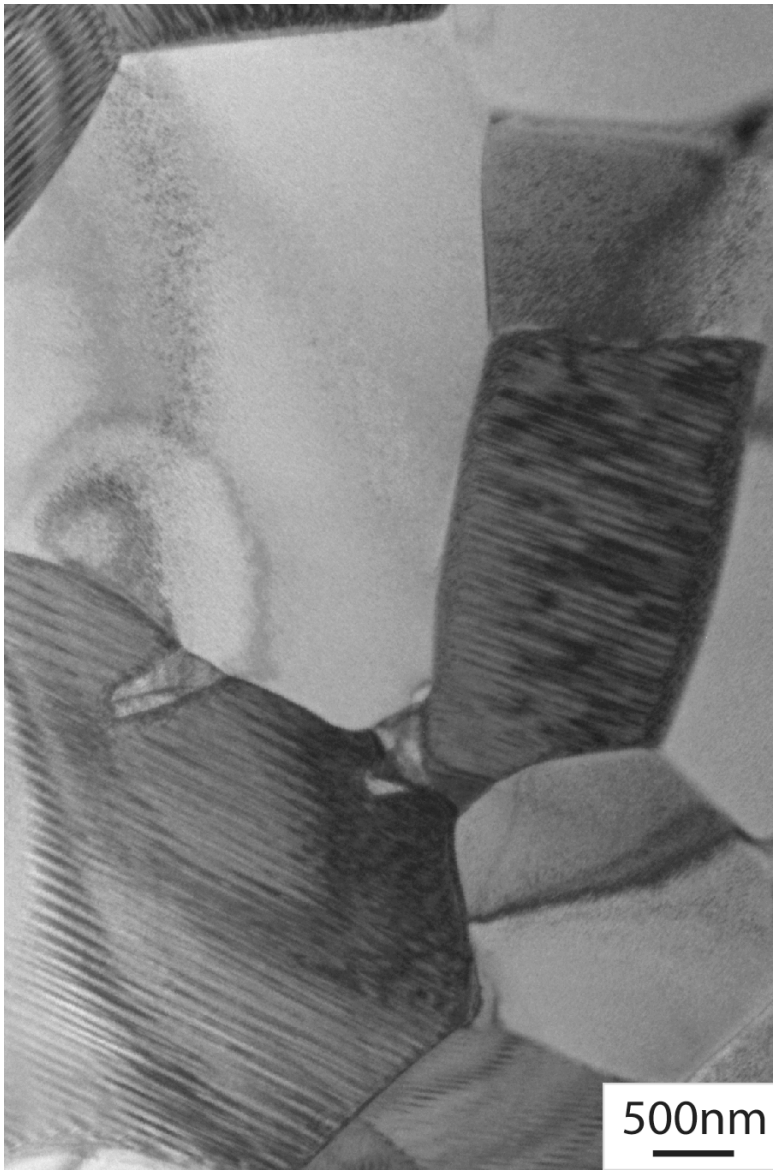

Figure 7.6 BF-TEM image indicates that after 100h at 1500°C, twinned *M*-YT (dark contrast) and *t*-ZrO_2 (light contrast) are present in 28Y28Ta.

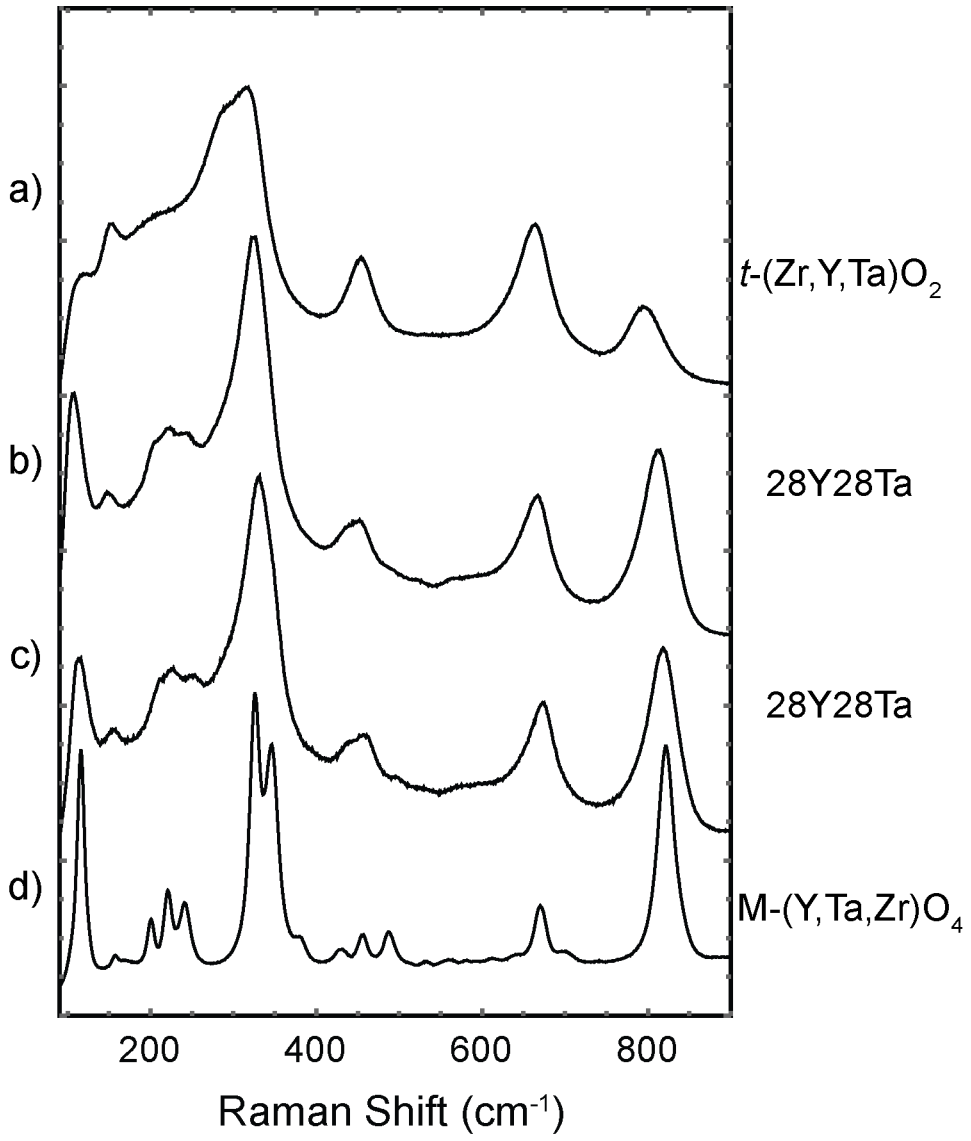

Figure 7.7 Raman spectra from 28Y28Ta after (b) 100h at 1500°C are identical to spectra in and around indents after being re-equilibrated at 1350°C, (c). Spectra from (a) *t*-ZrO_2 (16Y16Ta, 24h 1500°C) and (d) *M*-YT (47.5Y47.5Ta, 100h, 1500°C) are shown for reference.

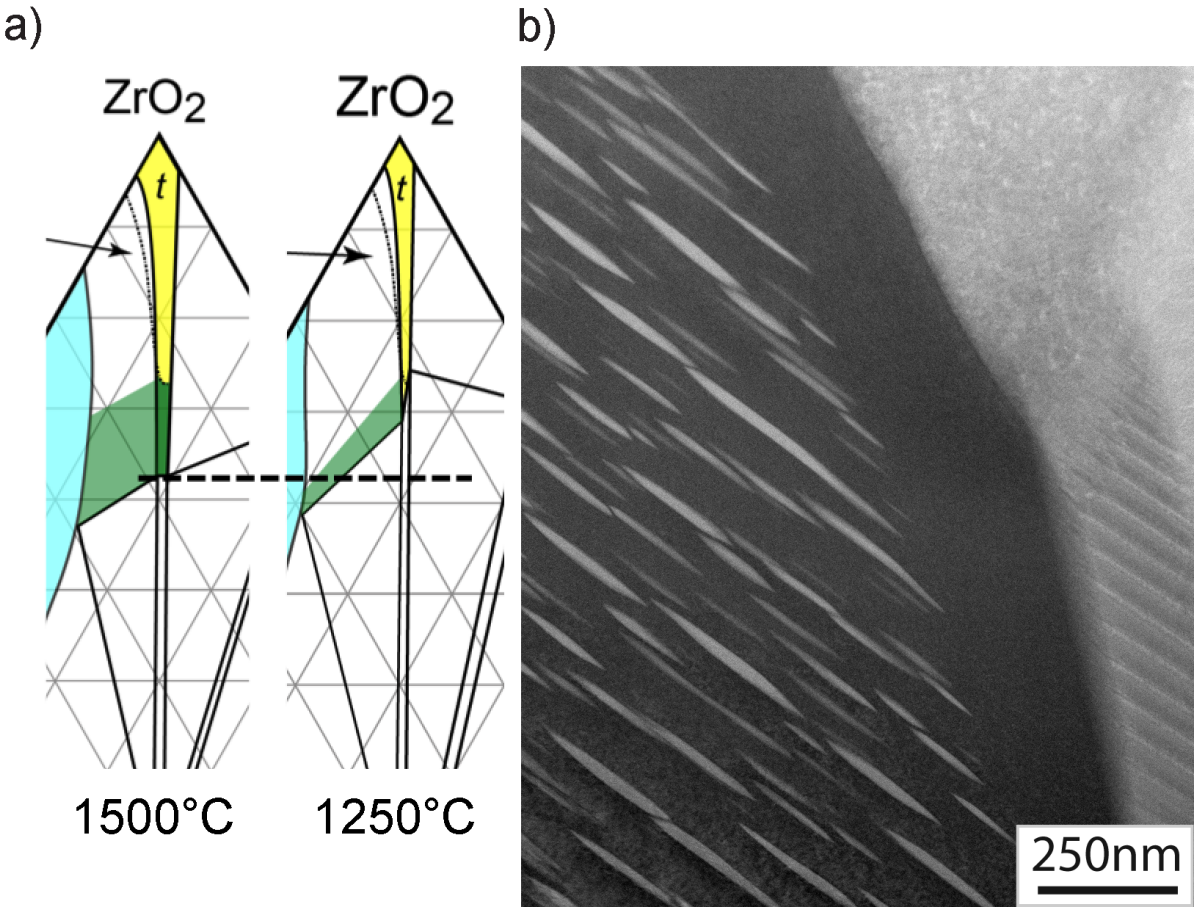

Figure 7.8 (a) The solubility of $YO_{1.5}$ and $TaO_{2.5}$ in *t* decreases at lower temperatures, resulting in precipitates of $YTaO_4$ within the *t* grains. (b) Additional HAADF image of 28Y28Ta (500h at T≤1550°C + 100h at 1350°C) effectively show the diffusion distance of Y and Ta in *t* at 1350°C.

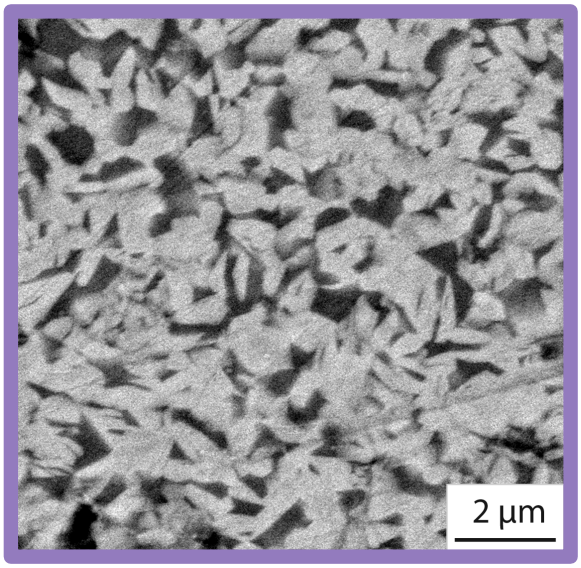

Figure 7.7.9 40Y33Ta after 24h at 1500°C. The grain size is approximately 750nm.

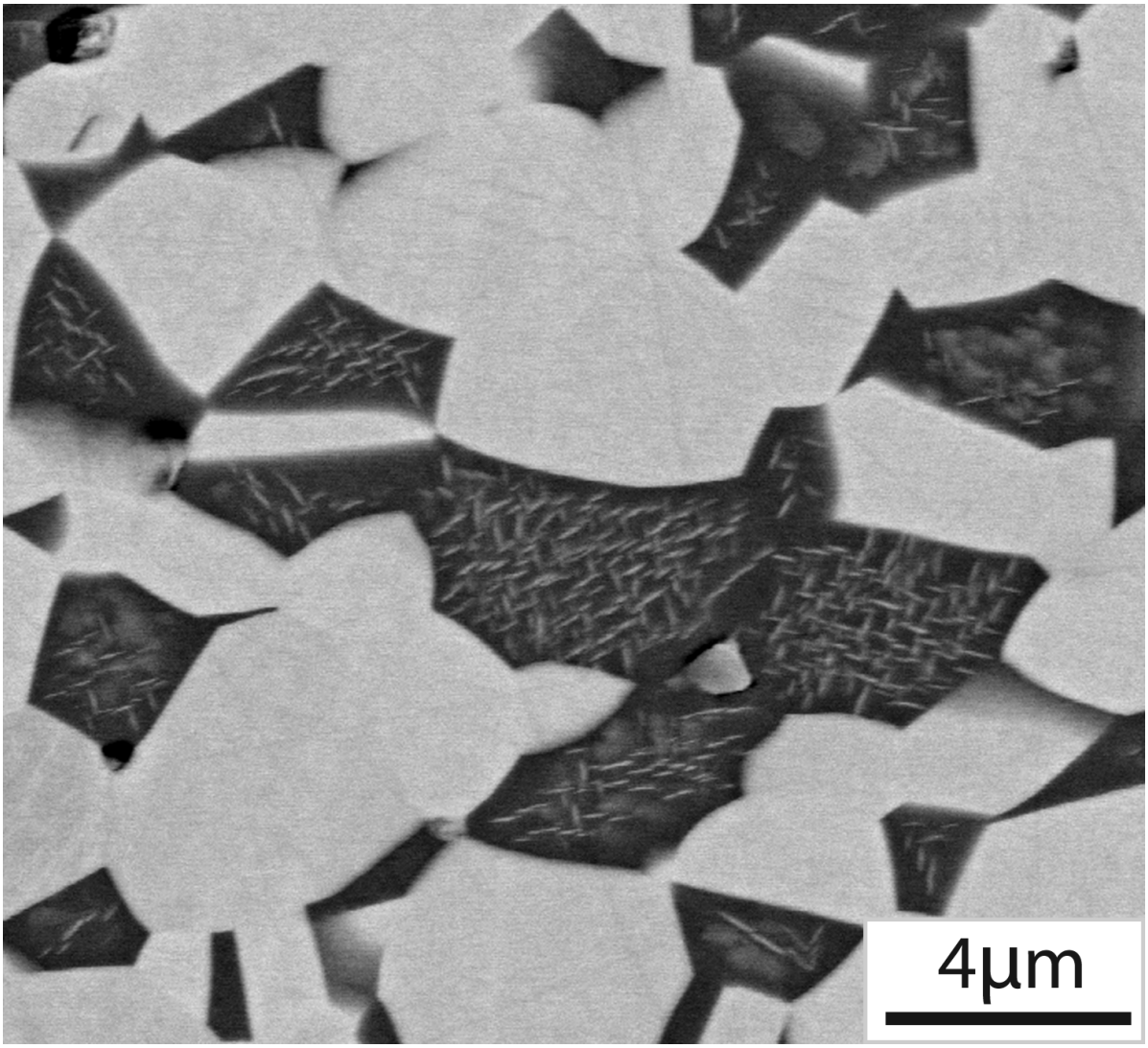

Figure 7.10 Higher magnification BSE image showing the different orientations of the $YTaO_4$ precipitates within the fluorite grains.

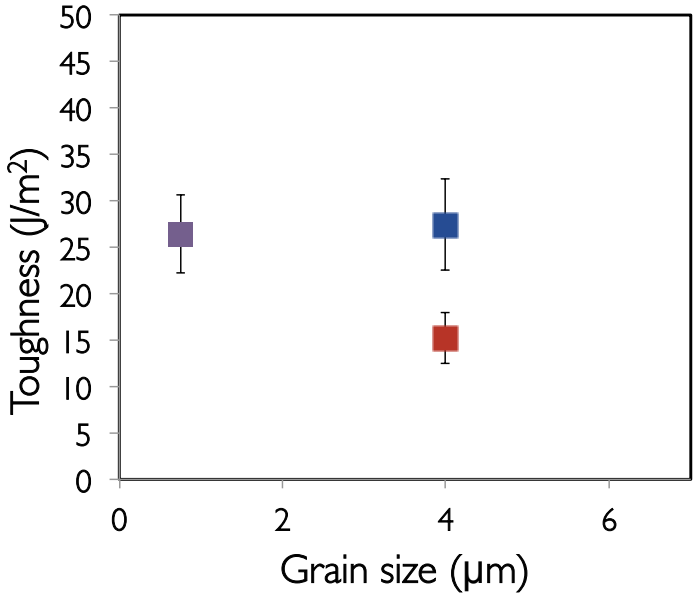

Figure 7.11 Toughness results from indentation of 40Y33Ta as a function of grain size. Purple square is after 24h at 1500°C, red square is after 100h at 1700°C and blue square is after the subsequent heat treatment at 1315°C for 500h. Microstructures are outlined in the same colors in previous figures.

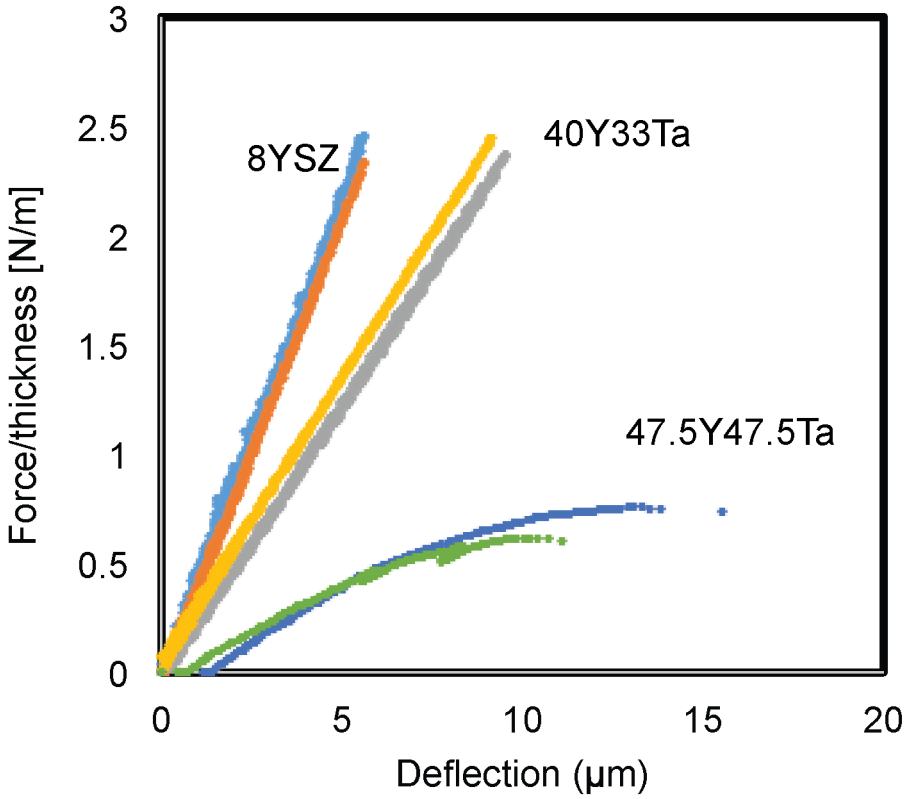

Figure 7.12 Load displacement curves used to measure the modulus of 8YSZ, 40Y33Ta and 47.5Y47.5Ta microbeam bending samples. Each color contains overlapping loading and unloading data for samples of 8YSZ and 40Y33Ta. Only loading curves are shown for 47.5Y47.5Ta, as the samples broke during the test. Applied force is divided by the thickness, *t*, of each beam as defined in Figure 7.3(b).

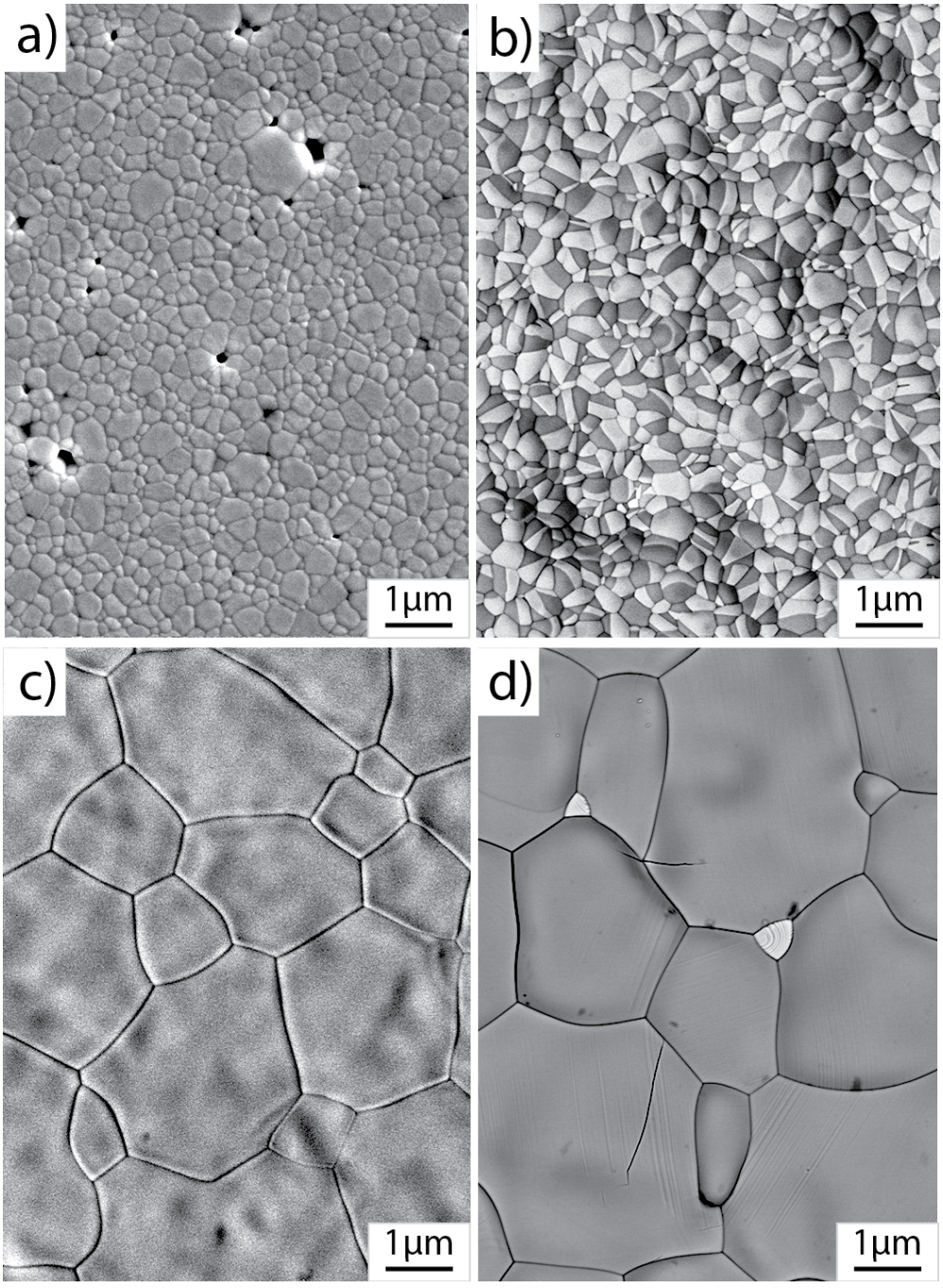

Figure 7.13 BSE images taken prior to fracture indicate the grain size and phase fractions in (a) 8YSZ, (b) 40Y33Ta, (c) 45Y5Ta, and (d) 47.5Y47.5Ta. $YTaO_4$ (light contrast) and fluorite (dark contrast) are present in 40Y33Ta. Small amounts of YTa_3O_9 (light contrast) are present in a matrix of $YTaO_4$ (dark contrast) in 47.5Y47.5Ta.

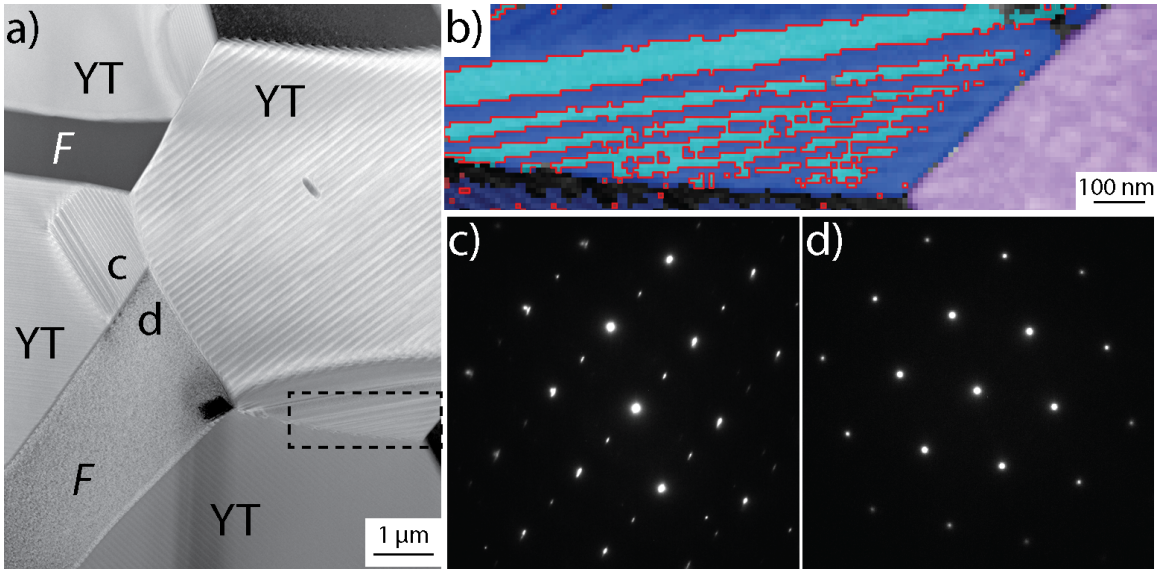

Figure 7.14 Twins visible in the (a) HAADF image of the two-phase, F+YT, 40Y33Ta sample show that $YTaO_4$ is present as M-YT. The red lines in the TKD image (b) indicate a 85° rotation around the $0\bar{1}0$ axis. SAED patterns from the $(111)_{F,}$ (c) and $(\bar{2}12)_{MYT}$ (d) zone axes were taken from locations indicated in (a). They suggest there is an orientation relationship between F and YT. TKD performed at University of Sydney with Dr. P. Trimbly.

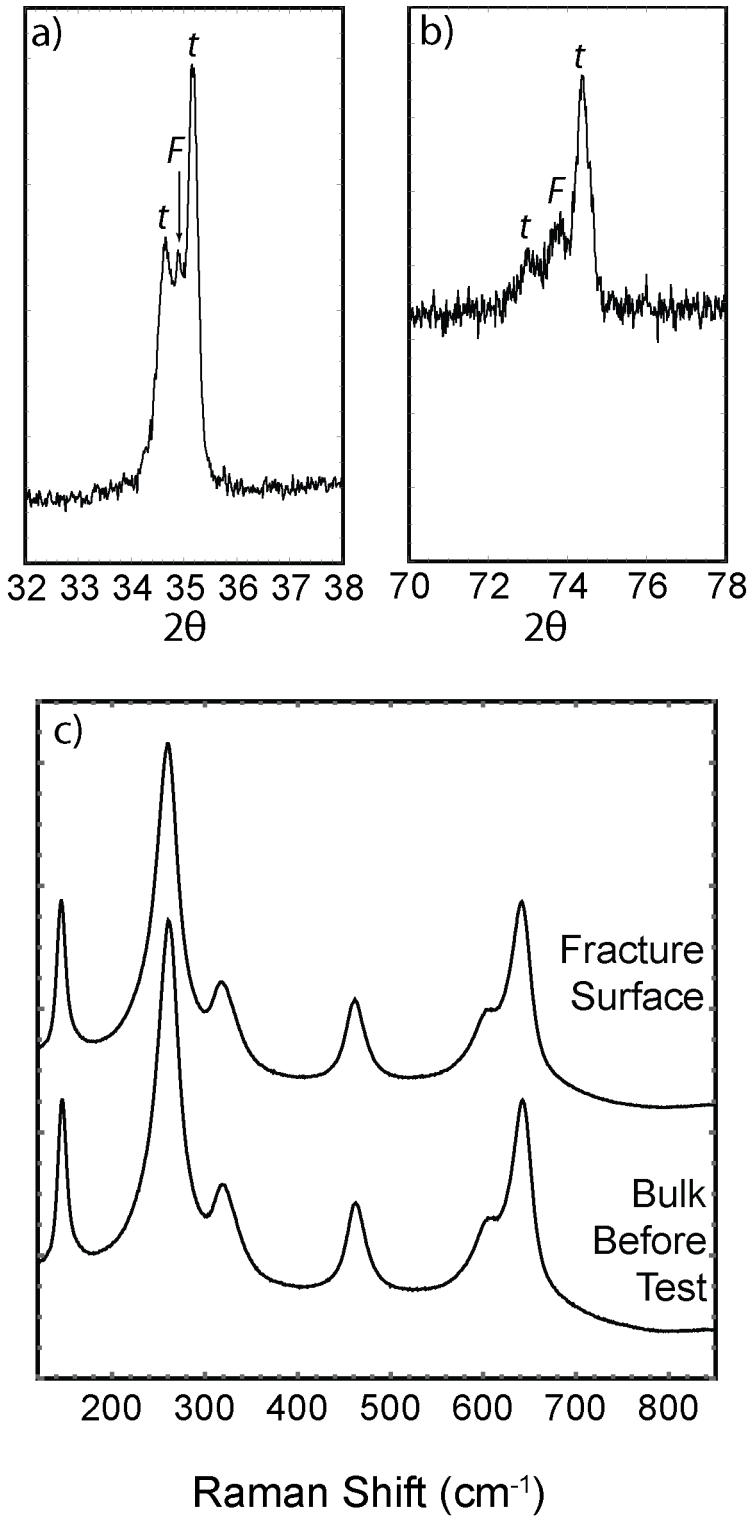

Figure 7.15 (a) and (b) *t* and *F* peaks are evident in the XRD of 8YSZ prior to the fracture experiment. (c) All peaks in the Raman spectra of 8YSZ before and after fracture can be attributed to *t* [09Mil]. Monoclinic (*m*) ZrO_2 is not observed.

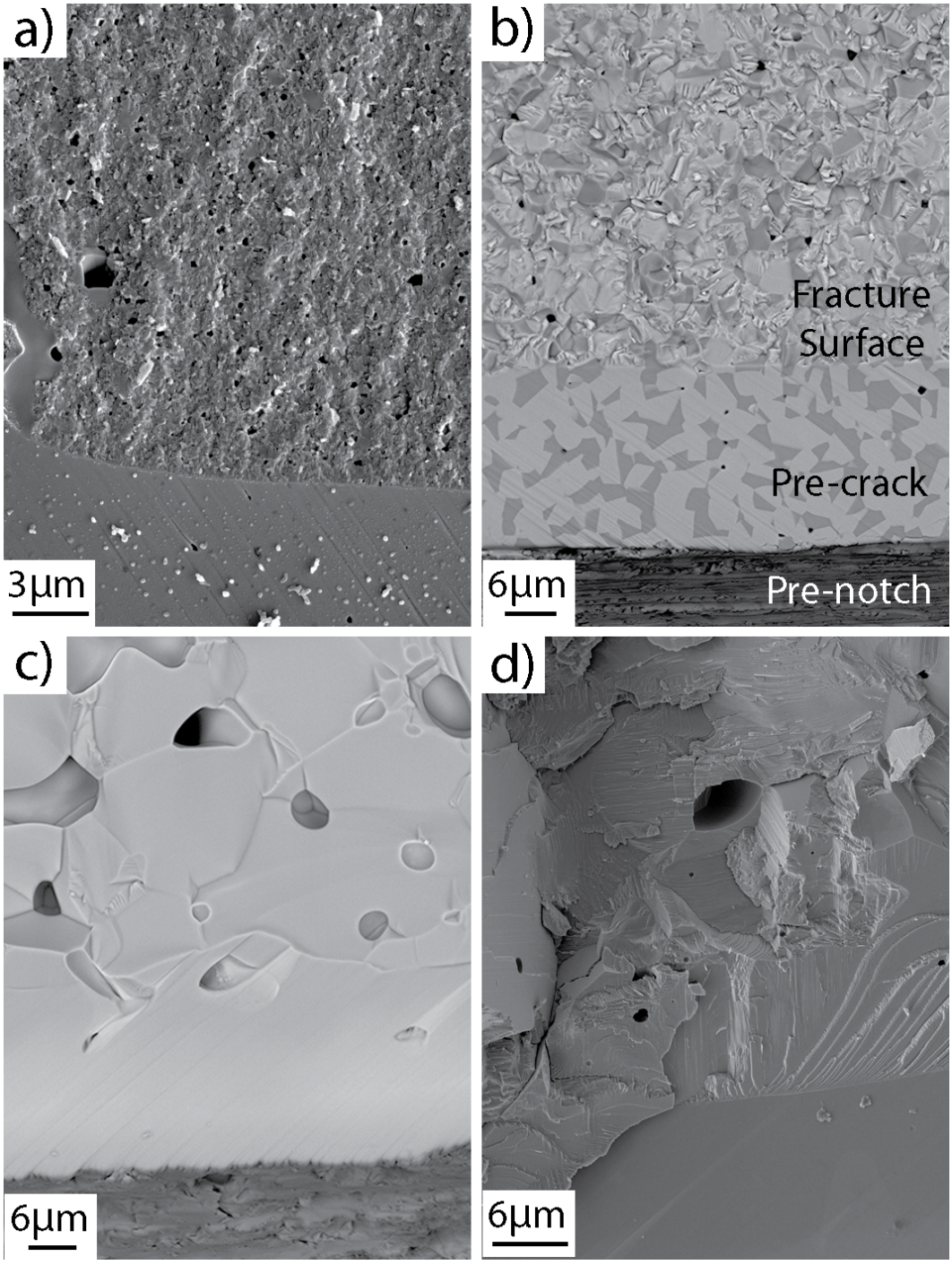

Figure 7.16 BSE images of the fracture surface of (a) 8YSZ, (b) 40Y33Ta, (c) 45Y5Ta, and (d) 47.5Y47.5Ta. In (b) and (c) the "pre-notch" is visible at the bottom of the image followed by the smooth surface of the FIB pre-crack. In (a) and (b) only the pre-crack is visible. Note the magnification of 8YSZ is approximately double that of the other samples.

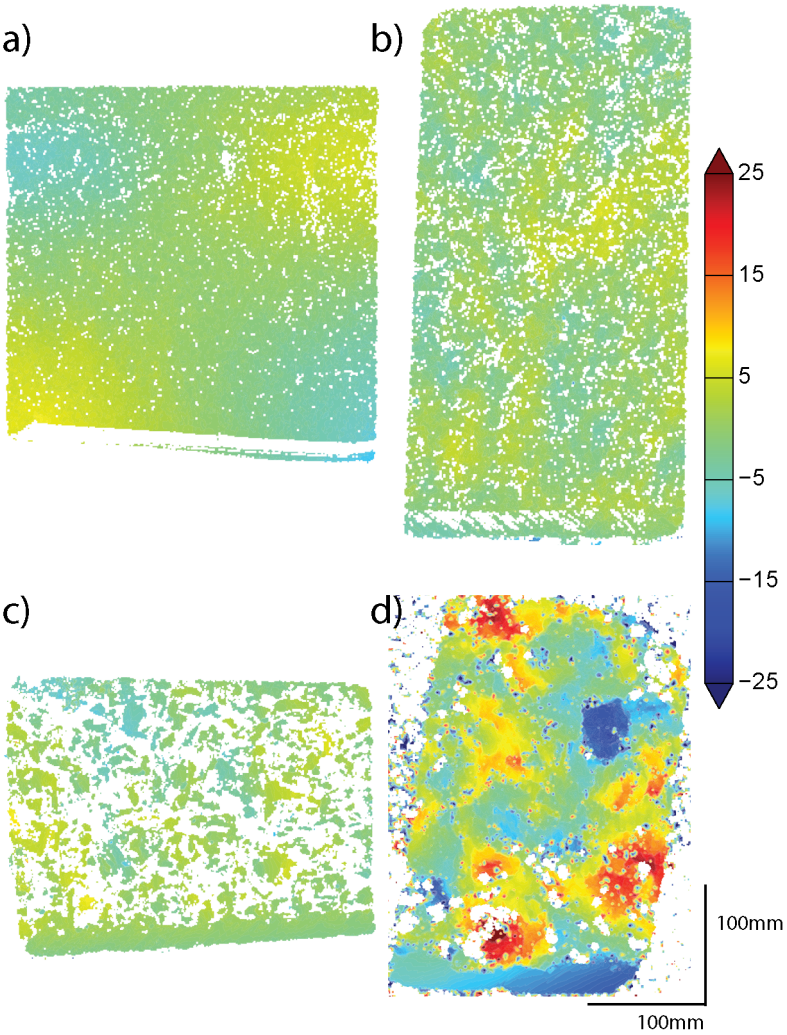

Figure 7.17 Optical profilometry of (a) 8YSZ, (b) 40Y33Ta, (c) 45Y5Ta, and (d) 47.5Y47.5Ta shows differences in roughness of the fracture surfaces. The pre-notch is at the bottom of each scan. The units of the colors are in micrometers.

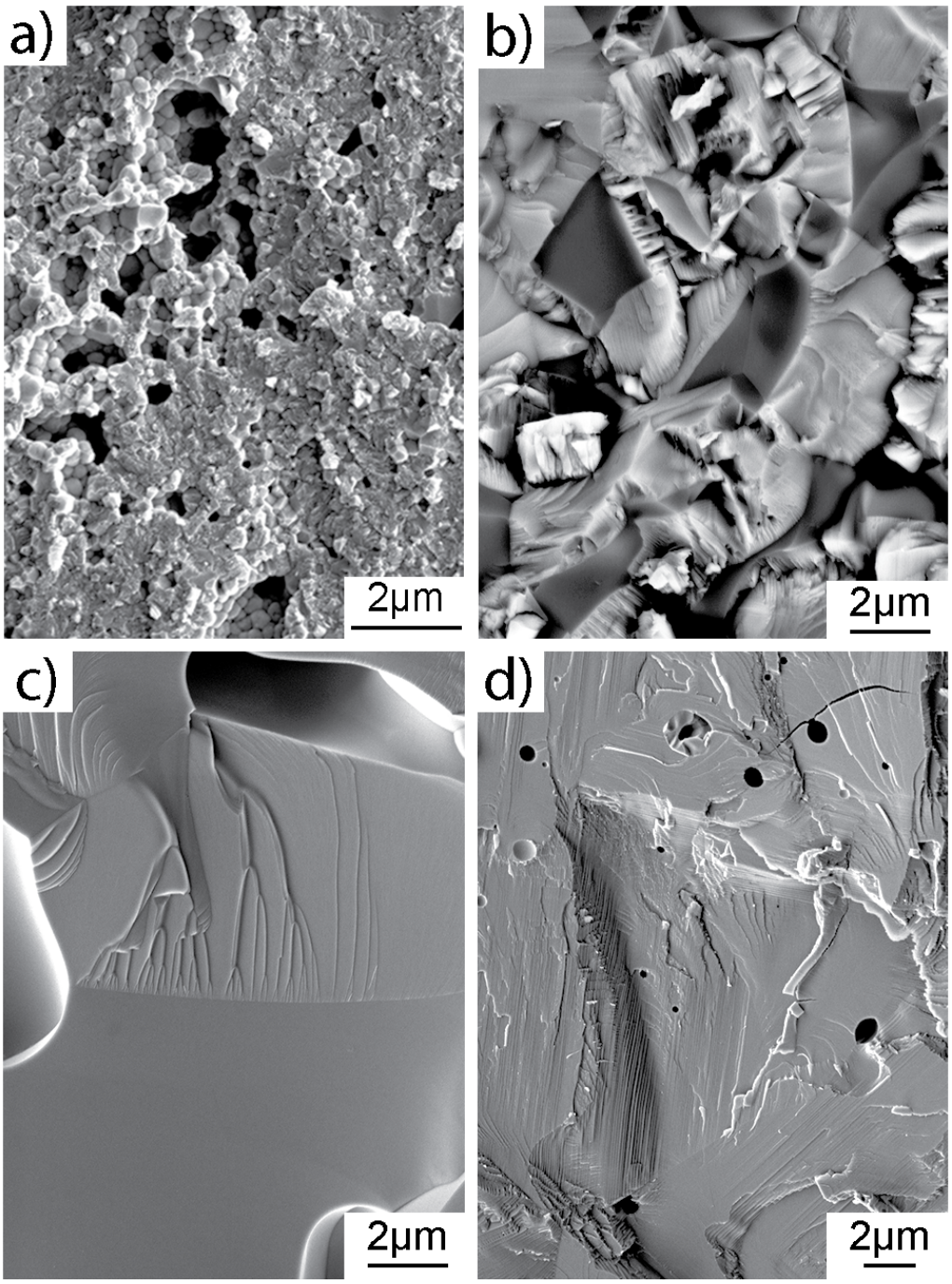

Figure 7.18 Higher magnification BSE images of (a) 8YSZ, (b) 40Y33Ta, (c) 45Y5Ta, and (d) 47.5Y47.5Ta suggest the fracture behavior changes with crystal structure. (a) Grains are too small in 8YSZ to discern toughening mechanisms. (b) Fracture surface of *M*-$YTaO_4$ (light) grains is significantly rougher than that of fluorite (dark) grains. (c) classic "river marks" are observed in fluorite (45Y5Ta) suggesting that there are not any significant toughening mechanisms active in fluorite. (d) Surface relief on the same scale as the twins in *M*-$YTaO_4$ is observed on the fracture surface of 47.5Y47.5Ta. Crack propagation direction is upward in each image.

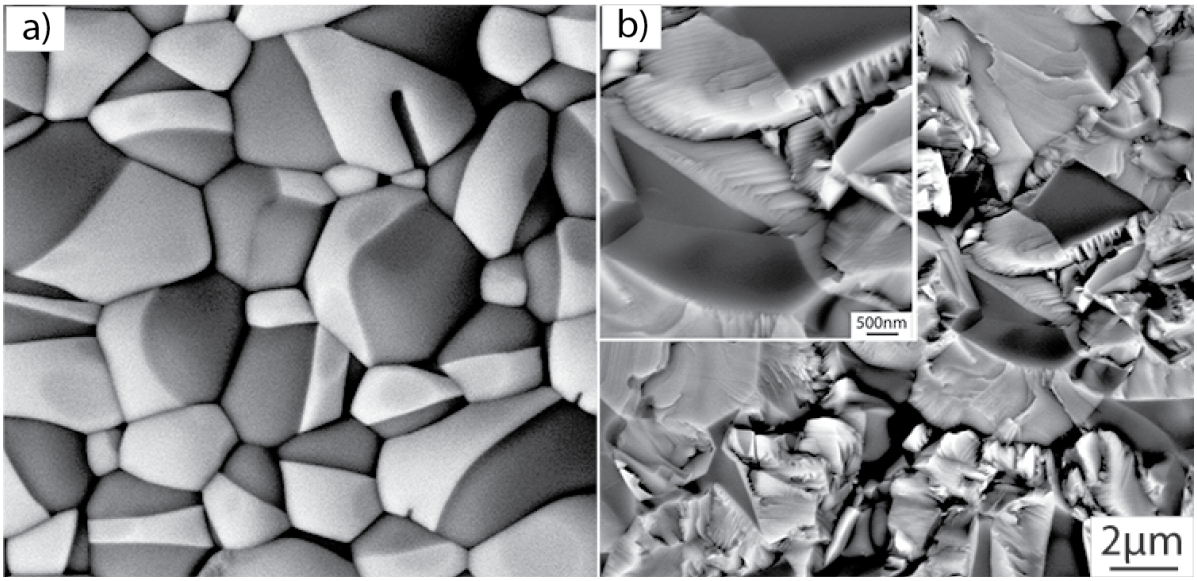

Figure 7.19 Additional BSE images of 40Y33Ta (a) before and after (b) fracture.

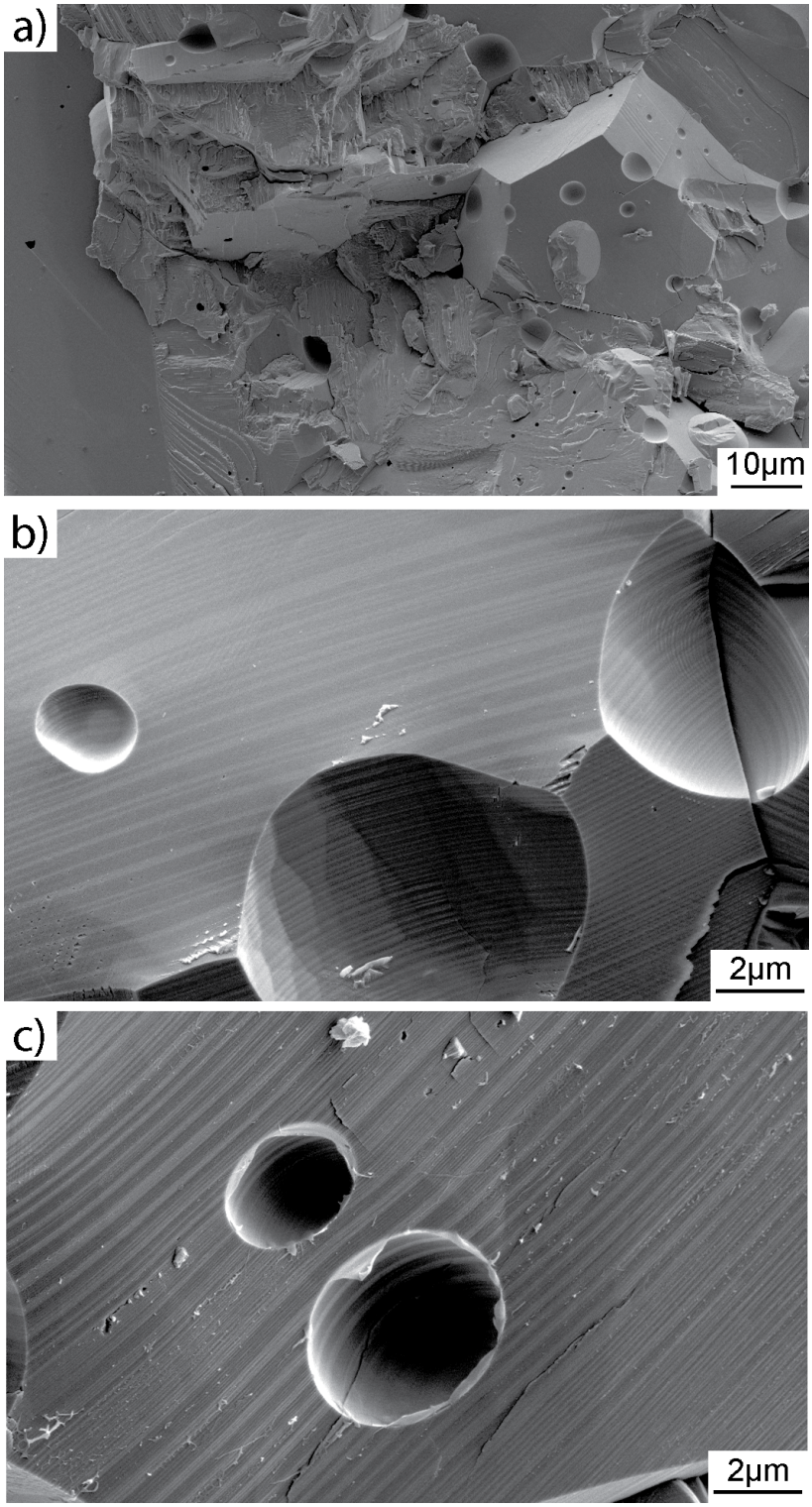

Figure 7.20 Additional BSE images of 47.5Y47.5Ta fracture surface show (a) trans- and (b) and (c) intergranular fracture. Striations are present on the surface of grains on the fracture surface that are of the same length scale as the twin domains in *M*-$YTaO_4$.

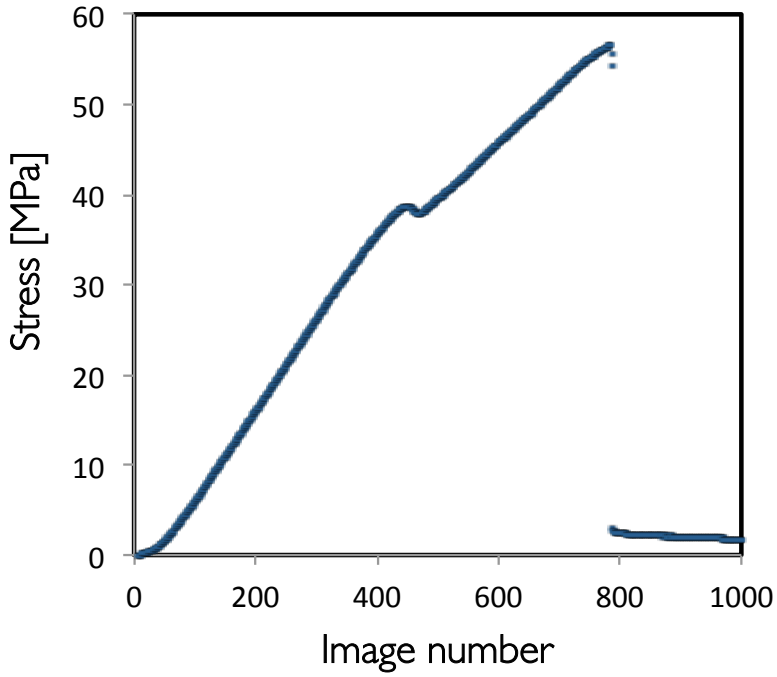

Figure 7.21 Measured stress as a function of image number during the three-point bend test of 47.5Y47.5Ta. At a stress of ~56.5MPa the sample broke.

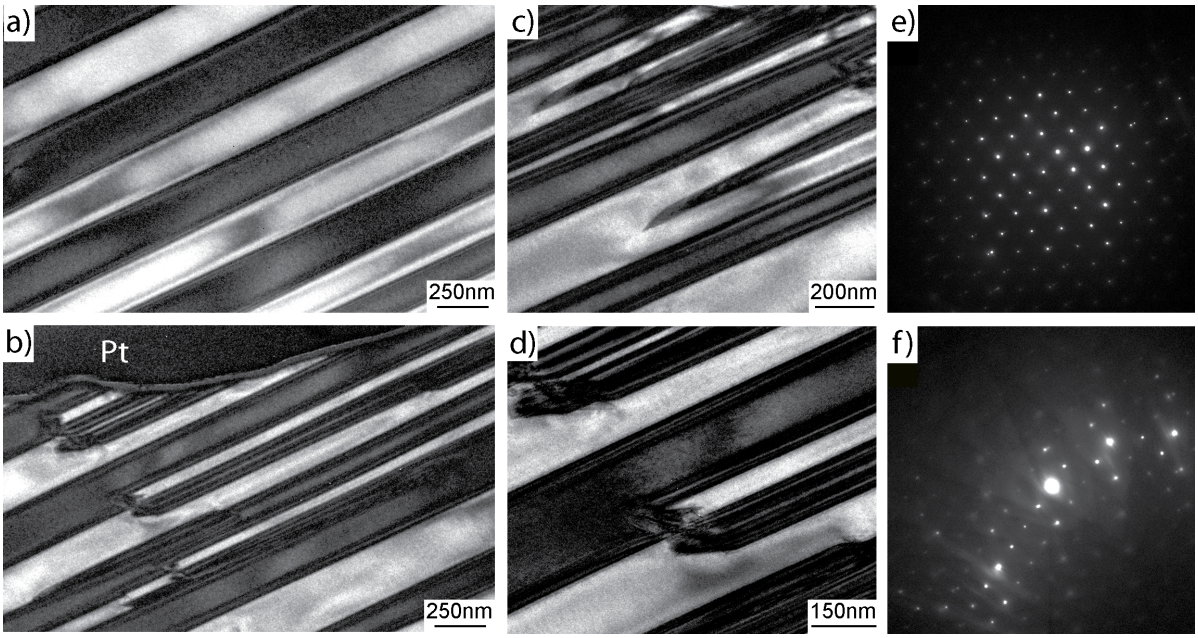

Figure 7.22 BF-TEM images away from the fracture surface (a) show the two *M*-$YTaO_4$ twin domains. At the fracture surface (b-d) the domain walls are no longer continuous and likely moved during the fracture event. In all BF images, the crack is propagating from right to left. In the BF images, the dark twins are oriented along the 111 *M*-$YTaO_4$ zone axis, (e). A SAED pattern also indicates the zone axis of a (f) light twin.

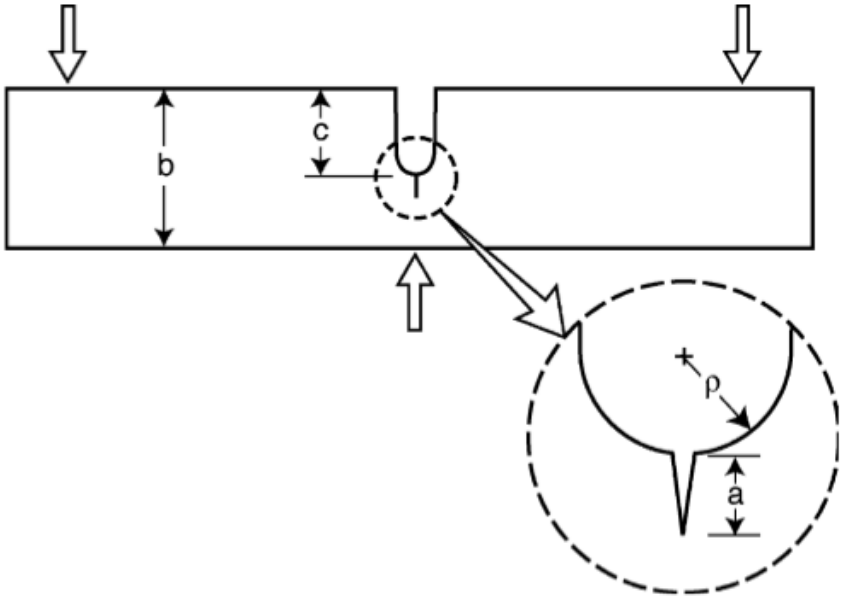

Figure 7.23 Schematic from [05Bos] used in the determination of a critical pre-crack length necessary for the pre-notch + pre-crack to act as a single sharp crack.

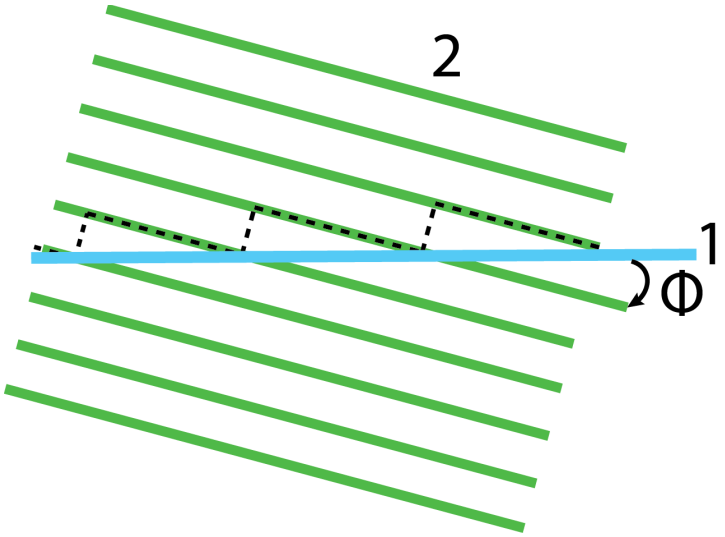

Figure 7.24 Schematic based on [99Hul, 93Law] depicting the origin of river patterns on the fracture surfaces of brittle materials.

CHAPTER 8: CONCLUSIONS AND OUTLOOK

The overarching objective of this work is to understand the phase equilibria and toughness of thermal barrier coatings (TBCs) that have the potential to exhibit superior combinations of properties to the industry standard 8 ± 0.5mole% $YO_{1.5}$-stabilized zirconia (8YSZ). The compositions investigated can be categorized into two groups: (i) single-phase, non-transformable tetragonal compositions that have adequate toughness and (ii) two-phase compositions that enable the combination of adequate toughness and CMAS resistance.

All of the preliminary phase equilibria and toughness investigations in the CeO_2-TiO_2-ZrO_2 (CeTiSZ) system had been conducted with precursor-derived samples. This part of the dissertation focused on elucidating the challenges associated with transitioning the earlier laboratory results to industrial-scale coatings. As-deposited air plasma sprayed (APS) coatings were found in a prior study to exhibit toughness values comparable to that of 8YSZ coatings, ascribed to a synergism between the high tetragonality of the crystal structure in the selected CeTiSZ compositions, and the segmented architecture that enhanced the work of fracture. However, there is evidence of segregation in the powder used to make the coatings, as well as in the as-deposited coatings themselves. As a result, the earlier solidification product becomes transformable to monoclinic upon cooling, even if the original composition was in the non-transformable region of the phase diagram. Moreover, the coatings exhibit accelerated sintering upon heating above 1500°C, presumably associated with evidence of liquid present at the heat-treatment temperature. An estimate of the liquidus surface in the ternary based on the constituent binary systems suggests a large driving force for segregation during solidification, consistent with experimental results, providing insight that will be critical to consider for other novel TBC compositions. The unexpected presence and extent of a liquid phase in coatings as well as precursor-derived samples indicates the observed degradation is also rooted in the inherent thermodynamics of

the system, rather than the kinetics of the deposition process. The reduction of at least one of the cations occurs at high temperatures, changing the phase equilibria. Although an understanding of the ternary phase equilibria involving Ce_2O_3 is needed to fully explain the presence of a liquid phase at high temperature, the importance of maintaining a constant oxidation state is evident. The reduction of Ce^{4+} places an inherent limit on the temperature capabilities of CeTiSZ coatings. This work then brings out two important effects not previously encountered in the deposition of YSZ or even pyrochlore based TBCs. One relates to the importance of segregation during deposition in preserving the phase stability of the coating, and the other relates to the potential reducibility of the cations upon heating, which can lead to unfavorable changes in the phase equilibria.

The main system of interest to this thesis is ZrO_2-$YO_{1.5}$-$TaO_{2.5}$ (ZYTO) system, which also exhibits a stable, non-transformable tetragonal phase at temperatures as high as 1500°C, albeit in a much narrower composition range, but does not experience reduction of the cations upon heating. The ZrO_2-rich region of the ternary had been studied previously, but there was a paucity of information on the phase equilibria in the rest of the diagram. Specifically the $YO_{1.5}$-$TaO_{2.5}$ binary phase diagram had only been investigated above 1600°C or below $YO_{1.5}$-concentrations of 50 mole%. Systematic investigation of the entire binary phase diagram elucidates the equilibrium phases and serves as a solid foundation for the investigation of the ZYTO ternary isothermal sections at 1250°C and 1500°C. The study reveals the temperature and composition ranges at which the various phases of $YTaO_4$, YTa_3O_9 and YTa_7O_{19} are stable. However, questions still remain regarding the crystallographically similar orthorhombic phases near 75 mole% $YO_{1.5}$. High temperature synchrotron x-ray diffraction is needed to identify the actual equilibrium structures at 1500°C. Given the importance of the liquidus in influencing the microstructure evolution during deposition of coatings via air plasma spray, it would also be valuable to study the liquidus of the $YO_{1.5}$-$TaO_{2.5}$ binary.

Using the newly acquired understanding of the $YO_{1.5}$-$TaO_{2.5}$ binary in combination with information in the ZrO_2-$YO_{1.5}$ and ZrO_2-$TaO_{2.5}$ binary phase diagrams, ternary isothermal sections were proposed and subsequently experimentally determined at 1250°C and 1500°C. The elucidation of the complete isothermal sections reveals several intriguing results. The quasibinary between $YTaO_4$ (YT) and tetragonal (*t*) zirconia is illuminated, correcting a previously published phase diagram that had been computationally generated. The extension of the *t* and YT phase fields to high equimolar concentrations of dopants are a result of the charge compensating stabilization mechanism in the system. At both temperatures, $YO_{1.5}$-rich compositions exhibit remarkable resistance to coarsening and densification, a property that is advantageous for the desired TBC application but problematic for compositional analysis. Interestingly, all phases in the $YO_{1.5}$-rich corner of the ternary are derivatives of the fluorite crystal structure. The presence of a large two-phase field in which *F* and YT are stable has also been identified. Such a large compositional space is promising because *F*, with sufficient rare earth content, can mitigate damage caused by molten silicates (calcium magnesium alumino-silicates, CMAS) by forming a desirable reaction product with the structure of $Ca_2RE_8(SiO_4)_6O_2$ apatite. Preliminary studies also indicate that compositions rich in YT react with CMAS to form a crystalline reaction product with potential to mitigate damage caused by molten silicates. While the details are still under investigation, the results motivate the investigation of multiphase compositions that have the potential to exhibit combinations of properties that are not currently available in single-phase TBCs.

Toughness is also an essential property of TBCs. Much was still unknown about the toughness and toughening mechanisms of compositions in the ZrO_2-lean portion of the ZYTO phase diagram. To remedy this, two approaches were pursued on single- and multiphase compositions in the ZYTO system. Micro-indentation toughness tests suggest that although two-phase, *t* + YT or *F* + YT compositions exhibit lower toughness than tetragonal 8YSZ, they have higher toughness than would be expected based on the amount

of *t* present. Thus it is evident that YT contributes to the toughness and two possible toughening mechanisms are suggested. Samples containing precipitates of YT embedded in an *F* or *t* matrix are tougher than the same compositions without precipitates. It is posited that transformation toughening involving the $T \rightarrow M$-YT transition can be activated by constraining *T*-YT precipitates below the transition temperature, analogous to transformation toughening in partially stabilized zirconias. However additional work is needed to verify the crystal structure of the precipitates. To rule out any additional toughening from the large *M*-YT grains, additional studies on *F* samples with YT precipitates should be conducted.

The second approach to understanding the toughness of ZrO_2-lean samples involves the development and utilization of a micro-three-point bend technique. Capitalizing on the distinct advantage of this approach, toughening mechanisms are illuminated by characterizing the fracture surfaces of each composition. Samples containing the fluorite crystal structure exhibit fracture surfaces characteristic of brittle fracture. It is shown for the first time that samples containing YT exhibit microstructural features clearly consistent with domain wall motion, the central mechanism underpinning ferroelastic toughening. While evidence of domain wall motion in $YTaO_4$ is presented for the first time, a fundamental understanding of the mechanics of domain motion and a more precise description of the contributions of coercive stress, process zone size etc. are needed to fully exploit the mechanism. Both first principles calculations and in-situ observations of similar tests using STEM capabilities in the SEM may prove invaluable in advancing the understanding of these mechanisms.

APPENDIX A: ADDITIONAL STUDIES IN THE ZYTO SYSTEM

While phase stability and adequate toughness are central to this dissertation, preliminary studies of other thermal barrier coating (TBC) properties, such as the ability to mitigate damage from molten silicates (CMAS), are also of interest but had not been previously investigated. In addition, the performance of compositions in the CeO_2-TiO_2-ZrO_2 (CeTiSZ) highlight the importance of oxidation state stability at high temperatures, since a change in cation valence has the potential to significantly change the phase equilibria. To depict a more complete picture of the ZrO_2-$YO_{1.5}$-$TaO_{2.5}$ (ZYTO) system, preliminary investigations of the oxidation state stability and resistance to molten silicates are presented in this appendix.

A.1 Background

As operating temperatures continue to increase to meet the efficiency targets of next generation gas turbines, additional TBC failure mechanisms due to siliceous contaminants known as calcium-magnesium alumino-silicates (CMAS) arise [12Lev]. To mitigate damage caused by molten silicates, TBC compositions must react with the melt quickly to produce a volume of precipitated products that sufficiently fill the spaces between TBC columns, preventing further infiltration [08Kra2]. Current zirconate ($RE_2Zr_2O_7$) TBCs rely on the precipitation of apatite ($Ca_2RE_8(SiO_4)_6O_2$ where RE = La, Nd, Sm, Gd, Y, Yb) to prevent infiltration [08Kra2, 15Poe]. High concentrations of RE, of order 50 mole% (cation base), are needed to effectively mitigate molten silicate attack. At present, other reaction products that have sufficiently fast precipitation kinetics to block infiltration are not known. The CMAS-resistance of compositions in the ZrO_2-lean portion of the ZYTO phase diagram has previously not been investigated.

A.2 Experimental details

TBC compositions were synthesized via reverse co-precipitation and pyrolyzed for 4h at 650°C, as described in Chapter 3. A pellet with the composition 40Y33Ta (light green circle in Figure A.1) was sintered for 100h at 1500°C prior to performing thermogravimetric analysis (TGA). All compositions will be presented in single cation units of $YO_{1.5}$ and $TaO_{2.5}$ with the balance ZrO_2, e.g. 40Y33Ta is 40 mole% $YO_{1.5}$, 33 mole% $TaO_{2.5}$, 27 mole% ZrO_2. In the TGA, the pellet was heated at a rate of 25°C/min up to 1500°C where it was held for 1h. The cooling rate was 15°C/min.

To assess the ZYTO system's ability to mitigate CMAS infiltration, 45Y15Ta (orange dot) and 37Y41Ta (blue dot), which were sintered for 100h at 1500°C, were studied, Figure A.1. As described in detail in Chapter 3, thin pellets of CMAS with the composition 33 mol% CaO – 9 mol% MgO – 13 mol% $AlO_{1.5}$ – 45 mol% SiO_2 [06Kra], were used in the experiments. The CMAS loading on the ZYTO pellets was approximately 20mg/cm^2. The reaction took place during a 4h heat treatment at 1300°C.

X-ray diffraction (XRD) was used to determine the phases of the ZYTO pellets prior to reaction with CMAS. Preliminary characterization of the CMAS-reacted samples was performed using backscattered electron (BSE) imaging on an FEI XL30 FEG scanning electron microscope (SEM). Chemical compositions were determined using energy dispersive x-ray spectroscopy (EDS) on the SEM. Lα EDS lines were used for Y, Ta and Zr while Kα EDS lines were used for Ca, Mg, Al, and Si. Oxygen was not measured but it was assumed, based on prior experience, that each cation was fully oxidized.

Transmission electron microscopy (TEM) was used to study the reaction products of 37Y41Ta. A TEM lamella was extracted using a focused ion beam (FIB). TEM was conducted utilizing bright field (BF) imaging.

A.3 Results

A.3.1 High temperature oxidation state stability

Negligible mass change is evident in the TGA results of 40Y33Ta as a function of temperature or time at 1500°C, Figure A.2(a) and (b), respectively. For the sake of comparison, the y-axis scale is the same as that used for the TGA results of the composition 14Ce14Ti in the CeO_2-TiO_2-ZrO_2 (CeTiSZ) system in Chapter 4. This confirms the previous assumption that the cations in ZYTO are not subject to any significant reduction or oxidation in the temperature range and atmosphere of interest.

A.3.2 CMAS resistance

The pellet of 45Y15Ta, which was single-phase fluorite by XRD, contained extensive porosity, similar to other samples in this region studied in Chapter 6. The porosity enabled the pellet to be completely infiltrated with CMAS. The reaction zone between the CMAS and 45Y15Ta sample is evident on the exposed surface depicted in Figure A.3. Within the reaction zone, Figure A.4(a) and (b), high aspect ratio grains are observed. Unstandardized SEM-EDS revealed these grains had a composition of ~15 mol% CaO, 36 mol% SiO_2, and 41 mol% $YO_{1.5}$ with 4 mol% ZrO_2 and small (~1mole%) amounts of $AlO_{1.5}$, MgO, and $TaO_{2.5}$.

The sample 37Y41Ta was mostly $YTaO_4$ (YT) but also contained small amounts of YTa_7O_{19} (YT_7) and orthorhombic, *O*-$Ta_2Zr_6O_{17}$ (*O*). It was the only sample that was not completely infiltrated and still had a glass deposit of CMAS on top at the end of the test, Figure A.5(a). The molten CMAS filled the cracks that were present in the sample from initial processing. A BSE image, Figure A.5(b), of the top of 37Y41Ta shows the glassy CMAS deposit (darkest contrast, right side of figure) as well as the reaction zone between the CMAS and unreacted TBC (grey contrast). The reaction zone is more clearly observed in higher

magnification BSE images from the top surface of the sample, Figure A.6(a-c). Trace amounts of YT_3 (white contrast) and *O* (dark grey contrast) are visible surrounded by YT (light grey contrast) within the unreacted 37Y41Ta (left side of Figure A.6(a)). The reaction zone contains phases with two distinct morphologies: small spherical grains and large, high aspect ratio grains, Figure A.6(b). Small dendritic crystals suggestive of a reaction product with hexagonal symmertry are present at the center of the CMAS deposit, Figure A.6(c). Unstandardized SEM-EDS indicated that the dendrites had a composition of: 21 mol% CaO, 21 mol% $YO_{1.5}$, 24 mol% $TaO_{2.5}$, 20 mol% ZrO_2, and smaller (4-5 mol%) amounts of MgO, $AlO_{1.5}$ and SiO_2. The glassy phase contained 23 mol% CaO, 6 mol% MgO, 12 mol% $AlO_{1.5}$, 50 mol% SiO_2, and small (2-4 mol%) amounts of $YO_{1.5}$, $TaO_{2.5}$ and ZrO_2. The reaction layer between the CMAS and the TBC pellet is evident in the BSE image of the cross-section of the pellet, (d). Although molten CMAS had penetrated through connected porosity in some regions, a reaction product (darker grey contrast) prevents further infiltration. The black regions within the TBC are unfilled pores.

Depth of penetration of the CMAS is confirmed via SEM-EDS composition maps, Figure A.7. The EDS map for Si is not shown since the Kα line for Si overlaps with the Mα line for Ta. The reaction products are mostly composed of ZrO_2, $YO_{1.5}$, $TaO_{2.5}$ and CaO, with lower concentrations of MgO and $AlO_{1.5}$.

A lamella was extracted from the region marked with a red line in Figure A.7. using FIB. BF-TEM images of the lamella are shown in Figure A.8. Unreacted monoclinic (*M*) YT is present and contains twins, similar to *M*-YT observed in Chapters 5 and 6. Spherical as well as faceted grains are observed. Unfortunately, the EDS peak overlap of Ta and Si prevented determination of a more precise chemistry of the reaction products.

A.4 Discussion

A.4.1 CMAS resistance

The goal of these preliminary pellet studies was not to determine if the compositions could prevent infiltration in an actual coating but rather characterize the reaction products that resulted from the interaction of the CMAS and ZYTO pellets. Given the substantial differences in porosity between the single-phase fluorite (45Y15Ta) and mostly $YTaO_4$ (37Y41Ta) samples, it would be inaccurate to compare the depths of CMAS penetration. Therefore the discussion of the results will focus on the chemistry and microstructure of the reaction product phases.

The high aspect ratio grains observed on the surface of 45Y15Ta are similar in composition and microstructure to the apatite phase responsible for mitigating CMAS attack in RE zirconates. The composition of the needle-like grains, in single cation units, was approximately ~$Ca_{0.15}Y_{0.43}Si_{0.36}$ which is very similar to the apatite phase $Ca_{0.125}RE_{0.5}Si_{0.375}$ (RE= Gd, Y) observed by [16Poe2, 15Poe, 08Kra2]. Additionally the high aspect ratio of the grains is reminiscent of that of apatite observed by several CMAS studies in a wide variety of TBC compositions [08Kra2, 16Poe2, 15Poe]. In agreement with other CMAS studies, reprecipitated fluorite is likely present in addition to apatite in sample 45Y15Ta. The high solubility of $YO_{1.5}$ in the silicate melt and reprecipitated fluorite phase reduces the efficacy of crystallization reactions for $YO_{1.5}$- compared to $GdO_{1.5}$-containing TBCs [16Poe2, 15Poe]. However the influence of $TaO_{2.5}$ on the crystallization kinetics is unclear. These results are preliminary and additional chemical and crystallographic analysis is required to confirm the presence of apatite. Nonetheless, these results are promising for the potential CMAS resistance of ZYTO compositions containing the fluorite phase with the composition 45Y15Ta.

The reaction of CMAS with 37Y41Ta results in the crystallization of a new reaction product. Despite the different grain morphology (Figure A.6 (b, d) all the reaction product grains are the same contrast, suggesting they have the same composition. The dendrites, Figure A.6(c), may be similar in composition to the reaction product layer. The dendrites contain significantly more ZrO_2 (20 mol% vs. ~0 mol%) and substantially less SiO_2 (5 mol% vs. 37.5 mol%) compared to the apatite phase [08Kra2, 15Poe]. Therefore the reaction product is not apatite but rather another phase. The SEM-EDS maps of the reaction zone of 37Y41Ta, Figure A.7, indicate the dissolution/re-precipitation zone is only ~15μm thick, which is similar to that of gadolinium zirconate pellets after the same exposure to CMAS [15Poe]. The crystal structure of this reaction product remains to be determined. Selected area electron diffraction (SAED) may be useful, however the extensive solid solubility of the reaction product would change the lattice parameters of the structure relative to any structure that contains only some of the cations involved, making zone axis determination difficult. While the reaction product is present after 4h at 1300°C, it remains to be seen if the rate of precipitation is competitive with the rate of infiltration in columnar TBC coatings.

A.5 Conclusions and outlook

Thermogravimetric analysis of the two phase, fluorite + $YTaO_4$ composition 40Y33Ta confirmed that the oxidation states of the cations are stable up to 1500°C. Unlike the CeO_2-TiO_2-ZrO_2 system investigated in Chapter 4, the phase equilibria of the ZrO_2-$YO_{1.5}$-$TaO_{2.5}$ (ZYTO) system do not change significantly at high temperatures. Thus ZYTO based TBCs will likely withstand temperature excursions common to gas turbines. Further stability studies on the ZYTO compositions in conditions similar to those experienced during coating deposition are required.

Preliminary experiments in the ZYTO system show potential for CMAS mitigation in the compositions investigated but additional work is greatly needed to confirm the reaction

products and their kinetics of evolution. For the composition 45Y15Ta, the observation of a reaction product with similar composition and microstructure to apatite suggests that ZYTO thermal barrier oxides based on the fluorite phase with at least 45 mol% $YO_{1.5}$ have potential to mitigate attack by molten silicates. The presence of an unknown reaction product as a result of the interaction of CMAS and $YTaO_4$ is intriguing because its composition is not that of apatite yet it appears to prevent infiltration of $YTaO_4$-rich pellets. The CMAS resistance of both fluorite and $YTaO_4$ in the ZYTO system is thus promising, warranting further investigation.

Future work should focus on confirming the crystal structure and composition of the reaction product of $YTaO_4$ and CMAS. Once the composition of the reaction product is determined, a single-phase sample containing only that phase can be produced via reverse co-precipitation. Subsequent synchrotron x-ray diffraction could reveal the crystal structure and atomic positions of the reaction product. Concomitant investigation of the kinetics of precipitation of the reaction product should also be conducted to verify that it forms on a time scale competitive with infiltration.

A.6 Figures

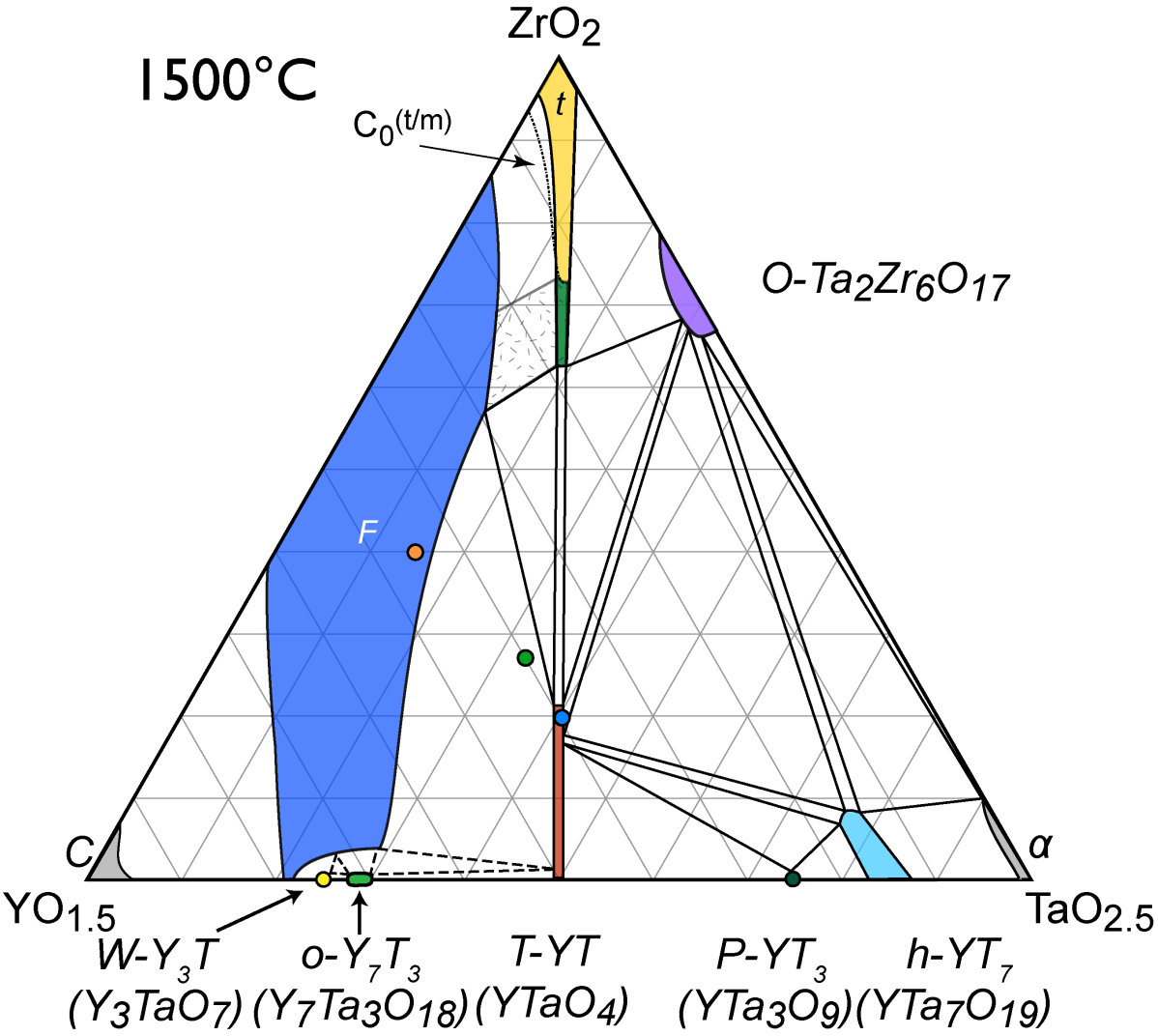

Figure A.1 The CMAS resistance of two ZYTO compositions was investigated. 45Y15Ta (orange circle) and 37Y41Ta (blue circle). TGA was performed on 40Y33Ta (light green circle).

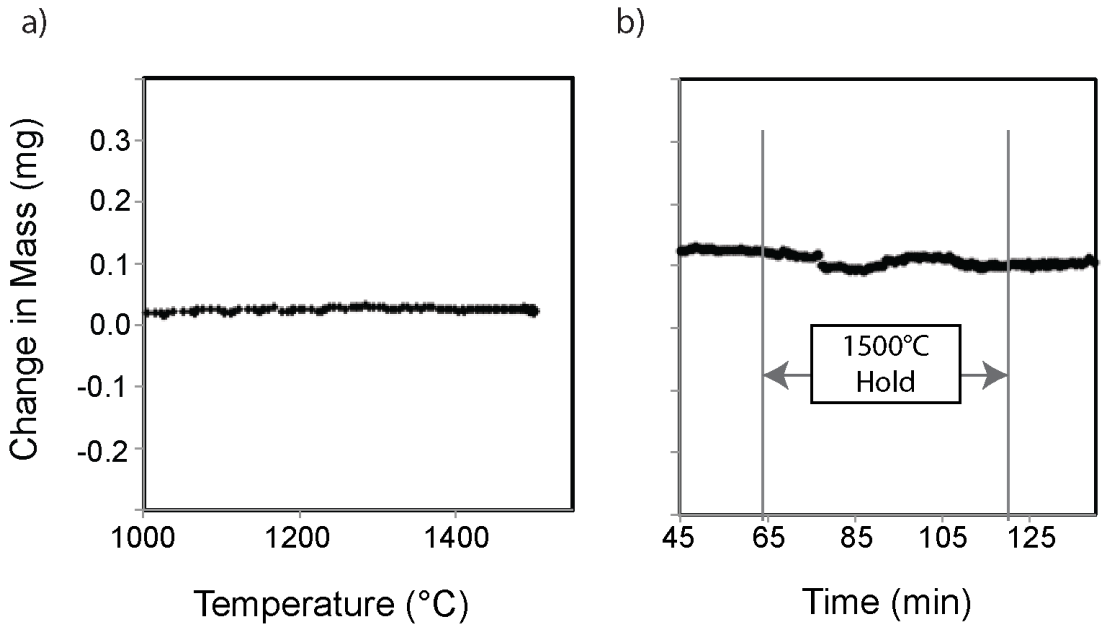

Figure A.2 Thermogravimetric analysis results for 40Y33Ta up to 1500°C indicate that reduction does not occur up to 1500°C. (a) Change in mass as a function of temperature and (b) as a function of time. Note, the y-axis is the same scale as that used for CeTiSZ powders in Chapter 4.

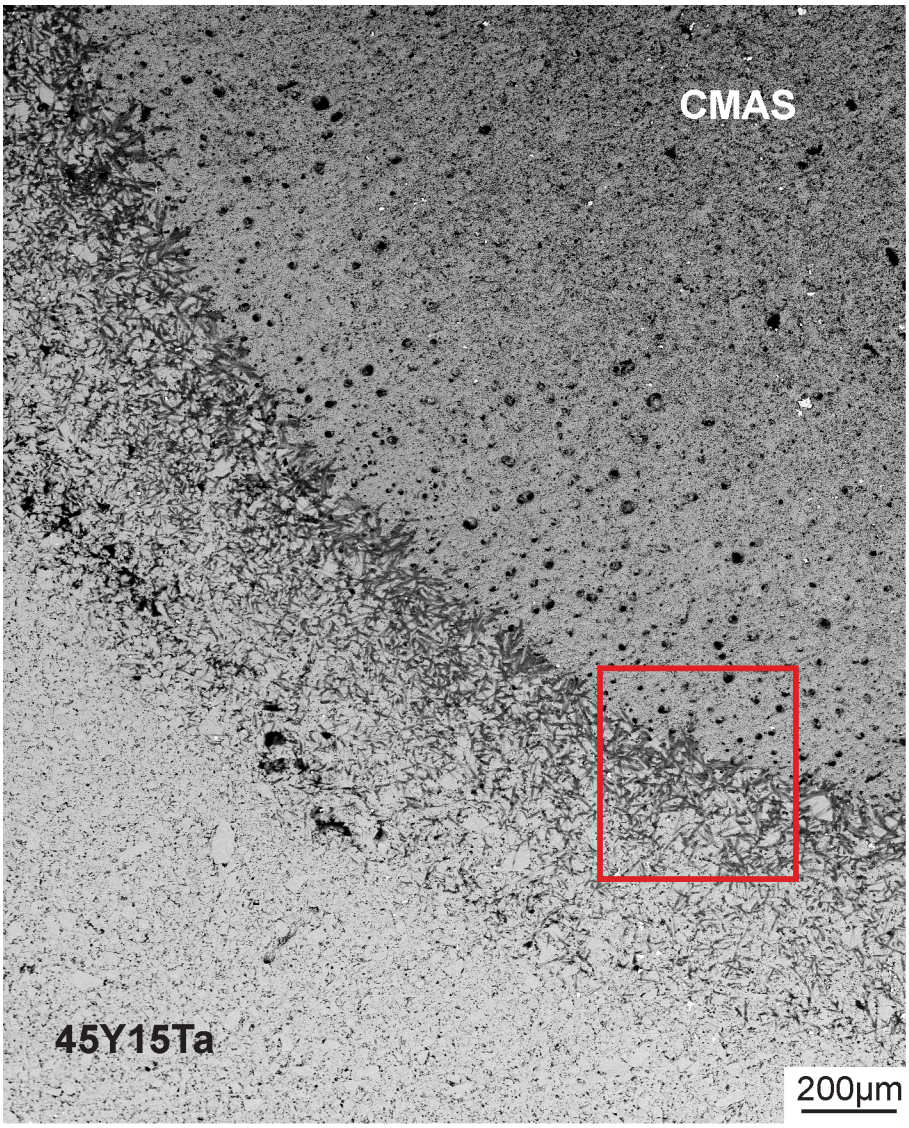

Figure A.3 Reaction front is observed on the surface of 45Y15Ta. Red box indicates representative location for the BSE image in Figure A.4(a).

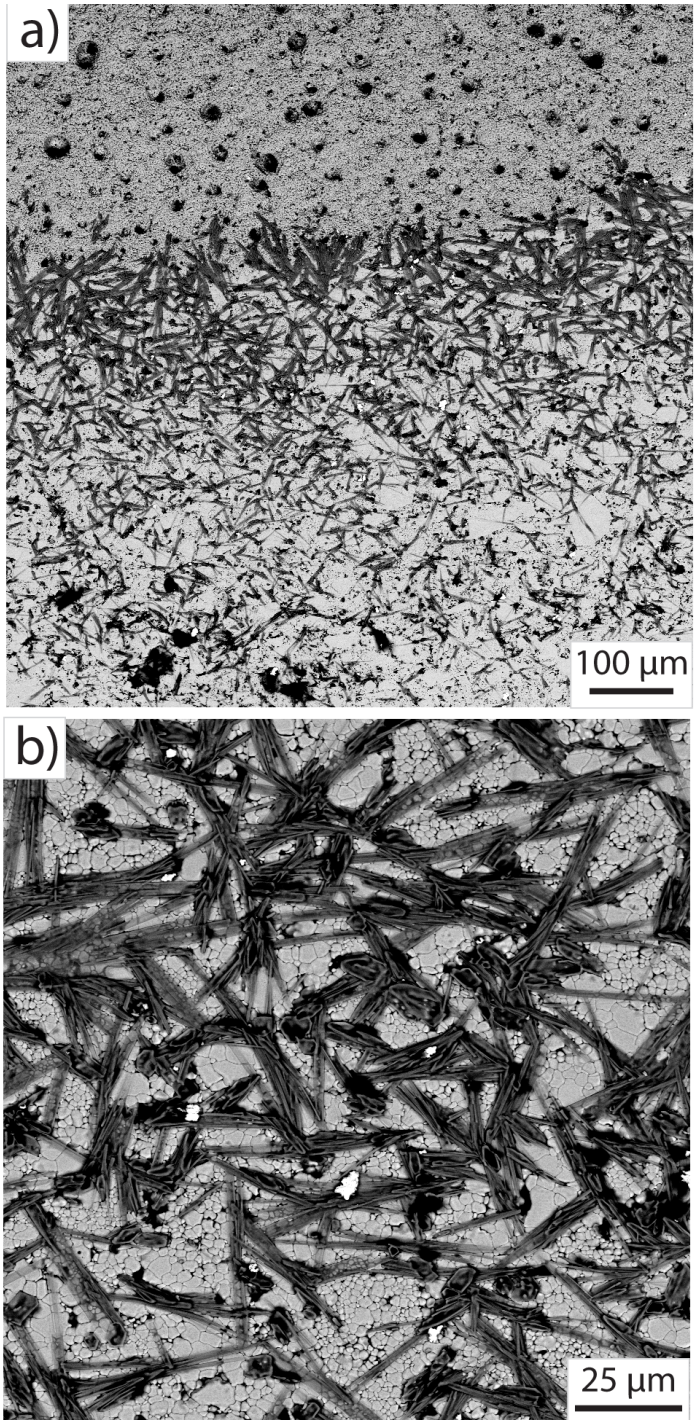

Figure A.4 (a) Lower magnification BSE image of the top surface of single-phase fluorite, 45Y15Ta reacted with CMAS. (b) Higher magnification BSE image of the same sample shows the presence of apatite. (c) The reaction layer on top of 37Y41Ta. Unfilled pores (black) are still present within the pellet and glassy CMAS (also black) is on top of the pellet.

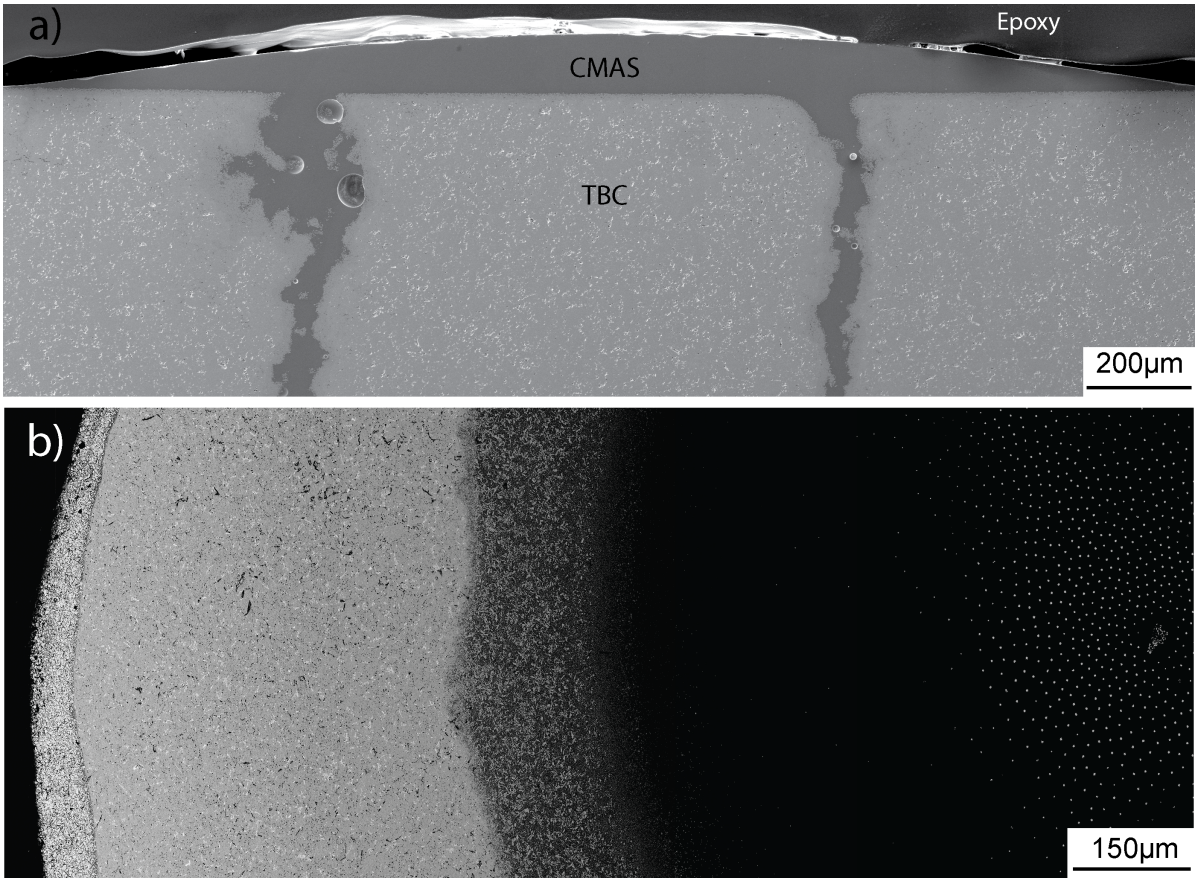

Figure A.5 BSE images of the (a) cross-section and (b) surface of 37Y41Ta reacted with CMAS. While the CMAS has infiltrated the cracks it has not penetrated the entire pellet, leaving a dome of glassy CMAS on top of the pellet. Black contrast on the right side in (b) is the glassy deposit.

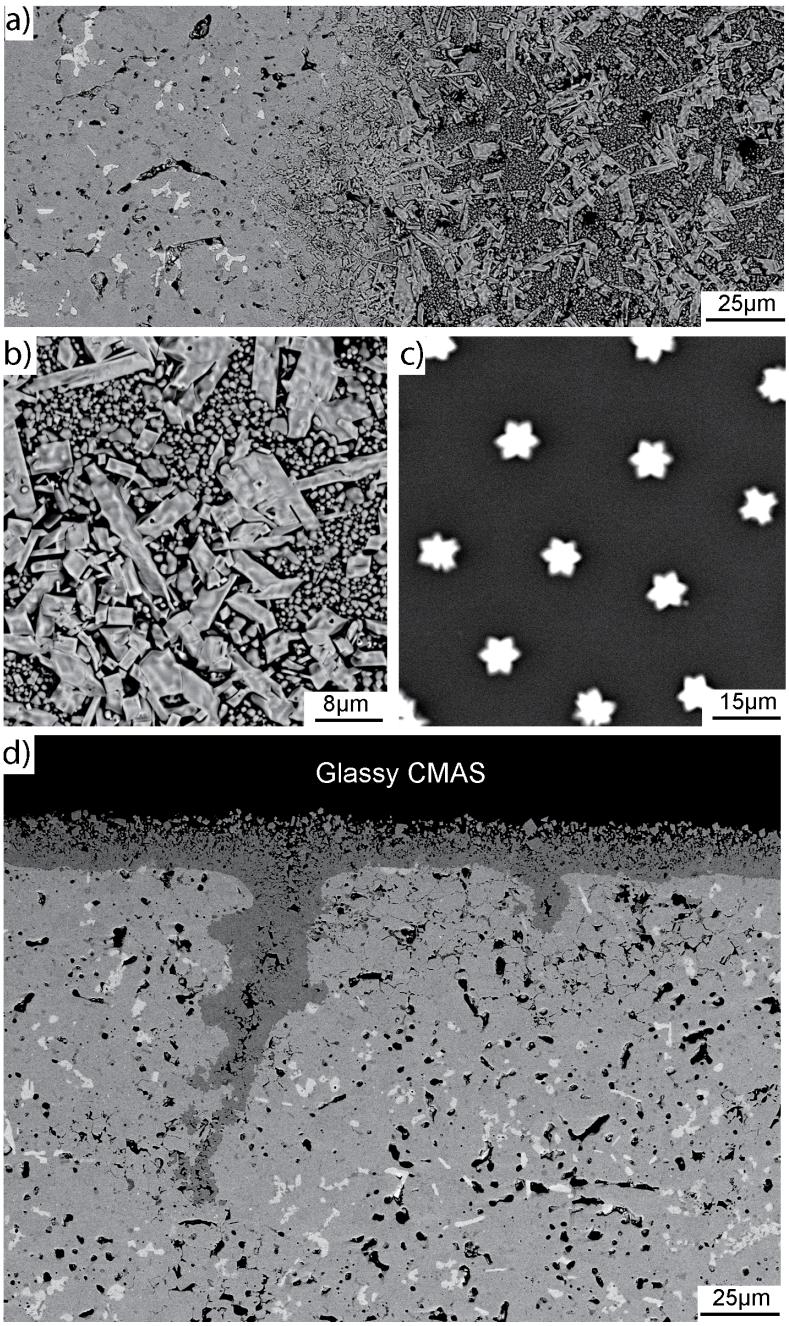

Figure A.6 (a) 37Y41Ta that has not be infiltrated is observed at the left while reaction products from the interaction with CMAS is on the right. (b) Higher magnification image of the reaction products. (c) Evenly spaced dendrites (white contrast) are observed in the glassy CMAS (black in both (c) and (d)) that remained on top of 37Y41Ta. (d) Although CMAS travelled through connected porosity into the pellet, reaction with 37Y41Ta prevented further penetration. Unfilled pores (black contrast in the pellet) are present.

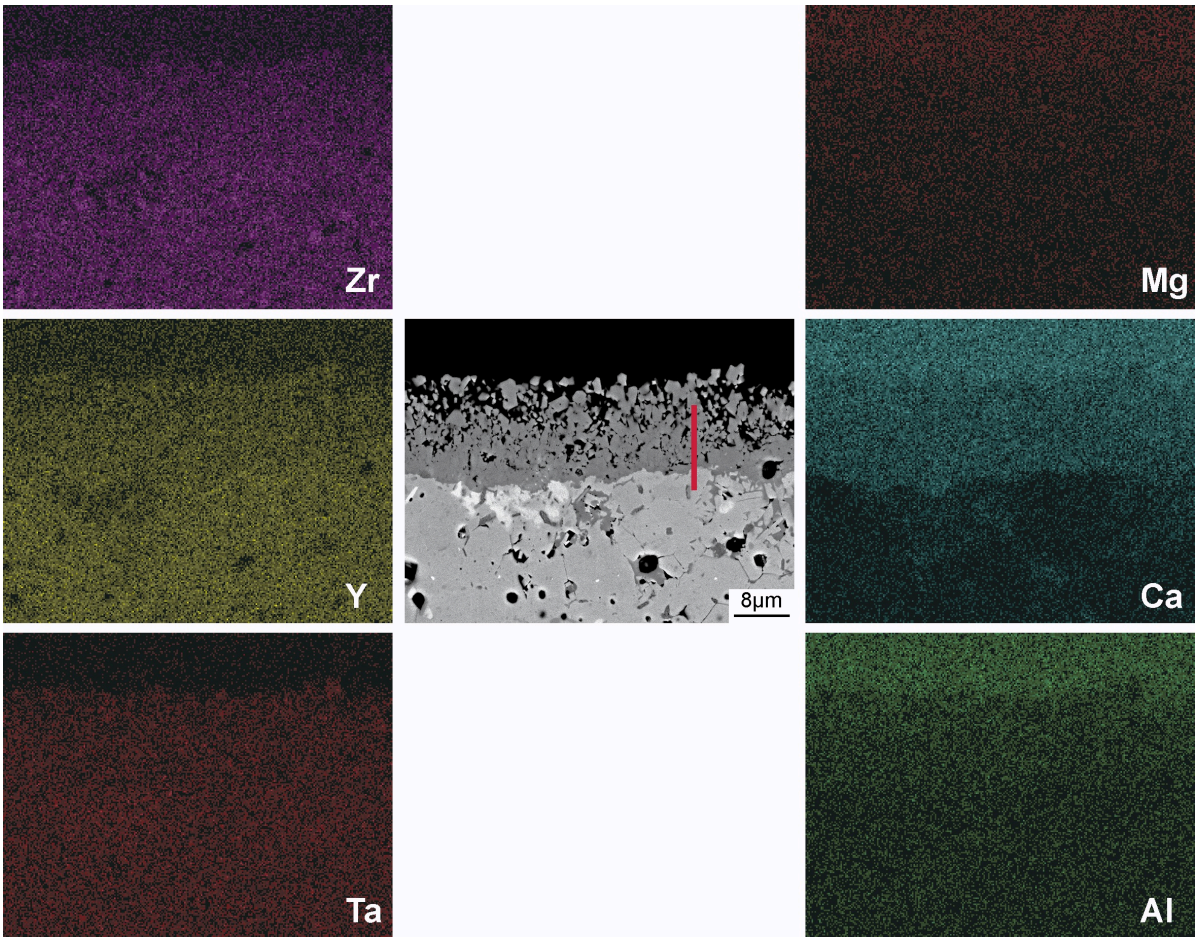

Figure A.7 EDS maps show the infiltration depth of CMAS on the 37Y41Ta samples. It is clear that the pores within the pellet are not filled with CMAS. The EDS maps of Si is not shown since the Kα EDS line for Si (1.74keV) overlaps with the Mα EDS line for Ta (1.709keV). Red line in the BSE image indicates where the TEM lamella was extracted.

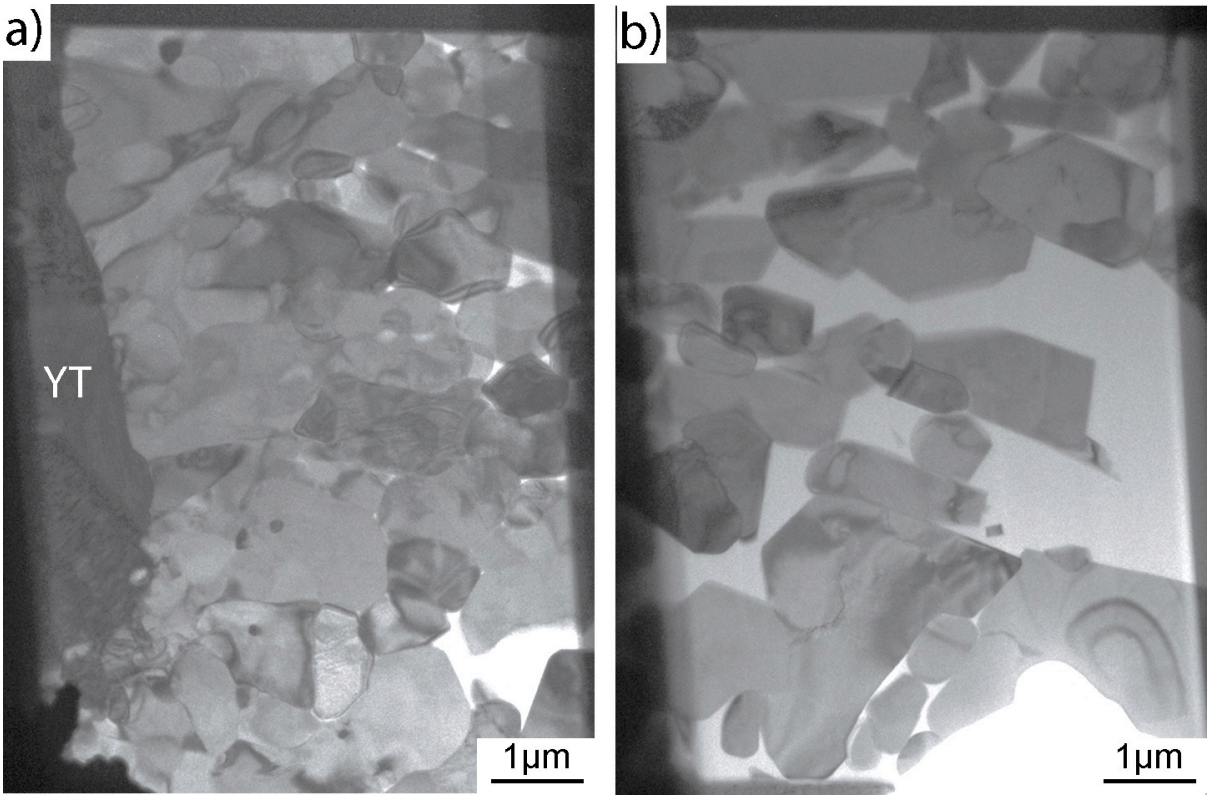

Figure A.8 BF TEM images from a single lamella extracted from the polished cross section, perpendicular to the sample surface, as shown by the redline in Figure A.. Region in (a) is closer to the interface of unreacted 37Y41Ta while the region in (b) contains areas of glassy CMAS (light contrast).

REFERENCES

00Bis J. F. Bisson, D. Fournier, M. Poulain, O. Lavigne and R. Mevrel (2000). Thermal conductivity of yttria-zirconia single crystals, determined with spatially resolved infrared thermography. Journal of the American Ceramic Society 83, 1993-1998.

00Cou T. Courtney (2000). Mechanical Behavior of Materials, Second ed. Long Grove, Illinois: Waveland Press, Inc.

00Gar S. Garcia-Martin, M. A. Alario-Franco, D. P. Fagg, A. J. Feighery and J. T. S. Irvine (2000). Modulated fluorite-type structure of materials from the (1-x)$Y_{0.5}Zr_{0.5}O_{1.75}$-x$Y_{0.75}Nb_{0.25}O_{1.75}$ (0 <= x <= 1) system. Chemistry of Materials 12, 1729-1737.

00Han R. H. J. Hannink, P. M. Kelly and B. C. Muddle (2000). Transformation toughening in zirconia-containing ceramics. Journal of the American Ceramic Society 83, 461-487.

00Irv J. T. S. Irvine, A. J. Feighery, D. P. Fagg and S. Garcia-Martin (2000). Structural studies on the optimisation of fast oxide ion transport. Solid State Ionics 136, 879-885.

00Kis H. Kishimoto, T. Omata, S. Otsuka-Yao-Matsuo, K. Ueda, H. Hosono and H. Kawazoe (2000). Crystal structure of metastable κ-$CeZrO_4$ phase possessing an ordered arrangement of Ce and Zr ions. Journal of Alloys and Compounds 312, 94-103.

00Mal M. Maloney (2000). United Technologies Corporation

00Vas R. Vassen, X. Q. Cao, F. Tietz, D. Basu and D. Stover (2000). Zirconates as new materials for thermal barrier coatings. Journal of the American Ceramic Society 83, 2023-2028.

01Bai D. Baither, M. Bartsch, B. Baufeld, A. Tikhonovsky, A. Foitzik, M. Ruhle and U. Messerschmidt (2001). Ferroelastic and plastic deformation of t '-zirconia single crystals. Journal of the American Ceramic Society 84, 1755-1762.

01Eva A. G. Evans, D. R. Mumm, J. W. Hutchinson, G. H. Meier and F. S. Pettit (2001). Mechanisms controlling the durability of thermal barrier coatings. Progress in Materials Science 46, 505-553.

01Rag S. Raghavan, H. Wang, W. D. Porter, R. B. Dinwiddie and M. J. Mayo (2001). Thermal properties of zirconia co-doped with trivalent and pentavalent oxides. Acta Materialia 49, 169-179.

01Sub R. Subramanian (2001).

02Fab S. Fabris, A. T. Paxton and M. W. Finnis (2002). A stabilization mechanism of zirconia based on oxygen vacancies only. Acta Materialia 50, 5171-5178.

02Li Y. L. Li and T. Ishigaki (2002). Thermodynamic analysis of nucleation of anatase and rutile from TiO_2 melt. Journal of Crystal Growth 242, 511-516.

02Rob J. Robertson (2002). Band offsets of high dielectric constant gate oxides on silicon. Journal of Non-Crystalline Solids 303, 94-100.

02Sko N. V. Skorodumova, S. I. Simak, B. I. Lundqvist, I. A. Abrikosov and B. Johansson (2002). Quantum origin of the oxygen storage capability of ceria. Physical Review Letters 89.

03Ask C. Askeljung, B. O. Marinder and M. Sundberg (2003). Effect of heat treatment on the structure of L-Ta_2O_5: a study by XRPD and HRTEM methods. Journal of Solid State Chemistry 176, 250-258.

03Che Y. S. Chen, J. L. G. Fierro, T. Tanaka and I. E. Wachs (2003). Supported tantalum oxide catalysts: Synthesis, physical characterization, and methanol oxidation chemical probe reaction. Journal of Physical Chemistry B 107, 5243-5250.

03Gre I. E. Grey, W. G. Mumme and R. S. Roth (2005). The crystal chemistry of L-Ta_2O_5 and related structures. Journal of Solid State Chemistry 178, 3308-3314.

03Hua S. G. Huang, L. Li, J. Vleugels, P. L. Wang and O. Van der Biest (2003). Thermodynamic prediction of the nonstoichiometric phase $Zr_{1-z}Ce_zO_{2-x}$ in the ZrO_2-$CeO_{1.5}$-CeO_2 system. Journal of the European Ceramic Society 23, 99-106.

03Kul A. Kulkarni, Z. Wang, T. Nakamura, S. Sampath, A. Goland, H. Herman, J. Allen, J. Ilavsky, G. Long, J. Frahm and R. W. Steinbrech (2003). Comprehensive microstructural characterization and predictive property modeling of plasma-sprayed zirconia coatings. Acta Materialia 51, 2457-2475.

03Leh H. Lehmann, D. Pitzer, G. Pracht, R. Vassen and D. Stover (2003). Thermal conductivity and thermal expansion coefficients of the lanthanum rare-earth-element zirconate system. Journal of the American Ceramic Society 86, 1338-1344.

03Sch U. Schulz, C. Leyens, K. Fritscher, M. Peters, B. Saruhan-Brings, O. Lavigne, J. M. Dorvaux, M. Poulain, R. Mevrel and M. L. Caliez (2003). Some recent trends in research and technology of advanced thermal barrier coatings. Aerospace Science and Technology 7, 73-80.

04Fab O. Fabrichnaya and F. Aldinger (2004). Assessment of thermodynamic parameters in the system ZrO_2-Y_2O_3-Al_2O_3. Zeitschrift Fur Metallkunde 95, 27-39.

04Fau P. Fauchais (2004). Understanding plasma spraying. Journal of Physics D-Applied Physics 37, R86-R108.

04Lev C. G. Levi (2004). Emerging materials and processes for thermal barrier systems. Current Opinion in Solid State & Materials Science 8, 77-91.

04Mol M. Moldovan, C. M. Weyant, D. L. Johnson and K. T. Faber (2004). Tantalum oxide coatings as candidate environmental barriers. Journal of Thermal Spray Technology 13, 51-56.

04Ots S. Otsuka-Yao-Matsuo, T. Omata and M. Yoshimura (2004). Photocatalytic behavior of cerium titanates, $CeTiO_4$ and $CeTi_2O_6$ and their composite powders with $SrTiO_3$. Journal of Alloys and Compounds 376, 262-267.

04Rag S. Raghavan, H. Wang, R. B. Dinwiddie, W. D. Porter, R. Vassen, D. Stover and M. J. Mayo (2004). Ta_2O_5/Nb_2O_5 and Y_2O_3 co-doped zirconias for thermal barrier coatings. Journal of the American Ceramic Society 87, 431-437.

04Wak M. Wakeshima, H. Nishimine and Y. Hinatsu (2004). Crystal structures and magnetic properties of rare earth tantalates RE_3TaO_7 (RE = rare earths). Journal of Physics-Condensed Matter 16, 4103-4120.

04Wan C. Wang, M. Zinkevich and F. Aldinger (2004). On the thermodynamic modeling of the Zr-O system. Calphad-Computer Coupling of Phase Diagrams and Thermochemistry 28, 281-292.

05Bos N. S. Bosco and F. W. Zok (2005). Strength of joints produced by transient liquid phase bonding in the Cu-Sn system. Acta Materialia 53, 2019-2027.

05Cla D. R. Clarke and S. R. Phillpot (2005). Thermal barrier coating materials. Materials Today 8, 22-29.

05Fab O. Fabrichnaya, C. Wang, M. Zinkevich, C. G. Levi and F. Aldinger (2005). Phase equilibria and thermodynamic properties of the ZrO_2-$GdO_{1.5}$-$YO_{1.5}$ system. Journal of Phase Equilibria and Diffusion 26, 591-604.

05Lec R. M. Leckie, S. Kramer, M. Ruhle and C. G. Levi (2005). Thermochemical compatibility between alumina and ZrO_2-$GdO_{3/2}$ thermal barrier coatings. Acta Materialia 53, 3281-3292.

05Prytz O. Prytz and J. Tafto (2005). Accurate determination of domain boundary orientation in $LaNbO_4$. Acta Materialia 53, 297-302.

05Una B. Unal, C. Y. Tai, D. P. Shepherd, J. S. Wilkinson, N. M. B. Perney, M. C. Netti and G. J. Parker (2005). Nd : Ta_2O_5 Rib Waveguide Lasers. Applied Physics Letters 86.

06Dut1 G. Dutta, U. V. Waghmare, T. Baidya, M. S. Hegde, K. R. Priolkar and P. R. Sarode (2006). Reducibility of $Ce_{1-x}Zr_xO_2$: origin of enhanced oxygen storage capacity. Catalysis Letters 108, 165-172.

06Dut2 G. Dutta, U. V. Waghmare, T. Baidya, M. S. Hegde, K. R. Priolkar and P. R. Sarode (2006). Origin of enhanced reducibility/oxygen storage capacity of $Ce_{1-x}Ti_xO_2$ compared to CeO_2 or TiO_2. Chemistry of Materials 18, 3249-3256.

06Eva A. G. Evans, N. A. Fleck, S. Faulhaber, N. Vermaak, M. Maloney and R. Darolia (2006). Scaling laws governing the erosion and impact resistance of thermal barrier coatings. Wear 260, 886-894.

06Flo A. Flores-Renteria, B. Saruhan, U. Schulz, H. J. Raetzer-Scheibe, J. Haug and A. Wiedemann (2006). Effect of morphology on thermal conductivity of EB-PVD PYSZ TBCs. Surface & Coatings Technology 201, 2611-2620.

06Kra S. Kramer, J. Yang, C. G. Levi and C. A. Johnson (2006). Thermochemical interaction of thermal barrier coatings with molten CaO-MgO-Al_2O_3-SiO_2 (CMAS) deposits. Journal of the American Ceramic Society 89, 3167-3175.

06Lec R. M. Leckie (2006). Fundamental issues regarding the implementation of gadolinium zirconate in thermal barrier systems, Thesis, University of California Santa Barbara, Santa Barbara, CA.

06Pit F. M. Pitek (2006). A Study of the Zirconia-Yttria-Tantala System as a Potential Thermal Barrier Oxide, Thesis, UC Santa Barbara, Santa Barbara, CA.

06Pol T. M. Pollock and S. Tin (2006). Nickel-based superalloys for advanced turbine engines: Chemistry, microstructure, and properties. Journal of Propulsion and Power 22, 361-374.

07Bre G. L. Brennecka, D. A. Payne, P. Sarin, J.-M. Zuo, W. M. Kriven and H. Hellwig (2007). Phase Transformations in the High-Temperature Form of Pure and TiO_2-Stabilized Ta_2O_5. Journal of the American Ceramic Society 90, 2947-2953.

07Fab O. Fabrichnaya, M. Zinkevich and F. Aldinger (2007). Thermodynamic modelling in the ZrO_2-La_2O_3-Y_2O_3-Al_2O_3 system. International Journal of Materials Research 98, 838-846.

07Gra K. M. Grant, S. Kramer, J. P. A. Lofvander and C. G. Levi (2007). CMAS degradation of environmental barrier coatings. Surface & Coatings Technology 202, 653-657.

07Leo N. I. Leonyuk, E. Cavalli, G. Calestani, N. V. Kuleshov, J. M. Dawes, V. V. Maltsev, E. V. Koporulina, E. A. Volkova and O. V. Pilipenko (2007). A new generation of nonlinear optical and laser crystals of rare earth borate and tantalate families. Journal of Optoelectronics and Advanced Materials 9, 1206-1214.

07Liu X. Q. Liu, X. D. Han, Z. Zhang, L. F. Ji and Y. J. Jiang (2007). The crystal structure of high temperature phase Ta_2O_5. Acta Materialia 55, 2385-2396.

07Mer C. Mercer, J. R. Williams, D. R. Clarke and A. G. Evans (2007). On a ferroelastic mechanism governing the toughness of metastable tetragonal-prime (t ') yttria-stabilized zirconia. Proceedings of the Royal Society a-Mathematical Physical and Engineering Sciences 463, 1393-1408.

07Pit F. M. Pitek and C. G. Levi (2007). Opportunities for TBCs in the ZrO_2-$YO_{1.5}$-$TaO_{2.5}$ system. Surface and Coatings Technology 201, 6044-6050.

07Sch T. A. Schaedler, R. M. Leckie, S. Kramer, A. G. Evans and C. G. Levi (2007). Toughening of nontransformable t '-YSZ by addition of titania. Journal of the American Ceramic Society 90, 3896-3901.

07Wel R. G. Wellman and J. R. Nicholls (2007). A review of the erosion of thermal barrier coatings. Journal of Physics D-Applied Physics 40, R293-R305.

07Yas M. Yashima and T. Tsuji (2007). Crystal structure, disorder, and diffusion path of oxygen ion conductors $Y_{1-x}Ta_xO_{1.5+x}$ (x=0.215 and 0.30). Chemistry of Materials 19, 3539-3544.

08Eva A. G. Evans, D. R. Clarke and C. G. Levi (2008). The influence of oxides on the performance of advanced gas turbines. Journal of the European Ceramic Society 28, 1405-1419.

08Kra S. Kramer, S. Faulhaber, M. Chambers, D. R. Clarke, C. G. Levi, J. W. Hutchinson and A. G. Evans (2008). Mechanisms of cracking and delamination within thick thermal barrier systems in aero-engines subject to calcium-magnesium-alumino-silicate (CMAS) penetration. Materials Science and Engineering a-Structural Materials Properties Microstructure and Processing 490, 26-35.

08Kra2 S. Kramer, J. Yang and C. G. Levi (2008). Infiltration-inhibiting reaction of gadolinium zirconate thermal barrier coatings with CMAS melts. Journal of the American Ceramic Society 91, 576-583.

08Mar M. Martos, B. Julian-Lopez, J. V. Folgado, E. Cordoncillo and P. Escribano (2008). Sol-gel synthesis of tunable cerium titanate materials. European Journal of Inorganic Chemistry, 3163-3171.

08Mom K. Momma and F. Izumi (2008). VESTA: a three-dimensional visualization system for electronic and structural analysis. Journal of Applied Crystallography 41, 653-658.

08Zho Q. D. Zhou, P. J. Saines, N. Sharma, J. Ting, B. J. Kennedy, Z. M. Zhang, R. L. Withers and K. S. Wallwork (2008). Crystal Structures and Phase Transitions in A-Site Deficient Perovskites $Ln_{1/3}TaO_3$. Chemistry of Materials 20, 6666-6676.

09Cav E. Cavalli, E. Volkova, G. Calsetani and N. Leonyuk (2009). Structural and morphological characterization of flux grown YTa_7O_{19}, Nd:YTa_7O_{19}, Nd:$LaTa_7O_{19}$ and $NdTa_7O_{19}$ crystals. Materials Research Bulletin 44, 1127-1131.

09Fu W. T. Fu and D. J. W. Ijdo (2009). On the crystal structures of Ln_3MO_7 (Ln = Nd, Sm, Y and M = Sb, Ta)-Rietveld refinement using X-ray powder diffraction data. Journal of Solid State Chemistry 182, 2451-2455.

09Li L. H. Li, N.; Knapp, J. (2009). Failure of thermal barrier coatings subjected to CMAS attack. Journal of Thermal Spray Technology 19, 148-155.

09Mil V. Milman, A. Perlov, K. Refson, S. J. Clark, J. Gavartin and B. Winkler (2009). Structural, electronic and vibrational properties of tetragonal zirconia under pressure: a density functional theory study. Journal of Physics-Condensed Matter 21.

09Mok T. Mokkelbost, H. L. Lein, P. E. Vullum, R. Holmestad, T. Grande and M. A. Einarsrud (2009). Thermal and mechanical properties of $LaNbO_4$-based ceramics. Ceramics International 35, 2877-2883.

09Per J. H. Perepezko (2009). The Hotter the Engine, the Better. Science 326, 1068-1069.

09Tan Y. Tan, J. P. Longtin, S. Sampath and H. Wang (2009). Effect of the Starting Microstructure on the Thermal Properties of As-Sprayed and Thermally Exposed Plasma-Sprayed YSZ Coatings. Journal of the American Ceramic Society 92, 710-716.

09Wan L. Wang, Y. X. Pan, Y. Ding, W. G. Yang, W. L. Mao, S. V. Sinogeikin, Y. Meng, G. Y. Shen and H. K. Mao (2009). High-pressure induced phase transitions of Y_2O_3 and Y_2O_3:Eu3+. Applied Physics Letters 94.

10Fle N. A. Fleck and T. Zisis (2010). The erosion of EB-PVD thermal barrier coatings: The competition between mechanisms. Wear 268, 1214-1224.

10Gao X. Gao, Y. Jiang, Y. Zhong, Z. Y. Luo and K. F. Cen (2010). The activity and characterization of CeO_2-TiO_2 catalysts prepared by the sol-gel method for selective catalytic reduction of NO with NH_3. Journal of Hazardous Materials 174, 734-739.

10Gra K. M. Grant, S. Kramer, G. G. E. Seward and C. G. Levi (2010). Calcium-Magnesium Alumino-Silicate Interaction with Yttrium Monosilicate Environmental Barrier Coatings. Journal of the American Ceramic Society 93, 3504-3511.

10Lep M. Lepple (2010). The Effects of Dopants in Zirconia-final report, Santa Barbara: University of California.

10She Y. Shen and D. R. Clarke (2010). Resistance to Low-Temperature Degradation of Equimolar $YO_{1.5}$-$TaO_{2.5}$ Stabilized Tetragonal ZrO_2 Ceramics in Air. Journal of the American Ceramic Society 93, 2024-2027.

10She2 Y. Shen, R. M. Leckie, C. G. Levi and D. R. Clarke (2010). Low thermal conductivity without oxygen vacancies in equimolar $YO_{1.5}$ + $TaO_{2.5}$ - and $YbO_{1.5}$ + $TaO_{2.5}$-stabilized tetragonal zirconia ceramics. Acta Materialia 58, 4424-4431.

10Son X. W. Song, M. Xie, S. L. An, X. H. Hao and R. D. Mu (2010). Structure and thermal properties of ZrO_2-Ta_2O_5-Y_2O_3-Ln_2O_3 (Ln = Nd, Sm or Gd) ceramics for thermal barrier coatings. Scripta Materialia 62, 879-882.

10Wan K. Wang, C. H. Li, H. Q. Dong, X. S. Ye, X. G. Lu and W. Z. Ding (2010). Thermodynamic Modeling of the ZrO_2-$YO_{1.5}$-TiO_2 System. Metallurgical and Materials Transactions a-Physical Metallurgy and Materials Science 41A, 3525-3534.

11Bha A. K. Bhattacharya, V. Shklover, W. Steurer, G. Witz, H. P. Bossmann and O. Fabrichnaya (2011). Ta_2O_5-Y_2O_3-ZrO_2 system: Experimental study and preliminary thermodynamic description. Journal of the European Ceramic Society 31, 249-257.

11Bha2 A. Bhattachaya, V. Shklover, K. Kunze and W. Steurer (2011). Effect of 7YSZ on the long-term stability of $YTaO_4$ doped ZrO_2 system. Journal of the European Ceramic Society 31, 2897-2901.

11Bol A. M. Bolon and M. M. Gentleman (2011). Raman Spectroscopic Observations of Ferroelastic Switching in Ceria-Stabilized Zirconia. Journal of the American Ceramic Society 94, 4478-4482.

11Kro J. A. Krogstad, S. Kramer, D. M. Lipkin, C. A. Johnson, D. R. G. Mitchell, J. M. Cairney and C. G. Levi (2011). Phase Stability of t '-Zirconia-Based Thermal Barrier Coatings: Mechanistic Insights. Journal of the American Ceramic Society 94, S168-S177.

11LeG A. a. S. A. Le Gal (2011). Catalytic investigation of ceria-zirconia solid solutions for solar hydrogen production. International Journal of Hydrogen Energy 36, 4739-4748.

11LeG A. Le Gal, S. Abanades, and G. Flamant (2011). CO_2 and H_2O Splitting for Thermochemical prediction of the nonstoichiometric phase $Zr_{1-x}Ce_zO_{2-x}$ in the ZrO_2-$CeO_{1.5}$-CeO_2 system. Energy Fuels 25, 4836-4845.

11LeG2 A. Le Gal, S. Abanades and G. Flamant (2011). CO_2 and H_2O Splitting for Thermochemical Production of Solar Fuels Using Nonstoichiometric Ceria and Ceria/Zirconia Solid Solutions. Energy & Fuels 25, 4836-4845.

11Lim A. M. Limarga, J. Iveland, M. Gentleman, D. M. Lipkin and D. R. Clarke (2011). The use of Larson-Miller parameters to monitor the evolution of Raman lines of tetragonal zirconia with high temperature aging. Acta Materialia 59, 1162-1167.

11Liu H. F. Liu, S. L. Li, Q. L. Li, Y. M. Li and W. X. Zhou (2011). Microstructure, phase stability and thermal conductivity of plasma sprayed Yb_2O_3, Y_2O_3 co-stabilized ZrO_2 coatings. Solid State Sciences 13, 513-519.

12Cla D. R. Clarke, M. Oechsner and N. P. Padture (2012). Thermal-barrier coatings for more efficient gas-turbine engines. MRS bulletin 37, 891-902.

12Joe C. Joseph, P. Bourson and M. D. Fontana (2012). Amorphous to crystalline transformation in Ta_2O_5 studied by Raman spectroscopy. Journal of Raman Spectroscopy 43, 1146-1150.

12Kro J. A. Krogstad (2012). Phase Stability of Zirconia-based Thermal Barrier Coatings, Thesis, University of California Santa Barbara, Santa Barbara, CA.

12LeG A. Le Gal and S. Abanades (2012). Dopant Incorporation in Ceria for Enhanced Water-Splitting Activity during Solar Thermochemical Hydrogen Generation. Journal of Physical Chemistry C 116, 13516-13523.

12Lev C. G. Levi, J. W. Hutchinson, M. H. Vidal-Setif and C. A. Johnson (2012). Environmental degradation of thermal-barrier coatings by molten deposits. Mrs Bulletin 37, 932-941.

12Sam S. Sampath, U. Schulz, M. O. Jarligo and S. Kuroda (2012). Processing science of advanced thermal-barrier systems. MRS bulletin 37, 903-910.

13Don E. M. Donohue, N. R. Philips, M. R. Begley and C. G. Levi (2013). Thermal barrier coating toughness: Measurement and identification of a bridging mechanism enabled by segmented microstructure. Materials Science and Engineering a-Structural Materials Properties Microstructure and Processing 564, 324-330.

13Gio C. Gionco, M. C. Paganini, S. Agnoli, A. E. Reeder and E. Giamello (2013). Structural and spectroscopic characterization of CeO_2-TiO_2 mixed oxides. Journal of Materials Chemistry A 1, 10918-10926.

13Kin G. King, C. M. Thompson, J. E. Greedan and A. Llobet (2013). Local structure of the vacancy disordered fluorite Yb_3TaO_7 from neutron total scattering. Journal of Materials Chemistry A 1, 10487-10494.

13Kro J. A. Krogstad, R. M. Leckie, S. Kramer, J. M. Cairney, D. M. Lipkin, C. A. Johnson and C. G. Levi (2013). Phase Evolution upon Aging of Air Plasma Sprayed t'-Zirconia Coatings: II-Microstructure Evolution. Journal of the American Ceramic Society 96, 299-307.

13Kro2 J. A. Krogstad, M. Lepple and C. G. Levi (2013). Opportunities for Improved TBC Durability in the CeO_2-TiO_2-ZrO_2 System. Surface & Coatings Technology 221, 44-52.

13Lip D. M. Lipkin, J. A. Krogstad, Y. Gao, C. A. Johnson, W. A. Nelson and C. G. Levi (2013). Phase Evolution upon Aging of Air-Plasma Sprayed t'-Zirconia Coatings: ISynchrotron X-Ray Diffraction. Journal of the American Ceramic Society 96, 290-298.

13Lop L. Lopez-Conesa, J. M. Rebled, M. H. Chambrier, K. Boulahya, J. M. Gonzalez-Calbet, M. D. Braida, G. Dezanneau, S. Estrade and F. Peiro (2013). Local Structure of Rare Earth Niobates (RE_3NbO_7, RE=Y, Er, Yb, Lu) for Proton Conduction Applications. Fuel Cells 13, 29-33.

13Siq K. P. F. Siqueira, R. M. Borges, E. Granado, L. M. Malard, A. M. de Paula, R. L. Moreira, E. M. Bittar and A. Dias (2013). Crystal structure of fluorite-related Ln_3SbO_7 (Ln=La-Dy) ceramics studied by synchrotron X-ray diffraction and Raman scattering. Journal of Solid State Chemistry 203, 326-332.

13Zal E. Zaleski (2013). Mechanisms and mitigation of CMAS attack on thermal barrier coatings, Thesis, University of California Santa Barbara, Santa Barbara, CA.

14Abr M. V. Abrashev, N. D. Todorov and J. Geshev (2014). Raman spectra of R_2O_3 (R-rare earth) sesquioxides with C-type bixbyite crystal structure: A comparative study. Journal of Applied Physics 116.

14Don E. M. Donohue (2014). Investigation of the parameters influencing thermal barrier coatings toughness through a novel measurement technique, Thesis, University of California Santa Barbara, Santa Barbara.

14Fen J. Feng, S. Shian, B. Xiao and D. R. Clarke (2014). First-principles calculations of the high-temperature phase transformation in yttrium tantalate. Physical Review B 90.

14Fer J. Fergus (2014). Zirconia and pyrochlore oxides for thermal barrier coatings in gas turbine engines. metallurgical and Materials Transactions E 1A, 118-131.

14Fra T. L. Francis, P. P. Rao, M. Thomas, S. K. Mahesh, V. R. Reshmi and T. S. Sreena (2014). Structural influence on the photoluminescence properties of Eu+3 doped Gd_3MO_7 (M = Nb, Sb, and Ta) red phosphors. Physical Chemistry Chemical Physics 16, 17108-17115.

14Hao Y. Hao, C. K. Yang and S. M. Haile (2014). Ceria-Zirconia Solid Solutions ($Ce_{1-x}Zr_xO_2$-delta, x <= 0.2) for Solar Thermochemical Water Splitting: A Thermodynamic Study. Chemistry of Materials 26, 6073-6082.

14Kra A. R. Krause, H. F. Garces, B. S. Senturk and N. P. Padture (2014). $2ZrO_2$-Y_2O_3 Thermal Barrier Coatings Resistant to Degradation by Molten CMAS: Part II, Interactions with Sand and Fly Ash. Journal of the American Ceramic Society 97, 3950-3957.

14Kra2 A. R. Krause, B. S. Senturk, H. F. Garces, G. Dwivedi, A. L. Ortiz, S. Sampath and N. P. Padture (2014). $2ZrO_2$-Y_2O_3 Thermal Barrier Coatings Resistant to Degradation by Molten CMAS: Part I, Optical Basicity Considerations and Processing. Journal of the American Ceramic Society 97, 3943-3949.

14Li Q. J. Li, H. F. Zhang, B. Y. Cheng, R. Liu, B. Liu, J. Liu, Z. Q. Chen, B. Zou, T. Cui and B. B. Liu (2014). Pressure-induced amorphization in orthorhombic Ta_2O_5: An intrinsic character of crystal. Journal of Applied Physics 115.

14Lim A. M. Limarga, S. Shian, R. M. Leckie, C. G. Levi and D. R. Clarke (2014). Thermal conductivity of single- and multi-phase compositions in the ZrO_2-Y_2O_3-Ta_2O_5 system. Journal of the European Ceramic Society 34, 3085-3094.

14Shi S. Shian, P. Sarin, M. Gurak, M. Baram, W. M. Kriven and D. R. Clarke (2014). The tetragonal-monoclinic, ferroelastic transformation in yttrium tantalate and effect of zirconia alloying. Acta Materialia 69, 196-202.

15Che A. Chesnaud, M. D. Braida, S. Estrade, F. Peiro, A. Tarancon, A. Morata and G. Dezanneau (2015). High-temperature anion and proton conduction in RE_3NbO_7

(RE = La, Gd, Y, Yb, Lu) compounds. Journal of the European Ceramic Society 35, 3051-3061.

15Cor S. Correa (2015). CMCEE, edited by p.^pp. Vancouver, British Columbia:

15Gan A. Ganvir, N. Curry, S. Bjorklund, N. Markocsan and P. Nylen (2015). Characterization of Microstructure and Thermal Properties of YSZ Coatings Obtained by Axial Suspension Plasma Spraying (ASPS). Journal of Thermal Spray Technology 24, 1195-1204.

15IATA IATA (2015). International Air Transport Association Air Passenger Forecast, http://www.iata.org/pressroom/pr/Pages/2015-11-26-01.aspx.

15Jac R. W. Jackson, E. M. Zaleski, D. L. Poerschke, B. T. Hazel, M. R. Begley and C. G. Levi (2015). Interaction of molten silicates with thermal barrier coatings under temperature gradients. Acta Materialia 89, 396-407.

15Kro J. A. Krogstad, Y. Gao, J. M. Bai, J. Wang, D. M. Lipkin and C. G. Levi (2015). In Situ Diffraction Study of the High-Temperature Decomposition of t '-Zirconia. Journal of the American Ceramic Society 98, 247-254.

15Mar D. B. Marshall, R. F. Cook, N. P. Padture, M. L. Oyen, A. Pajares, J. E. Bradby, I. E. Reimanis, R. Tandon, T. F. Page, G. M. Pharr and B. R. Lawn (2015). The Compelling Case for Indentation as a Functional Exploratory and Characterization Tool. Journal of the American Ceramic Society 98, 2671-2680.

15Pea B. Pearce (2015). Economic Performance of the Airline Industry, International Air Transport Association.

15Poe D. L. Poerschke and C. G. Levi (2015). Effects of cation substitution and temperature on the interaction between thermal barrier oxides and molten CMAS. Journal of the European Ceramic Society 35, 681-691.

15Van J. S. K. Van Sluytman, S.; Tolpygo, V.; Levi, C.G (2015). Microstructure evolution of ZrO_2-$YbTaO_4$ thermal barrier coatings. Acta Materialia 96, 133-142.

15Zha B. Zhang (2015). Experimental characterization of thermal barrier coatings using micro-scale bending techniques, Thesis, Johns Hopkins, Baltimore, MD.

16EIA EIA.gov (2016). Net Generation by Energy Source 2006-2016, http://www.eia.gov/electricity/monthly/epm_table_grapher.cfm?t=epmt_1_01.

16EIA2 EIA.gov (2016). Natural gas expected to surpass coal in mix of fuel used for U.S. power generation in 2016, http://www.eia.gov/todayinenergy/detail.cfm?id=25392.

16Hin J. Hines (2016). Better combustion for power generation, https://www.olcf.ornl.gov/2016/05/31/better-combustion-for-power-generation/.

16Jor D. J. Jorgensen, A. Suzuki, D. M. Lipkin and T. M. Pollock (2016). Bond coatings with high rumpling resistance: Design and characterization. Surface & Coatings Technology 300, 25-34.

16Mac C. A. F. Macauley, A.N.;Van Sluytman, J.S.;Levi, C.G. (In Preparation). Phase equilibria in the ZrO2-YO1.5-TaO2.5 system at 1500°C. Journal of the European Ceramic Society.

16Pad N. P. Padture (2016). Advanced structural ceramics in aerospace propulsion. Nature Materials 15, 804-809.

16Poe D. L. Poerschke, T. L. Barth, O. Fabrichnaya and C. G. Levi (2016). Phase equilibria and crystal chemistry in the calcia-silica-yttria system. Journal of the European Ceramic Society 36, 1743-1754.

16Poe2 D. L. Poerschke, T. L. Barth and C. G. Levi (2016). Equilibrium relationships between thermal barrier oxides and silicate melts. Acta Materialia 120, 302-314.

16Van J. S. M. Van Sluytman, C.A.; Levi, C.G. (2016). Tetragonal zirconia phase stability in the $YO_{1.5}$-$TaO_{2.5}$-ZrO_2 system. In Preparation.

48Tip C. F. Tipper (1948). Admiralty ship welding committee report No. R.3, London: H.M.S.O.

56Kin B. W. King, J. Schultz, E.A. Durbin and W.H. Duckworth (1956). Properties of Tantala Systems, pp. 1-40. Columbus, OH: Battelle Memorial Institute.

56Rei A. Reisman, F. Holtzberg, M. Berkenblit and M. Berry (1956). Reactions of the Group-Vb Pentoxides with Alkali Oxides and Carbonates .3. Thermal and X-Ray Phase Diagrams of the System K2o or K2co3 with Ta2o5. Journal of the American Chemical Society 78, 4514-4520.

59Kom A. I. Komkov (1959). The Structure of Natural Fergusonite and of a Polymorphic Modification. Kristallografiya 4, 836-841.

62Kel C. Keller (1962). Uber Ternare Oxide Des Niobs Und Tantals Vom Typ-ABO_4. Zeitschrift Fur Anorganische Und Allgemeine Chemie 318, 89-106.

64Roo H. P. Rooksby and E. A. D. White (1964). Rare-Earth Niobates and Tantalates of Defect Fluorite-Type and Weberite-Type Structures. Journal of the American Ceramic Society 47, 94-96.

65Pat M. G. M. Paton, E.N. (1965). A refinement of the crystal structure of yttria. Acta Crystallographica 19, 307-310.

65Roo H. P. Rooksby, E. A. D. White and S. A. Langston (1965). Perovskite-Type Rare-Earth Niobates and Tantalates. Journal of the American Ceramic Society 48, 447-&.

67Iye P. N. Iyer and A. J. Smith (1967). Double Oxides Containing Niobium, Tantalum, or Protactinium. IlL Systems Involving the Rare Earths Acta Crystallographica 23, 740-746.

67Wol G. M. Wolten (1967). The Structure of the *M′*-Phase of $YTaO_4$, a Third Fergusonite Polymorph. Acta Crystallographica 23, 939-944.

67Wol2 G. M. Wolten and A. B. Chase (1967). Synthetic Fergusonites and a New Polymorph of Yttrium Tantalate. American Mineralogist 52, 1536-&.

68Tru V. K. Trunov, L.N. Lykova, and N.S. Afonskii (1968). The structure of $Y_{0.33}TaO_3$ and $La_{0.33}TaO_3$. Vestnik Moskovskogo Universiteta, Khimiya 9, 55-58.

68War J. L. Waring and R. S. Roth (1968). Effect of Oxide Additions on Polymorphism of Tantalum Pentoxide (System Ta_2O_5-TiO_2). Journal of Research of the National Bureau of Standards Section a-Physics and Chemistry A 72, 175-+.

69Wol G. M. Wolten and A. B. Chase (1969). Single crystal data for β-Ta_2O_5 and A-KPO_3. Zeitschrift für Kristallographie 129, 365–368.

70Rot R. S. Roth, J. L. Waring and W. S. Brower (1970). Effect of Oxide Additions on Polymorphism of Tantalum Pentoxide .2. Stabilization of High Temperature Structure Type. Journal of Research of the National Bureau of Standards Section a-Physics and Chemistry A 74, 477-+.

70Rot2 R. S. Roth and J. L. Waring (1970). Effect of Oxide Additions on Polymorphism of Tantalum Pentoxide .3. Stabilization of Low Temperature Structure Type. Journal of Research of the National Bureau of Standards Section a-Physics and Chemistry A 74, 485-+.

70Rou A. Rouanet (1970). Contribution à l'étude des systèmes zircone-oxydes des lanthanides au voisinage de la fusion (Study of the zirconia-lanthanide oxides in the near the melting temperature), Thesis, Université des sciences et techniques de Montpellier 2, Montpellier.

71Phi C. M. Phillippi and K. S. Mazdiyasni (1971). Infrared and Raman Spectra of Zirconia Polymorphs. Journal of the American Ceramic Society 54, 254-+.

71Ste N. C. Stephenson and R. S. Roth (1971). Crystal Structure of High Temperature Form of Ta_2O_5. Journal of Solid State Chemistry 3, 145-&.

71Ste2 N. C. Stephenson and R. S. Roth (1971). Structural Systematics in Binary System Ta_2O_5-WO_3. V. Structure of Low-Temperature Form of Tantalum Oxide L-Ta_2O_5. Acta Crystallographica Section B-Structural Crystallography and Crystal Chemistry B 27, 1037-&.

72Gar R. C. Garvie and Nicholso.Ps (1972). Structure and Thermomechanical Properties of Partially Stabilized Zirconia in CaO-ZrO_2 System. Journal of the American Ceramic Society 55, 152-&.

72Gar2 R. C. Garvie (1972). Phase Analysis in Zirconia Systems. Journal of the American Ceramic Society 55, 303-&.

72Gla A. M. Glazer (1972). Classification of Tilted Octahedra in Perovskites. Acta Crystallographica Section B-Structural Science B 28, 3384-&.

72Jeh H. O. Jehn, E. (1972). High Temperature Solid-Solubility Limit and Phase Studies in the System Tantalum-Oxygen. Journal of Less-Common Metals 27, 297-309.

73Bla G. Blasse (1973). Vibrational-Spectra of Yttrium Niobate and Tantalate. Journal of Solid State Chemistry 7, 169-171.

73Bon I. A. Bondar, A.I. Kalinin, and L.N. Koroleva (1973). Physicochemical investigation of the system Y_2O_3-Ta_2O_5 and synthesis of single crystals of a series of niobates. Inorganic Materials 8, 1649-1650.

73Gal J. Galy and R. S. Roth (1973). Crystal-Structure of $Nb_2Zr_6O_{17}$. Journal of Solid State Chemistry 7, 277-285.

73Tad H. P. Tada, P.; Irwin, G. (1985). The stress analysis of cracks handbook, Second ed. St. Louis Missouri 63105: Paris Productions Incorp. .

74Gra J. Graham (1974). Crystal-Chemistry of Complex Niobium and Tantalum Oxides .3. Relationship between M, T, and M' Fergusonite Structures. American Mineralogist 59, 1045-1046.

74Sim L. A. H. Simpson, T.R.;Merrett, G. (1974). The application of the single-edge notched beam to fracture toughness testing of ceramics. Journal of Testing and Evaluation 2, 503-509.

75Gar R. C. Garvie, R. H. Hannink and R. T. Pascoe (1975). Ceramic Steel. Nature 258, 703-704.

76Ros H. J. H. G. S. Rossell (1976). The unit cell of YTa_7O_{19}, a new compound, and its isomorphism with the corresponding rare earth tantalates. Materials Research Bulletin 11, 1231-1236.

76Sha R. D. Shannon (1976). Revised Effective Ionic-Radii and Systematic Studies of Interatomic Distances in Halides and Chalcogenides. Acta Crystallographica Section A 32, 751-767.

76Tsu S. T. Tsunekawa, H. (1976). Domain switching behaviour of ferroelastic $LaNbO_4$ and $NdNbO_4$. Journal of Physical Society of Japan 50, 1523-1524.

77Bri L. H. Brixner, J. F. Whitney, F. C. Zumsteg and G. A. Jones (1977). Ferroelasticity in $LnNbO_4$-Type Rare-Earth Niobates. Abstracts of Papers of the American Chemical Society 173, 197-197.

77Por D. L. Porter and A. H. Heuer (1977). Mechanisms of Toughening Partially Stabilized Zirconia (Psz). Journal of the American Ceramic Society 60, 183-184.

77Ray S. P. Ray and V. S. Stubican (1977). Fluorite Related Ordered Compounds in ZrO_2-CaO and ZrO_2-Y_2O_3 Systems. Materials Research Bulletin 12, 549-556.

77Sco H. G. Scott (1977). The yttria-zirconia d phase. Acta Crystallographica B 33, 281-282.

78Han R. H. Hannink (1978). Growth morphology of the tetragonal phase in partially stabilized zirconia. Journal of Materials Science 13, 2487-2496.

79All J. G. Allpress and H. J. Rossell (1979). Fluorite-Related Phases Ln_3MO_7,Ln= Rare-Earth, Y, or Sc, M = Nb, Sb, or Ta .1. Crystal-Chemistry. Journal of Solid State Chemistry 27, 105-114.

79Ros H. J. Rossell (1979). Fluorite-Related Phases Ln_3MO_7, Ln = Rare-Earth, Y or Sc, M = Nb, Sb, or Ta .2. Structure Determination. Journal of Solid State Chemistry 27, 115-122.

79Ros2 H. J. Rossell (1979). Fluorite-Related Phases Ln_3MO_7, Ln = Rare-Earth, Y or Sc, M = Nb, Sb or Ta .3. Structure of the Nonstoichiometric Y_3TaO_7 Phase. Journal of Solid State Chemistry 27, 287-292.

79Ste S. Stecura (1979). Effects of compositional changes on the performance of a thermal barrier coating system, Third annual Conference on Composite and Advanced Materials, Meritt Island, Florida.

79Vas V. S. Vasil'ev, M.M. Pinaeva, and S.F. Shkirman (1979). Subsolidus Phase Equilibria in the Ta_2O_5-Y_2O_3 System. Russian Journal of Inorganic Chemistry 24, 1046-1053.

80Tsu2 S. Tsunekawa (1980). Mechanical Twins and Rubber-Like Behavior of Rare-Earth Orthoniobates .2. Mechanical behaviour in low temperature phase. Science Reports of the Research Institutes Tohoku University Series a-Physics Chemistry and Metallurgy 29, 1-28.

80TsuI S. Tsunekawa (1980). Mechanical Twins and Rubber-Like Behavior of Rare-Earth Orthoniobates .1. Structures and Domain-Walls of $RNbO_4$ Crystals. Science Reports of the Research Institutes Tohoku University Series a-Physics Chemistry and Metallurgy 29, 1-16.

81Ans G. R. Anstis, P. Chantikul, B. R. Lawn and D. B. Marshall (1981). A Critical-Evaluation of Indentation Techniques for Measuring Fracture-Toughness .1. Direct Crack Measurements. Journal of the American Ceramic Society 64, 533-538.

81Eva A. G. Evans, N. Burlingame, M. Drory and W. M. Kriven (1981). Martensitic Transformations in Zirconia - Particle-Size Effects and Toughening. Acta Metallurgica 29, 447-456.

81Kri W. M. F. Kriven, W.L.; Kennedy, S.W. (1981). The martensite crystallography of tetragonal zirconia, Vol. 3, Advances in Ceramics, Columbus, OH: American Ceramics Society.

82Heu A. H. Heuer, N. Claussen, W. M. Kriven and M. Ruhle (1982). Stability of Tetragonal ZrO_2 Particles in Ceramic Matrices. Journal of the American Ceramic Society 65, 642-650.

82Ho S. M. Ho (1982). On the Structural Chemistry of Zirconium-Oxide. Materials Science and Engineering 54, 23-29.

82McM R. M. Mcmeeking and A. G. Evans (1982). Mechanics of Transformation-Toughening in Brittle Materials. Journal of the American Ceramic Society 65, 242-246.

83And K. Ando, Y. Oishi, H. Hase and K. Kitazawa (1983). Oxygen Self-Diffusion in Single-Crystal Y_2O_3. Journal of the American Ceramic Society 66, C222-C223.

83Bri L. H. Brixner and H. Y. Chen (1983). On the Structural and Luminescent Properties of the M'LNTaO_4 Rare-Earth Tantalates. Journal of the Electrochemical Society 130, 2435-2443.

83Mic D. Michel, L. Mazerolles and M. P. Y. Jorba (1983). Fracture of Metastable Tetragonal Zirconia Crystals. Journal of Materials Science 18, 2618-2628.

83Pas C. Pascual and P. Duran (1983). Subsolidus Phase-Equilibria and Ordering in the System ZrO_2-Y_2O_3. Journal of the American Ceramic Society 66, 23-27.

83Tan E. Tani, M. Yoshimura and S. Sömiya (1983). Revised phase diagram of the system ZrO_2-CeO_2 below 1400°C. Journal of the American Ceramic Society 66, 506-510.

84Hor H. Horiuchi, A. J. Schultz, P. C. W. Leung and J. M. Williams (1984). Time-of-Flight Neutron-Diffraction Study of a Single-Crystal of Yttria-Stabilized Zirconia, $Zr(Y)O_{1.862}$, at High-Temperature and in an Applied Electrical-Field. Acta Crystallographica Section B-Structural Science 40, 367-372.

85Str T. E. Strangman (1985). Thermal Barrier Coatings for Turbine Airfoils. Thin Solid Films 127, 93-105.

86Vir A. V. Virkar and R. L. K. Matsumoto (1986). Ferroelastic domain switching as a toughening mechanism in tetragonal zirconia Journal of the American Ceramic Society 69, C224-C226.

87Heu A. H. Heuer (1987). Transformation Toughening in ZrO_2-Containing Ceramics. Journal of the American Ceramic Society 70, 689-698.

87Swa J. J. Swabb (1987). Evaluation of Japanese yttria tetragonal zirconia polycrystal (Y-TZP) materials. Ceramic Engineering and Science Proceedings 87, 886-891.

87Yok Y. Yokogawa, M. Yoshimura and S. Somiya (1987). Phase-Changes and Lattice Distortion in Fluorite-Related Phases of R_3TaO_7 ($3R_2O_3.Ta_2O_5$, R=Rare Earth). Materials Research Bulletin 22, 1449-1456.

88Yos M. Yoshimura (1988). Phase-Stability of Zirconia. American Ceramic Society Bulletin 67, 1950-1955.

89Mar K. M. Martin, G. (1989). ICDD Grant-in-Aid, Fargo, North Dakota, USA: North Dakota State University.

90Car O. N. Carlson (1990). The O-Y (Oxygen-Yttrium) System. Bulletin of Alloy Phase Diagrams 11, 61-66.

90Cif M. Ciftcioglu and M. J. Mayo (1990). Processing of nanocrystalline ceramics, Vol. 196, Superplasticity in Metals, Ceramics and Intermetallics,, edited by M. J. Mayo, M. Kobayashi and J. Wadsworth, pp. 77-86. San Francisco, CA: Materials Research Society.

90Dur P. Duran, M. Gonzalez, C. Moure, J. R. Jurado and C. Pascual (1990). A New Tentative Phase-Equilibrium Diagram for the ZrO_2-CeO_2 System in Air. Journal of Materials Science 25, 5001-5006.

90Iku Y. Ikuma, Y. Tsubaki, Y. Nakao, Y. Yokogawa and M. Yoshimura (1990). Oxygen Diffusion in the Fluorite-Related Phases of Y_2O_3-Ta_2O_5 and Ho_2O_3-Ta_2O_5 Systems. Solid State Ionics 40-1, 258-261.

90Jue J. F. Jue and A. V. Virkar (1990). Fabrication, Microstructural Characterization, and Mechanical-Properties of Polycrystalline T'-Zirconia. Journal of the American Ceramic Society 73, 3650-3657.

90Kim D. J. Kim (1990). Effect of Ta_2O_5, Nb_2O_5, and HfO_2 Alloying on the Transformability of Y_2O_3-Stabilized Tetragonal ZrO_2. Journal of the American Ceramic Society 73, 115-120.

90Meh K. Mehta and A. V. Virkar (1990). Fracture Mechanisms in Ferroelectric-Ferroelastic Lead Zirconate Titanate [Zr-Ti=0.54-0.46] Ceramics. Journal of the American Ceramic Society 73, 567-574.

90Sch U. Schaffrath and R. Gruehn (1990). Chemical-Transport Reactions of Compounds $LnTa_7O_{19}$-$NdTa_7O_{19}$ and Structure Refinement of $NdTa_7O_{19}$. Zeitschrift Fur Anorganische Und Allgemeine Chemie 588, 43-54.

91Cha C. J. Chan, F. F. Lange, M. Ruhle, J. F. Jue and A. V. Virkar (1991). Ferroelastic Domain Switching in Tetragonal Zirconia Single-Crystals Microstructural Aspects. Journal of the American Ceramic Society 74, 807-813.

91Hil M. Hillert and T. Sakuma (1991). Thermodynamic Modeling of the C-T Transformation in ZrO_2 Alloys. Acta Metallurgica Et Materialia 39, 1111-1115.

91Kim D.-J. Kim and T.-Y. Tien (1991). Phase stability and physical properties of cubic and tetragonal ZrO_2 in the system ZrO_2-Y_2O_3-Ta_2O_5. Journal of the American Ceramic Society 74, 3061-3065.

91Yok Y. Yokogawa and M. Yoshimura (1991). High-Temperature Phase-Relations in the System Y_2O_3-Ta_2O_5. Journal of the American Ceramic Society 74, 2077-2081.

91Zhe C. G. Zheng and A. R. West (1991). Compound and Solid-Solution Formation, Phase-Equilibria and Electrical-Properties in the Ceramic System Zro2-La2o3-Ta2o5. Journal of Materials Chemistry 1, 163-167.

92Bec P. F. Becher and M. V. Swain (1992). Grain-Size-Dependent Transformation Behavior in Polycrystalline Tetragonal Zirconia. Journal of the American Ceramic Society 75, 493-502.

93Kim S. Kim, M. Yashima, M. Kakihana and M. Yoshimura (1993). Electrical-Properties of Defect-Fluorite Phase in the System R_2O_3-Ta_2O_5 (R=Gd, Y, Er and Yb). Journal of Alloys and Compounds 192, 72-74.

93Law B. Lawn (1993). Fracture of Brittle Solids- Second Edition, ed. New York, USA: Cambridge University Press.

93May M. J. Mayo (1993). Synthesis and applications of nanocrystalline ceramics. Materials & Design 14, 323-329.

93Rus R. A. Russell and P. P. Phule (1993). Chemical Synthesis of Tantalum Zirconate from Alkoxide Precursors. Materials Science and Engineering B-Solid State Materials for Advanced Technology 21, 88-93.

94Bam C. E. Bamberger, T. J. Haverlock, S. S. Shoup, O. C. Kopp and N. A. Stump (1994). Compounds of Cerium, Titanium and Oxygen. Journal of Alloys and Compounds 204, 101-107.

94Gri G. Gritzner and C. Puchner (1994). V_2O_5, Nb_2O_5 and Ta_2O_5 Doped Zirconia Ceramics. Journal of the European Ceramic Society 13, 387-394.

94Li1 P. Li, I. W. Chen and J. E. Pennerhahn (1994). Effect of Dopants on Zirconia Stabilization - an X-Ray-Absorption Study .1. Trivalent Dopants. Journal of the American Ceramic Society 77, 118-128.

94Li2 P. Li and I. W. Chen (1994). Effect of Dopants on Zirconia Stabilization - an X-Ray-Absorption Study .2. Tetravalent Dopants. Journal of the American Ceramic Society 77, 1281-1288.

94Li3 P. Li, I. W. Chen and J. E. Pennerhahn (1994). Effect of Dopants on Zirconia Stabilization - an X-Ray-Absorption Study .3. Charge-Compensating Dopants. Journal of the American Ceramic Society 77, 1289-1295.

94Mii R. Miida, M. Tanaka, H. Arashi and M. Ishigame (1994). Electron-Diffraction and Microscope Studies of Zirconium-Oxides Stabilized by Several Metal-Oxides. Journal of Applied Crystallography 27, 67-73.

94Pre A. Preuss and R. Gruehn (1994). Preparation and Structure of Cerium Titanates Ce_2TiO_5, $Ce_2Ti_2O_7$, and $Ce_4Ti_9O_{24}$. Journal of Solid State Chemistry 110, 363-369.

95Mat S. A. Mather and P. K. Davies (1995). Nonequilibrium Phase-Formation in Oxides Prepared at Low-Temperature - Fergusonite-Related Phases. Journal of the American Ceramic Society 78, 2737-2745.

96Bor M. P. Borom, C. A. Johnson and L. A. Peluso (1996). Role of environmental deposits and operating surface temperature in spallation of air plasma sprayed thermal barrier coatings. Surface & Coatings Technology 86, 116-126.

96Jia L. Jian and C. M. Wayman (1996). Domain boundary and domain switching in a ceramic rare-earth orthoniobate $LaNbO_4$. Journal of the American Ceramic Society 79, 1642-1648.

96Jia2 L. Jian and C. M. Wayman (1996). Compressive behavior and domain-related shape memory effect in $LaNbO_4$ ceramics. Materials Letters 26, 1-7.

96Jon R. L. Jones (1996). Thermal barrier coatings, Metallurgical and Ceramic Protective Coatings, edited by K. H. Stern, pp. 194-235. London: Chapman & Hall.

96Yas M. Yashima, M. Kakihana and M. Yoshimura (1996). Metastable-stable phase diagrams in the zirconia-containing systems utilized in solid-oxide fuel cell application. Solid State Ionics 86-88, 1131-1149.

97Ada J. W. Adams, R. Ruh and K. S. Mazdiyasni (1997). Young's modulus, flexural strength, and fracture of yttria-stabilized zirconia versus temperature. Journal of the American Ceramic Society 80, 903-908.

97Irv J. T. S. Irvine, D. P. Fagg, J. Labrincha and F. M. B. Marques (1997). Development of novel anodes for solid oxide fuel cells. Catalysis Today 38, 467-472.

97Jia L. Jian and C. M. Wayman (1997). Monoclinic-to-tetragonal phase transformation in a ceramic rare-earth orthoniobate, $LaNbO_4$. Journal of the American Ceramic Society 80, 803-806.

97Kim D. J. Kim, J. W. Jang and H. L. Lee (1997). Effect of tetravalent dopants on Raman spectra of tetragonal zirconia. Journal of the American Ceramic Society 80, 1453-1461.

97Mii R. Miida, F. Sato, M. Tanaka, H. Naito and H. Arashi (1997). Locally modulated structures of fluorite-related Y_2O_3-Nb_2O_5 solid solutions. Journal of Applied Crystallography 30, 272-279.

97Yas M. Yashima, J. H. Lee, M. Kakihana and M. Yoshimura (1997). Raman spectral characterization of existing phases in the Y_2O_3-Nb_2O_5 system. Journal of Physics and Chemistry of Solids 58, 1593-1597.

98Fag D. P. Fagg and J. T. S. Irvine (1998). The Optimisation of Mixed Conduction in Potential SOFC Anode Materials. Ionics 4, 61-71.

98Kis E. H. Kisi and C. J. Howard (1998). Crystal structures of zirconia phase and their inter-relation. Key Engineering Materials 153-154, 1-36.

98Lev C. G. Levi (1998). Metastability and microstructure evolution in the synthesis of inorganics from precursors. Acta Materialia 46, 787-800.

98Sur G. Suresh, G. Seenivasan, M. V. Krishnaiah and P. S. Murti (1998). Investigation of the thermal conductivity of selected compounds of lanthanum, samarium and europium. Journal of Alloys and Compounds 269, L9-L12.

98Vir A. V. Virkar (1998). Role of ferroelasticity in toughening of zirconia ceramics. Key Engineering Materials 153-154, 183-210.

99Hul D. Hull (1999). Fractography - observing, measuring and interpreting fracture surface topography., ed. Cambridge, United Kingdom: Cambridge University Press.

99Nic J. R. Nicholls, M. J. Deakin and D. S. Rickerby (1999). A comparison between the erosion behaviour of thermal spray and electron beam physical vapour deposition thermal barrier coatings. Wear 233, 352-361.